AN IMPROVED SYNTHESIS OF THE PACIFIC BLUE FLUOROPHORE AND FLUORESCENCE-BASED STUDIES OF RECEPTOR-LIGAND INTERACTIONS

By

Molly M. Lee

Submitted to the graduate degree program in Medicinal Chemistry and the Graduate Faculty of the University of Kansas in partial fulfillment of the requirements for the degree of Doctor of Philosophy.

Chairperson Dr. Blake R. Peterson

Dr. Paul Hanson

Dr. Michael F. Rafferty

Dr. Michael S. Wolfe

Dr. Mario Rivera

Date Defended: December 12, 2016

The Dissertation Committee for Molly M. Lee

certifies that this is the approved version of the final dissertation:

AN IMPROVED SYNTHESIS OF THE PACIFIC BLUE FLUOROPHORE AND FLUORESCENCE-BASED STUDIES OF RECEPTOR-LIGAND INTERACTIONS

Chairperson Dr. Blake R. Peterson

Date Approved: December 12, 2016

ABSTRACT

Early-stage drug discovery and chemical biology projects often use fluorescence-based assays to obtain information about biological interactions and cellular processes. However, many of the best and brightest fluorophores suffer from major limitations such as very high cost and/or restrictive chemical properties that hinder their utility for studies of living biological systems. To create improved fluorescent molecular probes of receptor-ligand interactions and dynamic cellular processes, a major focus of this dissertation is on the bright coumarin-derived fluorophore Pacific Blue. Although Pacific Blue is commercially available, its high cost has restricted its utility as a building block for preparation of small molecule-derived and peptide-derived molecular probes. To overcome this limitation, we developed a new synthetic route that readily allows access to gram quantities of this fluorophore. This synthetic route is superior to previously published routes, and it can facilitate access to a wide variety of fluorescent ligands of receptors, biosensors, and related cellular probes.

Quantification of receptor-ligand interactions is important for screening of both on-target and off-target affinities of chemical probes and drug candidates. These assays must be cost-effective, efficient, and high-throughput to keep up with fast-paced needs of drug discovery projects. Toward this end, we characterized a new FRET pair, comprising the endogenous fluorescent amino acid tryptophan and Pacific Blue. We demonstrate that these fluorophores allow quantification of interactions between small molecules and tryptophan-containing proteins *in vitro*. We also synthesized and evaluated Pacific Blue derivatives of paclitaxel (Taxol) as tools to label microtubules, detect cellular efflux by P-glycoprotein (P-gp), and potentially explore some of the paradoxical clinical responses associated with the parent anticancer drug. We also characterized two other new FRET pairs, Pacific Blue-Pennsylvania Green and Pacific Blue-Oregon Green, and investigated the stability of disulfide linkers both *in vitro* and in living cells as models of drug delivery systems. Finally, using an alternative detection platform of fluorescence polarization, we describe the development of methods for the characterization of inhibitors of a protein-protein interaction involved in iron homeostasis in the pathogenic bacterium *Pseudomonas aeruginosa.* This research extends the utility of Pacific Blue and related fluorophores as tools for studies of chemical biology and drug discovery.

ACKNOWLEDGMENTS

First of all, I would like to thank my advisor, Dr. Blake R. Peterson, for his mentorship and guidance over the past five years. I sincerely appreciate the support he provided during both my research and academic endeavors. I thank the entire Department of Medicinal Chemistry Faculty for their support both in and out of the classroom and for the opportunities presented to me as a student in this department. Added graditude goes to the members of my dissertation committee, Dr. Mike Rafferty, Dr. Paul Hanson, Dr. Michael Wolfe, and Dr. Mario Rivera, for their time and consideration. Additionally, I would like to thank the Faculty of the NIH Dynamic Aspects of Chemical Biology Training Program, Dr. Tom Prisinzano, Dr. Audrey Lamb, and Dr. Paul Hanson for their mentorship and guidance throughout graduate school. Finally, I would like to thank Dr. Dan Appella for allowing me to complete my research rotation in his laboratory at the National Institute of Diabetes and Digestive and Kidney Diseases.

I also thank the members of the Peterson group that contributed to the work presented in this dissertation, particularly Zhe Gao. Dr. Chamani Perera, and Kelsey Knewtson. Additionally, I thank past and present Peterson group members Dr. David Hymel, Dr. Matt Meinig, Dr. Digamber Rane, and Yuwen Yin for thoughtful discussions and great friendship. Our collaboration with the Mario Rivera group is greatly appreciated, and I particularly thank Dr. Huili Yao for her contributions to this work.

Finally, I need to thank my parents, Don and Mary, my sisters Megan and Erin, and friends Leah Forsberg and Manwika Charaschanya for their continued support throughout my graduate career.

TABLE OF CONTENTS

ABSTRACT iii

ACKNOWLEDGMENTS v

TABLE OF CONTENTS vi

LIST OF FIGURES viii

LIST OF TABLES xxi

LIST OF SCHEMES xxii

Chapter 1. Fluorophores in Chemical Biology and Drug Discovery 1

- 1.1 Fluorescence in biology and medicine 1
- 1.2 Common fluorophores 4
  - 1.2.1 Fluorophores excited by UV light 4
  - 1.2.2 Fluorescein and its derivatives 5
- 1.3 Methods for quantifying receptor-ligand interactions 6
  - 1.3.1 Fluorescence polarization 8
  - 1.3.2 Förster resonance energy transfer 10
- 1.4 Outline of this dissertation 13
- 1.5 References 14

Chapter 2. Quantification of Small Molecule-Protein Interactions by FRET Between Tryptophan and the Pacific Blue Fluorophore 25

- 2.1 Introduction 25
- 2.2 Practical synthesis of the Pacific Blue fluorophore 28
- 2.3 Comparison of Trp-FRET acceptors 31
- 2.4 Ligand binding assay using Pacific Blue labeled biotin analogues 34

2.5 Competition-based assays with analogues of biotin 37
2.6 Comparison with fluorescence enhancement or quenching-based assays 39
2.7 Examination of Trp-FRET upon binding of a peptide to an antibody 40
2.8 Examination of the cell permeability of Pacific Blue derivatives 43
2.9 Conclusions 45
2.10 Experimental 46
    2.10.1 General experimental section 46
    2.10.2 Biological assays and protocols 49
    2.10.3 Synthetic procedures and compound characterization data ... 55
2.11 References 75

Chapter 3. Pacific Blue Derivatives of Paclitaxel Enable Selective Imaging of Mictrotubules and Assays of Efflux by P-glycoprotein in Living Cells 81
3.1 Introduction 81
3.2 Synthesis of Pacific Blue-Taxol derivatives 85
3.3 Quantification of affinities of PB-Taxols for microtubules 86
3.4 Confocal laser scanning microscopy of HeLa cells treated with fluorescence Taxol derivatives 90
3.5 Cellular toxicity of PB-Taxols in the presence and absence of verapamil ... 92
3.6 PB-Taxols label microtubules with greater specificity than Flutax-2 in live cells 95
3.7 PB-Taxol 44 is a substrate of P-glycoprotein 96
3.8 Conclusions 102
3.9 Experimental 103
    3.9.1 General experimental section 103
    3.9.2 Biological assays and protocols 104
    3.9.3 Synthetic procedures and compound characterization data 109
3.10 References 123

Chapter 4. Studies of Stability of Disulfides Using Förster Resonance Energy Transfer 133

4.1 Introduction 133
4.2 Characterization of Pacific Blue and Pennsylvania Green as a FRET pair 140
4.3 Stability of the disulfide of a cholesteryl carbamate delivery system in living Jurkat cells 144
4.4 Examination of the stability of disulfides linked to cholesteryl carbamate *in vitro* 146
4.5 Studies of the stability of disulfides conjugated to antibodies 151
4.6 Conclusions and future directions 154
4.7 Experimental 156
    4.7.1 General experimental section 156
    4.7.2 Biological assays and protocols 157
    4.7.3 Synthetic procedures and compound characterization data 162
4.8 References 193

Chapter 5. Development of Fluorescence-based Assays of Inhibitors of BfrB 199
5.1 Introduction 199
5.2 A new strategy to overcome multidrug resistance in *P. aeruginosa* 201
5.3 Toward a new fluorescence polarization assay for BfrB:Bfd inhibitors ... 203
5.4 Conclusions and future directions 208
5.5 Experimental 209
5.6 References 211

APPENDIX A. NMR Spectra of Compounds 215
APPENDIX B. Lists of Cell Lines and Plasmids 258

LIST OF FIGURES

Figure 1.1 Jablonski diagram illustrating the three-stage process of fluorescence, as well as the FRET process of energy transfer (described in Section 1.3.2) 3

Figure 1.2 Fluorophores excited with ultraviolet light. 5

Figure 1.3 Fluorophores excited with blue and green light. 6

Figure 1.4 Schematic representation of fluorescence polarization of two samples: protein-ligand complex (top) and free ligand in solution (bottom). 9

Figure 1.5 Energy transfer is dependent on the distance between two fluorophores and their spectral overlap. A: Schematic of the FRET process. B: Dependence of FRET efficiency on the distance between the FRET pair. The donor and acceptor are represented as blue and red circles. C: Graphical representation of spectral overlap of an ideal FRET pair. The emission spectra of donor fluorophore is depicted as a blue line, and absorption spectra of acceptor fluorophore as a red line, and spectral overlap J(λ) is shaded grey 12

Figure 2.1 Structures of tryptophan (**1**) and other fluorophores (**2**–**5**).. 27

Figure 2.2 Absorbance (Abs., solid lines) and emission (Em., dotted lines) spectra of Trp (**1**, black lines, 32 μM for Abs and 2 μM for Em.) and PB (**5**, blue lines, 32 μM for Abs and 50 nM for Em.) in PBS (pH 7.4). The spectral overlap integral (J(λ)) critical for FRET is shaded grey 27

Figure 2.3 A model of streptavidin (PDB 3RY2) docked to the PB-Biotin derivative **20** (CPK model) with autodock vina. In each monomer, residues Trp79, Trp108, and Trp120 are shown as CPK models. The distance between the most proximal Trp120 (marked) and the Pacific Blue moiety of **20** is ~ 11 Å. For clarity, only one bound ligand is shown. 32

Figure 2.4 A: Normalized absorbance (Abs., solid lines) and fluorescence (Fluor.) emission (Em., dotted lines) spectra of **20**-**23** (32 μM for Abs., 50 nM for Fluor.) in PBS. **20**-**23** were excited at their λ_{max} (405 nm (**20**), 330 nm (**21**), 375 nm (**22**), and 390 nm (**23**)). Intensities are % of λ_{max} of **20**. B: Structures of fluorophores linked to biotin (**20**-**23**). 32

Figure 2.5 Analysis of FRET upon binding of **20**-**23** (100 nM) to SA ([monomer] = 400 nM). Ex. of SA (295 nm) results in maximal Em. at 340 nm. After binding of **20**-**23**, FRET Em. was observed at 457 nm (**20**), 532 nm (**21**), 467 nm (**22**), and 475 nm (**23**). Addition of biotin (10 μM) blocked FRET from **20**. 33

Figure 2.6 A: Structures of analogues of biotin (**24**–**26**) used in direct binding assays. B: Quantification of the affinity (K_d) of SA for probes **24** (25 nM), **25** (5 nM), and **26** (25 nM) in PBS (pH 7.4) by Trp-FRET. Trp residues were excited at 295 nM and FRET was measured at 460 nm. Values were corrected to account for fluorescence quenching or enhancement upon binding. [SA] was based on monomeric protein. Dissociation constants (K_d) were calculated using a one-site binding model in GraphPad Prism. 35

Figure 2.7 A and B: Quantification of binding of **25** (A) and **26** (B) to SA in PBS (pH 7.4) by ITC. Thermodynamic parameters and K_d were calculated with Origin software. For **25**: [SA in sample cell] = 4 μM, [**25** in syringe] = 50 μM. For **26**: [SA in sample cell] = 10 μM, [**26** in syringe] = 150 μM. .. 36

Figure 2.8 Quantification of binding of **24** (25 nM) to SA in PBS (pH 7.4) by FP compared with Trp FRET. For Trp FRET, Trp residues were excited at 295 nm and FRET was measured at 460 nm. For FP, Pacific Blue was excited at 400 nm and polarization was measured at 460 nm. Values were corrected to account for fluorescence quenching or enhancement upon binding. [SA] was based on monomeric protein. Dissociation constants (K_d) were calculated using a one-site binding model in GraphPad Prism 36

Figure 2.9 A: Structures of non-fluorescent analogues of biotin (**27**–**30**) used in competition binding assays. B: Quantification of competitive inhibitory constants (K_i) of **27**–**30** for SA complexed with **26** (175 nM for SA, 25 nM for 26) by Trp-FRET. Trp residues were excited at 295 nM and FRET was measured at 460 nm. Values were corrected to account for fluorescence quenching upon binding. [SA] was based on monomeric protein. Half maximal inhibitory concentrations (IC_{50}) were calculated using a log(inhibitor) vs. response model in GraphPad Prism, and IC_{50} values were converted to K_i values. C: Evaluation of direct binding of **28** to SA by ITC. **28** was titrated into [SA] in PBS (pH 7.4) and thermodynamic parameters and K_d values were calculated with Origin software. [SA in sample cell] = 20 μM, [28 in syringe] = 250 μM. 38

Figure 2.10 Analysis of interactions with SA by quenching or enhancement of fluorescence. PB was excited at 400 nm, and intensity of fluorescence emission at 460 nm was measured. A–C: Quantification of K_d values for direct binding. D: Fluorescence resulting from competition of **28** for SA bound to probe **26** (25 nM). In D, due to poor fit to the binding model, the K_i value was not calculated. 40

Figure 2.11 A model of Fab fragment of Anti c-Myc (clone 9E10, PDB 2OR9[39]) bound to the c-Myc tag peptide (EQKLISEEDLN, CPK model). Tryptophan residues of the Fab are shown as CPK models. 41

Figure 2.12 Structures of free and Pacific Blue-linked Myc tag peptides **31**–**33** (Sequence of c-Myc tag: EQLISEEDLN)... 42

Figure 2.13 Analysis of FRET upon binding of **32** (100 nM) to anti c-Myc IgG (500 nM). Excitation of Trp (295 nm) results in maximal emission at 340 nm. After binding of **32**, emission due to FRET was observed at 455 nm (**32**). Addition of **31** (500 μM) blocked FRET from **32**. 42

Figure 2.14 Quantification of binding of **32** and **33** (100 nM) to anti c-Myc IgG in PBS (pH 7.4) by Trp FRET compared with FP. For FRET, Trp residues were excited at 295 nm and emission was measured at 460 nm. For FP, Pacific Blue was excited at 400 nm and polarization was measured at 460 nm. Dissociation constants (K_d) were calculated using a one-site binding model in GraphPad Prism.. 43

Figure 2.15 Confocal and DIC micrographs of HeLa cells treated with PB-biotin **20** (ethylenediamine linker, Figure 2.6) and PB-Hexyl-Biotin **34** (hexamethylenediamine linker). A: HeLa cells transiently transfected with pPA2-TS7A-WT-GTP-mRFP (false colored red) for 48 h and then treated with **20** (2 μM, false colored blue) for 30 min. B: HeLa cells transiently transfected with pPA2-TS7A-WT-GTP-mRFP (false colored red) for 48 h and then treated with **34** (2 μM, false colored blue) for 30 min. C: Structure of PB-Hexyl-Biotin, **34**.. 45

Figure 2.16 Analysis of compounds in PBS (pH 7.4) containing DMSO (0.5%). A: Determination of extinction coefficients of **20**–**23**. B: Measurement of the quantum yield of **20** in PBS (pH 7.4) relative to coumarin 102. 55

Figure 2.17 Analytical HPLC profile of **31** after preparative HPLC. Retention time = 7.5 min monitored by UV absorbance at 254 nm. Purity >95% by HPLC. 72

Figure 2.18 Analytical HPLC profile of **32** after preparative HPLC. Retention time = 9 min monitored by UV absorbance at 254 nm. Purity >95% by HPLC. 72

Figure 2.19 Analytical HPLC profile of **33** after preparative HPLC. Retention time = 9.5 min monitored by UV absorbance at 254 nm. Purity >95% by HPLC.. 73

Figure 3.1 A and C: Effect of Taxol on dynamics of tubulin polymerization. B: Structure of paclitaxel (Taxol, **41**).. 81

Figure 3.2 Structures of the known fluorescent taxoid Flutax-2 (**42**) and new Pacific Blue-linked derivatives of taxol (**43**–**45**). 84

Figure 3.3 Synthesis of PB-linked Taxol derivatives **43**–**45**. Reagents and conditions: a) *tert*-butyldimethylchlorosilane, imidazole; b) Fmoc-Gly-OH (**47**), Fmoc-βAla-OH (**48**), or Fmoc-GABA-OH (**49**), EDC, DMAP; c) piperidine (20%) in DMF; d) **15**, DIEA; e) TBAF (1.0 M) in THF. 86

Figure 3.4 Absorbance (Abs., solid lines, 10 μM) and emission (Em., dotted lines, 10 nM) spectra of **44** (blue lines) and Flutax-2 (**42**, green lines) in PBS (pH 7.4) with DMSO (10%) and triton X-100 (0.5%) added to prevent aggregation. 87

Figure 3.5 Quantification of the affinity (K_d) of cross-linked microtubules for probes **43**–**45** (25 nM) in GAB buffer (10 mM phosphate, 1 mM EDTA, 1 mM GTP, 3.4 M glycerol, pH 6.5) by enhancement of fluorescence upon binding. Protein concentration was based on monomeric tubulin. Dissociation constants (K_d) were calculated using a one-site binding model in GraphPad Prism. Addition of Taxol (10 μM) blocked the increase in fluorescence of **43**–**45** upon binding to cross-linked microtubules, suggesting the increase in fluorescent signal was due to a specific interaction of **43**–**45** at the Taxol-binding site. 88

Figure 3.6 Comparison of a cryo-EM structure of paclitaxel (**41**) bound to beta tubulin (PDB 3J6G,[56] panel A) with models of **42** (panel B) and **44** (panel C) generated by docking with Autodock vina. Low energy poses of **42** and **44** with high similarity to the bound geometry of **41** (panel A) are shown. 89

Figure 3.7 Verapamil enhances specific staining of microtubules by **44** in a dose dependent manner in HeLa cells. A: Confocal laser scanning (Ex. 405 nm, Em. 425-500 nm) and DIC micrographs of living HeLa cells treated with **44** (1 μM) and verapamil for 1 h at 37 °C. The concentrations of verapamil are increased from left to right (from 0, 0.1, 1, 10, 25 μM). B: Quantification of the intensity of blue fluorescence of HeLa cells by flow cytometry (Ex. 405 nm, Pacific Blue emission channel, 450/40 nm) after treatment with 44 (1 μM) in the presence (shaded blue) and absence (shaded grey) of 25 μM verapamil. An 8-fold increase was observed upon treatment with verapamil. C: Structure of verapamil, a P-gp inhibitor. 91

Figure 3.8 Confocal laser scanning and DIC micrographs of living HeLa cells treated with **43**–**45** (1 μM) in the presence (Panels B, D, F) or absence (Panels A, C, E) of verapamil (25 μM) for 1 h at 37 °C. 92

Figure 3.9 Analysis of cytotoxicity by flow cytometry. The cancer cell lines HeLa (A), PC-3 (B), and Jurkat (C) were treated with Taxol (**41**), Flutax-2 (**42**), Taxol-Gly-PB (**43**), Taxol-bAla-PB (**44**) and Taxol-GABA-PB (**45**) for 48 h in the absence (left) or presence (right) of verapamil (25 μM). Of the three lines, HeLa cells are reported to express P-gp. Under these conditions, verapamil was non-toxic below 1 mM. 94

Figure 3.10 Confocal laser scanning and DIC micrographs of HeLa cells treated with (A) **44** (1 µM) and **42** (5 µM) or (B) **42** (42, 5 µM) and Nile Red (0.5 µM) for 1 h at 37 °C in the presence of verapamil (25 µM). 96

Figure 3.11 Confocal and DIC micrographs of PC-3 cells treated with PB-Taxol **44**. A: PC-3 cells treated with **44** (1 µM) for 1 h. B: PC-3 cells transiently transfected with pHaMDR-EGFP plasmid for 48 h and then treated with **44** (1 µM) for 1 h. C: PC-3 cells transiently transfected with pHaMDR-EGFP plasmid for 48 h and treated with **44** (1 µM) and verapamil (25 µM) for 1 h. 97

Figure 3.12 Comparison of **44** with commercial fluorescent probes of efflux by P-gp. HCT-15 cells that overexpress P-gp were treated with **44** (5 µM, top row), Rho123 (1 µM, middle row), and $DiOC_2(3)$ (1 µM, bottom row) in the presence and absence of verapamil (25 µM) for 1 h at 37 °C. A and B: Confocal micrographs in the absence and presence of verapamil, respectively. C: Quantification of the intensity of blue fluorescence (**44**, Pacific Blue emission channel, 450/40 nm) or green fluorescence (Rho123, $DiOC_2(3)$, FITC emission channel, 530/30) by flow cytometry. D: Structures of Rhodamine 123 and $DiOC_2(3)$.......... 99

Figure 3.13 Fluorescence intensity measurements of probe **44** detect efflux by P-gp on 96-well plates. HeLa, HCT-15, and Jurkat cells were treated with **44** (1 µM for HeLa and Jurkat, 5 µM for HCT-15) in the presence (shaded blue) and absence (shaded grey) of verapamil (25 µM) for 30 min at 37 °C. Jurkat cells provide a negative control line that does not express P-gp. *p*-Values for HeLa: <0.0001 (****) and HCT-15: $p < 0.02$ (**) were calculated using a *t* test in GraphPad Prism. 101

Figure 3.14 Determination of extinction coefficients of **43**–**45** in PBS (pH 7.4) containing DMSO (10%) and triton X-100 (0.5%). 109

Figure 3.15 Analytical HPLC profile of **42** after preparative HPLC. Retention time = 17 min monitored by UV absorbance at 254 nm. Purity >95% by HPLC. 122

Figure 4.1 Receptor-mediated endocytosis of low-density lipoprotein (LDL)...... 134

Figure 4.2 A: Proposed mechanism of release of fluorescent probe **54** upon disruption of early endosomes. B: Structure of the cholesterylamine-PC4 endosome disruptor (**55**), a fluorescent disulfide *N*-alkyl-3β-cholesterylamine (**54**) and the products of cleavage (**56**, **57**). C: Confocal fluorescence and DIC micrographs[8] of Jurkat lymphocytes treated for 12 h with (i) **54** (2.5 μM) and (ii) **54** (2.5 μM) + **55** (2 μM). 136

Figure 4.3 Structures of the folate receptor-targeted disulfide-containing agents vintafolide (EC145) and a FRET reporter.[24] 139

Figure 4.4 Absorbance (Abs., solid lines) and emission (Em., dotted lines) spectra of PB (**5**, blue lines) and PG (**58**, green lines) in PBS (pH 7.4). The spectral overlap integral (J(λ)) critical for FRET is shaded grey. 140

Figure 4.5 A: Structures of the Pacific Blue-Pennsylvania Green FRET probe **59** and products of cleavage by DTT. B: Structure of the amide control **60**. C: Emission spectra of **60** (25 nM) alone (dashed black line) and with the addition of DTT (25 mM) for 75 min (solid red line). Panels D and E show spectroscopic properties of **59** over a 75 minute period following the addition of DTT (25 mM) in PBS (1% triton-X 100, pH=7.4). D: Emission spectra (λ_{ex} = 400 nm) over a 75 minute period. Spectra was collected at time = 0, 1, 4, 8, 13, 20, 30, and 75 min. The PB emission signal (λ_{max} = 455 nm) grew in intensity over time, while the PG emission signal (λ_{max} = 530 nm) decreased as the disulfide bond was cleaved over time. E: Cleavage kinetics of the increase in PB emission signal (λ_{max} = 455 nm) over time after the addition of DTT. The half-time of disulfide cleavage was determined using GraphPad Prism software. 143

Figure 4.6 A: Structures of PG-PB cholesteryl carbamate FRET probes **61** and **62**. B: Emission spectra of **61** (50 nM) alone (solid line) and with the addition of β-mercaptoethanol (300 mM, β-ME) for 3 h (dashed line). C: Cleavage kinetics of the increase in PB emission signal (λ_{max} = 460 nm) over time after the addition of DTT (100 mM) to **61** or **62** (20 nM). The half life and rate constant were determined using GraphPad Prism software. All experiments were run in PBS pH 7.4 containing 0.5% triton X-100. . 146

Figure 4.7 A: Structures of PB-OG cholesteryl carbamate FRET probes **63** and **64**. B: Emission spectra of **63** and **64** (50 nM) alone (**63**, blue dotted line; **64**, black dashed line) and with the addition of DTT (10 mM) for 2 h (**63**, blue solid line; **64**, red solid line). C: Kinetics of the increase in PB emission signal (λ_{max} = 460 nm) over time after the addition of DTT (10 mM) to **63** (50 nM). The half-time for cleavage of the disulfide was calculated using GraphPad Prism software. All experiments were run in PBS pH 7.4 containing 0.5% triton X-100 and 1% DMSO. 148

Figure 4.8 Measurement of the stability of the disulfide of **63** in Jurkat cells. A: Schematic representation of disulfide cleavage on cell surface and in endosomal compartments over time. B and C: Confocal laser scanning and DIC micrographs of living Jurkat cells treated with **63** (10 μM, panel B) or **64** (10 μM, panel C) for 28 h. At 28 h, treatment with **63** shows significantly less fluorescence in the FRET channel (Ex. 405 nm, Em. 515-600 nm, 2nd column, colored purple) in comparison to the PB channel (Ex. 405 nm, Em. 425-475 nm, 2nd column, colored cyan). Conversely, at 28 h, treatment with **64**, which has a stable amide bond, shows little fluorescence in the PB channel, and significant fluorescence in the FRET channel, indicating the molecule is still intact. D: Kinetics of cleavage calculated based on the increase in the FRET ratio over time after addition of **63** (10 μM) to living Jurkat cells, as measured by flow cytometry. The half-life was determined using GraphPad Prism software. FRET ratio = PB (Ex. 405 nm, 450 emission channel) / FRET (Ex. 405 nm, 530 nm emission channel) 150

Figure 4.9 Structures of the FRET-NHS esters (**65**–**69**) and conjugates of the anti-HER2 antibody Herceptin (**70**–**74**). 152

Figure 4.10 *In vitro* kinetics of cleavage of disulfides by following the increase in PB emission (λ_{max} = 455 nm) over time after the addition of GSH (5 mM) to **70** (DOL = 1.3) and **71** (DOL = 1.0) (100 nM, panel A) and **72** (50 nM, DOL = 2.3, panel B), **73** (50 nM, DOL = 1.0, panel B), and **74** (25 nM, DOL = 1.0, panel B) in PBS pH 7.4. The half-lives were determined using GraphPad Prism software. C: Kinetics of cleavage of the disulfide of **70** (5 μM, DOL = 1.3) based on the increase in FRET ratio over time after addition to living SkBr3 cells, as measured by confocal laser scanning microscopy. Blue/Green ratio = PB (Ex. 405 nm, Em. 415-500 nm) / Green (Ex. 488 nm, Em. 500-600 nm). Concentrations were based on [Herceptin]. .. 154

Figure 4.11 Structures of the FRET-NHS esters (**75**–**76**) and conjugates of Herceptin (**77**–**78**). 156

Figure 4.12 Reagents and conditions: a) **35,** TFA (30%) in DCM; b) HBTU, HOBt, DIEA, DMF; c) TFA (30%) in DCM. PG = 4-Carboxy Pennsylvania Green, PB = Pacific Blue. Schematic shown for **61**, but applies to **62** following general procedure 4A. 171

Figure 4.13 Analytical HPLC profile of **61** after preparative HPLC. Retention time = 19.5 min monitored by UV absorbance at 254 nm. Purity >95% by HPLC. 174

Figure 4.14 Analytical HPLC profile of **62** after preparative HPLC. Retention time = 19 min monitored by UV absorbance at 254 nm. Purity >90% by HPLC. 175

Figure 4.15 Reagents and conditions: d) *N*-Boc-ethylenediamine**,** HATU, DIEA, DMF; e) 30% TFA in DCM; f) DIEA, DMF; OG = Oregon Green, PB = Pacific Blue. 175

Figure 4.16 Analytical HPLC profile of **63** after preparative HPLC. Retention time = 19 min monitored by UV absorbance at 254 nm. Purity >95% by HPLC. 178

Figure 4.17 Analytical HPLC profile of **64** after preparative HPLC. Retention time = 18.5 min monitored by UV absorbance at 254 nm. Purity >95% by HPLC. 180

Figure 4.18 Reagents and conditions: g) **79,** 30% TFA in DCM; h) HATU, DIEA, DMF; j) i. 30% TFA in DCM, ii. DIEA, DMF. Schematic shown for **66**, but applies to **65**–**69** following general procedure 4D 181

Figure 4.19 Analytical HPLC profile of **65** after preparative HPLC. Retention time = 10.5 min monitored by UV absorbance at 254 nm. Purity >90% by HPLC. 183

Figure 4.20 Analytical HPLC profile of **66** after preparative HPLC. Retention time = 10 min monitored by UV absorbance at 254 nm. Purity >90% by HPLC. 184

Figure 4.21 Analytical HPLC profile of **67** after preparative HPLC. Retention time = 11 min monitored by UV absorbance at 254 nm. Purity >90% by HPLC.. 185

Figure 4.22 Analytical HPLC profile of **68** after preparative HPLC. Retention time = 10.5 min monitored by UV absorbance at 254 nm. Purity >95% by HPLC. 186

Figure 4.23 Analytical HPLC profile of **69** after preparative HPLC. Retention time = 10 min monitored by UV absorbance at 254 nm. Purity >90% by HPLC.. 187

Figure 4.24 Reagents and conditions: k) OG-NHS ester, DIEA, DMF; l) 20% piperidine in DMF; m) DIEA, DMF 187

Figure 4.25 Analytical HPLC profile of **75** after preparative HPLC. Retention time = 15 min monitored by UV absorbance at 254 nm. Purity >90% by HPLC. 190

Figure 4.26 Analytical HPLC profile of **76** after preparative HPLC. Retention time = 13.5 min monitored by UV absorbance at 254 nm. Purity >95% by HPLC. 192

Figure 5.1 Structure of FC996 (4-hydroxyphthalimide), the initial hit found by the Rivera group via a FBDD screen. The phthalimide ring is numbered to clarify the differential substitution patterns of analogues that were later investigated 202

Figure 5.2 A: Structure of inhibitor **92**, a second generation derivative of FC996. B: The excitation spectrum (λ_{em} = 530 nm, solid line) and emission spectrum (λ_{em} = 380 nm dotted line) of **92** (10 μM) in KP_i (100 mM, pH 7.6), containing TCEP (1 mM) are shown. 204

Figure 5.3 Spectral evidence of degradation of compound **92** in KP_i buffer (100 mM). Absorbance (panel A) and emission (panel B) spectra of **92** over a 90-minute period. As **92** is incubated in buffer, it degrades to form 3-aminophthalmide (panel C). The absorbance is slightly decreased and blue-shifted, while the emission is significantly increased. D: Quantification of the affinity (K_d) of Apo-BfrB for probe **92** (5 μM) in KP_i (100 mM, pH 7.6) containing TCEP (1 mM) by FP. The probe was briefly incubated in buffer for 5 min and with protein for 5 min to minimize degradation. Values were corrected to account for fluorescence enhancement upon binding. [Apo-BfrB] was based on a dimer (two subunits). Dissociation constants (K_d) were calculated using a one-site binding model in GraphPad Prism. 206

Figure 5.4 X-ray crystal structure of *Pa*-BfrB[20] (PDB 3IS7) with models of 3-aminophthalimide bound in two different poses generated with Autodock vina. 207

Figure 5.4 A: Structure of the third generation inhibitor **93**. B: Quantification of the affinity (K_d) of Apo-BfrB for probe **93** (1 μM) in 100 mM KP_i (pH 7.6) with TCEP (1 mM) by FP. Values were corrected to account for fluorescence enhancement upon binding. [ApoBfrB] was based on monomeric protein. Dissociation constants (K_d) were calculated using a one-site binding model in GraphPad Prism. 208

Figure 6.1 ^{1}H NMR (500 MHz, DMSO-d_6) spectrum of **5** 215

Figure 6.2 ^{13}C NMR (126 MHz, DMSO-d_6) spectrum of **5**. 215

Figure 6.3 ^{19}F NMR (376 MHz, DMSO-d_6, decoupled) spectrum of **5**. 216

Figure 6.4 ^{1}H NMR (500 MHz, DMSO-d_6) spectrum of **11** 216

Figure 6.5 ^{13}C NMR (126 MHz, DMSO-d_6) spectrum of **11**. 217

Figure 6.6 ^{19}F NMR (376 MHz, DMSO-d_6, decoupled) spectrum of **11**. 217

Figure 6.7 ^{1}H NMR (500 MHz, DMSO-d_6) spectrum of **15** 218

Figure 6.8 ^{13}C NMR (126 MHz, DMSO-d_6) spectrum of **15**. 218

Figure 6.9 ^{19}F NMR (376 MHz, DMSO-d_6, decoupled) spectrum of **15**. 219

Figure 6.10 ^{1}H NMR (500 MHz, CDCl$_3$) spectrum of **17**. 219

Figure 6.11 ^{13}C NMR (126 MHz, CDCl$_3$) spectrum of **17**. 220

Figure 6.12 ^{19}F NMR (376 MHz, CDCl$_3$, decoupled) spectrum of **17**. 220

Figure 6.13 ^{1}H NMR (500 MHz, CDCl$_3$) spectrum of **18**. 221

Figure 6.14 ^{13}C NMR (126 MHz, CDCl$_3$) spectrum of **18**. 221

Figure 6.15 ^{19}F NMR (376 MHz, CDCl$_3$, decoupled) spectrum of **18**. 222

Figure 6.16 ^{1}H NMR (500 MHz, CDCl$_3$) spectrum of **19**. 222

Figure 6.17 ^{13}C NMR (126 MHz, CDCl$_3$) spectrum of **19**. 223

Figure 6.18 ^{19}F NMR (376 MHz, CDCl$_3$, decoupled) spectrum of **19**. 223

Figure 6.19 ^{1}H NMR (500 MHz, DMSO-d_6) spectrum of **20** 224

Figure 6.20 ^{13}C NMR (126 MHz, DMSO-d_6) spectrum of **20**. 224

Figure 6.21 ^{1}H NMR (500 MHz, DMSO-d_6) spectrum of **21** 225

Figure 6.22 ^{13}C NMR (126 MHz, DMSO-d_6) spectrum of **21**. 225

Figure 6.23 ^{1}H NMR (500 MHz, DMSO-d_6) spectrum of **22** 226

Figure 6.24 ^{13}C NMR (126 MHz, DMSO-d_6) spectrum of **22**. 226

Figure 6.25 ^{1}H NMR (500 MHz, DMSO-d_6) spectrum of **23** 227

Figure 6.26 ^{13}C NMR (126 MHz, DMSO-d_6) spectrum of **23**. 227

Figure 6.27 ^{1}H NMR (500 MHz, DMSO-d_6) spectrum of **24** 228

Figure 6.28 ^{13}C NMR (126 MHz, DMSO-d_6) spectrum of **24**. 228

Figure 6.29 ^{1}H NMR (500 MHz, DMSO-d_6) spectrum of **25** 229

Figure 6.30 ^{13}C NMR (126 MHz, DMSO-d_6) spectrum of **25**. 229

Figure 6.31 ^{1}H NMR (500 MHz, DMSO-d_6) spectrum of **26** 230

Figure 6.32 ^{13}C NMR (126 MHz, DMSO-d_6) spectrum of **26**. 230

Figure 6.33 ^{1}H NMR (500 MHz, CD_3OD) spectrum of **28** 231

Figure 6.34 ^{13}C NMR (126 MHz, CD_3OD) spectrum of **28**. 231

Figure 6.35 ^{1}H NMR (500 MHz, $CDCl_3$) spectrum of **29** 232

Figure 6.36 ^{13}C NMR (126 MHz, $CDCl_3$) spectrum of **29**. 232

Figure 6.37 ^{1}H NMR (500 MHz, $CDCl_3$) spectrum of **30** 233

Figure 6.38 ^{13}C NMR (126 MHz, $CDCl_3$) spectrum of **30** 233

Figure 6.39 ^{1}H NMR (500 MHz, DMSO-d_6) spectrum of **34** 234

Figure 6.40 ^{13}C NMR (126 MHz, DMSO-d_6) spectrum of **34** 234

Figure 6.41 ^{1}H NMR (500 MHz, DMSO-d_6) spectrum of **35** 235

Figure 6.42 ^{13}C NMR (126 MHz, DMSO-d_6) spectrum of **35** 235

Figure 6.43 ^{1}H NMR (500 MHz, DMSO-d_6) spectrum of **36** 236

Figure 6.44 ^{13}C NMR (126 MHz, DMSO-d_6) spectrum of **36** 236

Figure 6.45 ^{1}H NMR (500 MHz, DMSO-d_6) spectrum of **37** 237

Figure 6.46 ^{13}C NMR (126 MHz, DMSO-d_6) spectrum of **37** 237

Figure 6.47 ^{1}H NMR (500 MHz, $CDCl_3$) spectrum of **38** 238

Figure 6.48 ^{13}C NMR (126 MHz, $CDCl_3$) spectrum of **38** 238

Figure 6.49 ^{1}H NMR (500 MHz, $CDCl_3$) spectrum of **39** 239

Figure 6.50 ^{13}C NMR (126 MHz, $CDCl_3$) spectrum of **39** 239

Figure 6.51 ^{1}H NMR (500 MHz, DMSO-d_6) spectrum of **40** 240

Figure 6.52 ^{13}C NMR (126 MHz, DMSO-d_6) spectrum of **40** 240

Figure 6.53 ^{1}H NMR (500 MHz, $CDCl_3$) spectrum of **43** 241

Figure 6.54 ^{13}C NMR (126 MHz, $CDCl_3$) spectrum of **43** 241

Figure 6.55 ^{1}H NMR (500 MHz, $CDCl_3$) spectrum of **44** 242
Figure 6.56 ^{13}C NMR (126 MHz, $CDCl_3$) spectrum of **44** 242
Figure 6.57 ^{1}H NMR (500 MHz, $CDCl_3$) spectrum of **45** 243
Figure 6.58 ^{13}C NMR (126 MHz, $CDCl_3$) spectrum of **45** 243
Figure 6.59 ^{1}H NMR (500 MHz, $CDCl_3$) spectrum of **46** 244
Figure 6.60 ^{13}C NMR (126 MHz, $CDCl_3$) spectrum of **46** 244
Figure 6.61 ^{1}H NMR (500 MHz, $CDCl_3$) spectrum of **47** 245
Figure 6.62 ^{13}C NMR (126 MHz, $CDCl_3$) spectrum of **47** 245
Figure 6.63 ^{1}H NMR (500 MHz, $CDCl_3$) spectrum of **48** 246
Figure 6.64 ^{13}C NMR (126 MHz, $CDCl_3$) spectrum of **48** 246
Figure 6.65 ^{1}H NMR (500 MHz, $CDCl_3$) spectrum of **49** 247
Figure 6.66 ^{13}C NMR (126 MHz, $CDCl_3$) spectrum of **49** 247
Figure 6.67 ^{1}H NMR (500 MHz, $CDCl_3$) spectrum of **51** 248
Figure 6.68 ^{13}C NMR (126 MHz, $CDCl_3$) spectrum of **51** 248
Figure 6.69 ^{1}H NMR (500 MHz, CD_3OD) spectrum of **59** 249
Figure 6.70 ^{13}C NMR (126 MHz, CD_3OD) spectrum of **59**. 249
Figure 6.71 ^{1}H NMR (500 MHz, CD_3OD) spectrum of **60** 250
Figure 6.72 ^{13}C NMR (126 MHz, CD_3OD) spectrum of **60**. 250
Figure 6.73 ^{1}H NMR (500 MHz, DMSO-d_6) spectrum of **79** 251
Figure 6.74 ^{13}C NMR (126 MHz, DMSO-d_6) spectrum of **79** 251
Figure 6.75 ^{1}H NMR (500 MHz, DMSO-d_6) spectrum of **80** 252
Figure 6.76 ^{13}C NMR (126 MHz, DMSO-d_6) spectrum of **80** 252
Figure 6.77 ^{1}H NMR (500 MHz, DMSO-d_6) spectrum of **81** 253

Figure 6.78 ^{13}C NMR (126 MHz, DMSO-d_6) spectrum of **81** 253

Figure 6.79 ^{1}H NMR (500 MHz, DMSO-d_6) spectrum of **82** 254

Figure 6.80 ^{13}C NMR (126 MHz, DMSO-d_6) spectrum of **82** 254

Figure 6.81 ^{1}H NMR (500 MHz, DMSO-d_6) spectrum of **83** 255

Figure 6.82 ^{13}C NMR (126 MHz, DMSO-d_6) spectrum of **83** 255

Figure 6.83 ^{1}H NMR (500 MHz, DMSO-d_6) spectrum of **86** 256

Figure 6.84 ^{13}C NMR (126 MHz, DMSO-d_6) spectrum of **86** 256

Figure 6.85 ^{1}H NMR (500 MHz, DMSO-d_6) spectrum of **87** 257

Figure 6.86 ^{13}C NMR (126 MHz, DMSO-d_6) spectrum of **87** 257

LIST OF TABLES

Table 1.1 Representative spectroscopic properties of fluorescent dyes as illustrated for fluorescein in 0.1 M NaOH. 3

Table 1.2 Summary of biophysical techniques for detecting and/or quantifying small molecule-protein interactions. 7

Table 2.1 Comparison of the cost of reagents needed to make one gram of Pacific Blue-NHS ester (**15**). Costs were estimated based on yields published for each synthetic step and the least expensive reagents available for purchase from Sigma Aldrich, Acros Organics, Alfa Aesar, Oakwood Chemicals, or Chem-Impex International. 31

Table 2.2 Photophysical properties of fluorescent probes. The intensity (I_{ad}) of FRET acceptors (100 nM) was measured at Em. λ_{max} when bound to SA (400 nM, Ex. 295 nm) and normalized to I_d. The efficiency (E) of FRET with Trp when bound to SA was calculated as $E = 1 - I_{da}/I_d$. The FRET fold effect (FF) was calculated as $FF = I_{ad}/I_a$. R_0 is the theoretical Förster distance calculated for each Trp-acceptor pair. I_{da} = intensity of Em. of Trp (340 nm) in the presence of the acceptor. I_d = intensity of Em. of Trp (340 nm) in the absence of acceptor. I_{ad} and I_a = intensity of Em. of the acceptor (457 nm (**20**), 532 nm (**21**), 467 nm (**22**), and 475 nm (**23**)) in the presence and absence of the donor (SA), respectively 34

Table 3.1 Photophysical properties of fluorescent probes. The intensity (I_{ad}) of FRET acceptors (100 nM) was measured at Em. λ_{max} when bound to SA (400 nM, Ex. 295 nm) and normalized to I_d. The efficiency (E) of FRET with Trp when bound to SA was calculated as $E = 1 - I_{da}/I_d$. The FRET fold effect (FF) was calculated as $FF = I_{ad}/I_a$. R_0 is the theoretical Förster distance calculated for each Trp-acceptor pair. I_{da} = intensity of Em. of Trp (340 nm) in the presence of the acceptor. I_d = intensity of Em. of Trp (340 nm) in the absence of acceptor. I_{ad} and I_a = intensity of Em. of the acceptor (457 nm (**20**), 532 nm (**21**), 467 nm (**22**), and 475 nm (**23**)) in the presence and absence of the donor (SA), respectively 100

LIST OF SCHEMES

Scheme 2.1 A previously published synthesis of the Pacific Blue fluorophore...... 29

Scheme 2.2 An improved gram-scale synthesis of the Pacific Blue fluorophore.... 30

Chapter 1

Fluorophores in Chemical Biology and Drug Discovery

Unmet medical needs are often addressed by initiation of a drug discovery program. This program is generally designed to target a specific protein, pathway, or phenotype thought to be important for the etiology of a particular disease. This process is often very challenging and costly and can require 12–15 years from initiation to approval and cost over $1 billion.[1] An integral part of this process can involve chemical biology, where small molecule probes are used to screen for new 'hits' using high throughput platforms, validate targets, and investigate potential off-target effects. Chemical biology, a field at the interface between chemistry and biology, focuses on the use of small molecules to study biology. This field utilizes interdisciplinary methods that draw from diverse areas including chemical synthesis, analytical chemistry, medicinal chemistry, and drug discovery. The use of small molecule probes in biochemical (*in vitro*) and cellular assays is often critical in the understanding of biological processes and quantification of biomolecular interactions that form the basis of unmet clinical needs.

1.1. Fluorescence in biology and medicine

Fluorescent biosensors are widely used to study molecular interactions in biology and medicine. These types of chemical probes have been vital for understanding complex biological processes in cells, tissues, and animals. Fluorescence has been particularly important in the development of live cell imaging and high throughput screening in drug discovery. Molecules that fluoresce are called fluorophores. In biology, fluorophores are typically designed to localize in a particular region of a biological specimen (e.g. through interactions with a specific protein target) or respond to a stimulus (e.g. activation of enzymatic substrates). [2-4]

Fluorescence, a photophysical process first described in 1852,[5] involves three stages: excitation, excited-state lifetime, and fluorescence emission (depicted in Figure 1.1). The fluorophore first absorbs photons from an external source such as an incandescent lamp or laser.[6] Following excitation, the molecule undergoes conformational changes and interacts readily with its environment until it relaxes to the singlet excited state (S_1). A photon of energy is then emitted to return the fluorophore to its ground state through the release of energy. Not all molecules are returned to the ground state through fluorescence emission, as other processes such as Förster resonance energy transfer (FRET, discussed in Section 1.3.2) and collisional quenching can occur.[7] Fluorophores have several specific properties, including defined absorbance, excitation, and emission spectra, extinction coefficient (ε), quantum yield (Φ), and fluorescence lifetime (τ). Examples of these properties are listed in Table 1.1 for the common fluorophore fluorescein.

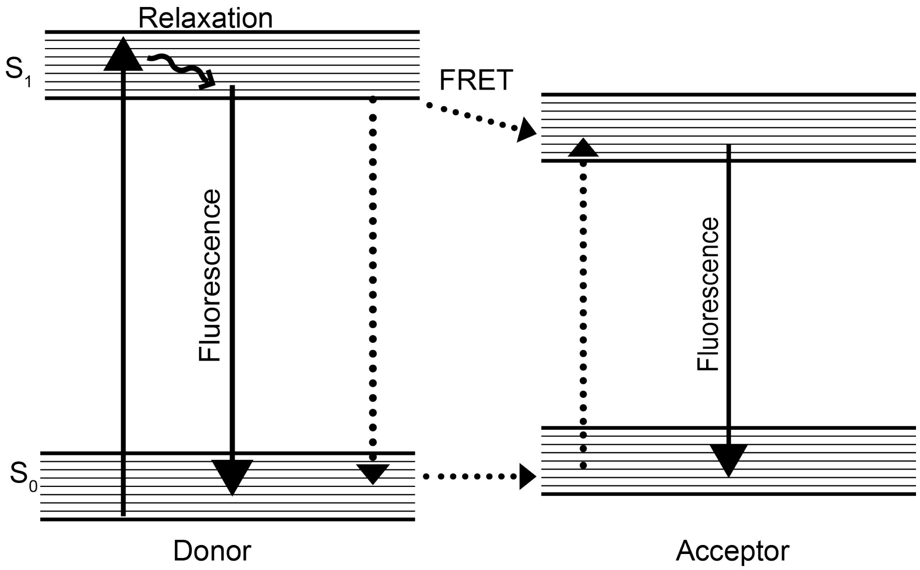

Figure 1.1. Jablonski diagram illustrating the three-stage process of fluorescence, as well as the FRET process of energy transfer (described in Section 1.3.2).

Table 1.1. Representative spectroscopic properties of fluorescent dyes as illustrated for fluorescein in 0.1 M NaOH.

Property	**Description**	**Value for fluorescein**[8, 9]
Absorbance spectra	A plot of wavelength versus absorbance	λ_{max} = 490 nm
Excitation spectra	A plot of wavelength versus the number of photons excited for a given emission wavelength	λ_{max} = 490 nm
Extinction coefficient (ε)	Capacity for absorption of light at a given wavelength	76,900 $M^{-1}cm^{-1}$ at λ_{max}
Fluorescence emission spectra	A plot of emission wavelength versus emitted photons	λ_{max} = 510 nm
Quantum yield (Φ)	Amount of photons emitted per photons absorbed	0.86
Fluorescence lifetime (τ)	The average time between excitation and emission (typically 1-10 ns)	4.16 ns

1.2. Common fluorophores

Small molecule fluorophores typically consist of polyaromatic hydrocarbons or heterocycles. Extended conjugation shifts the absorption and fluorescence emission spectra to longer wavelengths. Other types of fluorophores, including quantum dots[10] and fluorescent polymers[11] and proteins[12] are well known but will not be described in detail here. Changes to the environment surrounding the fluorophore (i.e. solvents, the presence of quenchers, and pH) can have a large effect on spectroscopic properties. Some general classes of fluorophores, categorized by excitation wavelength, are described below.

1.2.1. Fluorophores excited by UV light

Two of the most abundant fluorescent molecules commonly observed in nature are the natural amino acids tryptophan and tyrosine (Figure 1.2). Because these fluorophores absorb photons at ~280 nm,[13] they have limited use in live cell imaging, as toxicity and autofluorescence arise when cells and tissue are exposed to the high energy UV radiation needed to excite these residues. Nonetheless, these fluorophores are useful for *in vitro* applications including studies of protein folding and dynamics, and small molecule-protein and peptide-protein interactions.[14-18] Longer wavelength fluorophores excited by UV light include the coumarins and pyrenes. Coumarins are abundant in nature,[19] and substitution at the 7-position gives rise to highly fluorescent molecules. These fluorophores are attractive, as they are smaller in size and often are spectrally orthogonal to other popular fluorophores with longer wavelength absorption and emission properties. Fluorophores such as the pyrene derivative Alexa Fluor 405[2] and the coumarin derivative Pacific Blue[20] (Figure 1.2) are valued since they are well matched to the 405 nm spectra line of violet diode lasers found on flow cytometry and fluorescence microscopy instrumentation.

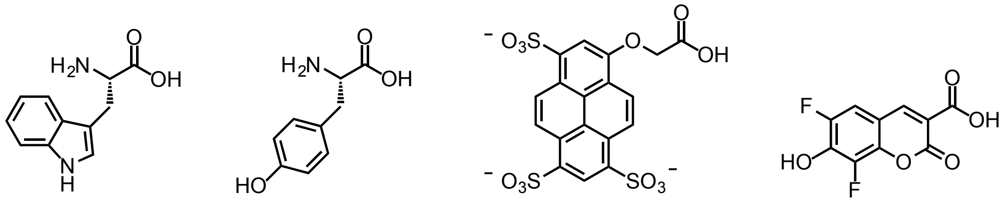

Tryptophan Tyrosine Alexa Fluor 405 Pacific Blue

Figure 1.2. Fluorophores excited with ultraviolet light.

1.2.2. Fluorescein and its derivatives

Fluorophores that can be excited by blue and green light are generally more commonly used for chemical biology applications. This class of molecules includes fluoresceins, BODIPY, and rhodamines (Figure 1.3). Following its original synthesis in 1871,[21] fluorescein has now become the most widely used fluorophore in science due to its high absorptivity, quantum yield, and water solubility. Countless fluorescein derivatives have been made to date.[22-29] Some derivatives, including Oregon Green[23] and Pennsylvania Green[22] (Figure 1.3), have incorporated fluorine atoms on the xanthene core to increase photostability by reducing reactivity with photogenerated singlet oxygen.[30] In addition, the fluorine groups decrease the pK_a of the phenol of compounds such as Oregon Green and Pennsylvania Green to ~4.8, thus reducing the strong sensitivity of fluorescein to changes in pH in biological systems. Fluorescein and its derivatives have traditionally been attractive because their absorption and fluorescence emission properties closely match the 488 nm spectral line of the common argon-ion laser. Other derivatives include rhodamines, corresponding to amino analogues of fluorescein. The rhodamine scaffold was first described in 1887,[31] and this class of molecules is generally red-shifted in comparison to fluorescein, absorbing green light and emitting yellow light.[32] These fluorophores are typically pH insensitive and possess high photostability. Numerous derivatives have been developed for use as fluorescent labels for diverse applications including dyes for imaging of biological processes of the nematode worm *C. elegans*[33, 34] and mice.[35, 36]

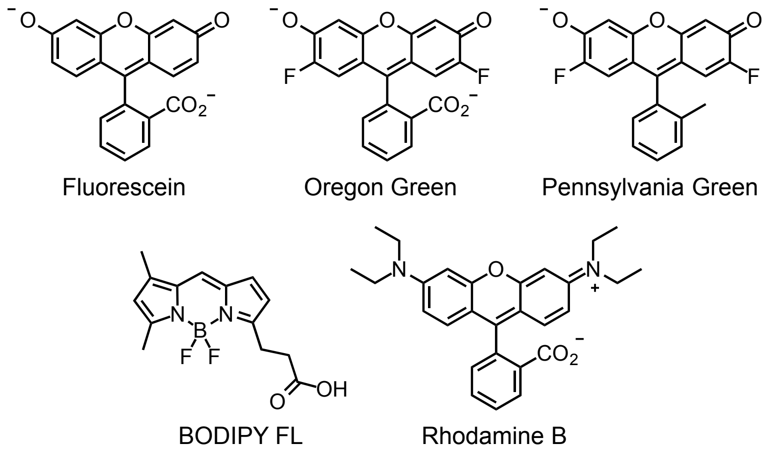

Fluorescein Oregon Green Pennsylvania Green

BODIPY FL Rhodamine B

Figure 1.3. Fluorophores excited with blue and green light.

1.3. Methods for quantifying receptor-ligand interactions

Receptor-ligand interactions play a fundamental role in countless biological processes. Discovering and quantifying these interactions is vital for studying cellular pathways and finding new molecules of medical importance. In the early stages of drug discovery, compounds of interest are identified based on many factors, often starting with affinity for a biological target. Labeled compounds that show high affinity and specificity for a target can be used in high throughput screens to identify other compounds that bind the same target, and also can be used later in the process, for example in competition binding assays, to quantify and categorize other compounds on the path to finding a clinical drug candidate. Approaches for quantifying these interactions can be categorized into fluorescence-based and non-fluorescence based methods. Fluorescence-based methods include fluorescence polarization (FP),[37] Förster resonance energy transfer (FRET),[38] and fluorescence intensity,[39] while non-fluorescence based techniques include isothermal titration calorimetry (ITC),[40] surface plasmon resonance (SPR),[41] ligand-observed NMR,[42] differential scanning fluorimetry (DSF),[43] protein X-ray crystallography,[44] UV/Vis spectroscopy,[45] equilibrium dialysis,[46] and radiolabeling.[47] The limitations of each technique are listed in Table 1.2, while Sections 1.3.1-2 focus on FP and FRET application.

Table 1.2. Summary of biophysical techniques for detecting and/or quantifying small molecule-protein interactions.[48, 49]

Technique	**Throughput**	**Disadvantages**
Fluorescence-based methods (FP, FRET, Fl. intensity)	High	• Prone to false positives • Typically require a competition assay format
Isothermal titration calorimetry (ITC)	Low	• Material intensive • Not applicable to all systems, as large heat changes are required
Surface plasmon resonance (SPR)	Intermediate	• Prone to false positives • Target or ligand must be immobilized
Differential scanning fluorimetry (DSF)	High	• Extensive optimization necessary • Prone to artifacts
Ligand-observed NMR	Intermediate	• Material intensive • Expensive isotope labeling may be required • Generally, limited to small proteins
X-ray crystallography	Low	• Protein target must crystallize • Expensive X-ray sources required

UV/VIS spectroscopy	Medium	• False negatives and positives • Low sensitivity requires high concentrations
Equilibrium dialysis	Low	• A separation step is required • Lengthy experiment (48 h)
Radiolabeling	Low	• Expensive and tedious process to develop radioligand • A separation step is required • Radioactive waste must be disposed

1.3.1. Fluorescence polarization

Fluorescence polarization (FP), first used in a biological system in 1952,[50, 51] has found wide applicability in clinical and biomedical studies. FP assays are particularly useful because they are homogeneous, high throughput, and can be inexpensive. FP assays provide information on molecular mobility, as this method measures changes in the rotational rate of a fluorescent ligand when the free form binds a protein target.[52] Plane-polarized light is used to excite a fluorophore, and the fluorescence intensities in planes both in the parallel (F_{II}) and perpendicular ($F_{\perp}$) direction to the plane of excitation are measured. The polarization (P) of a sample can then be determined using the following equation:[48]

$$P = \frac{F_{II} - F_{\perp}}{F_{II} + F_{\perp}}$$

A free ligand in solution (i.e. one not bound to the protein target) is able to rapidly rotate, and is therefore not aligned with the source. As depicted in Figure 1.4, following excitation with polarized light, this low molecular weight complex leads to depolarization of the emitted light, and produces a low polarization signal. However, when a ligand is bound to a protein target, the ligand tumbles more slowly and this high molecular weight complex is not able to rotate as freely as when unbound, leading to an increase in polarization.[53]

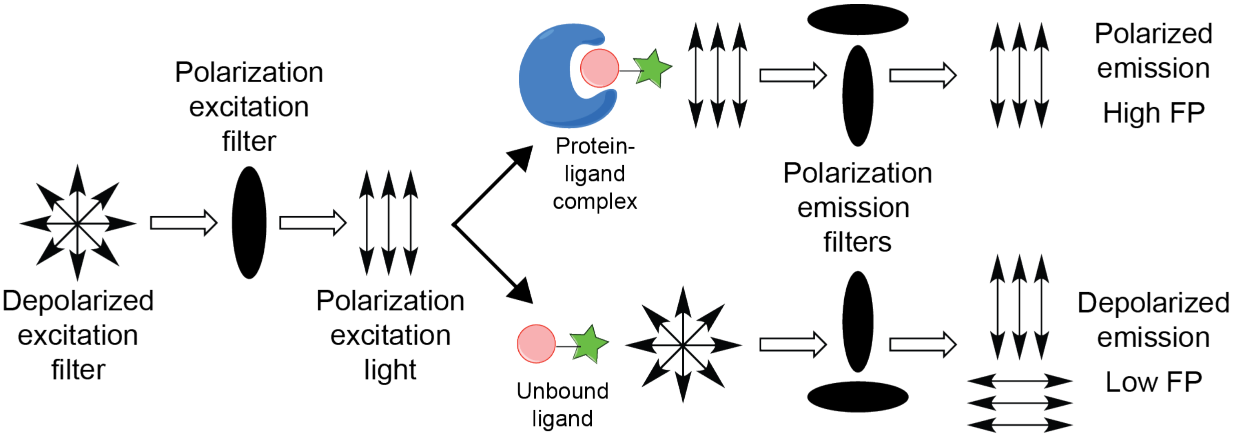

Figure 1.4. Schematic representation of fluorescence polarization of two samples: protein-ligand complex (top) and free ligand in solution (bottom).

Polarization is measured using a fluorometer equipped with an excitation source (typically a Xe or Hg arc lamp), excitation polarizer, rotatable emission polarizer, excitation and emission monochromators or filters, detector, and sample platform (i.e. cuvette or multiwell plate).[52] To measure the affinity of a fluorescent ligand for a protein, the protein of interest is titrated into a fixed concentration of fluorescent ligand (below K_d) and allowed to reach equilibrium. Generally, FP is used for competition-based assays, where an unlabeled small molecule of interest is titrated into a sample of a fixed concentration of ligand:protein complex, and a loss of polarization is measured as a function of the concentration of the unlabeled small molecule.[37]

Polarization assays are limited by the fluorescence lifetime of the fluorescent ligand, interference with unlabeled ligands, autofluorescence, shifts in quantum yield, and molecular weight and flexibility of the fluorescent ligand.[54] The fluorescence lifetime of a dye can be limiting in FP assays, and it is important to choose a dye with a fluorescence lifetime that closely matches its rate of rotation. The fluorescence polarization decreases as the fluorescence lifetime increases. A fluorophore with a short lifetime has high polarization, even when unbound, and therefore is limited to a small molecule-protein mass of ~100 kDa. Conversely, fluorophores with long lifetimes can be depolarized even when in complex with the protein, and therefore few changes in polarization can be detected over the free ligand.[55-57] Fluorescence enhancement or quenching can occur based on changes in the microenvironment of the dye (i.e. when free in solution versus bound) and changes in the fluorescence lifetime of the dye. The fluorescence enhancement or quenching must be independently evaluated for accurate affinity measurements by FP.[56] Finally, interference from the unlabeled ligands within a competition assay can cause false positives and negatives within a screen. This interference has been studied[58, 59] and should be considered when developing assays.

1.3.2. Förster resonance energy transfer

Förster resonance energy transfer (FRET) is a well-established photophysical phenomenon that was first described in 1948.[60] Through a non-radiative process, a donor molecule transfers energy to a nearby acceptor chromophore or fluorophore via dipole-dipole interactions. The amount of energy transfer that occurs is dependent on three criteria: the distance between the two fluorophores, spectral overlap between the emission spectrum of the donor and the absorbance spectrum of the acceptor, and the dipole-dipole moments of the two molecules.[7] This phenomenon measures interactions between molecules in close proximity (~1–10 nm), making this a popular technique for ratiometric studies in chemical biology.[61] The FRET efficiency (*E*) is inversely proportional to the sixth power of distance between the two fluorophores (Figure 1.5, panel B) and is defined by the following equation, where R is the distance between the fluorophores:

$$E = \frac{{R_0}^6}{({R_0}^6 + R^6)}$$

The Förster distance (R_0) is the distance at which the transfer efficiency equals 50% and can be calculated for a FRET pair by the following equation (in Å):

$$R_0 = 0.211[\kappa^2 \eta^{-4} \phi_D J_{DA}]^{1/6}$$

where η is the refractive index of the solvent, κ is the average squared orientational part of a dipole-dipole interaction, Φ_D is the quantum yield of the donor, and *J* is spectral overlap of the FRET pair (overlap between the donor emission and acceptor absorption, Figure 1.5, panel C).[7, 61]

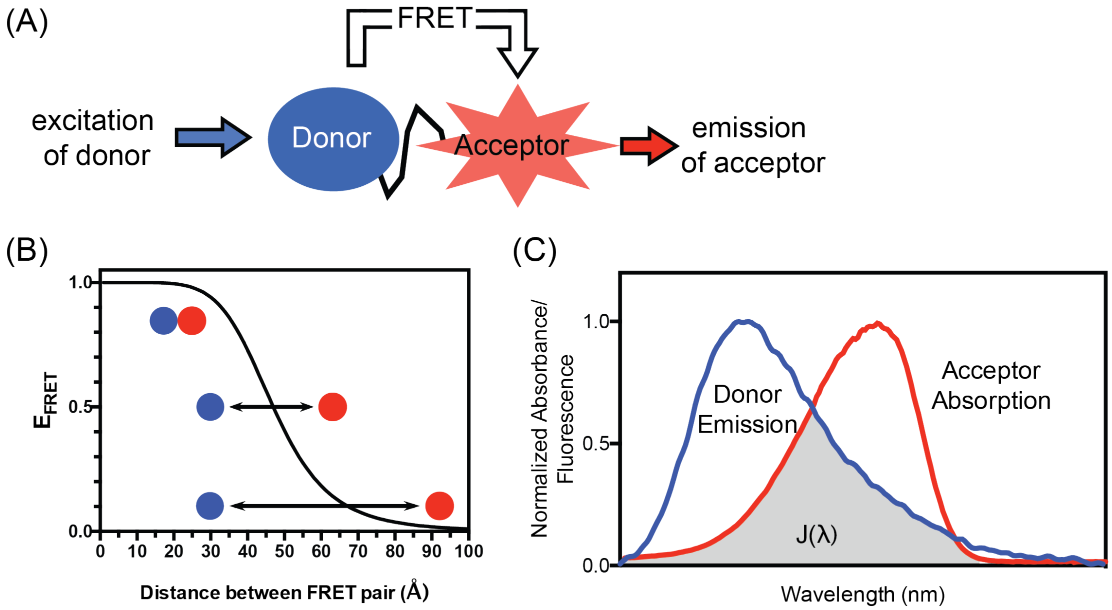

Figure 1.5. Energy transfer is dependent on the distance between two fluorophores and their spectral overlap. A: Schematic of the FRET process. B: Dependence of FRET efficiency on the distance between the FRET pair. The donor and acceptor are represented as blue and red circles. C: Graphical representation of spectral overlap of an ideal FRET pair. The emission spectra of donor fluorophore is depicted as blue line, and absorption spectra of acceptor fluorophore as a red line, and spectral overlap J(λ) shaded grey.

FRET can be classified as two categories: intrinsic and extrinsic. Intrinsic FRET (iFRET) involves a fluorophore that occurs in nature, such as tryptophan and tyrosine residues within a protein of interest. Since tryptophan is excited by UV light, this application is limited to *in vitro* studies, but has been powerful in investigating changes in protein conformation and studies of macromolecule-ligand interactions.[62-66] Because the quantum yield of tryptophan is low[13] in comparison to other commonly used fluorophores for FRET applications, it is critical that a bright acceptor fluorophore is used to enable efficient and sensitive assays. Some homogenous Trp-FRET assays have been developed for quantification of receptor-ligand interactions,[67-70] but the field is still limited by the need to use high probe concentrations to detect these signals.

For cellular studies, FRET pairs than absorb and emit in the visible range (400-600 nm) are commonly used. These FRET pairs have larger Förster distances than UV fluorophores, and therefore can examine somewhat longer-range interactions.[71] Commonly used FRET pairs include the Alexa fluorophores[27] (i.e. Alexa 488/Alex 594) and fluorescent proteins, such as green fluorescent protein (GFP)/yellow fluorescent protein (YFP).[72-74] Generally, these are limited by high cost (Alexa Fluors), which hinders synthesis of complex FRET based probes, and/or large molecular size (fused fluorescent proteins), which can affect the interactions under investigation.

FRET-based ligand binding assays are generally homogenous, can be inexpensive (dependent on the FRET pair), high throughput, and flexible.[74] In assays that use small molecule FRET pairs, a protein is typically labeled with the fluorophore via covalent modification with lysine or cysteine residues and interactions with a fluorescent ligand are measured. In general, these applications can be limited by heterogeneous and poorly defined conjugation of the fluorescent molecule to the protein of interest. However, recent advances in this field using SNAP-Tag technology and unnatural fluorescent amino acids have been described to help overcome some of these limitations.[75-78]

1.4. Outline of this dissertation

In early stage drug discovery, fluorescence-based assays often play a vital role in understanding biological interactions and cellular processes. My research has focused on the development of new fluorescent probes and assays that advance our knowledge of these biological events. My research has centered on the Pacific Blue fluorophore, a bright coumarin derivative used in fluorescence imaging and flow cytometry applications. In this dissertation, Chapter 2 describes a new synthetic route to access gram quantities of Pacific Blue and overcome the high cost of this commercial fluorophore. The chapter also investigates a new FRET pair, tryptophan-Pacific Blue, and its use in quantifying small molecule-protein interactions, both through direct binding and competition-based platforms. Chapter 3 describes the synthesis and biological evaluation of fluorescent derivatives of paclitaxel (Taxol) that we are investigating to create new probes of cellular efflux by P-glycoprotein (P-gp) and explore some of the paradoxical clinical responses associated with the parent anticancer drug. Chapter 4 characterizes other FRET pairs, Pacific Blue-Pennsylvania Green and Pacific Blue-Oregon Green, and describes studies directed towards better understanding a targeted drug delivery system under development in the Peterson group. Finally, Chapter 5 reports the development of a fluorescence polarization assay for studies of ligands that inhibit a protein-protein interaction involved in iron homeostasis in pathogenic bacteria.

1.5. References

1. Hughes, J. P.; Rees, S.; Kalindjian, S. B.; Philpott, K. L., Principles of early drug discovery. *Br. J. Pharmacol.* **2011,** *162*, 1239-1249.

2. *Molecular Probes Handbook, A Guide to Fluorescent Probes and Labeling Technologies, 11th Edition*.

3. Ettinger, A.; Wittmann, T., Fluorescence Live Cell Imaging. *Methods Cell Biol.* **2014,** *123*, 77-94.

4. Bisswanger, H., Enzyme assays. *Perspec. Sci.* **2014,** *1*, 41-55.

5. Stokes, G. G., On the Change of Refrangibility of Light. *Philosoph. Trans. Roy. Soc. Lond.* **1852,** *142*, 463-562.

6. Valeur, B.; Berberan-Santos, M. N., A Brief History of Fluorescence and Phosphorescence before the Emergence of Quantum Theory. *J. Chem. Ed.* **2011,** *88*, 731-738.

7. Lakowicz, J. R., *Principles of Fluorescence Spectroscopy*. 3 ed.; Springer: New York, 2006.

8. Lavis, L. D.; Raines, R. T., Bright Building Blocks for Chemical Biology. *ACS Chem. Biol.* **2014,** *9*, 855-866.

9. Sjöback, R.; Nygren, J.; Kubista, M., Absorption and fluorescence properties of fluorescein. *Spectrochim. Acta A Mol. Biomol. Spectrosc.* **1995,** *51*, L7-L21.

10. Algar, W. R.; Tavares, A. J.; Krull, U. J., Beyond labels: A review of the application of quantum dots as integrated components of assays, bioprobes, and biosensors utilizing optical transduction. *Anal. Chim. Acta* **2010,** *673*, 1-25.

11. Kim, H. N.; Guo, Z.; Zhu, W.; Yoon, J.; Tian, H., Recent progress on polymer-based fluorescent and colorimetric chemosensors. *Chem. Soc. Rev.* **2011,** *40*, 79-93.

12. Kremers, G.-J.; Gilbert, S. G.; Cranfill, P. J.; Davidson, M. W.; Piston, D. W., Fluorescent proteins at a glance. *J. Cell Sci.* **2011,** *124*, 157-160.

13. Chen, R. F., Fluorescence Quantum Yields of Tryptophan and Tyrosine. *Anal. Lett.* **1967,** *1*, 35-42.

14. Doody, M. C.; Gotto, A. M.; Smith, L. C., 5-(Dimethylamino)naphthalene-1-sulfonic acid, a fluorescent probe of the medium chain fatty acid binding site of serum albumin. *Biochemistry* **1982,** *21*, 28-33.

15. Lakowicz, J. R.; Gryczynski, I.; Cheung, H. C.; Wang, C. K.; Johnson, M. L.; Joshi, N., Distance distributions in proteins recovered by using frequency-domain fluorometry. Applications to troponin I and its complex with troponin C. *Biochemistry* **1988,** *27*, 9149-9160.

16. Gustiananda, M.; Liggins, J. R.; Cummins, P. L.; Gready, J. E., Conformation of Prion Protein Repeat Peptides Probed by FRET Measurements and Molecular Dynamics Simulations. *Biophys. J.* **2004,** *86*, 2467-2483.

17. Christiaens, B.; Symoens, S.; Vanderheyden, S.; Engelborghs, Y.; Joliot, A.; Prochiantz, A.; Vandekerckhove, J.; Rosseneu, M.; Vanloo, B., Tryptophan fluorescence study of the interaction of penetratin peptides with model membranes. *Eur. J. Biochem.* **2002,** *269*, 2918-2926.

18. Munishkina, L. A.; Fink, A. L., Fluorescence as a method to reveal structures and membrane-interactions of amyloidogenic proteins. *Biochim. Biophys. Acta (BBA) - Biomembranes* **2007,** *1768*, 1862-1885.

19. Riveiro, M. E.; Kimpe, N. D.; Moglioni, A.; Vazquez, R.; Monczor, F.; Shayo, C.; Davio, C., Coumarins: Old Compounds with Novel Promising Therapeutic Perspectives. *Curr. Med. Chem.* **2010,** *17*, 1325-1338.

20. Sun, W. C.; Gee, K. R.; Haugland, R. P., Synthesis of novel fluorinated coumarins: excellent UV-light excitable fluorescent dyes. *Bioorg. Med. Chem. Lett.* **1998,** *8*, 3107-10.

21. Baeyer, A., Ueber eine neue Klasse von Farbstoffen. *Ber. Dtsch. Chem. Ges.* **1871,** *4*.

22. Mottram, L. F.; Boonyarattanakalin, S.; Kovel, R. E.; Peterson, B. R., The Pennsylvania Green Fluorophore: A Hybrid of Oregon Green and Tokyo Green for the Construction of Hydrophobic and pH-Insensitive Molecular Probes. *Org. Lett.* **2006,** *8*, 581-584.

23. Sun, W.-C.; Gee, K. R.; Klaubert, D. H.; Haugland, R. P., Synthesis of Fluorinated Fluoresceins. *J. Org. Chem.* **1997,** *62*, 6469-6475.

24. Grimm, J. B.; Sung, A. J.; Legant, W. R.; Hulamm, P.; Matlosz, S. M.; Betzig, E.; Lavis, L. D., Carbofluoresceins and Carborhodamines as Scaffolds for High-Contrast Fluorogenic Probes. *ACS Chem. Biol.* **2013,** *8*, 1303-1310.

25. Lavis, L. D.; Rutkoski, T. J.; Raines, R. T., Tuning the pKa of Fluorescein to Optimize Binding Assays. *Anal. Chem.* **2007,** *79*, 6775-6782.

26. Urano, Y.; Kamiya, M.; Kanda, K.; Ueno, T.; Hirose, K.; Nagano, T., Evolution of Fluorescein as a Platform for Finely Tunable Fluorescence Probes. *J. Am. Chem. Soc.* **2005,** *127*, 4888-4894.

27. Panchuk-Voloshina, N.; Haugland, R. P.; Bishop-Stewart, J.; Bhalgat, M. K.; Millard, P. J.; Mao, F.; Leung, W.-Y.; Haugland, R. P., Alexa Dyes, a Series of New Fluorescent Dyes that Yield Exceptionally Bright, Photostable Conjugates. *J. Histochem. Cytochem.* **1999,** *47*, 1179-1188.

28. Khanna, P. L.; Ullman, E. F., 4',5'-dimethoxy-6-carboxyfluorescein: A novel dipole-dipole coupled fluorescence energy transfer acceptor useful for fluorescence immunoassays. *Anal. Biochem.* **1980,** *108*, 156-161.

29. Tian, M.; Wu, X.-L.; Zhang, B.; Li, J.-L.; Shi, Z., Synthesis of chlorinated fluoresceins for labeling proteins. *Bioorg. Med. Chem. Lett.* **2008,** *18*, 1977-1979.

30. Jacobson, K.; Rajfur, Z.; Vitriol, E.; Hahn, K., Chromophore-assisted laser inactivation in cell biology. *Trends Cell Biol.* **2008,** *18*, 443-450.

31. Ceresole, M. Verfahren zur Darstellung von Farbstoffen aus der Gruppe des Meta-amidophenol-Phtaleins. 1887.

32. Beija, M.; Afonso, C. A. M.; Martinho, J. M. G., Synthesis and applications of Rhodamine derivatives as fluorescent probes. *Chem. Soc. Rev.* **2009,** *38*, 2410-2433.

33. Mottram, L. F.; Forbes, S.; Ackley, B. D.; Peterson, B. R., Hydrophobic analogues of rhodamine B and rhodamine 101: potent fluorescent probes of mitochondria in living C. elegans. *Beilstein J. Org. Chem.* **2012,** *8*, 2156-2165.

34. Bender, A.; Woydziak, Z. R.; Fu, L.; Branden, M.; Zhou, Z.; Ackley, B. D.; Peterson, B. R., Novel Acid-Activated Fluorophores Reveal a Dynamic Wave of Protons in the Intestine of Caenorhabditis elegans. *ACS Chem. Biol.* **2013,** *8*, 636-642.

35. Lukinavicius, G.; Reymond, L.; D'Este, E.; Masharina, A.; Gottfert, F.; Ta, H.; Guther, A.; Fournier, M.; Rizzo, S.; Waldmann, H.; Blaukopf, C.; Sommer, C.; Gerlich, D. W.; Arndt, H.-D.; Hell, S. W.; Johnsson, K., Fluorogenic probes for live-cell imaging of the cytoskeleton. *Nat. Meth.* **2014,** *11*, 731-733.

36. Longmire, M.; Ogawa, M.; Hama, Y.; Kosaka, N.; Regino, C. A. S.; Choyke, P. L.; Kobayashi, H., Determination of Optimal Rhodamine Flurophore for In Vivo Optical Imaging. *Bioconjugate Chem.* **2008,** *19*, 1735-1742.

37. Lea, W. A.; Simeonov, A., Fluorescence Polarization Assays in Small Molecule Screening. *Exp. Opin. Drug Discov.* **2011,** *6*, 17-32.

38. Nikiforov, T. T.; Beechem, J. M., Development of homogeneous binding assays based on fluorescence resonance energy transfer between quantum dots and Alexa Fluor fluorophores. *Anal. Biochem.* **2006,** *357*, 68-76.

39. Pollard, T. D., A Guide to Simple and Informative Binding Assays. *Mol. Biol. Cell* **2010,** *21*, 4061-4067.

40. Freyer, M. W.; Lewis, E. A., Isothermal Titration Calorimetry: Experimental Design, Data Analysis, and Probing Macromolecule/Ligand Binding and Kinetic Interactions. In *Methods in Cell Biology*, Academic Press2008; Vol. Volume 84, pp 79-113.

41. Nguyen, H.; Park, J.; Kang, S.; Kim, M., Surface Plasmon Resonance: A Versatile Technique for Biosensor Applications. *Sensors* **2015,** *15*, 10481.

42. Cala, O.; Guillière, F.; Krimm, I., NMR-based analysis of protein–ligand interactions. *Anal. Bioanal. Chem.* **2014,** *406*, 943-956.

43. Vivoli, M.; Novak, H. R.; Littlechild, J. A.; Harmer, N. J., Determination of Protein-ligand Interactions Using Differential Scanning Fluorimetry. *J. Vis. Exp.* **2014**, 51809.

44. Schlichting, I., X-Ray Crystallography of Protein-Ligand Interactions. In *Protein-Ligand Interactions: Methods and Applications*, Ulrich Nienhaus, G., Ed. Humana Press: Totowa, NJ, 2005; pp 155-165.

45. Nienhaus, K.; Nienhaus, G. U., Probing Heme Protein-Ligand Interactions by UV/Visible Absorption Spectroscopy. In *Protein-Ligand Interactions: Methods and Applications*, Ulrich Nienhaus, G., Ed. Humana Press: Totowa, NJ, 2005; pp 215-241.

46. Barré, J.; Chamouard, J. M.; Houin, G.; Tillement, J. P., Equilibrium dialysis, ultrafiltration, and ultracentrifugation compared for determining the plasma-protein-binding characteristics of valproic acid. *Clin. Chem.* **1985,** *31*, 60-64.

47. Maguire, J. J.; Kuc, R. E.; Davenport, A. P., Radioligand Binding Assays and Their Analysis. In *Receptor Binding Techniques*, Davenport, A. P., Ed. Humana Press: Totowa, NJ, 2012; pp 31-77.

48. Ciulli, A., Biophysical Screening for the Discovery of Small-Molecule Ligands. In *Protein-Ligand Interactions: Methods and Applications*, Williams, A. M.; Daviter, T., Eds. Humana Press: Totowa, NJ, 2013; pp 357-388.

49. Rossi, A. M.; Taylor, C. W., Analysis of protein-ligand interactions by fluorescence polarization. *Nat. Protocols* **2011,** *6*, 365-387.

50. Weber, G., Polarization of the fluorescence of macromolecules. 1. Theory and experimental method. *Biochem. J.* **1952,** *51*, 145-155.

51. Weber, G., Polarization of the fluorescence of macromolecules. 2. Fluorescent conjugates of ovalbumin and bovine serum albumin. *Biochem. J.* **1952,** *51*, 155-167.

52. Jameson, D. M.; Ross, J. A., Fluorescence Polarization/Anisotropy in Diagnostics and Imaging. *Chem. Rev.* **2010,** *110*, 2685-2708.

53. Pagano, J. M.; Clingman, C. C.; Ryder, S. P., Quantitative approaches to monitor protein–nucleic acid interactions using fluorescent probes. *RNA* **2011,** *17*, 14-20.

54. Gribbon, P.; Sewing, A., Fluorescence readouts in HTS: no gain without pain? *Drug Discov. Today* **2003,** *8*, 1035-1043.

55. Chen, R. F.; Scott, C. H., Atlas of Fluorescence Spectra and Lifetimes of Dyes Attached to Protein. *Anal. Lett.* **1985,** *18*, 393-421.

56. Jing, M.; Bowser, M. T., Methods for measuring aptamer-protein equilibria: A review. *Anal. Chim. Acta* **2011,** *686*, 9-18.

57. Pope, A. J.; Haupts, U. M.; Moore, K. J., Homogeneous fluorescence readouts for miniaturized high-throughput screening: theory and practice. *Drug Discov. Today* **1999,** *4*, 350-362.

58. Turek-Etienne, T. C.; Small, E. C.; Soh, S. C.; Xin, T. A.; Gaitonde, P. V.; Barrabee, E. B.; Hart, R. F.; Bryant, R. W., Evaluation of Fluorescent Compound Interference in 4 Fluorescence Polarization Assays: 2 Kinases, 1 Protease, and 1 Phosphatase. *J. Biomol. Screen.* **2003,** *8*, 176-184.

59. Vedvik, K. L.; Eliason, H. C.; Hoffman, R. L.; Gibson, J. R.; Kupcho, K. R.; Somberg, R. L.; Vogel, K. W., Overcoming Compound Interference in Fluorescence Polarization-Based Kinase Assays Using Far-Red Tracers. *Assay Drug Dev. Technol.* **2004,** *2*, 193-203.

60. Förster, T., Zwischenmolekulare Energiewanderung und Fluoreszenz. *Annalen. der Physik.* **1948,** *437*, 55-75.

61. Yuan, L.; Lin, W.; Zheng, K.; Zhu, S., FRET-Based Small-Molecule Fluorescent Probes: Rational Design and Bioimaging Applications. *Acc. Chem. Res.* **2013,** *46*, 1462-1473.

62. Xie, Y.; Maxson, T.; Tor, Y., Fluorescent Ribonucleoside as a FRET Acceptor for Tryptophan in Native Proteins. *J. Am. Chem. Soc.* **2010,** *132*, 11896-11897.

63. Thévenin, D.; Lazarova, T., Identifying and Measuring Transmembrane Helix–Helix Interactions by FRET. In *Membrane Protein Structure and Dynamics: Methods*

and Protocols, Vaidehi, N.; Klein-Seetharaman, J., Eds. Humana Press: Totowa, NJ, 2012; pp 87-106.

64. Das, P.; Mallick, A.; Haldar, B.; Chakrabarty, A.; Chattopadhyay, N., Fluorescence resonance energy transfer from tryptophan in human serum albumin to a bioactive indoloquinolizine system. *J. Chem. Sci.* **2007,** *119*, 77-82.

65. Nannepaga, S. J.; Gawalapu, R.; Velasquez, D.; Renthal, R., Estimation of Helix−Helix Association Free Energy from Partial Unfolding of Bacterioopsin. *Biochemistry* **2004,** *43*, 550-559.

66. Talavera, M. A.; M., D. L. C. E., Equilibrium and Kinetic Analysis of Nucleotide Binding to the DEAD-Box RNA Helicase DbpA. *Biochemistry* **2005,** *44*, 959-970.

67. zhang, Y.; Yang, X.; Liu, L.; Huang, X.; Pu, J.; Long, G.; Zhang, L.; Liu, D.; Xu, B.; Liao, J.; Liao, F., Comparison of Forster-resonance-energy-transfer acceptors for tryptophan and tyrosine residues in native proteins as donors. *J. Fluoresc.* **2013,** *23*, 147-57.

68. Kim, J. H.; Sumranjit, J.; Kang, H. J.; Chung, S. J., Discovery of coumarin derivatives as fluorescence acceptors for intrinsic fluorescence resonance energy transfer of proteins. *Mol. Biosyst.* **2014,** *10*, 30-3.

69. Xie, Y.; Yang, X.; Pu, J.; Zhao, Y.; Zhang, Y.; Xie, G.; Zheng, J.; Yuan, H.; Liao, F., Homogeneous competitive assay of ligand affinities based on quenching fluorescence of tyrosine/tryptophan residues in a protein via Forster-resonance-energy-transfer. *Spectrochim. Acta A Mol. Biomol. Spectrosc.* **2010,** *77*, 869-76.

70. Feng, Y.; Shen, X.; Chen, K.; Jiang, H.; Liu, D., A New Assay Based on Fluorescence Resonance Energy Transfer to Determine the Binding Affinity of Bcl-xL Inhibitors. *Biosci. Biotechnol. Biochem.* **2008,** *72*, 1936-1939.

71. Wu, P. G.; Brand, L., Resonance Energy Transfer: Methods and Applications. *Anal. Biochem.* **1994,** *218*, 1-13.

72. Heim, R.; Tsien, R. Y., Engineering green fluorescent protein for improved brightness, longer wavelengths and fluorescence resonance energy transfer. *Curr. Biol.* **1996,** *6*, 178-182.

73. Pollok, B. A.; Heim, R., Using GFP in FRET-based applications. *Trends Cell Biol.* **1999,** *9*, 57-60.

74. Sahoo, H., Förster resonance energy transfer – A spectroscopic nanoruler: Principle and applications. *J. Photochem. Photobiol. C: Photochem. Rev.* **2011,** *12*, 20-30.

75. Kim, J.; Seo, M.-H.; Lee, S.; Cho, K.; Yang, A.; Woo, K.; Kim, H.-S.; Park, H.-S., Simple and Efficient Strategy for Site-Specific Dual Labeling of Proteins for Single-Molecule Fluorescence Resonance Energy Transfer Analysis. *Anal. Chem.* **2013,** *85*, 1468-1474.

76. Liu, J.; Hanne, J.; Britton, B. M.; Shoffner, M.; Albers, A. E.; Bennett, J.; Zatezalo, R.; Barfield, R.; Rabuka, D.; Lee, J.-B.; Fishel, R., An Efficient Site-Specific Method for Irreversible Covalent Labeling of Proteins with a Fluorophore. *Sci. Rep.* **2015,** *5*, 16883.

77. Jäger, M.; Nir, E.; Weiss, S., Site-specific labeling of proteins for single-molecule FRET by combining chemical and enzymatic modification. *Protein Sci.* **2006,** *15*, 640-646.

78. Cole, N. B., Site-Specific Protein Labeling with SNAP-Tags. In *Current Protocols in Protein Science*, John Wiley & Sons, Inc.2001.

Chapter 2

Quantification of Small Molecule-Protein Interactions by FRET Between Tryptophan and the Pacific Blue Fluorophore

2.1. Introduction

To quantify the affinity of small molecules for proteins, a wide variety of biophysical techniques have been developed. Homogeneous methods include isothermal titration calorimetry (ITC),[1, 2] fluorescence polarization (FP),[3] and Förster resonance energy transfer (FRET).[4] Although these techniques are powerful, each has limitations. ITC, considered the gold standard for affinity determination, is material intensive, low throughput, and requires an appreciable change in heat upon binding. In widely employed FP (or related fluorescence anisotropy),[3, 5] small molecules linked to fluorophores report changes in the polarization of emitted photons when a rapidly rotating small molecule binds a slowly tumbling protein. However, probe size, solvent viscosity, fluorescence quenching, and linker flexibility can limit applicability.[3]

FRET has the potential to overcome some of these limitations. This method involves non-radiative transfer of excitation (Ex.) energy from a donor fluorophore to a proximal acceptor fluorophore.[4] This transfer is highly distance dependent, with an efficiency of 50% at the Förster distance (R_0, typically < ~ 5 nm). FRET-based binding assays generally involve one fluorophore attached to a receptor of interest and another fluorophore conjugated to a ligand. However, this requirement for two exogenous fluorophores poses challenges, given that conjugation of fluorophores to proteins can result in heterogeneity, or require site-directed labeling reactions.

As an alternative method for detection of small molecule-protein interactions, FRET initiated by excitation of intrinsically fluorescent tryptophan (Trp, **1**, Figure 1) residues is of increasing interest.[6-8] Beneficially, these residues are commonly found in or near protein ligand binding sites, and at interfaces between proteins and other biomolecules.[9, 10] Although maximally excited at 280 nm, Trp can be selectively excited over Tyr at 295 nm. Fluorescent photons emitted by Trp range from ~308 nm to ~355 nm, roughly correlated with exposure to aqueous solution,[11] with modest quantum yield ($\Phi = 0.2$). A previously reported[11] comparison of 19 Trp residues from 17 proteins with experimentally determined structures revealed an average Trp emission of 333 nm. Because the emission λ_{max} and quantum yield of Trp are affected by the polarity of the local environment,[12] its environmental sensitivity and quenching by exogenous factors has been widely used to study changes in protein conformation and binding of ligands. The intrinsic emission of Trp can also participate in FRET with other fluorophores (termed Trp-FRET),[7] and this approach has been extensively employed to study protein folding and dynamics.[13-15] Fluorophores known to participate in Trp-FRET include dansyl (**2**), 7-hydroxycoumarin (7HC, **3**), and dimethylaminocoumarin (DMACA, **4**).[4] Coumarins **3** and **4** were recently reported[6] by Chung to be the best Trp-FRET acceptors identified to date. However, environmental effects, limited brightness, small Stokes shifts, and low efficiency continues to hinder their sensitivity.[13] A few noncompetitive and competitive binding assays using Trp-FRET have been reported,[16-18] but generally require high concentrations of fluorescent probes for detection. These high concentrations can prevent quantitative measurements of the low dissociation constants (K_d) and competitive inhibition constants (K_i) that are frequently observed between small molecules and proteins.

To identify a more sensitive FRET acceptor for Trp, we examined overlap between the emission spectrum of this amino acid (Ex. 280 nm, Em. ~350 nm, ε = 5,600 M^{-1} cm^{-1}) and the absorbance spectrum of 6,8-difluoro-7-hydroxycoumarin, a fluorophore known as Pacific Blue (PB, **5**).[19] Because of its favorable photophysical properties (Ex. 400 nm, Em. 447 nm, ε = 29,500 M^{-1} cm^{-1}, Φ = 0.75, pKa = 3.7), PB is of substantial interest for labeling of proteins and other biomolecules.[20, 21] As shown in Figure 2.2, the large overlap between the emission of Trp and the absorption of PB suggested that this fluorophore might be a particularly sensitive FRET partner.

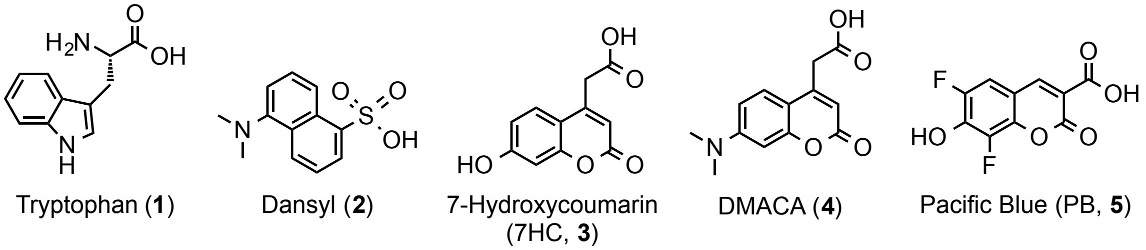

Figure 2.1. Structures of tryptophan (**1**) and other fluorophores (**2–5**).

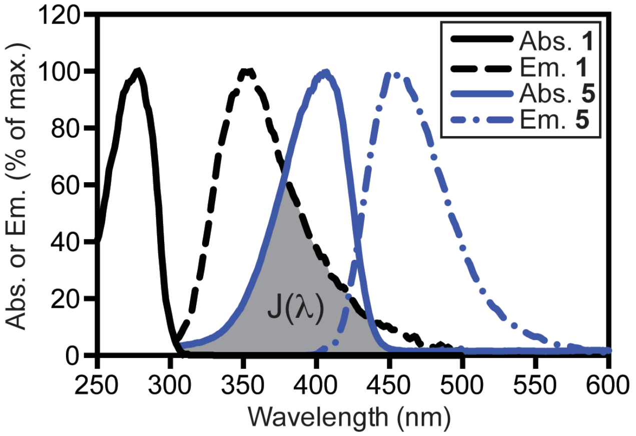

Figure 2.2. Absorbance (Abs., solid lines) and emission (Em., dotted lines) spectra of Trp (**1**, black lines, 32 μM for Abs and 2 μM for Em.) and PB (**5**, blue lines, 32 μM for Abs and 50 nM for Em.) in PBS (pH 7.4). The spectral overlap integral (J(λ)) critical for FRET is shaded grey.

2.2. A Practical synthesis of the Pacific Blue fluorophore

Pacific Blue (**5,** 6,8-difluoro-7-hydroxycoumarin 3-carboxylic acid) is a coumarin-based fluorophore that is becoming increasingly popular for chemical biology applications. These applications include labeling of antibodies for research and diagnostics,[22] labeling of specific proteins inside living cells,[20] and tagging of peptides for analysis by mass spectrometry.[23] This derivative of umbelliferone is of particular interest due to its low phenol pKa of 3.7, resulting from difluorination.[19] This high acidity enables bright fluorescence in all compartments of cells, including acidic organelles such as endosomes and lysosomes, providing substantial advantages over other more pH-sensitive dyes. In addition, the high photostability and high quantum yield of Pacific Blue make this molecule useful for fluorescence microscopy, flow cytometry, and other applications.

We found that the existing 7-step synthesis (Scheme 2.1) of Pacific Blue substantially limits access to this compound. The previously reported routes based on costly 2,4-difluororesorcinol (**10**, $24 / g, Matrix Scientific, PB **5** can be prepared in two steps with 41% yield[19]) or 2,3,4,5-tetrafluoronitrobenzene (**6**, $1.80 / g, Oakwood Chemicals, PB **5** can be prepared from this material in seven steps with 29% yield[24]) are expensive and inefficient. In addition, the published[24, 25] syntheses include difficult purifications, low yielding steps, and unstable intermediates. These issues prevented access to the gram quantities of Pacific Blue fluorophore desired for diverse studies of chemical biology by our group. To improve access to the fluorophore, we developed a new 5-step synthesis that achieves an overall yield of 50%. Moreover, our new synthetic route utilizes inexpensive starting materials and reagents and avoids extensive column chromatography, greatly improving access to this valuable fluorophore.

Scheme 2.1. A previously published synthesis of the Pacific Blue fluorophore.[24]

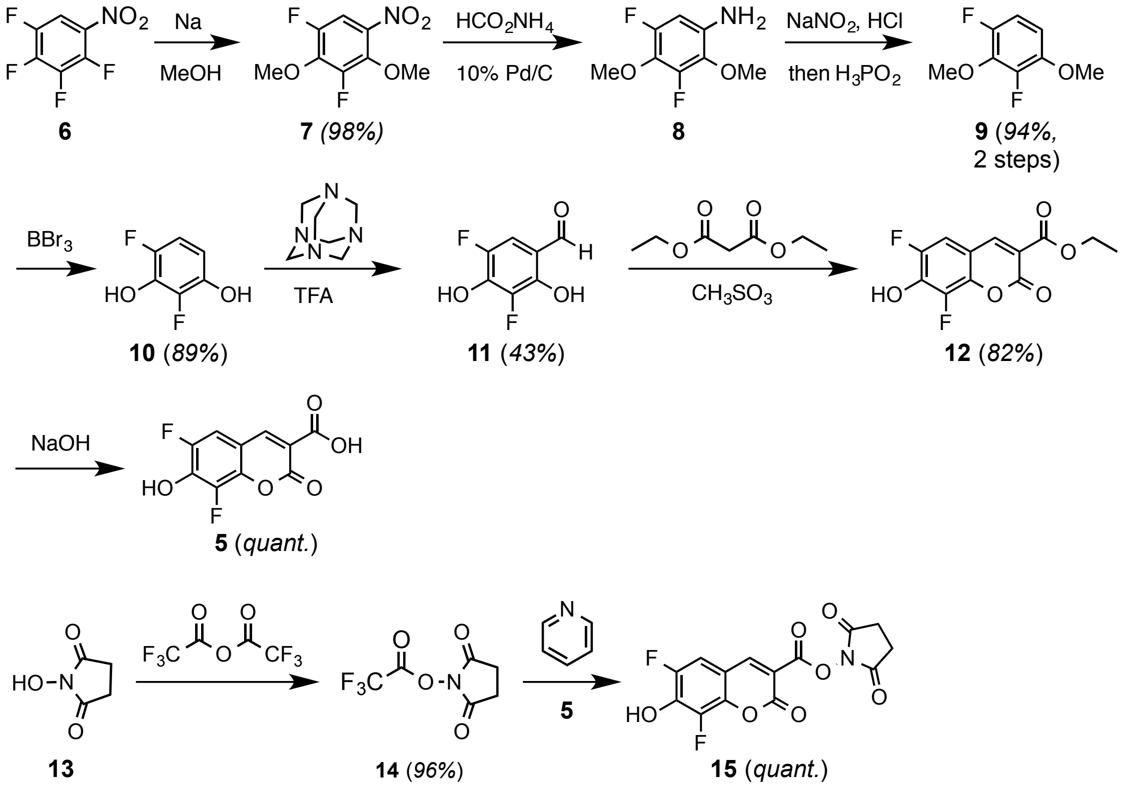

To develop an improved synthesis of Pacific Blue (**5**, PB), we chose to start with the inexpensive fluorinated building block 2,3,4,5-tetrafluorobenzoic acid (**16**, Scheme 2.2, \$0.4 / g, Oakwood Chemicals). This compound was converted into tetrafluorobenzonitrile **17** by reaction with oxalyl chloride, ammonium hydroxide, and catalytic DMF followed by dehydration with phosphoryl chloride. This approach produced the desired product with no column purification necessary (this product can also be purchased for \$3 / g from Oakwood Chemicals). This tetrafluorobenzonitrile was transformed to nitrile **18** by nucleophilic aromatic substitution with two equivalents of benzyl alcohol. During optimization of this step, three bases: sodium hydride (NaH), potassium tert-butoxide (KO*t*Bu), and potassium carbonate (K_2CO_3) were investigated for this S_NAr reaction. Even at low temperatures, NaH and KO*t*Bu created undesired side reactions, whereas heating overnight with K_2CO_3 gave the desired disubstituted product **18**, in 87% yield. By using potassium carbonate, side reactions observed with stronger bases were suppressed, and no other products were isolated by column chromatography. Reduction of **18** with DIBAL-H, followed by precipitation from ethanol, provided the tetrasubstituted benzaldehyde **19**. Deprotection by hydrogenolysis of **19** yielded the difluororesorcinol aldehyde **11**, a common intermediate also reported in the previously published syntheses of Pacific Blue. We found that relatively inexpensive 2,3,4,5-tetrafluorobenzoic acid (**16,** \$0.4 / g, Oakwood Chemicals) can be converted to the common intermediate aldehyde **11**[19, 24] in 66% overall yield in a four-pot process. Optimization of the final Knoevenagel condensation, utilizing meldum's acid, resulted in **5**, which was then efficiently converted to the amine-reactive Pacific Blue-NHS ester **15** using an improved route. Based on reagent costs alone, this new synthesis is approximately ten times less expensive than the previously published synthesis (Table 2.1) and requires three fewer synthetic steps.[24]

Scheme 2.2. An improved gram-scale synthesis of the Pacific Blue fluorophore.

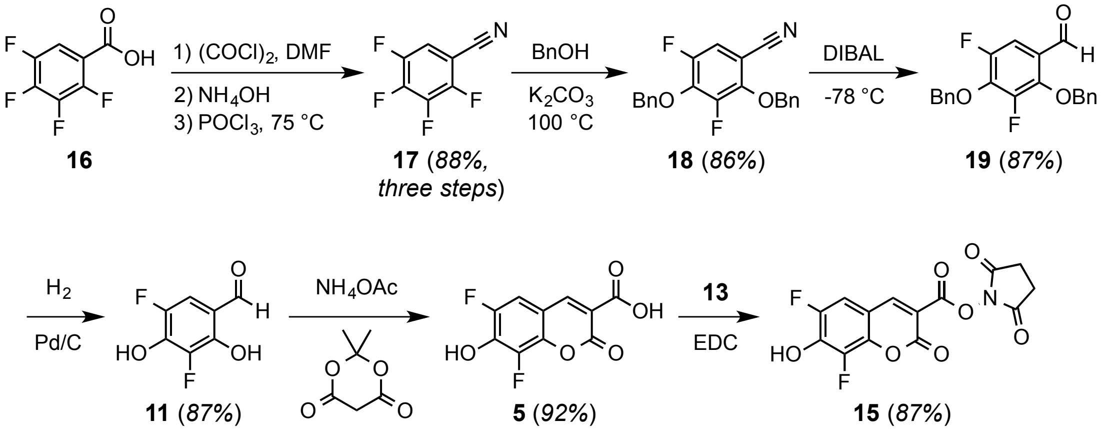

Table 2.1: Comparison of the cost of reagents needed to make one gram of Pacific Blue-NHS ester (**15**). Costs were estimated based on yields published for each synthetic step and the least expensive reagents available for purchase from Sigma Aldrich, Acros Organics, Alfa Aesar, Oakwood Chemicals, or Chem-Impex International.

	Kerkovius and Menard[24]	**Lee and Peterson** (This work, starting with **16**)	**Lee and Peterson** (This work, using a commerical source of **17**)
Number of steps	9	6	5
Starting Material	**6**	**16**	**17**
Cost of reagents needed to make **15** (1 g)	\$58.74	\$5.65	\$12.06

2.3. Comparison of Trp-FRET acceptors

To investigate the potential of Pacific Blue as a FRET acceptor for tryptophan residues in proteins, we investigated binding of the bacterial protein streptavidin (SA) to biotin and analogues. This tetrameric protein binds biotin with exceptionally high affinity ($K_d = 10^{-14}$ M^{-1}),[26] and X-ray crystallography[27] has revealed six Trp residues in close proximity to each of its four biotin-binding sites. Additionally, Trp79, Trp108, and Trp120 are critical for binding of SA to biotin via van der Waals and hydrophobic interactions.[27, 28] Moreover, these Trp residues can initiate FRET with biotinylated fluorophores.[16, 29, 30] Correspondingly, docking[31] of this X-ray structure (Figure 2.3) to PB-biotin derivative **20** (Figure 2.4, panel B) supported the notion that binding of SA would favorably position the fluorophore in close proximity to endogenous Trp residues from the monomer that makes the majority of non-covalent contacts, as well as Trp residues in other subunits of the SA tetramer.

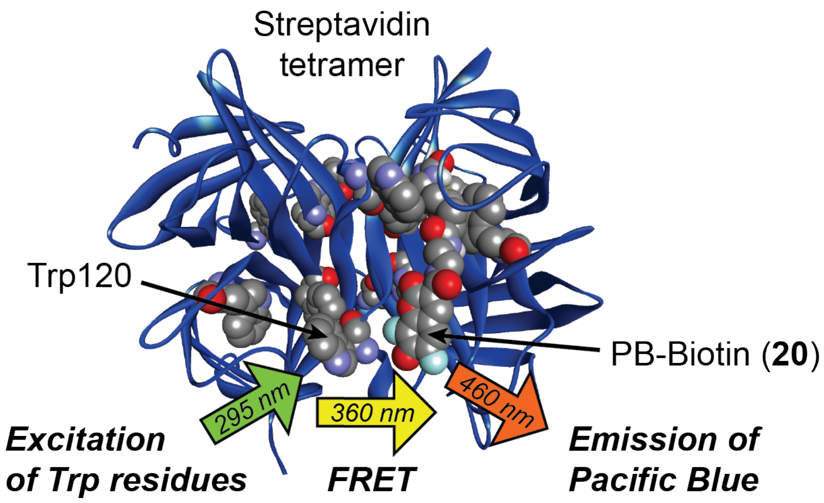

Figure 2.3. A model of streptavidin (PDB 3RY2) docked to the PB-Biotin derivative **20** (CPK model) with autodock vina. In each monomer, residues Trp79, Trp108, and Trp120 are shown as CPK models. The distance between the most proximal Trp120 (marked) and the Pacific Blue moiety of **20** is ~ 11 Å. For clarity, only one bound ligand is shown.

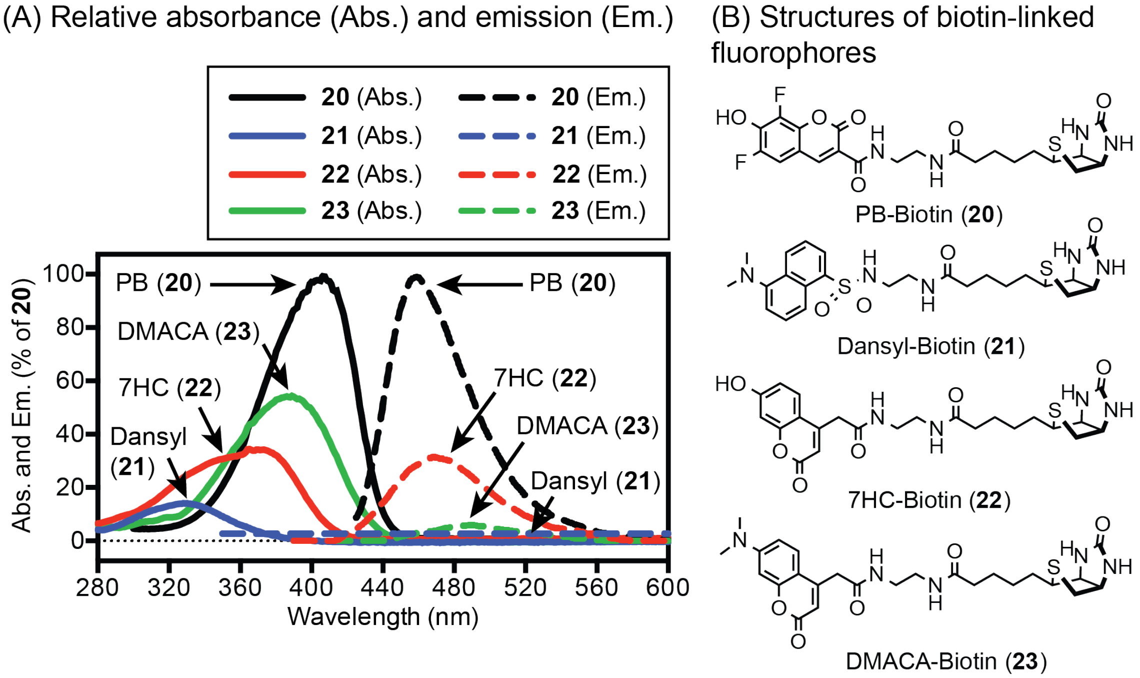
(A) Relative absorbance (Abs.) and emission (Em.)

(B) Structures of biotin-linked fluorophores

Figure 2.4. A: Normalized absorbance (Abs., solid lines) and fluorescence (Fluor.) emission (Em., dotted lines) spectra of **20-23** (32 μM for Abs., 50 nM for Fluor.) in PBS. **20-23** were excited at their λ_{max} (405 nm (**20**), 330 nm (**21**), 375 nm (**22**), and 390 nm (**23**)). Intensities are % of λ_{max} of **20**. B: Structures of fluorophores linked to biotin (**20-23**).

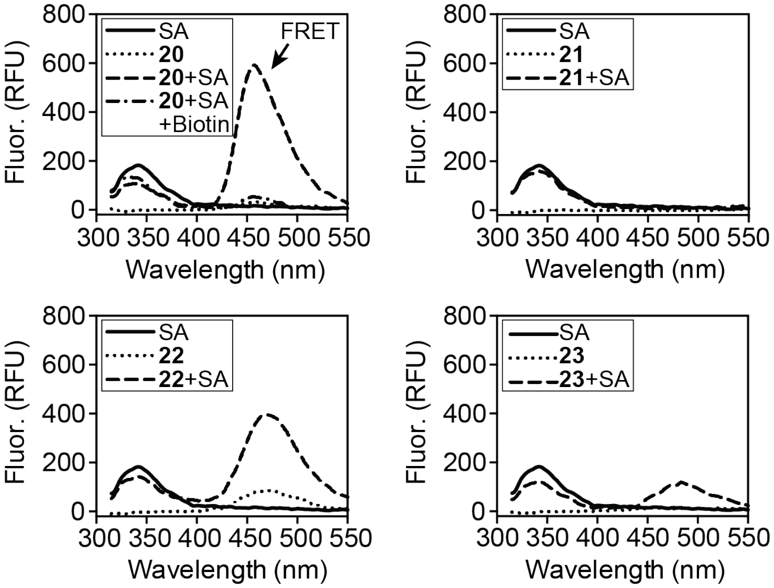

Figure 2.5. Analysis of FRET upon binding of **20-23** (100 nM) to SA ([monomer] = 400 nM). Ex. of SA (295 nm) results in maximal Em. at 340 nm. After binding of **20-23**, FRET Em. was observed at 457 nm (**20**), 532 nm (**21**), 467 nm (**22**), and 475 nm (**23**). Addition of biotin (10 μM) blocked FRET from **20**.

To compare PB (**5**) with known Trp-FRET acceptors (**2–4**), we synthesized biotin derivatives **20–23** (Figure 2.4, panel B). Comparison of normalized absorbance and emission spectra of these compounds (Figure 2.4, panel A) revealed that the PB-derived probe **20** was ~3-fold brighter than **22**, ~17-fold brighter than **23**, and > 100-fold brighter than **21** in aqueous phosphate buffered saline (PBS, pH 7.4).

FRET can be measured as the relative fluorescence intensity of the donor in the absence (I_d) and presence (I_{da}) of the acceptor.[4] When probes **20-23** were added to SA, excitation of Trp revealed substantial differences in emission due to FRET (Figure 2.5). As listed in Table 2.2, values from these studies were used to analyze the sensitivity (I_{ad}), efficiency (E), and other properties of these fluorophore pairs. Compared with PB (**20**), dansyl (**21**) was 33-fold less sensitive, 7HC (**22**) was 1.5-fold less sensitive, and DMACA (**23**) was 6-fold less sensitive. Additionally, the blue-shifted absorbance of 7HC (**22**) increased its excitation at 295 nm, reducing its FRET fold effect by a factor of four. The specificity of the FRET signal of **20** upon binding to SA was confirmed by addition of biotin as a competitor (Figure 2.5). Consequently, PB proved to be the most efficient and sensitive FRET acceptor for Trp.

Table 2.2. Photophysical properties of fluorescent probes. The intensity (I_{ad}) of FRET acceptors (100 nM) was measured at Em. λ_{max} when bound to SA (400 nM, Ex. 295 nm) and normalized to I_d. The efficiency (E) of FRET with Trp when bound to SA was calculated as $E = 1 - I_{da}/I_d$. The FRET fold effect (FF) was calculated as $FF = I_{ad}/I_a$. R_0 is the theoretical Förster distance calculated for each Trp-acceptor pair. I_{da} = intensity of Em. of Trp (340 nm) in the presence of the acceptor. I_d = intensity of Em. of Trp (340 nm) in the absence of acceptor. I_{ad} and I_a = intensity of Em. of the acceptor (457 nm (**20**), 532 nm (**21**), 467 nm (**22**), and 475 nm (**23**)) in the presence and absence of the donor (SA), respectively.

Probe	I_{ad}	E	FF	R_0 (nm)	Φ_f	ε (M^{-1} cm^{-1})
20	3.3	0.40	19.2	3.0	0.74	24,200
21	0.1	0.13	6.8	2.1	0.06[8]	3,500
22	2.2	0.21	4.8	2.7	0.47[6]	7,800
23	0.6	0.35	8.0	2.8	0.06[6]	11,600

2.4. Ligand binding assay using Pacific Blue labeled biotin analogues

Biotin binds SA with such high affinity that its association is essentially irreversible. To investigate fluorescent analogues with lower affinity that might be suitable for equilibrium binding measurements, we synthesized probes **24**–**26** (Figure 2.6, panel A).[32, 33] To generate equilibrium binding curves, SA was titrated into a low fixed concentration of the fluorescent probe (below the K_d), followed by excitation of Trp at 295 nm to trigger FRET (measured at 460 nm). Curve fitting was used to calculate direct binding K_d values of 11 ± 2 nM for thiobiotin-PB derivative **25**, 145 ± 19 nM for imidazolidinethione-PB **26**, and 2,730 ± 340 nM for iminobiotin-PB **24** in PBS (Figure 2.6). These values were in excellent agreement with independent assessments of K_d by ITC under the same conditions (12 ± 4 nM for **25** and 125 ± 45 nM for **26**, Figure 2.7). For these high affinity probes, attempts to measure affinities by FP were unsuccessful due to fluorescence quenching, which dramatically affects the lifetime of the fluorophore.[3] However, using higher concentrations of the lower affinity probe **24**, FP yielded a comparable K_d value of 2,950 ± 270 nM, (Figure 2.8).

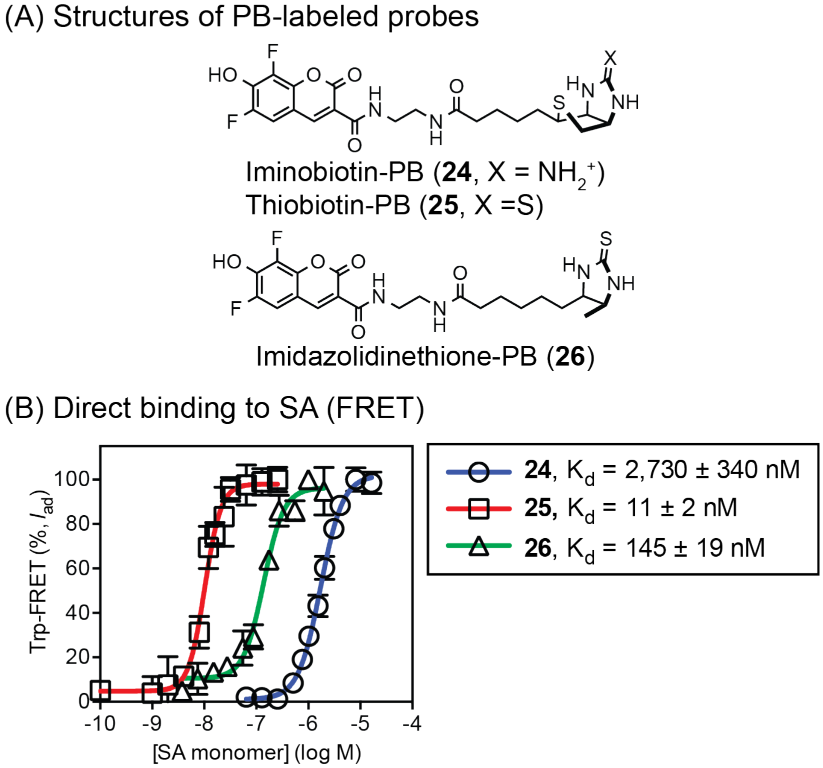
(A) Structures of PB-labeled probes

Iminobiotin-PB (**24**, X = NH_2^+)
Thiobiotin-PB (**25**, X =S)

Imidazolidinethione-PB (**26**)

(B) Direct binding to SA (FRET)

Figure 2.6. A: Structures of analogues of biotin (**24–26**) used in direct binding assays. B: Quantification of the affinity (K_d) of SA for probes **24** (25 nM), **25** (5 nM), and **26** (25 nM) in PBS (pH 7.4) by Trp-FRET. Trp residues were excited at 295 nM and FRET was measured at 460 nm. Values were corrected to account for fluorescence quenching or enhancement upon binding. [SA] was based on monomeric protein. Dissociation constants (K_d) were calculated using a one-site binding model in GraphPad Prism.

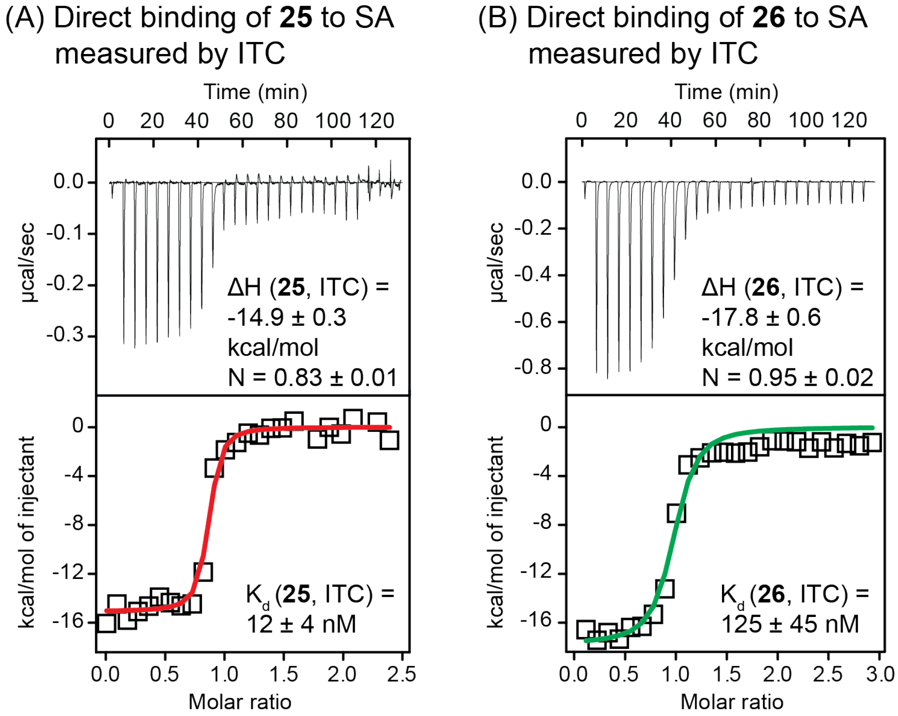

Figure 2.7. A and B: Quantification of binding of **25** (A) and **26** (B) to SA in PBS (pH 7.4) by ITC. Thermodynamic parameters and K_d were calculated with Origin software. For **25**: [SA in sample cell] = 4 μM, [**25** in syringe] = 50 μM. For **26**: [SA in sample cell] = 10 μM, [**26** in syringe] = 150 μM.

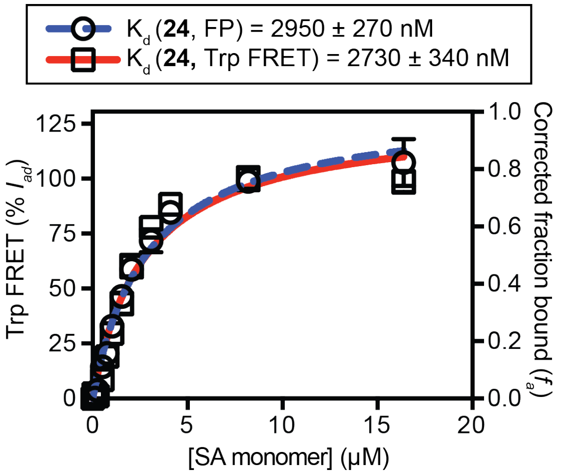

Figure 2.8. Quantification of binding of **24** (25 nM) to SA in PBS (pH 7.4) by FP compared with Trp FRET. For Trp FRET, Trp residues were excited at 295 nm and FRET was measured at 460 nm. For FP, Pacific Blue was excited at 400 nm and polarization was measured at 460 nm. Values were corrected to account for fluorescence quenching or enhancement upon binding. [SA] was based on monomeric protein. Dissociation constants (K_d) were calculated using a one-site binding model in GraphPad Prism.

2.5. Competition-based assays with analogues of biotin

We hypothesized that the high sensitivity of Trp-FRET with PB might be particularly valuable for quantifying small molecule-protein interactions in a competition assay format. To test this hypothesis, we quantified competitive inhibition constants (K_i) of the unlabeled biotin analogues **27**–**30** (Figure 2.9, panel A) using the PB-imidazolidinethione **26** as a fluorescent probe. The unlabeled ligands **27**–**30** were added to SA (held at a concentration near the K_d) bound to **26** (held below K_d, 25 nM). After incubation to achieve equilibrium, excitation of Trp at 295 nm was used to trigger FRET (measured at 460 nm). This approach allowed calculation of K_i values of 188 ± 25 nM for the benzyl ester imidazolidinethione derivative **30**, 693 ± 91 nM for the methyl ester imidazolidinethione **29**, 1,350 ± 180 nM for imidazolidinethione **28**, and 44,600 ± 5,800 nM for iminobiotin **27** in PBS (Figure 2.9, panel C) by non-linear curve fitting. Moreover, the affinity of the imidazolidinethione analogue **28** measured by ITC (K_d = 1,550 ± 270 nM) was in excellent agreement with the K_i quantified by Trp-FRET. Additionally, other previously published studies[34, 35] of **27** have reported values similar to the K_i value measured by Trp-FRET.

(A) Structures of competitors

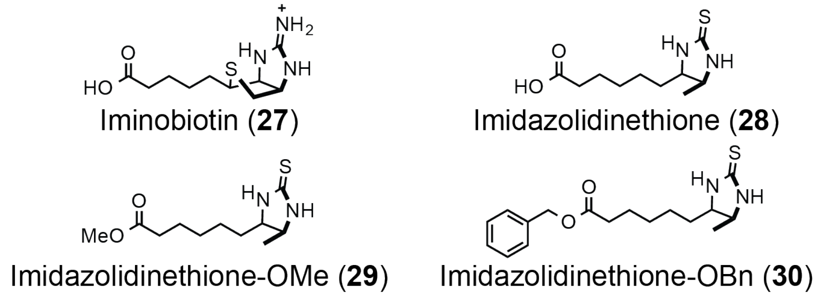

(B) Competition binding to SA with **26** as a fluorescence probe

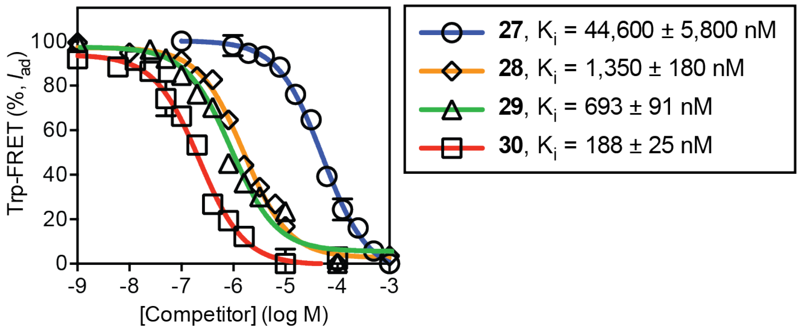

(C) Direct binding of **28** to SA quantified by ITC

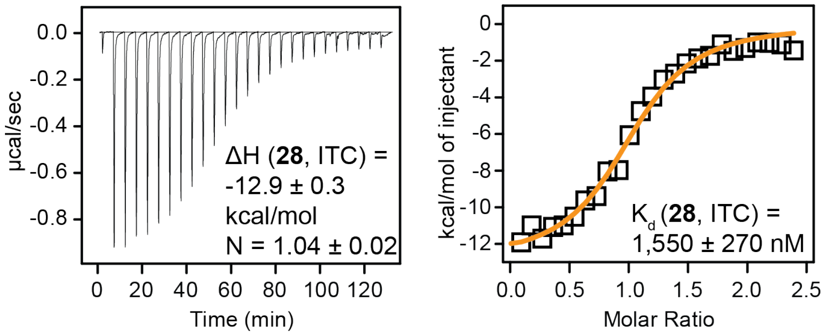

Figure 2.9. A: Structures of non-fluorescent analogues of biotin (**27**–**30**) used in competition binding assays. B: Quantification of competitive inhibitory constants (K$_i$) of **27**–**30** for SA complexed with **26** (175 nM for SA, 25 nM for **26**) by Trp-FRET. Trp residues were excited at 295 nM and FRET was measured at 460 nm. Values were corrected to account for fluorescence quenching upon binding. [SA] was based on monomeric protein. Half maximal inhibitory concentrations (IC$_{50}$) were calculated using a log(inhibitor) vs. response model in GraphPad Prism, and IC$_{50}$ values were converted to K$_i$ values. C: Evaluation of direct binding of **28** to SA by ITC. **28** was titrated into [SA] in PBS (pH 7.4) and thermodynamic parameters and K$_d$ values were calculated with Origin software. [SA in sample cell] = 20 µM, [**28** in syringe] = 250 µM.

2.6. Comparison with fluoresence enhancement or quenching-based assays

When PB-linked ligands bind to SA, their fluorescence is partially quenched (**24**, **25**) or enhanced (**26**). Hence, simple changes in fluorescence could potentially allow determination of their affinities for this protein. To examine the merits of this approach, we quantified the K_d of **24**–**25** for SA using only fluorescence quenching or enhancement, and we examined changes in fluorescence upon addition of the non-fluorescent competitor **28** to SA-**26**. As shown in Figure 2.10, we found that simple fluorescence quenching or enhancement could be used to estimate the affinity of **24**–**26** for SA, but K_d values obtained by this method differed by 2-fold (**26**) to 6-fold (**25**) from gold-standard measurements by ITC. Moreover, examination of competitive binding of **28** to SA-**26** revealed substantial deviation from the binding model at high concentrations (Figure 2.10, panel D), which prevented accurate determination of K_i. This lower accuracy and precision associated with the sole use of fluorescence intensity presumably arises from its high sensitivity to aggregation of fluorophores and other environmental factors. In contrast, the dependence of FRET on the distance between fluorophores presumably reduces its susceptibility to these confounding factors. Based on these results, we conclude that Trp-FRET with PB is superior to fluorescence intensity measurements for quantifying equilibrium binding in this system.

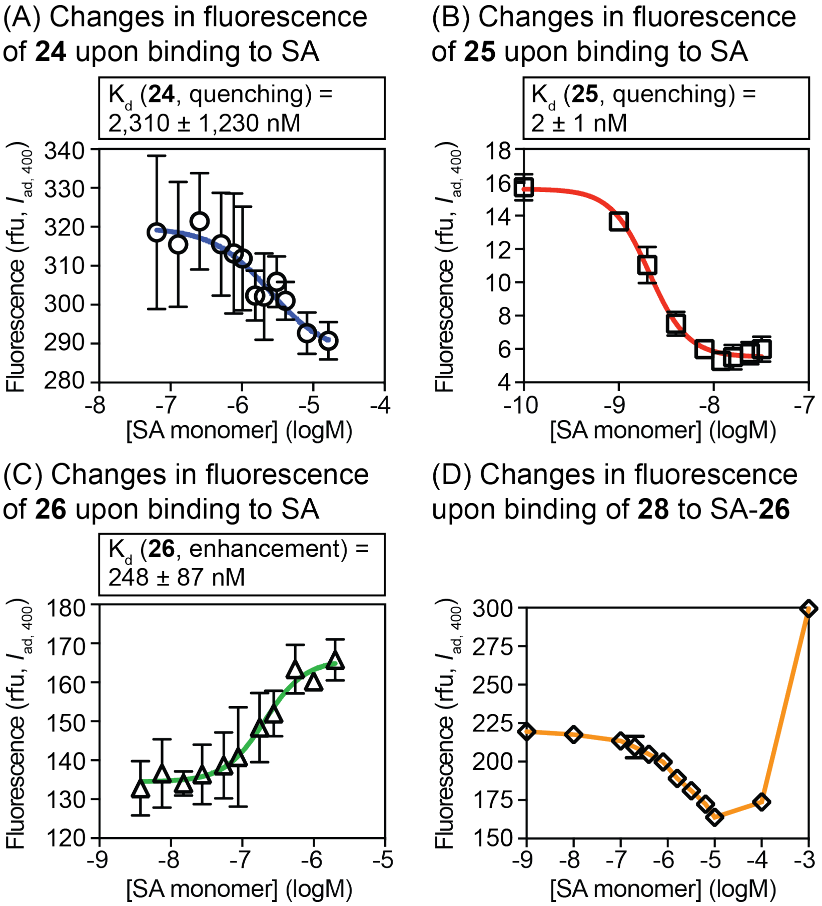

Figure 2.10. Analysis of interactions with SA by quenching or enhancement of fluorescence. PB was excited at 400 nm, and intensity of fluorescence emission at 460 nm was measured. A–C: Quantification of K$_d$ values for direct binding. D: Fluorescence resulting from competition of **28** for SA bound to probe **26** (25 nM). In D, due to poor fit to the binding model, the K$_i$ value was not calculated.

2.7. Examination of Trp-FRET upon binding of a peptide to an antibody

After characterizing Trp-FRET between small molecules and streptavidin, we sought to further examine the utility of this approach for quantifying peptide-protein interactions. In this case, we evaluated interactions between a monoclonal anti c-Myc antibody 9E10[36] and c-Myc tag peptide.[37] The c-Myc tag peptide has been reported to interact with the Fab fragment of the antibody with K$_d$ value of 250 nM to 700 nM as measured by ITC.[38] Important for this approach, X-ray crystallography of the Fab fragment of anti c-Myc antibody 9E10 bound to the c-Myc tag peptide[38] revealed three Trp residues in close proximity to the bound peptide. We hypothesized that by attaching PB to the N-terminus of the peptide, the fluorophore would be favorably positioned in close proximity to endogenous Trp residues and enable FRET.

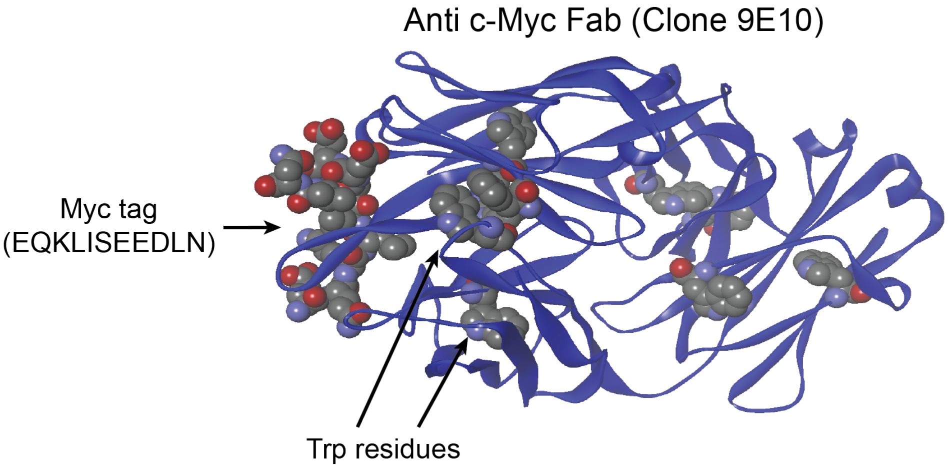

Figure 2.11. A model of Fab fragment of Anti c-Myc (clone 9E10, PDB 2OR9[38]) bound to the c-Myc tag peptide (EQKLISEEDLN, CPK model). Tryptophan residues of the Fab are shown as CPK models.

We synthesized two fluorescent derivatives (**32**–**33**, Figure 2.12) of the Myc-peptide using solid phase peptide synthesis (SPPS). These derivatives linked PB to the peptide N-terminus through glycine (**32**) or a miniature polyethylene glycol amino acid (mPEG, **33**). When the antibody was added to peptide **32**, excitation of Trp residues revealed changes in emission due to FRET (Figure 2.13). Values from this study were used to analyze a FRET efficiency (*E*) of 0.35, and a FRET fold effect (FF) of 6.1 for this system. The specificity of binding of **32** to the anti c-Myc antibody was confirmed by addition of **31** as a competitor (Figure 2.12).

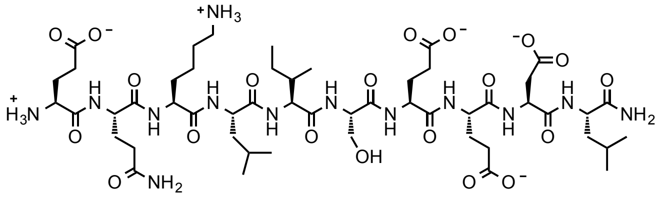

EQKLISEEDLN (**31**)

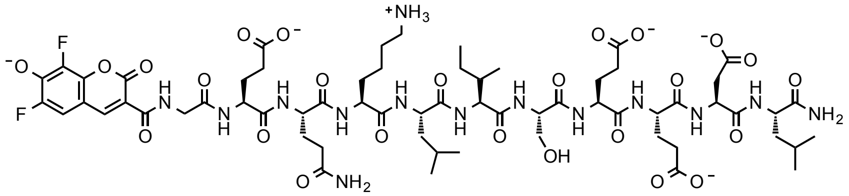

PB-GEQKLISEEDLN (**32**)

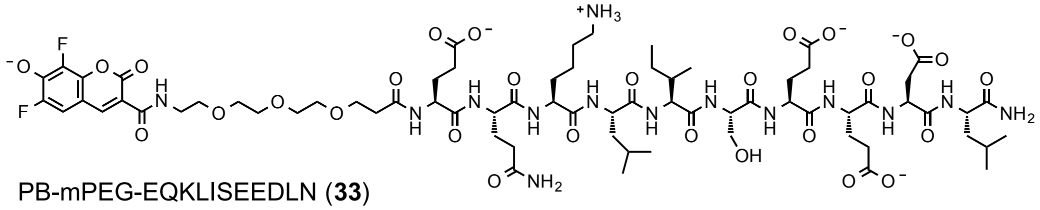

PB-mPEG-EQKLISEEDLN (**33**)

Figure 2.12. Structures of free and Pacific Blue-linked c-Myc tag peptides **31–33** (Sequence of c-Myc tag: EQLISEEDLN).

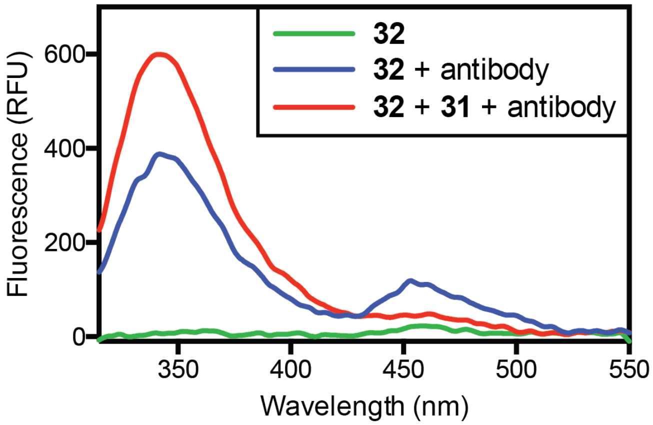

Figure 2.13. Analysis of FRET upon binding of **32** (100 nM) to anti c-Myc IgG (500 nM). Excitation of Trp (295 nm) results in maximal emission at 340 nm. After binding of **32**, emission due to FRET was observed at 455 nm (**32**). Addition of **31** (500 μM) blocked FRET from **32**.

To generate equilibrium binding curves, the anti c-Myc antibody was titrated into a low fixed concentration of **32** or **33,** followed by excitation of Trp at 295 nm to trigger FRET (measured at 460 nm). Curve fitting was used to calculate direct binding K$_d$ values of 270 ± 70 nM for **32** and 670 ± 190 nM for **33** (Figure 2.14). We further compared this FRET approach with the more commonly used method of fluorescence polarization. We found that K$_d$ values measured by FP were ~1.5 fold higher (400 ± 60 nM for **32** and 1,250 ± 470 nM for **33**) than those measured by Trp-FRET. These studies revealed that K$_d$ values measured by Trp-FRET match literature values reported for this protein-peptide interaction. It is likely that the higher values measured by FP could result from problems arising with quenching upon binding (which effects the lifetime of the fluorophore) or the flexible linker and the relatively large molecular weight of the peptides under investigation. Direct binding by ITC should be measured to confirm this hypothesis.

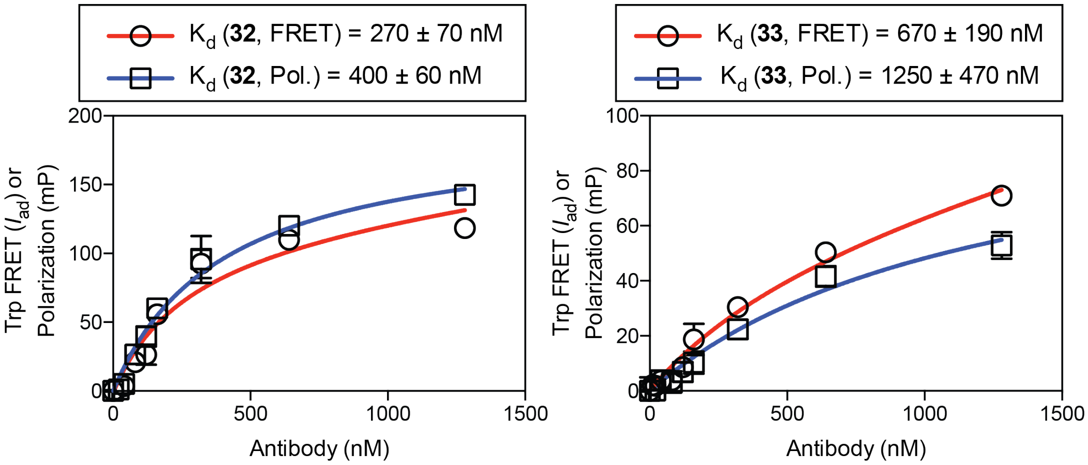

Figure 2.14. Quantification of binding of **32** and **33** (100 nM) to anti c-Myc IgG in PBS (pH 7.4) by Trp FRET compared with FP. For FRET, Trp residues were excited at 295 nm and emission was measured at 460 nm. For FP, Pacific Blue was excited at 400 nm and polarization was measured at 460 nm. Dissociation constants (K$_d$) were calculated using a one-site binding model in GraphPad Prism.

2.8. Examination of the cell permeability of Pacific Blue derivatives

Since Pacific Blue is more ‘drug-like’ than other common fluorophores (e.g. as compared to the much more polar fluorescein), and fluorescein and its derivatives are generally cell-impermeable, we sought to investigate the cell permeability of conjugates of this fluorophore. For these studies, as shown in Figure 2.4 (panel A) we synthesized PB-Hexyl-Biotin (**34**, Figure 2.15, panel C), as a more hydrophobic ($cLogD_{pH\ 7.4}$= -0.39 as calculated with ChemAxon MarvinView using the software default pKa of the PB phenol of 5.89) derivative of **20** ($cLogD_{pH\ 7.4}$= -1.68 as calculated with ChemAxon MarvinView using the software default pKa of the PB phenol of 5.89). To assess cellular permeability, we transiently tranfected HeLa cells with pPA2-T7SA-WT-GTP-mRFP, a mammalian expression vector that expresses streptavidin fused at its C-terminus to a monomeric red fluorescent protein. If the small molecule is cell-permeable and binds to streptavidin, the biotin conjugate would be trapped inside the cell and visible by confocal laser scanning microscopy of living cells. We found that compound **34** (Figure 2.15, panel B) penetrates through the cell membrane, whereas **20** (Figure 2.15, panel A) did not enter cells. Based on a measured $LogD_{pH\ 7.4}$ (**20**) = –1.4 ± 0.02 and $LogD_{pH\ 7.4}$ (**34**) = –0.38 ± 0.08, we conclude that the 10-fold (measured) to 20-fold (calculated) greater hydrophobicity (differences in cLogD of 1 to 1.3) enables cellular permeability of this Pacific Blue derivative, and these results help establish thresholds of hydrophobicity that should be useful for design of cell permeable derivatives of Pacific Blue.

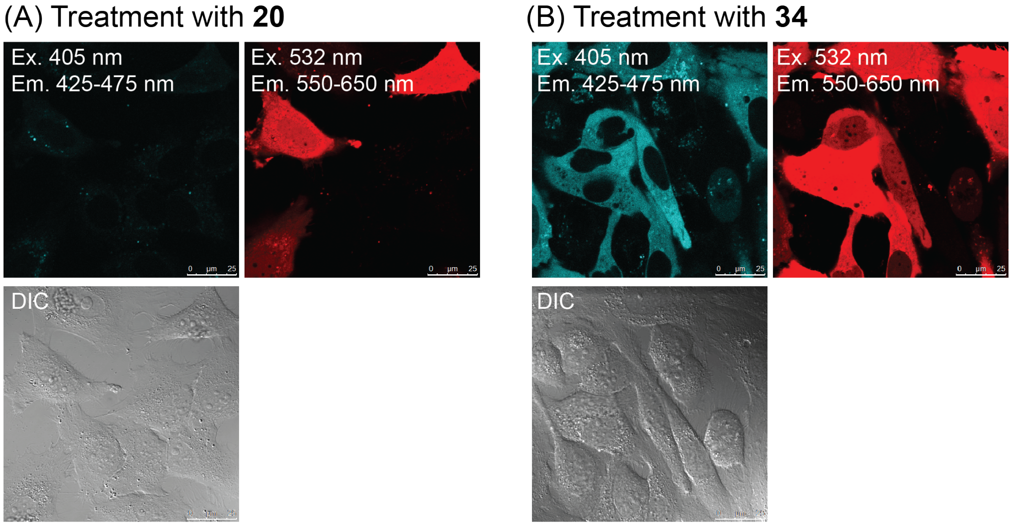
(A) Treatment with **20**

(B) Treatment with **34**

(C)

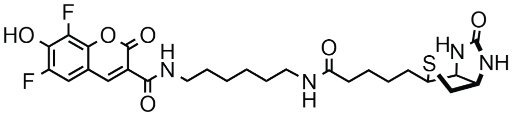

PB-Hexyl-Biotin (**34**)

Figure 2.15. Confocal and DIC micrographs of HeLa cells treated with PB-biotin **20** (ethylenediamine linker, Figure 2.6) and PB-Hexyl-Biotin **34** (hexamethylenediamine linker). A: HeLa cells transiently transfected with pPA2-TS7A-WT-GTP-mRFP (false colored red) for 48 h and then treated with **20** (2 µM, false colored blue) for 30 min. B: HeLa cells transiently transfected with pPA2-TS7A-WT-GTP-mRFP (false colored red) for 48 h and then treated with **34** (2 µM, false colored blue) for 30 min. C: Structure of PB-Hexyl-Biotin, **34**.

2.9. Conclusions

In conclusion, we developed a new synthetic route that allows access to multi-gram quantities of the Pacific Blue fluorophore. The previously published synthetic route posed several challenges including difficult purification of intermediates, low yields, unstable intermediates, and expensive reagents. Our new synthesis reduces both the issues listed, as well as the need for column purification. The new synthesis lowers the amount of steps by two and increases the overall yield to 50%. Additionally, based on the cost of reagents, this new route is 10 times less expensive.

With large quantities of PB on hand, we prepared fluorescent molecular probes that bind the Trp-containing protein SA. Comparison with other SA-binding fluorescent probes revealed that PB is a highly sensitive and efficient FRET acceptor for Trp. This high sensitivity enabled quantification of K_d and competitive K_i values into the nM range. Moreover, these values were independently validated by ITC and FP methods, establishing the high accuracy and precision of this method. We further applied the Trp-FRET assay to a peptide-protein system to quantify binding affinities of this more complex system and established parameters for the design of cell-permeable derivatives of PB. FRET between Trp and PB offers a new method for quantification of small molecule-protein interactions.

2.10. Experimental

2.10.1. General experimental section

Chemicals were purchased from Sigma Aldrich, Acros Organics, Alfa Aesar, Oakwood Chemical, or Chem-Impex International. Streptavidin (SA) was purchased from Alfa Aesar. Monoclonal Anti c-Myc antibody, clone 9E10 (M4439, produced in mouse) was purchased from Sigma Aldrich. ^{1}H NMR, ^{13}C NMR and ^{19}F NMR spectra were acquired on Bruker DRX-400 or Avance AVIII 500 MHz instruments. For ^{1}H and ^{13}C, chemical shifts (δ) are reported in ppm referenced to $CDCl_3$ (7.26 ppm for ^{1}H and 77.2 ppm for ^{13}C), CD_3OD (3.31 ppm for ^{1}H, 49.0 ppm for ^{13}C), or DMSO-d_6 (2.50 ppm for ^{1}H, 39.5 ppm for ^{13}C). For ^{19}F, chemical shifts (δ) are reported in ppm referenced to trifluoroethanol (-77.0 ppm for ^{19}F). ^{1}H coupling constants (J_{HH}, Hz), ^{13}C coupling constants (J_{CF}, Hz), and ^{19}F coupling constants (J_{FF}, Hz) are reported as: chemical shift, multiplicity (br = broad, s = singlet, d = doublet, t = triplet, q = quartet, m = multiplet, dt = doublet of triplets, dd = doublet of doublets, ddd = doublet of doublet of doublets, dddd = doublet of doublet of doublet of doublets, td = triplet of doublets), coupling constant, and integration. High resolution mass spectra were obtained at the Mass Spectrometry Laboratory at the University of Kansas on a Micromass LCT Premier. Thin layer chromatography (TLC) was performed using EMD aluminum-backed (0.20 mm) silica plates (60 F-254), and flash chromatography used ICN silica gel (200-400 mesh). TLC plates were visualized with a UV lamp or by staining with I_2. Preparative HPLC was performed with an Agilent 1200 instrument equipped with a Hamilton PRP-1 reverse phase column (250 mm length, 21.2 mm ID, 7 μm particle size) with detection by absorbance at 215, 254, and 370 nm. All non-aqueous reactions were carried out using flame- or oven-dried glassware under an atmosphere of dry argon or nitrogen. Tetrahydrofuran (THF), dichloromethane (CH_2Cl_2), *N*,*N*-dimethylformamide (DMF), and methanol (CH_3OH), were purified via filtration through two columns of activated basic alumina under an atmosphere of Ar using a solvent purification system from Pure Process Technology (GlassContour). Other commercial reagents were used as received unless otherwise noted. Absorbance spectra and measurements of molar extinction coefficients (ε) were generated using semimicro (1.4 mL) UV quartz cuvettes (Sigma-Aldrich, Z27667-7) on an Agilent 8452A diode array spectrometer. All optical spectroscopy and protein binding assays were conducted in PBS (10 mM Na_2HPO_4, 137 mM NaCl, 2.7 mM KCl, 1.8 mM KH_2PO_4, pH 7.4), unless otherwise noted. Molar extinction coefficients were determined in PBS containing 0.5% DMSO and were calculated from Beer's Law plots of absorbance λ_{max} versus concentration as shown in Figure 2.16. Linear least squares fitting of the data (including a zero intercept) was used to determine the slope (corresponding to ε). Values (M^{-1} cm^{-1}) were calculated as follows: Absorbance = ε [concentration (M)] L, where L = 1 cm.

Absorbance data for Streptavidin concentrations were quantified by UV absorbance at 280 nm based on its calculated molar extinction coefficient ($\varepsilon_{monomer}$ = 41,326 M^{-1} cm^{-1}) using a Thermo Scientific NanoDrop 1000 spectrophotometer. All fluorescence spectra were acquired using a SUPRASIL ultra-micro quartz cuvette (PerkinElmer, B0631079) on a Perkin-Elmer LS55 Fluorescence Spectrometer (10 nm excitation slit width). Relative quantum yields (Φ) in PBS were determined by the method of Williams.[39] In brief, fluorophores were excited at 396 nm and the integrated fluorescence emission (415 nm to 700 nm) was quantified (concentrations of 5 nM to 160 nM). Coumarin 102 (Φ = 0.66 in water) provided the standard.[40] The integrated fluorescence emission at a given concentration was plotted against the maximum absorbance of the sample at that concentration determined by extrapolation based on absorbance measurements at higher concentrations. Linear least squares fitting of the data (including a zero intercept) was used to calculate the slope, which is proportional to the quantum yield. Quantum yields were calculated as follows: $\Phi_x = \Phi_{st}(Grad_x/Grad_{st})$, where Φ_{st} represents the quantum yield of the standard, Φ_x represents the quantum yield of the unknown, and Grad is the slope of the best linear fit. Theoretical Förster distances were calculated using a previously described protocol.[41, 42] The following parameters and equations were used: Φ_D is the quantum yield of the donor, η is the refractive index of the solvent, κ is the orientation factor, *J* is the degree of spectral overlap between the donor and acceptor, $F_D(\lambda)$ is the normalized donor fluorescence intensity, and $\varepsilon_A(\lambda)$ is the absorbance spectrum of the acceptor normalized to its maximum molar extinction coefficient.

$$R_o = 0.0211[\kappa^2 \phi_D \eta^{-4} J]^{1/6}$$
$$J = \int_{300}^{500} F_D(\lambda)\varepsilon_A(\lambda)\lambda^4 d\lambda$$

Theoretical Förster distances were calculated using PhotoChemCAD software, the measured extinction coefficient for each probe, $\Phi_{\text{tryptophan}} = 0.2$, $\eta_{\text{phosphate buffer, pH 7.4}} = 1.33$, and $\kappa = 2/3$.

2.10.2. Biological assays and protocols

Determination of K_d values by Förster Resonance Energy Transfer (FRET) from tryptophan to Pacific Blue

Different concentrations of the SA protein, chosen to span a range of at least 20% to 80% complexation, were incubated with fixed concentrations of **24** (25 nM), **25** (5 nM), or **26** (25 nM) in PBS (pH 7.4) at room temperature with shaking for 1 h. These fixed probe concentrations were chosen to be substantially below the predicted K_d values to assure equilibrium binding measurements. Measurements of raw FRET values (I_{295}, λ_{ex}= 295 nm, λ_{em}= 460 nm) and fluorescence intensity values (I_{400}, λ_{ex}= 400 nm, λ_{em}= 460 nm) were recorded for each sample. Averages of raw FRET ($I_{d,295}$) values and fluorescence ($I_{d,400}$) intensities of SA alone (background fluorescence) were calculated by averaging of three values for each concentration of SA. The fluorescence emission of the free ligand at 460 nm upon excitation at 295 nm ($I_{a,295}$) and 400 nm ($I_{a,400}$) were calculated by averaging three measurements of the Pacific Blue probe in PBS buffer. Background-subtracted FRET (I_{FRET}) and fluorescence ($I_{ad,400}$) signals were calculated as follows:

$$I_{FRET} = I_{295} - I_{a,295} - I_{d,295}$$

$$I_{ad,400} = I_{400} - I_{d,400}$$

The quenching ratio (Q_r) was calculated as follows:

$$Q_r = \frac{I_{ad,400}}{I_{a,400}}$$

Background-subtracted FRET signals (I_{FRET}) were processed to directly factor in quenching or enhancement of the fluorophore using the following equation, where I_{ad} is the corrected FRET signal:

$$I_{ad} = \frac{I_{FRET}}{Q_r}$$

To calculate the dissociation constant (K_d) using FRET data, the corrected FRET signal (I_{ad}) was plotted against the concentration of streptavidin (monomer). The experiments were run in triplicate, and the one site - specific binding model of GraphPad Prism 6.0 was used for curve fitting.

To calculate the dissociation constant (K_d) using fluorescence quenching data, the change in fluorescence (enhancement or quenching, $I_{ad,400}$) was normalized and plotted against the concentration of streptavidin (monomer). The experiments were run in triplicate, and the one site - specific binding model of GraphPad Prism 6.0 was used for curve fitting. For **25**, the fluorescence intensity values for the three highest concentrations SA monomer (64, 128, and 256 nM) were excluded from the analysis in order for the one site – specific binding model to fit. Note: for compound **32**–**33** (Myc tag derivatives), the same procedure was followed with the exception of the following; Protein: Monoclonal Anti c-Myc antibody, ligand concentration: 100 nM, excitation and emission wavelengths were as follows: λ_{ex}= 400 nm and λ_{em}= 460 nm.

Determination of K_i values via competition assay (loss of Trp-PB FRET signal)

The unlabeled ligand was added to a fixed concentration of pre-complexed SA and fluorescent probe **26** (SA = 175 nM, **26** = 25 nM) in PBS (pH 7.4) at room temperature with shaking for 1 h. The concentration of SA was chosen to be close to the K_d value measured for the fluorescent probe, and the concentration of **26** was chosen to be substantially below K_d to assure equilibrium binding. Measurements of raw FRET values (I_{295}, λ_{ex}= 295 nm, λ_{em}= 460 nm) and fluorescence intensity values (I_{400}, λ_{ex}= 400 nm, λ_{em}= 460 nm) were recorded for each sample. Averages of raw FRET ($I_{d,295}$) values and fluorescence ($I_{d,400}$) intensities of SA alone (background fluorescence) were calculated by averaging of three values for each concentration of SA. The fluorescence emission of the free ligand at 460 nm upon excitation at 295 nm ($I_{a,295}$) was calculated by averaging three measurements of **26** in PBS buffer. Background-subtracted FRET (I_{FRET}) and fluorescence ($I_{ad,400}$) signals were calculated as follows:

$$I_{FRET} = I_{295} - I_{a,295} - I_{d,295}$$

$$I_{ad,400} = I_{400} - I_{d,400}$$

The quenching ratio (Q_r) was calculated as follows:

$$Q_r = \frac{I_{ad,400}}{I_{a,400}}$$

Background-subtracted FRET signals (I_{FRET}) were processed to directly factor in quenching or enhancement of the fluorophore using the following equation, where I_{ad} is the corrected FRET signal:

$$I_{ad} = \frac{I_{FRET}}{Q_r}$$

To calculate the IC_{50}, the corrected FRET signal (I_{ad}) was plotted against the concentration of unlabeled ligand. The experiments were run in triplicate, and the log(inhibitor) vs. response model of GraphPad Prism 6.0 was used for curve fitting. The inhibitory constant (K_i) was calculated as follows:

$$K_i = \frac{IC_{50}}{\frac{L}{K_d} + 1}$$

Isothermal titration calorimetry (ITC)

ITC experiments were performed using a MicroCal Auto-Isothermal Titration Calorimeter with protein and ligand solutions prepared in PBS. Titrations were performed at 25 °C and consisted of 25 injections (10 μL) of ligand (50–250 μM) into streptavidin (1.46 mL, 4–20 μM), with 6 min between injections. The experimental data were fit to a one-site binding model (Origin software) where ΔH (enthalpy change, kcal/mol), K_a (association constant, M^{-1}), and n (number of binding sites) were variables.

Determination of K_d values by fluorescence polarization (FP) of Pacific Blue

FP is very sensitive to fluorescence quenching because of effects on the lifetime of the fluorophore. This quenching prevented attempts to use FP to independently quantify the affinity of ligands **25** and **26** for SA.[3] However, quenching was less significant for the lower affinity ligand **24**, and a previously described[43] FP method was used to independently analyze this probe. Measurements of fluorescence intensity (I_{400}, λ_{ex}= 400 nm, λ_{em}= 460 nm) and fluorescence polarization (P, λ_{ex}= 400 nm, λ_{em}= 460 nm) were recorded for each sample. The change in polarization for each sample was calculated by subtracting the average (n=3) polarization of the free ligand (P_f). This change was plotted against the concentration of SA, and the maximum polarization of the fully bound complex was estimated (B_{max}) based on a one-site specific binding model (GraphPad Prism 6.0). This polarization of the complex (P_b) was used in the following equation to calculate the apparent fraction bound (F_a):

$$F_a = \frac{P - P_f}{P_b - P_f}$$

Background-subtracted fluorescence signals ($I_{ad,400}$) were calculated as previously described. In order to correct for fluorescence enhancement or quenching, a fluorescence enhancement factor (Q) was calculated using the following equation, where $I_{ad,400}$ and $I_{a,400}$ are the fluorescence intensity (λ_{ex}= 400 nm, λ_{em}= 460 nm) of the sample and free ligand, respectively:

$$Q = \frac{I_{ad,400} - I_{a,400}}{I_{a,400}}$$

To incorporate fluorescence enhancement/quenching into the measurements, the corrected fraction bound (f_a) was calculated using the following equation:

$$f_a = \frac{F_a}{1 + Q(1 - F_a)}$$

To calculate the dissociation constant (K_d), the corrected fraction bound was plotted against the concentration of streptavidin, and a one site- specific binding equation of GraphPad Prism 6.0 was used for curve fitting.

Cell culture: HeLa cells, obtained from ATCC (CCL-2), were cultured in Dulbecco's Modified Eagle Medium (DMEM, Sigma D6429). All media was supplemented with fetal bovine serum (FBS, 10%), penicillin (100 units/mL), and streptomycin (100 µg/mL) and incubated in a humidified 5% CO_2 incubator at 37 °C unless otherwise noted.

Transient transfection of HeLa cells: The plasmid pPA2-TS7A-WT-GTP-mRFP was studied previously by Drs. Laurie Mottram and Sonalee Athavankar of the Peterson group and are described in their PhD theses. Prior to transfection, HeLa cells in DMEM were seeded onto an 8-well cover glass slide (Ibidi µ-Slide, 300 µL, 10,000 cells/well) and allowed to proliferate for 16 h at 37 °C. To form a DNA complex, the plasmid DNA (2 μg) was incubated at 22 °C with the DNA transfection reagent X-tremeGENE HP (2 μL, Roche) in serum free DMEM medium (200 μL). After 30 min, the DNA complex (20 μL) was added to each well. The cells were further incubated at 37 °C for 48 h. After transfection, the cells were washed with medium, further treated with probes, and analyzed by confocal microscopy.

Confocal microscopy: Compounds in DMSO stock solutions were serially diluted 1,000-fold with complete media (final concentration of 0.1% DMSO) prior to addition to cells. Transiently transfected cells were treated with compounds at 37 °C for 30 min before imaging by a Leica SPE2 confocal laser-scanning microscope with a 63X oil-immersion objective. **20** and **34** were excited with a 405 nm laser and emitted photons were collected from 425-475 nm. The mRFP was excited with a 532 nm laser and emitted photons were collected from 550-650 nm.

LogD measurements: 5 mM solutions of **20** or **34** were made by dissolving the solid compounds in 1:1 octanol/phosphate buffer (4 mL total volume, 5 mM phosphate, pH 7.4). Samples were shaken for 24 h at 22 °C to equilibrate. Following shaking, the samples were allowed to settle, and 1 mL from the top and bottom were removed and centrifuged at 14,000 rpm (no precipitate was observed for any of the samples). Aliquots of these fractions were diluted in octanol (derived from the top fraction) or 5 mM phosphate buffer (derived bottom fraction) to generate stock solutions that were then further diluted into a solvent mixture comprising ethanol (80%), octanol (10%), and 5 mM phosphate buffer (10%, pH 7.4) the for analysis by fluorescence spectroscopy. The ratio of fluorescence emission (λ_{max} = 458 nm) was used to calculate logD.

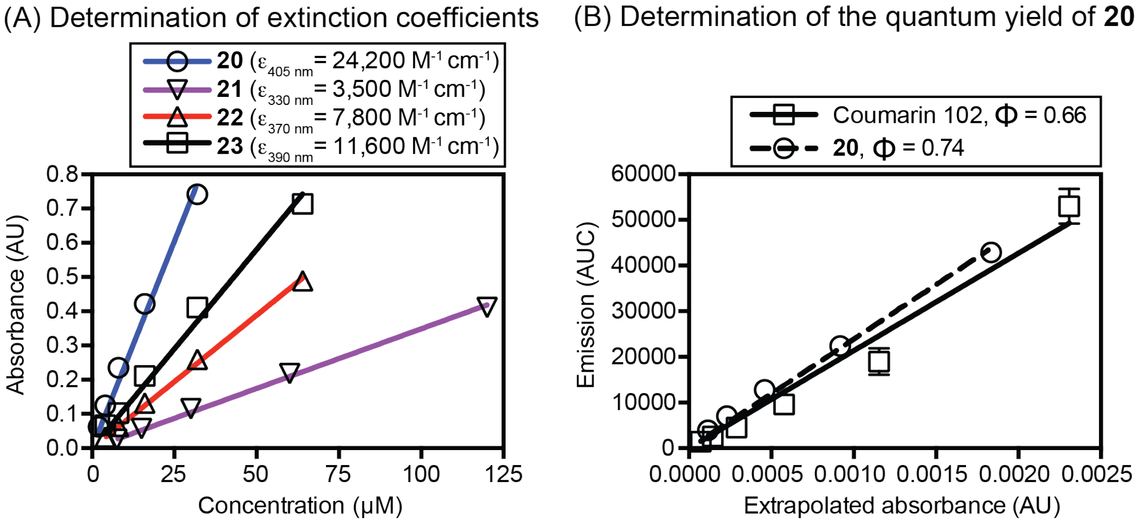

Figure 2.16. Analysis of compounds in PBS (pH 7.4) containing DMSO (0.5%). A: Determination of extinction coefficients of **20**–**23**. B: Measurement of the quantum yield of **20** in PBS (pH 7.4) relative to coumarin 102.

2.10.3 Synthetic procedures and compound characterization data

General procedure 2A: Synthesis of fluorescent biotin derivatives **20** and **21**. *N*-Boc-ethylenediamine-D-biotin (64–87 mg, 1.5 eq), prepared as previously reported,[44] was treated with a solution of trifluoroacetic acid (TFA) / CH_2Cl_2 (2 mL, 30:70) for 20 min. The mixture was concentrated under vacuum and washed with CH_2Cl_2 (5 mL) and ether (5 mL x 2) to remove excess TFA. The activated fluorophore (1 eq.), *N*,*N*-diisopropylethylamine (DIEA, 5 eq.), and DMF (1–3 mL) were added, and the reaction was stirred at 22 °C for 16 h. The solvent was removed under vacuum, the residue was dissolved in DMSO (1.5 mL), and the product purified by preparative RP-HPLC (Gradient: H_2O:CH_3CN (9:1) to (0:100) with added TFA (0.1%) over 20 min; elution time = 6–10 min). Pure fractions were collected, combined, and solvent was removed by lyophilization.

General procedure 2B: Synthesis of fluorescent biotin derivatives **22** and **23**. *N*-Boc-ethylenediamine-D-biotin (92–120 mg, 1.5 eq), prepared as previously reported,[44] was treated with a solution of TFA / CH_2Cl_2 (2 mL, 30:70) for 20 min. The mixture was concentrated under vacuum and washed with CH_2Cl_2 (5 mL) and ether (5 mL x 2) to remove excess TFA. The fluorophore (1 eq.), 1-ethyl-3-(3-dimethylaminopropyl)carbodiimide (EDC, 1.1 eq.), 4-dimethylaminopyridine (DMAP, 0.5 eq.), and DMF (2 mL), were added, and the reaction was stirred at 22 °C for 16 h. The solvent was removed under vacuum, the residue was dissolved in DMSO (1.5 mL), and the product was purified by preparative RP-HPLC (Gradient: H_2O:CH_3CN (9:1) to (0:100) with added TFA (0.1%) over 20 min; elution time = 6–10 min). Pure fractions were collected, combined, and dried by lyophilization.

General procedure 2C: Synthesis of biotin analogues linked to Pacific Blue (**24**–**26**). *N*-Boc-ethylenediamine-Pacific Blue (**35**, 23-29 mg, 1 eq.) was treated with a solution of TFA / CH_2Cl_2 (2 mL, 30:70) for 20 min. The mixture was concentrated and washed with CH_2Cl_2 (5 mL) and MeOH (5 mL x 2) to remove excess TFA. The biotin analogue (1.3 eq.), HBTU (1.5 eq.), hydroxybenzotriazole (HOBt, 1.5 eq.), DIEA (5 eq.), and DMF (1 mL) were added. The reaction was stirred at 22 °C for 16 h. The solvent was removed under vacuum, the residue was dissolved in DMSO (1.5 mL), and the product was purified by preparative RP-HPLC (Gradient: H_2O:CH_3CN (9:1) to (0:100) with added TFA (0.1%) over 20 min; elution time = 6-10 min). Pure fractions were collected, combined, and dried by lyophilization.

General procedure 2D: Solid phase peptide synthesis (SPPS) for compounds **31**–**33** was performed on a Mettler Toledo Miniblock reactor (Model No: Bohdan 2080; 12-well block with glass reaction vessels, 600 rpm) utilizing standard Fmoc chemistry employing Rink amide MBHA resin (0.36 mmol/g, 140 mg, 0.05 mmol). The resin was first swelled in DMF for 2 h and the Fmoc group was removed with deblocking solution (20% piperidine in DMF (2 mL), 2 x 4 min with shaking). The resin was washed with DMF (4x, 2 mL) to remove excess piperidine, and treated with Fmoc-amino acids (4 eq.), HATU coupling reagents (3.8 eq.), and DIEA (8 eq.) in DMF (2 mL) with agitation until coupling was completed (3–12 h). The reaction solution was removed and resin was washed with DMF (4x, 2 mL). This coupling protocol was repeated for each additional amino acid. For **32**–**33**, the final amine was capped by agitating with PB-NHS (**15**, 2 eq.) and DIEA (5 eq.) in DMF (2 mL) for 6 h. Cleavage from resin was done using a mixture of TFA:H_2O:TIPS (95:2.5:2.5) with agitation for 2 h. The resin was removed by filtration and washed with DCM (3x, 2 mL). The filtrates were combined and concentrated under vacuum to give crude products. Purification was done using preparative reverse-phase HPLC (Gradient: H_2O:CH_3CN (9:1) to (0:100) with added TFA (0.1%) over 20 min; elution time = 5-9 min). Pure fractions were collected, combined, and dried by lyophilization.

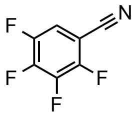

17

2,3,4,5-Tetrafluorobenzonitrile (17). To a solution of 2,3,4,5-tetrafluorobenzoic acid (**16**, 10 g, 51 mmol), in CH_2Cl_2 (50 mL) was added oxalyl chloride (5.4 mL, 62.9 mmol) and DMF (ca. 2 drops) and the reaction mixture was stirred at 22 °C for 16 h while vented to the atmosphere to allow escape of evolved gasses. The solvent was removed under reduced pressure, and the vessel was placed on high vacuum for 2 h to afford the acid chloride as a viscous oil. This oil was dissolved in chloroform (40 mL) and cooled to 4 °C. Aqueous ammonia (28%, 55 mL) was slowly added and the reaction was stirred at 4 °C for 30 min. The mixture was extracted with chloroform, and the organic layer was dried, filtered, and concentrated under reduced pressure to afford a white solid. To the solid was added phosphoryl chloride (32 mL) and the mixture was stirred at 80 °C for 3 h. The mixture was treated with diethyl ether (150 mL) and ice water (100 mL), followed by sat. aqueous $NaHCO_3$ (100 mL) for 1 h. The mixture was extracted with diethyl ether, and the organic layer was washed with sat. aqueous $NaHCO_3$ (3 x 100 mL). The organic layer was dried, filtered, and concentrated under reduced pressure to afford **17** (7.9 g, 88%) as a colorless oil. ^{1}H NMR (500 MHz, $CDCl_3$) δ 7.33 (dddd, *J* = 8.8, 7.6, 5.3, 2.6 Hz, 1H); ^{13}C NMR (126 MHz, $CDCl_3$) δ 149.5 (dddd, *J* = 269.0, 12.1, 4.0, 2.0 Hz), 147.4 (dddd, *J* = 259.0, 10.8, 3.9, 2.2 Hz), 144.4 (dddd, *J* = 265.6, 15.9, 12.2, 3.2 Hz), 143.4 (ddd, *J* = 16.0, 12.1, 3.2 Hz), 141.3 (dddd, *J* = 258.6, 15.0, 12.7, 4.0 Hz), 115.0 (dd, *J* = 21.9, 4.1 Hz), 111.2 (m), 97.8 (dddd, *J* = 14.2, 9.3, 4.7, 1.7 Hz); ^{19}F NMR (376 MHz, $CDCl_3$) δ -129.99 (dddt, *J* = 31.8, 19.9, 11.9, 6.9 Hz), -134.49 (dddt, *J* = 32.4, 20.6, 11.8, 5.3 Hz), -143.33 (tdd, *J* = 20.5, 12.9, 8.3 Hz), -150.62 (dddd, *J* = 39.3, 24.4, 17.3, 6.4 Hz); HRMS (ESI-) m/z 173.9993 ($M-H^+$, C_7F_4N requires 173.9967). Note: This compound is also commercially available (Oakwood Chemicals, 25 g / $75).

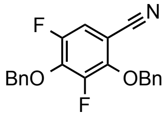

18

2,4-Bis(benzyloxy)-3,5-difluorobenzonitrile (18). To a solution of **17** (7.8 g, 45 mmol) in DMF (5 mL) was added benzyl alcohol (23 mL, 223 mmol) and potassium carbonate (37 g, 267 mmol). The reaction was heated to 105 °C for 16 h. The vessel was placed on high vacuum for 2 h to remove DMF followed by purification by column chromatography on silica gel (eluent: hexanes/ethyl acetate (17:1)) to afford **18** (13.5 g, 86%) as a viscous colorless oil. ^{1}H NMR (500 MHz, $CDCl_3$) δ 7.46-7.33 (m, 11H), 7.04 (dd, *J* = 10.0, 2.3 Hz, 1H), 5.29 (s, 2H), 5.2251 (d, *J* = 1.0 Hz, 2H); ^{13}C NMR (126 MHz, $CDCl_3$) δ 151.1 (dd, *J* = 247.5, 4.8 Hz), 149.4 (dd, *J* = 251.5, 6.3

Hz), 146.3 (dd, *J* = 11.9, 3.3 Hz), 140.7 (dd, *J* = 14.7, 12.1 Hz), 135.5, 135.2, 129.1, 129.0, 128.84, 128.80, 128.77, 128.4, 114.9 (dd, *J* = 23.6, 3.7 Hz), 114.8 (d, *J* = 3.0 Hz), 101.0 (dd, *J* = 10.5, 5.0 Hz), 76.8 (d, *J* = 5.6 Hz), 76.2 (t, *J* = 3.9 Hz); ^{19}F NMR (376 MHz, $CDCl_3$) δ -129.79 (d, *J* = 6.9 Hz), -138.96 (d, *J* = 6.9 Hz); HRMS (ESI+) m/z 374.0979 (M+Na$^+$, $C_{21}H_{15}F_2NO_2Na$ requires 374.0969).

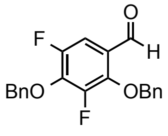

19

2,4-Bis(benzyloxy)-3,5-difluorobenzaldehyde (19). To a solution of **18** (13.4 g, 38 mmol) in CH_2Cl_2 (20 mL) at -78 °C was added diisobutylaluminum hydride (Acros Organics, 1 M in cyclohexane, 45.9 mL). The reaction mixture was stirred at -78 °C for 3.5 h, and was then warmed to 22 °C. The reaction was quenched by stirring with aqueous HCl (0.5 M, 150 mL) for 1 h. The mixture was extracted with ethyl acetate, dried, filtered, and evaporated under reduced pressure. The resulting solid was recrystallized with ethanol to afford **18** (11.6 g, 87%) as a white solid. ^{1}H NMR (500 MHz, $CDCl_3$) δ 10.01 (d, *J* = 3.3 Hz, 1H), 7.49 - 7.27 (m, 11H), 5.34 (s, 2H), 5.17 (d, *J* = 1.0 Hz, 2H); ^{13}C NMR (126 MHz, $CDCl_3$) δ 187.1 (dd, *J* = 3.2, 1.8 Hz), 151.8 (dd, *J* = 247.3, 4.0 Hz), 149.1 (dd, *J* = 250.8, 5.5 Hz), 146.6 (dd, *J* = 10.1, 2.9 Hz), 141.6 (dd, *J* = 15.4, 12.2 Hz), 135.8, 135.3, 129.2, 128.94, 128.91, 128.90, 128.8, 128.4, 124.1 (dd, *J* = 6.3, 1.6 Hz), 109.2 (dd, *J* = 21.2, 3.1 Hz), 77.4 (d, *J* = 6.5 Hz), 76.0 (t, *J* = 4.0 Hz); ^{19}F NMR (376 MHz, $CDCl_3$) δ -130.48 (d, *J* = 5.7 Hz), -140.71 (dd, *J* = 6.0, 2.5 Hz); HRMS (ESI+) m/z 377.0983 (M+Na$^+$, $C_{21}H_{16}F_2O_3Na$ requires 377.0965).

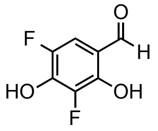

11

3,5-Difluoro-2,4-dihydroxybenzaldehyde (11). To a solution of **19** (11.0 g, 31 mmol) in CH_3OH / THF (100 mL, 7:3) was added Pd/C (10%, 1.67 g), and the mixture was stirred under an atmosphere of hydrogen (1 atm) at 22 °C for 8 h. After removing the catalyst by filtration over celite, the filtrate was concentrated under reduced pressure and purified by column chromatography over silica gel (eluent: hexanes/ethyl acetate/acetic acid (82:18:1)) to afford **11** (4.6 g, 83%) as a light pink solid. ^1H NMR (500 MHz, DMSO-*d*$_6$) δ 11.58 (s, 1H), 10.86 (s, 1H), 10.0439 (d, *J* = 2.4 Hz, 1H), 7.29 (dd, *J* = 10.8, 2.1 Hz, 1H); ^{13}C NMR (126 MHz, DMSO-*d*$_6$) δ 189.5, 146.8 (d, *J* = 11.8 Hz), 145.6 (dd, *J* = 236.6, 4.5 Hz), 141.5 (dd, *J* = 18.0, 13.5 Hz), 141.2 (dd, *J* = 238.9, 5.7 Hz), 113.9 (d, *J* = 5.8 Hz), 109. 4 (dd, *J* = 19.4, 2.9 Hz); ^{19}F NMR (376 MHz, DMSO-*d*$_6$) δ -144.25, -156.25 (d, *J* = 6.4 Hz); HRMS (ESI-) m/z 173.0038 (M-H$^+$, $C_7H_3F_2O_3$ requires 173.0050). Note: This product can be carried forward without further purification. Following simple filtration through celite and concentration, this crude material has yielded Pacific Blue (**5**) in high purity (79% yield over two steps, 8.5 mmol scale).

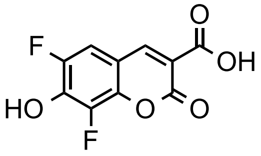

Pacific Blue (**5**)

6,8-Difluoro-7-hydroxy-2-oxo-2*H*-chromene-3-carboxylic acid (Pacific Blue, 5). To a suspension of **11** (4.2 g, 24.1 mmol) in water (110 mL) was added Meldrum's acid (3.8 g, 26.6 mmol) and ammonium acetate (550 mg, 7.2 mmol). The suspension was stirred at 22 °C for 3.5 h. Aqueous HCl (2 M, 75 mL) was added and the reaction was placed at 4 °C for 1 h. A precipitate formed that was filtered, washed with cold water (2 x 25 mL), and dried under high vacuum to give Pacific Blue (**5,** 5.4 g, 92%) as a light yellow solid. ^{1}H NMR (500 MHz, DMSO-*d*$_6$) δ 8.67 (d, *J* = 1.4 Hz, 1H), 7.66 (dd, *J* = 10.5, 2.0 Hz, 1H); ^{13}C NMR (126 MHz, DMSO-*d*$_6$) δ 163.9, 155.6, 148.6 (dd, *J* = 240.8, 4.7 Hz), 148.5 (t, *J* = 2.9 Hz), 141.3 (d, *J* = 9.6 Hz), 140.3 (dd, *J* = 18.1, 12.6 Hz), 138.7 (dd, *J* = 244.7, 6.4 Hz), 115.3, 110.5 (dd, *J* = 20.9, 3.0 Hz), 109.0 (d, *J* = 10.2 Hz). ^{19}F NMR (376 MHz, DMSO-*d*$_6$) δ -137.33 (d, *J* = 9.3 Hz), -155.68 (d, *J* = 9.8 Hz); HRMS (ESI-) m/z 240.9944 (M-H$^+$, $C_{10}H_3F_2O_5$ requires 240.9949).

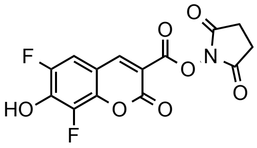

15

2,5-Dioxopyrrolidin-1-yl 6,8-difluoro-7-hydroxy-2-oxo-2*H*-chromene-3-carboxylate (Pacific Blue NHS ester, 15). To a solution of **5** (0.75 g, 3.1 mmol) in DMF (5 mL) was added *N*-(3-dimethylaminopropyl)-*N*′-ethylcarbodiimide hydrochloride (EDC, 1.2 g, 6.2 mmol) and *N*-hydroxysuccinimide (0.89 g, 7.8 mmol). The reaction mixture was stirred at 22 °C for 16 h. This reaction mixture was added dropwise to cold 1 N HCl (75 mL). A precipitate formed that was filtered, washed with cold aq. HCl (1N, 25 mL), and dried under high vacuum to give **15** (920 mg, 87%) as a yellow solid. ^{1}H NMR (500 MHz, DMSO-*d*$_6$) δ 9.01 (d, *J* = 1.4 Hz, 1H), 7.78 (dd, *J* = 10.2, 1.9 Hz, 1H), 2.89 (s, 4H); ^{13}C NMR (126 MHz, DMSO-*d*$_6$) δ 170.3, 158.4, 154.4, 152.1 (t, *J* = 2.9 Hz), 148.8 (dd, *J* = 241.3, 4.9 Hz), 142.4 (d, *J* = 9.0 Hz), 138.7 (dd, *J* = 244.8, 6.6 Hz), 111.5 (dd, *J* = 21.1, 2.8 Hz), 108.8, 108.4 (d, *J* = 10.3

Hz), 25.6; ^{19}F NMR (376 MHz, DMSO-d_6) δ -136.84, -155.95 (d, J = 13.4 Hz); HRMS (ESI-) m/z 338.0129 (M-H$^+$, $C_{14}H_6F_2NO_7$ requires 338.0112).

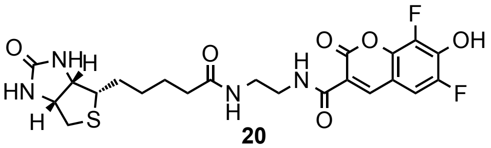

20

6,8-Difluoro-7-hydroxy-2-oxo-*N*-(2-(5-((3a*S*,4*S*,6a*R*)-2-oxohexahydro-1*H*-thieno[3,4-*d*]imidazol-4-yl)pentanamido)ethyl)-2*H*-chromene-3-carboxamide (Pacific Blue-Biotin, 20). Following general procedure 2A, Pacific Blue NHS ester (**15**, 50 mg, 0.15 mmol) yielded compound **20** (45 mg, 60%) as a pale yellow solid. ^{1}H NMR (500 MHz, DMSO-d_6) δ 8.82 (d, J = 1.4 Hz, 1H), 8.67 (t, J = 5.8 Hz, 1H), 7.93 (t, J = 5.6 Hz, 1H), 7.78 (dd, J = 10.5, 1.9 Hz, 1H), 6.44 (s, 1H), 6.36 (s, 1H), 4.29 (dd, J = 7.7, 4.9 Hz, 1H), 4.11 (dd, J = 7.8, 4.4 Hz, 1H), 3.39 (q, J = 6.2 Hz, 2H), 3.22 (q, J = 6.1 Hz, 2H), 3.07 (ddd, J = 8.5, 6.3, 4.4 Hz, 1H), 2.78 (dd, J = 12.4, 5.1 Hz, 1H), 2.55 (d, J = 12.4 Hz, 1H), 2.06 (t, J = 7.4 Hz, 2H), 1.64-1.26 (m, 6H); ^{13}C NMR (126 MHz, DMSO-d_6) δ 172.3, 162.7, 161.3, 159.5, 148.8 (dd, J = 241.2, 4.6 Hz), 147.3 (t, J = 2.9 Hz), 140.5 (d, J = 9.2 Hz), 140.0 (d, J = 13.2 Hz), 138.8 (dd, J = 245.1, 6.6 Hz), 116.2, 110.6 (dd, J = 21.0, 3.0 Hz), 109.6 (d, J = 10.2 Hz), 61.0, 59.2, 55.4, 40.1, 39.4, 38.5, 38.1, 35.2, 28.2, 28.1, 28.0, 25.3; HRMS (ESI-) m/z 509.1298 (M-H$^+$, $C_{22}H_{23}F_2N_4O_6S$ requires 509.1306).

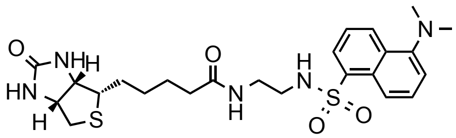

21

***N*-(2-((5-(Dimethylamino)naphthalene)-1-sulfonamido)ethyl)-5-((3a*S*,4*S*,6a*R*)-2-oxohexahydro-1*H*-thieno[3,4-*d*]imidazol-4-yl)pentanamide (Dansyl-Biotin, 21).**

Following general procedure 2A, dansyl chloride (30 mg, 0.11 mmol) yielded compound **21** (25 mg, 42%) as a white solid. ^{1}H NMR (500 MHz, DMSO-d_6) δ 8.47 (dt, *J* = 8.6, 1.1 Hz, 1H), 8.28 (dt, *J* = 8.8, 0.9 Hz, 1H), 8.10 (dd, *J* = 7.3, 1.2 Hz, 1H), 7.99 (t, *J* = 5.9 Hz, 1H), 7.73 (t, *J* = 5.8 Hz, 1H), 7.62 (m, 2H), 7.28 (d, *J* = 7.4 Hz, 1H), 6.42 (s, 1H), 4.30 (dd, *J* = 7.4, 4.7 Hz, 1H), 4.11 (dd, *J* = 7.7, 4.4 Hz, 1H), 3.13-3.05 (m, 1H), 3.03 (dt, *J* = 7.5, 5.9 Hz, 2H), 2.85 (s, 6H), 2.83-2.75 (m, 3H), 2.57 (d, *J* = 12.5 Hz, 1H), 1.93 (t, *J* = 7.4 Hz, 2H), 1.66-1.15 (m, 6H).^{13}C NMR (126 MHz, DMSO-d_6) δ 172.2, 162.7, 158.3, 158.0, 151.2, 135.8, 129.5, 129.0, 128.4, 128.3, 127.9, 123.7, 117.0, 115.2, 114.7, 61.0, 59.2, 55.4, 45.1, 42.0, 39.5, 35.1, 28.2, 25.1; HRMS (ESI+) m/z 542.1900 (M+Na$^+$, $C_{24}H_{33}N_5O_4S_2Na$ requires 542.1872).

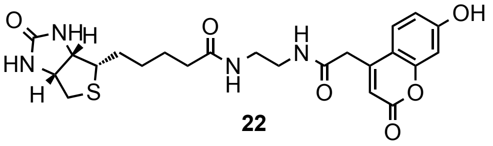

22

N-(2-(2-(7-Hydroxy-2-oxo-2*H*-chromen-4-yl)acetamido)ethyl)-5-((3a*S*,4*S*,6a*R*)-2-oxohexahydro-1*H*-thieno[3,4-*d*]imidazol-4-yl)pentanamide (7-hydroxycoumarin-Biotin, 7HC-Biotin, 22). 2-(7-Hydroxy-2-oxo-2*H*-chromen-4-yl)acetic acid was prepared as previously reported.[45] Following general procedure 2B, 2-(7-hydroxy-2-oxo-2*H*-chromen-4-yl)acetic acid (45 mg, 0.21 mmol) yielded compound **22** (57 mg, 57%) as a yellow solid. ^{1}H NMR (500 MHz, DMSO-d_6) δ 10.57 (s, 1H), 8.27-8.15 (m, 1H), 7.93-7.75 (m, 1H), 7.58 (d, *J* = 8.7 Hz, 1H), 6.79 (dd, *J* = 8.7, 2.4 Hz, 1H), 6.71 (d, *J* = 2.4 Hz, 1H), 6.40 (d, *J* = 27.8 Hz, 2H), 6.16 (s, 1H), 4.30 (dd, *J* = 7.7, 5.0 Hz, 1H), 4.12 (ddd, *J* = 7.7, 4.4, 1.8 Hz, 1H), 3.74-3.50 (m, 2H), 3.09 (m, 5H), 2.81 (dd, *J* = 12.4, 5.1 Hz, 1H), 2.57 (d, *J* = 12.5 Hz, 2H), 2.02 (t, *J* = 7.4 Hz, 2H), 1.67-1.18 (m, 6H); ^{13}C NMR (126 MHz, DMSO) δ 172.3, 167.8, 162.7, 161.2, 160.3, 155.0, 151.1, 126.8, 112.9, 111.9, 111.5, 102.3, 61.0, 59.2, 55.4, 40.4, 40.1, 40.0, 39.94, 39.86, 39.78, 39.69, 39.61, 39.5, 39.4, 39.2, 39.0, 38.9, 38.7, 38.1, 35.2, 28.2, 28.1, 25.2; HRMS (ESI-) m/z 487.1647 (M-H$^+$, $C_{23}H_{27}N_4O_6S$ requires 487.1651).

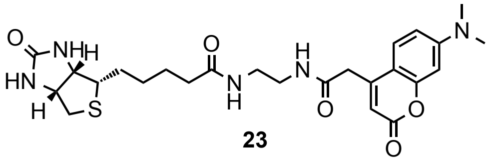

23

***N*-(2-(2-(7-(Dimethylamino)-2-oxo-2*H*-chromen-4-yl)acetamido)ethyl)-5-((3a*S*,4*S*,6a*R*)-2-oxohexahydro-1*H*-thieno[3,4-*d*]imidazol-4-yl)pentanamide (DMACA-Biotin, 23).** 2-(7-(Dimethylamino)-2-oxo-2*H*-chromen-4-yl)acetic acid was prepared as previously reported.[45] Following general procedure 2B, 2-(7-(dimethylamino)-2-oxo-2*H*-chromen-4-yl)acetic acid (DMACA, 40 mg, 0.16 mmol) yielded compound **23** (36 mg, 43%) as a yellow solid. ^{1}H NMR (500 MHz, DMSO-d_6) δ 8.25- 8.18 (m, 1H), 7.82 (d, *J* = 5.4 Hz, 1H), 7.53 (d, *J* = 9.0 Hz, 1H), 6.73 (dd, *J* = 9.0, 2.6 Hz, 1H), 6.56 (d, *J* = 2.5 Hz, 1H), 6.46-6.41 (m, 1H), 6.38 (s, 1H), 6.00 (s, 1H), 4.30 (ddd, *J* = 7.7, 5.2, 1.0 Hz, 1H), 4.16-4.10 (m, 1H), 3.61-3.57 (m, 2H), 3.10 (m, 5H), 3.02 (s, 6H), 2.82 (dd, *J* = 12.4, 5.1 Hz, 1H), 2.58 (d, *J* = 12.5 Hz, 1H), 2.03 (t, *J* = 7.4 Hz, 2H), 1.69-1.18 (m, 6H); ^{13}C NMR (126 MHz, DMSO) δ 172.7, 168.4, 163.2, 161.2, 155.8, 153.2, 151.6, 126.5, 109.9, 109.5, 108.7, 97.9, 61.5, 59.6, 55.9, 40.9, 39.3, 39.1, 38.6, 35.7, 28.7, 28.5, 25.6; HRMS (ESI+) m/z 516.2291 (M+H$^+$, $C_{25}H_{34}N_5O_5S$ requires 516.2281).

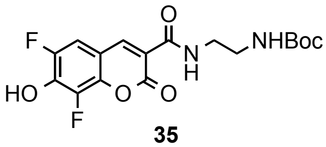

35

***tert*-Butyl(2-(6,8-difluoro-7-hydroxy-2-oxo-2*H*-chromene-3-carboxamido)ethyl)carbamate (*N*-Boc-ethylenediamine-Pacific Blue, 35).** To a solution of **15** (200 mg, 0.59 mmol) in DMF (5 mL) was added *N*-Boc-ethylenediamine (114 mg, 0.71 mmol). The reaction mixture was stirred at 22 °C for 16 h. The vessel was placed on high vacuum for 1 h to remove 4 mL of DMF. The remaining reaction mixture was added dropwise to cold 1 N HCl (40 mL). A precipitate formed that was filtered, washed with cold 1 N HCl (10 mL), and dried under high vacuum to give **35** (200 mg, 88%) as a yellow solid. ^{1}H NMR (500 MHz, DMSO-d_6) δ 8.81 (d, *J* = 1.4 Hz, 1H), 8.67 (t, *J* = 5.8 Hz, 1H), 7.77 (dd, *J* = 10.4, 1.9 Hz, 1H), 6.95 (t, *J* = 5.6 Hz, 1H), 3.36 (q, *J* = 6.1 Hz, 2H), 3.10 (q, *J* = 6.0 Hz, 2H), 1.37 (s, 11H), 1.45-1.39 (m, 1H); ^{13}C NMR (126 MHz, DMSO-d_6) δ 161.3, 159.5, 155.7, 148.9 (dd, *J* = 240.9, 4.8 Hz), 147.3, 140.5 (d, *J* = 9.0 Hz), 140.1, 138.8 (dd, *J* = 245.0, 6.4 Hz), 116.2, 110.7, 110.5, 109.5, 109.5, 77.7, 28.2; HRMS (ESI-) m/z 383.1043 (M-H$^+$, $C_{17}H_{17}F_2N_2O_6$ requires 383.1055).

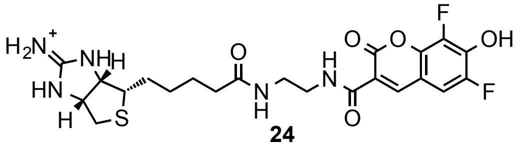
24

(3a*S*,4*S*,6a*R*)-4-(5-((2-(6,8-Difluoro-7-hydroxy-2-oxo-2*H*-chromene-3-carboxamido)ethyl)amino)-5-oxopentyl)tetrahydro-1*H*-thieno[3,4-*d*]imidazol-2(3*H*)-iminium (PB-iminobiotin, 24). Following general procedure 2C, 2-iminobiotin (19 mg, 0.077 mmol) yielded compound **24** (12 mg, 40%) as a pale yellow solid. ^{1}H NMR (500 MHz, DMSO-d_6) δ 8.80 (d, *J* = 1.4 Hz, 1H), 8.67 (t, *J* = 5.8 Hz, 1H), 8.22 (d, *J* = 6.5 Hz, 1H), 8.11-8.01 (m, 1H), 7.94 (t, *J* = 5.6 Hz, 1H), 7.82-7.70 (m, 1H), 7.62 (s, 2H), 6.55 (s, 1H), 4.63 (dd, *J* = 7.9, 4.8 Hz, 1H), 4.44 (ddd, *J* = 7.9, 4.5, 1.7 Hz, 1H), 3.38 (d, *J* = 6.3 Hz, 2H), 3.22 (dd, *J* = 7.7, 3.7 Hz, 2H), 3.01-2.82 (m, 2H), 2.77 (d, *J* = 12.9 Hz, 1H), 2.07 (t, *J* = 7.3 Hz, 2H), 1.75-1.23 (m, 6H); ^{13}C NMR (126 MHz, DMSO-d_6) δ 172.3, 161.3, 159.5 (d, *J* = 3.0 Hz), 159.4, 148.9 (dd, *J* = 240.8, 4.8 Hz), 147.4 (t, *J* = 3.0 Hz), 140.6 (d, *J* = 8.8 Hz), 140.2 (d, *J* = 17.4 Hz), 138.8 (dd, *J* = 245.3, 6.6 Hz), 116.1, 110. 6 (dd, *J* = 21.1, 2.9 Hz), 109.5 (d, *J* = 10.2 Hz), 64.4, 63.0, 55.1, 40.1, 39.7, 38.1, 35.2, 28.2, 27.9, 25.2; HRMS (ESI-) m/z 508.1471 (M-H^+, $C_{22}H_{24}F_2N_5O_5S$ requires 508.1466).

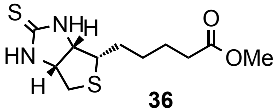

36

Methyl 5-((3a*S*,4*S*,6a*R*)-2-thioxohexahydro-1*H*-thieno[3,4-*d*]imidazol-4-yl)pentanoate (36). d-Biotin methyl ester (387 mg, 1.50 mmol), prepared as previously reported,[46] was dissolved in xylenes (6 mL). Lawesson's reagent (607 mg, 1.50 mmol) was then added and the reaction mixture was heated to 95 °C for 1 h. The solvent was removed under reduced pressure, and the resulting residue was extracted with ethyl acetate, dried, filtered, and evaporated under reduced pressure. The residue was purified by column chromatography over silica gel (eluent: CH_2Cl_2 / CH_3OH (50:1)) to afford **36** (330 mg, 80%) as a white solid. ^1H NMR (500 MHz, DMSO-d_6) δ 8.24 (m, 1H), 8.17 (s, 1H), 4.54 (dd, *J* = 8.4, 5.0 Hz, 1H), 4.36 (ddd, *J* = 8.4, 4.5, 1.5 Hz, 1H), 3.58 (s, 3H), 3.17 (ddd, *J* = 8.6, 6.0, 4.5 Hz, 1H), 2.86 (dd, *J* = 12.6, 5.1 Hz, 1H), 2.67 (d, *J* = 12.7 Hz, 1H), 2.30 (t, *J* = 7.5 Hz, 2H), 1.77-1.24 (m, 6H); ^{13}C NMR (126 MHz, $CDCl_3$) δ 182.4, 173.3, 66.0, 64.1, 55.7, 39.8, 33.1, 28.1, 27.9, 24.5; HRMS (ESI+) m/z 297.0707 (M+Na^+, $C_{11}H_{18}N_2O_2S_2Na$ requires 297.0707).

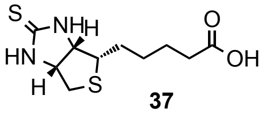

37

5-((3a*S*,4*S*,6a*R*)-2-Thioxohexahydro-1*H*-thieno[3,4-*d*]imidazol-4-yl)pentanoic acid (37). To a solution of **36** (125 mg, 0.46 mmol) in CH_3OH (4 mL) was added aq. NaOH (1 N, 2 mL). The reaction mixture was heated to 35 °C for 0.5 h, followed by acidification with aq. HCl (1 N, 10 mL). A precipitate formed that was filtered, washed with cold aq. HCl (1 N, 5 mL), and dried under high vacuum to give **37** (90 mg, 76%) as a white solid. ^1H NMR (500 MHz, DMSO-*d*$_6$) δ 12.00 (s, 1H), 8.24 (s, 1H), 8.17 (s, 1H), 4.54 (dd, *J* = 8.4, 4.9 Hz, 1H), 4.36 (ddd, *J* = 8.5, 4.7, 1.4 Hz, 1H), 3.17 (ddd, *J* = 8.8, 5.9, 4.4 Hz, 1H), 2.86 (dd, *J* = 12.6, 5.0 Hz, 1H), 2.67 (d, *J* = 12.6 Hz, 1H), 2.20 (t, *J* = 7.4 Hz, 2H), 1.75-1.20 (m, 6H); ^{13}C NMR (126 MHz, DMSO-*d*$_6$) δ 182.4, 174.5, 66.0, 64.1, 55.7, 40.1, 33.5, 28.2, 28.0, 24.6; HRMS (ESI-) m/z 259.0572 (M-H^+, $C_{10}H_{15}N_2O_2S_2$ requires 259.0575).

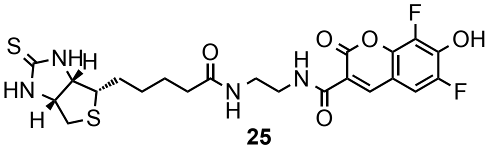

25

6,8-Difluoro-7-hydroxy-2-oxo-*N*-(2-(5-((3a*S*,4*S*,6a*R*)-2-thioxohexahydro-1*H*-thieno[3,4-*d*]imidazol-4-yl)pentanamido)ethyl)-2*H*-chromene-3-carboxamide (PB-thiobiotin, 25). Following general procedure 2C, **37** (24 mg, 0.091 mmol) yielded compound **25** (18 mg, 49%) as a pale yellow solid. ^1H NMR (500 MHz, DMSO-*d*$_6$) δ 8.79 (d, *J* = 1.4 Hz, 1H), 8.66 (t, *J* = 5.8 Hz, 1H), 8.23 (s, 1H), 8.15 (s, 1H), 7.92 (t, *J* = 5.6 Hz, 1H), 7.73 (d, *J* = 10.5 Hz 1H), 4.69-4.46 (m, 1H), 4.34 (ddd, *J* = 8.5, 4.6, 1.6 Hz, 1H), 3.54-3.28 (m, 10H), 3.28-3.10 (m, 4H), 2.82 (dd, *J* = 12.7, 5.1 Hz, 1H), 2.65 (d, *J* = 12.7 Hz, 1H), 2.15-1.97 (m, 2H), 1.74-1.16 (m, 6H); ^{13}C NMR (126 MHz, DMSO-*d*$_6$) δ 182.4, 172.4, 161.5, 159.7, 149.3 (d, *J* = 239.7 Hz), 147.4 (t, *J* = 2.8 Hz), 140.8, 140.7, 139.0 (dd, *J* = 244.6, 6.8 Hz), 115.3, 110.6, 108.8, 66.0, 64.2, 55.8, 40.4, 40.1, 38.9, 35.3, 30.8, 28.3, 28.0, 25.3; HRMS (ESI-) m/z 525.1050 (M-H$^+$, $C_{22}H_{23}F_2N_4O_5S_2$ requires 525.1078).

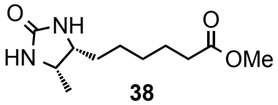

38

Methyl 6-((4*R*,5*S*)-5-methyl-2-oxoimidazolidin-4-yl)hexanoate (38). To a solution of d-Desthiobiotin (215 mg, 1.0 mmol) in CH_3OH (5 mL), thionyl chloride (218 µL, 3.0 mmol) was added dropwise. The reaction mixture was stirred at 22 °C for 3 h. The solvent was removed under reduced pressure followed by purification by column chromatography on silica gel (eluent: CH_2Cl_2 / CH_3OH (20:1)) to afford **38** (217 mg, 95%) as a white solid. ^{1}H NMR (500 MHz, $CDCl_3$) δ 5.34 (s, 1H), 5.07 (s, 1H), 3.89-3.78 (m, 1H), 3.70 (ddd, *J* = 9.2, 7.8, 4.9 Hz, 1H), 3.66 (s, 3H), 2.31 (t, *J* = 7.4 Hz, 2H), 1.77 -1.17 (m, 8H), 1.12 (d, *J* = 6.5 Hz, 3H); ^{13}C NMR (126 MHz, $CDCl_3$) δ 174.3, 164.0, 77.41, 77.36, 77.2, 76.9, 56.2, 51.7, 51.6, 34.0, 29.6, 29.1, 26.3, 24.8, 15.8; HRMS (ESI+) m/z 251.1374 (M+H$^+$, $C_{11}H_{20}N_2O_3Na$ requires 251.1372).

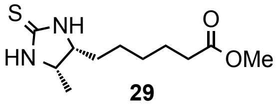

29

Methyl 6-((4*R*,5*S*)-5-methyl-2-thioxoimidazolidin-4-yl)hexanoate (29). To a solution of **38** (100 mg, 0.44 mmol) in xylenes (3 mL) was added Lawesson's reagent (178 mg, 0.44 mmol). The reaction mixture was heated to 95 °C for 1 h. The solvent was removed under reduced pressure and the resulting residue was extracted with ethyl acetate, dried, filtered, and evaporated under reduced pressure. The residue was purified by column chromatography over silica gel (eluent: CH_2Cl_2 / CH_3OH (50:1)) to afford **29** (91 mg, 85%) as a white solid. ^{1}H NMR (500 MHz,

$CDCl_3$) δ 6.29 (br, 2H), 4.10 (t, *J* = 7.2 Hz, 1H), 4.01-3.87 (m, 1H), 3.67 (s, 3H), 2.32 (t, *J* = 7.3 Hz, 2H), 1.81-1.23 (m, 8H), 1.18 (d, *J* = 6.1 Hz, 3H); ^{13}C NMR (126 MHz, $CDCl_3$) δ 182.8, 174.1, 60.5, 55.9, 51.7, 34.0, 29.0, 28.9, 26.4, 24.8, 15.2; HRMS (ESI+) m/z 267.1146 (M+Na$^+$, $C_{11}H_{20}N_2O_2SNa$ requires 267.1143).

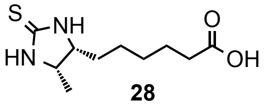
28

6-((4*R*,5*S*)-5-Methyl-2-thioxoimidazolidin-4-yl)hexanoic acid (imidazolidinethione, 28). To a solution of **29** (63 mg, 0.26 mmol) in CH_3OH (2 mL) was added aq. NaOH (1 N, 1 mL). The reaction mixture was heated to 35 °C for 0.5 h followed by acidification with aq. HCl (1 N, 5 mL). The resulting mixture was extracted with ethyl acetate, dried, filtered, and evaporated under reduced pressure. The residue was purified by column chromatography over silica gel (eluent: CH_2Cl_2 / CH_3OH (25:1)) to afford **28** (55 mg, 93%) as an off-white solid. ^{1}H NMR (500 MHz, CD_3OD) δ 4.11-3.96 (m, 1H), 3.87 (dt, *J* = 8.8, 6.8 Hz, 1H), 2.30 (t, *J* = 7.4 Hz, 2H), 1.71-1.25 (m, 8H), 1.13 (d, *J* = 6.6 Hz, 3H); ^{13}C NMR (126 MHz, CD_3OD) δ 183.5, 177.7, 61.4, 56.7, 34.8, 30.2, 30.0, 27.1, 25.9, 14.8; HRMS (ESI-) m/z 229.1006 (M-H$^+$, $C_{10}H_{17}N_2O_2S$ requires 229.1011).

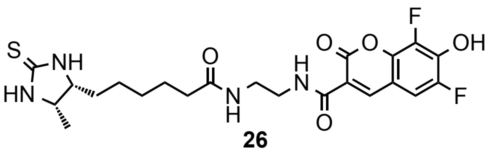
26

6,8-Difluoro-7-hydroxy-*N*-(2-(6-((4*R*,5*S*)-5-methyl-2-thioxoimidazolidin-4-yl)hexanamido)ethyl)-2-oxo-2*H*-chromene-3-carboxamide (PB-imidazolidinethione, 26). Following general procedure 2C, **28** (23 mg, 0.1 mmol) yielded compound **26** (26 mg, 68%) as a pale yellow solid. ^{1}H NMR (500 MHz, DMSO-d_6) δ 8.81 (br, 1H), 8.66 (t, *J* = 5.9 Hz, 1H), 8.18 (s, 1H), 8.02 (s, 1H), 7.91 (t, *J* = 5.7 Hz, 1H), 7.77 (dd, *J* = 10.6, 2.0 Hz, 1H), 3.92-3.77 (m, 1H), 3.68 (td, *J* = 8.2, 4.7 Hz, 1H), 3.37 (m, 2H), 3.21 (q, *J* = 6.1 Hz, 2H), 2.05 (t, *J* = 7.4 Hz, 2H), 1.58-1.08 (m, 8H), 0.96 (d, *J* = 6.4 Hz, 3H); ^{13}C NMR (126 MHz, DMSO-d_6) δ 181.8, 172.4, 161.3, 159.5, 148.9 (dd, *J* = 240.1, 4.1 Hz), 147.3 (d, *J* = 3.3 Hz), 140.6 (d, *J* = 8.6 Hz), 138.8 (dd, *J* = 245.1, 6.7 Hz), 116.1, 110.6 (dd, *J* = 21.6, 2.2 Hz), 109.4, 59.1, 54.4, 38.1, 35.4, 28.7, 28.6 , 25.5, 25.2, 20.7, 14.6; HRMS (ESI-) m/z 495.1534 (M-H$^+$, $C_{22}H_{25}F_2N_4O_5S$ requires 495.1514).

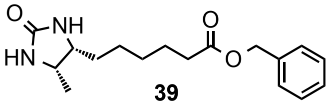

39

Benzyl 6-((5*S*)-5-methyl-2-oxoimidazolidin-4-yl)hexanoate (39). To a solution of d-Desthiobiotin (100 mg, 0.46 mmol) in DMF (2 mL) was added benzyl alcohol (95 µL, 0.92 mmol), *N*-(3-dimethylaminopropyl)-*N′*-ethylcarbodiimide hydrochloride (EDC, 56 mg, 0.6 mmol), HOBt (92 mg, 0.6 mmol), DMAP (56 mg, 0.46 mmol),The reaction mixture was stirred at 22 °C for 16 h. . The solvent was removed under vacuum and the residue was purified by column chromatography over silica gel (eluent: CH_2Cl_2 / CH_3OH (50:2)) to afford **39** (137 mg, 96%) as an off-white solid. ^{1}H NMR (500 MHz, $CDCl_3$) δ 7.34-7.22 (m, 5H), 5.05 (s, 2H), 3.87-3.76 (m, 1H), 3.65 (td, *J* = 8.3, 5.0 Hz, 1H), 2.30 (t, *J* = 7.4 Hz, 2H), 1.68-1.13 (m, 8H), 1.07 (d, *J* = 6.4 Hz, 3H); ^{13}C NMR (126 MHz, $CDCl_3$) δ 173.6, 163.4, 136.1, 128.7, 128.4, 66.3, 56.4, 51.8, 34.2, 29.5, 29.0, 26.3, 24.8, 15.8; HRMS (ESI+) m/z 305.1889 (M+H$^+$, $C_{17}H_{24}N_2O_3$ requires 305.1865).

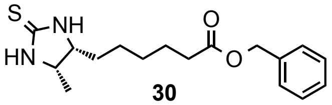

30

Benzyl 6-((5*S*)-5-methyl-2-thioxoimidazolidin-4-yl) hexanoate (imidazolidinethione-OBn, 30). To a solution of **39** (100 mg, 0.33 mmol) in xylenes (2.5 mL) was added Lawesson's reagent (133 mg, 0.33 mmol). The reaction mixture was heated to 95 °C for 1.5 h. The solvent was removed under reduced pressure and the resulting residue was extracted with ethyl acetate, dried, filtered, and evaporated under reduced pressure. The residue was purified by column chromatography over silica gel (eluent: CH_2Cl_2 / CH_3OH (50:1)) to afford **30** (86 mg, 82%) as an off-white solid. ^{1}H NMR (500 MHz, $CDCl_3$) δ 7.45-7.27 (m, 5H), 5.11 (s, 2H), 4.07 (dq, *J* = 8.8, 6.5 Hz, 1H), 3.90 (td, *J* = 9.0, 4.8 Hz, 1H), 2.36 (t, *J* = 7.4 Hz, 2H), 1.73-1.21 (m, 8H), 1.16 (d, *J* = 6.6 Hz, 3H); ^{13}C NMR (126 MHz, $CDCl_3$) δ 182.5, 173.4, 136.0, 128.6, 128.3, 66.2, 60.3, 55.8, 34.1, 28.8, 28.7, 26.2, 24.6, 15.0; HRMS (ESI+) m/z 321.1652 (M+H$^+$, $C_{17}H_{24}N_2O_2S$ requires 321.1637).

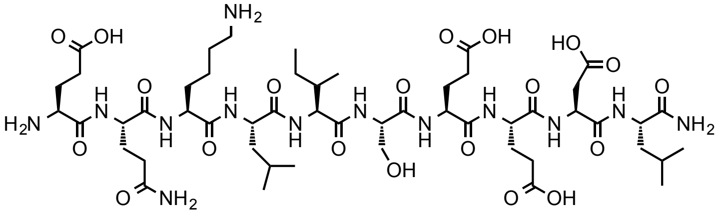

31

***N*-(Acetyl)-L-Glutamyl-L-Glutaminyl-L-Leucyl-L-Leucyl-L-Seryl-L-Glutamyl-L-Glutamyl-L-Aspartyl-L-Leucinamide (31).** Using general procedure 2D, Rink amide MBHA resin (0.7 mmol/g, 71 mg, 0.05 mmol) was used to produce **31** (38 mg, 0.032 mmol, 63% yield overall) as a white solid. LRMS (ESI+) m/z 1202.9 (M+H$^+$, $C_{51}H_{88}N_{13}O_{20}$ requires 1202.6).

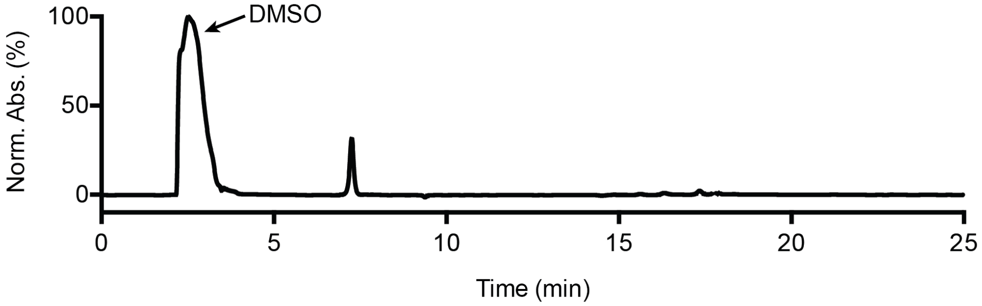

Figure 2.17. Analytical HPLC profile of **31** after preparative HPLC. Retention time = 7.5 min monitored by UV absorbance at 254 nm. Purity >95% by HPLC.

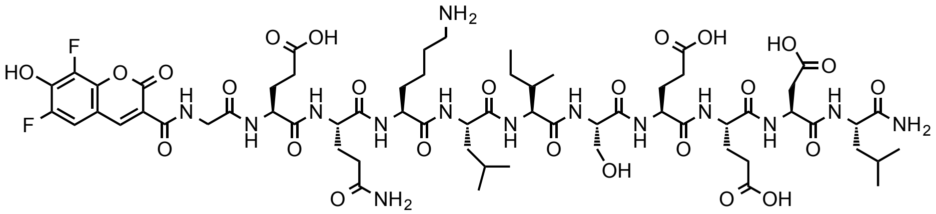

32

((6,8-Difluoro-7-hydroxy-2-oxo-2H-chromene)-3-carboxamide))-Glysyl-L-Glutamyl-L-Glutaminyl-L-Leucyl-L-Leucyl-L-Seryl-L-Glutamyl-L-Glutamyl-L-Aspartyl-L-Leucinamide (32). Using general procedure 2D, Rink amide MBHA resin (0.7 mmol/g, 36 mg, 0.025 mmol) was used to produce **32** (21 mg, 0.014 mmol, 57% yield overall) as a light yellow solid. LRMS (ESI-) m/z 1481.6 (M-H+, $C_{63}H_{91}F_2N_{14}O_{25}$ requires 1481.6).

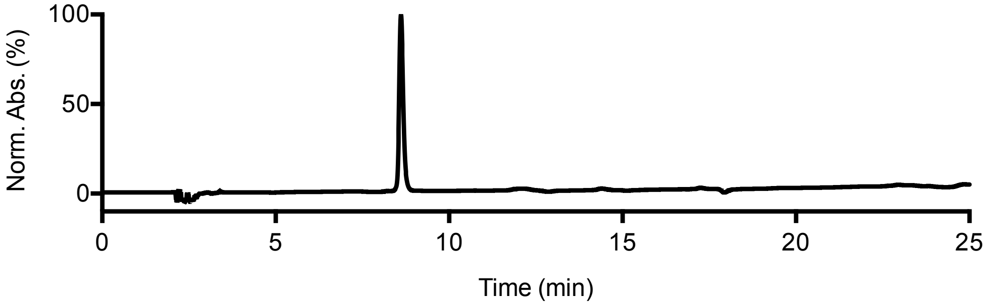

Figure 2.18. Analytical HPLC profile of **32** after preparative HPLC. Retention time = 9 min monitored by UV absorbance at 254 nm. Purity >95% by HPLC.

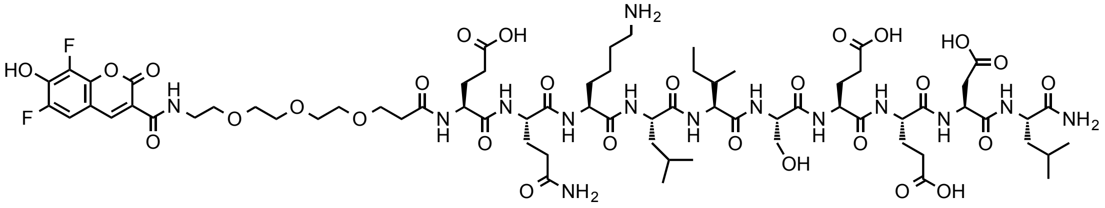

33

((6,8-Difluoro-7-hydroxy-2-oxo-2H-chromene)-3-carboxamide))-mPEG-L-Glutamyl-L-Glutaminyl-L-Leucyl-L-Leucyl-L-Seryl-L-Glutamyl-L-Glutamyl-L-Aspartyl-L-Leucinamide (33). Using general procedure 2D, Rink amide MBHA resin (0.7 mmol/g, 72 mg, 0.05 mmol) was used to produce **33** (22 mg, 0.022 mmol, 10% yield overall) as a light yellow solid. LRMS (ESI-) m/z 1627.9 (M-H$^+$, $C_{70}H_{105}F_2N_{14}O_{28}$ requires 1627.7).

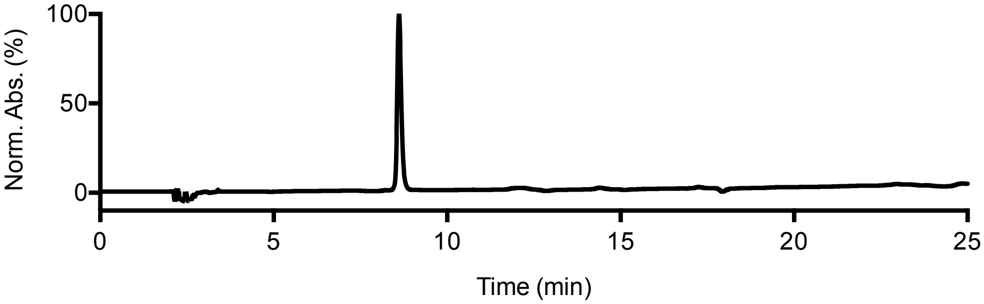

Figure 2.19. Analytical HPLC profile of **33** after preparative HPLC. Retention time = 9.5 min monitored by UV absorbance at 254 nm. Purity >95% by HPLC.

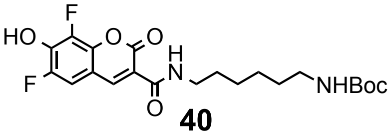

40

***tert*-Butyl (6-(6,8-difluoro-7-hydroxy-2-oxo-2*H*-chromene-3-carboxamido)hexyl)carbamate (40).** To a solution of **15** (45 mg, 0.13 mmol) in DMF (1 mL) was added *N*-Boc-hexylenediamine (55 mg, 0.25 mmol) and DIEA (90 µL, 0.52 mmol. The reaction mixture was stirred at 22 °C for 24 h. The vessel was placed on high vacuum for 1 h to remove 4 mL of DMF. The remaining reaction mixture was added dropwise to cold 1 N HCl (25 mL). A precipitate formed that was filtered, washed with cold 1 N HCl (10 mL), and dried under high vacuum to give **40** (45 mg, 80%) as a yellow solid. ^{1}H NMR (500 MHz, DMSO-d_6) δ 8.78 (d, *J* = 1.4 Hz, 1H), 8.58 (t, *J* = 5.8 Hz, 1H), 7.75 (dd, *J* = 10.5, 2.0 Hz, 1H), 6.78 (t, *J* = 5.6 Hz, 1H), 3.29 (q, *J* = 6.7 Hz, 2H), 2.93–2.84 (m, 2H), 1.56–1.44 (m, 2H), 1.37–1.17 (m, 15H); ^{13}C NMR (126 MHz, DMSO-d_6) δ 160.9, 159.7, 155.6, 148.8 (dd, *J* = 240.8, 4.9 Hz), 147.1 (d, *J* = 3.2 Hz), 140.5 (d, *J* = 8.7 Hz), 140.2–139.8 (m), 138.8 (dd, *J* = 245.0, 6.5 Hz), 116.5, 110.5 (dd, *J* = 21.1, 3.0 Hz), 109.6 (d, *J* = 10.2 Hz), 77.3, 39.9, 39.8, 29.4, 29.0, 28.3, 26.1, 26.0; HRMS (ESI-) m/z 439.1667 (M-H$^+$, $C_{17}H_{17}F_2N_2O_6$ requires 439.1681).

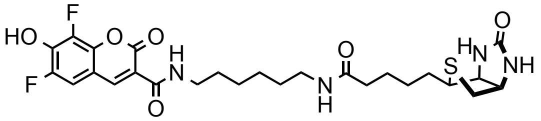

34

6,8-Difluoro-7-hydroxy-2-oxo-*N*-(6-(5-((3a*S*,4*R*,6a*R*)-2-oxohexahydro-1*H*-thieno[3,4-*d*]imidazol-4-yl)pentanamido)hexyl)-2*H*-chromene-3-carboxamide (PB-Hexyl-Biotin, 34). Compound **40** (40 mg, 0.09 mmol), was treated with a solution of trifluoroacetic acid (TFA) / CH_2Cl_2 (2 mL, 30:70) for 20 min. The mixture was concentrated under vacuum and washed with CH_2Cl_2 (5 mL) and ether (5 mL x 2) to remove excess TFA. Biotin-NHS ester (60 mg, 0.18 mmol), DIEA, (60 µL, 0.36 mmol), and DMF (1 mL) were added, and the reaction was stirred at 22 °C for 16 h. The solvent was removed under vacuum, the residue was dissolved in DMSO (1.5 mL), and the product purified by preparative RP-HPLC (Gradient: H_2O:CH_3CN (9:1) to (0:100) with added TFA (0.1%) over 20 min; elution time = 8 min). Pure fractions were collected, combined, and solvent was removed by lyophilization to yield compound **34** (19 mg, 50%) as a pale yellow solid. ^{1}H NMR (400 MHz, DMSO) δ 8.15 (t, *J* = 5.9 Hz, 1H), 7.95 (d, *J* = 1.5 Hz, 1H), 6.66 (dd, *J* = 10.1, 2.1 Hz, 1H), 3.72–3.63 (m, 1H), 3.49 (dd, J = 7.9, 4.4 Hz, 1H), 2.61 (q, J = 6.8 Hz, 2H), 2.38 (ddt, J = 11.7, 9.1, 5.7 Hz, 3H), 2.11 (dd, J = 12.8, 4.9 Hz, 1H), 1.99–1.81 (m, 1H), 1.39 (t, J = 7.3 Hz, 2H), 1.01–0.50 (m, 14H); ^{13}C NMR (126 MHz, DMSO-d_6) δ 173.8, 163.9, 161.5, 159.4, 148.7 (dd, J = 242.4, 4.7 Hz), 146.6 (t, J = 3.0 Hz), 140.1 (d, J = 10.5 Hz), 140.0 (d, J = 12.6 Hz), 138.3 (dd, J = 246.7, 6.3 Hz), 114.9, 109.0 (dd, J = 21.3, 3.3 Hz), 108.9 (d, J = 10.3 Hz), 61.2, 59.4, 54.8, 38.8, 38.5, 38.0, 34.6, 28.09, 28.08, 28.07, 27.6, 27.3, 25.5, 25.4, 24.7; HRMS (ESI-) m/z 565.1929 (M-H$^+$, $C_{17}H_{17}F_2N_2O_6$ requires 565.1932).

2.11. References

1. Jelesarov, I.; Bosshard, H. R., Isothermal titration calorimetry and differential scanning calorimetry as complementary tools to investigate the energetics of biomolecular recognition. *J. Mol. Recognit.* **1999,** *12*, 3-18.

2. Bogan, A. A.; Thorn, K. S., Anatomy of hot spots in protein interfaces1. *J. Mol. Biol.* **1998,** *280*, 1-9.

3. Jameson, D. M.; Ross, J. A., Fluorescence polarization/anisotropy in diagnostics and imaging. *Chem. Rev.* **2010,** *110*, 2685-2708.

4. Wu, P.; Brand, L., Resonance energy transfer: methods and applications. *Anal. Biochem.* **1994,** *218*, 1-13.

5. Zhang, H.; Wu, Q.; Berezin, M. Y., Fluorescence anisotropy (polarization): from drug screening to precision medicine. *Expert Opin. Drug Discov.* **2015,** *10*, 1145-1161.

6. Kim, J. H.; Sumranjit, J.; Kang, H. J.; Chung, S. J., Discovery of coumarin derivatives as fluorescence acceptors for intrinsic fluorescence resonance energy transfer of proteins. *Mol. Biosyst.* **2014,** *10*, 30-3.

7. Ghisaidoobe, A. B.; Chung, S. J., Intrinsic tryptophan fluorescence in the detection and analysis of proteins: a focus on Forster resonance energy transfer techniques. *Int. J. Mol. Sci.* **2014,** *15*, 22518-22538.

8. zhang, Y.; Yang, X.; Liu, L.; Huang, X.; Pu, J.; Long, G.; Zhang, L.; Liu, D.; Xu, B.; Liao, J.; Liao, F., Comparison of Forster-resonance-energy-transfer acceptors for tryptophan and tyrosine residues in native proteins as donors. *J. Fluoresc.* **2013,** *23*, 147-57.

9. Khazanov, N. A.; Carlson, H. A., Exploring the Composition of Protein-Ligand Binding Sites on a Large Scale. *PLoS Comput. Biol.* **2013,** *9*, e1003321.

10. Bogan, A. A.; Thorn, K. S., Anatomy of hot spots in protein interfaces. *J. Mol. Biol.* **1998,** *280*, 1-9.

11. Vivian, J. T.; Callis, P. R., Mechanisms of tryptophan fluorescence shifts in proteins. *Biophys. J.* **2001,** *80*, 2093-2109.

12. Chen, Y.; Barkley, M. D., Toward understanding tryptophan fluorescence in proteins. *Biochemistry* **1998,** *37*, 9976-9982.

13. Doody, M. C.; Gotto, A. M.; Smith, L. C., 5-(Dimethylamino)naphthalene-1-sulfonic acid, a fluorescent probe of the medium chain fatty acid binding site of serum albumin. *Biochemistry* **1982,** *21*, 28-33.

14. Lakowicz, J. R.; Gryczynski, I.; Cheung, H. C.; Wang, C. K.; Johnson, M. L.; Joshi, N., Distance distributions in proteins recovered by using frequency-domain fluorometry. Applications to troponin I and its complex with troponin C. *Biochemistry* **1988,** *27*, 9149-9160.

15. Gustiananda, M.; Liggins, J. R.; Cummins, P. L.; Gready, J. E., Conformation of Prion Protein Repeat Peptides Probed by FRET Measurements and Molecular Dynamics Simulations. *Biophys. J.* **2004,** *86*, 2467-2483.

16. Liao, F.; Xie, Y.; Yang, X.; Deng, P.; Chen, Y.; Xie, G.; Zhu, S.; Liu, B.; Yuan, H.; Liao, J.; Zhao, Y.; Yu, M., Homogeneous noncompetitive assay of protein via Forster-resonance-energy-transfer with tryptophan residue(s) as intrinsic donor(s) and fluorescent ligand as acceptor. *Biosens. Bioelectron.* **2009,** *25*, 112-117.

17. Feng, Y.; Shen, X.; Chen, K.; Jiang, H.; Liu, D., A New Assay Based on Fluorescence Resonance Energy Transfer to Determine the Binding Affinity of Bcl-xL Inhibitors. *Biosci. Biotechnol. Biochem.* **2008,** *72*, 1936-1939.

18. Xie, Y.; Maxson, T.; Tor, Y., Fluorescent Ribonucleoside as a FRET Acceptor for Tryptophan in Native Proteins. *J. Am. Chem. Soc.* **2010,** *132*, 11896-11897.

19. Sun, W. C.; Gee, K. R.; Haugland, R. P., Synthesis of novel fluorinated coumarins: excellent UV-light excitable fluorescent dyes. *Bioorg. Med. Chem. Lett.* **1998,** *8*, 3107-10.

20. Cohen, J. D.; Thompson, S.; Ting, A. Y., Structure-guided engineering of a Pacific Blue fluorophore ligase for specific protein imaging in living cells. *Biochemistry* **2011,** *50*, 8221-5.

21. Chiesl, T. N.; Chu, W. K.; Stockton, A. M.; Amashukeli, X.; Grunthaner, F.; Mathies, R. A., Enhanced Amine and Amino Acid Analysis Using Pacific Blue and the Mars Organic Analyzer Microchip Capillary Electrophoresis System. *Anal. Chem.* **2009,** *81*, 2537-2544.

22. Fromm, J. R.; Thomas, A.; Wood, B. L., Flow cytometry can diagnose classical hodgkin lymphoma in lymph nodes with high sensitivity and specificity. *Am. J. Clin. Pathol.* **2009,** *131*, 322-32.

23. Pashkova, A.; Moskovets, E.; Karger, B. L., Coumarin tags for improved analysis of peptides by MALDI-TOF MS and MS/MS. 1. Enhancement in MALDI MS signal intensities. *Anal. Chem.* **2004,** *76*, 4550-7.

24. Kerkovius, J. K.; Menard, F., A Practical Synthesis of 6,8-Difluoro-7-hydroxycoumarin Derivatives for Fluorescence Applications. *Synthesis* **2016,** *48*, 1622-1629.

25. Gee, K. R.; Haugland, R. P.; Sun, W. C., Derivatives of 6,8-difluoro-7-hydroxycoumarin. *Brit. UK Pat. Appl.* **1997,** *GB 2319250 A 19980520*.

26. Green, N. M., Avidin. In *Advances in Protein Chemistry*, C.B. Anfinsen, J. T. E.; Frederic, M. R., Eds. Academic Press1975; Vol. Volume 29, pp 85-133.

27. Le Trong, I.; Wang, Z.; Hyre, D. E.; Lybrand, T. P.; Stayton, P. S.; Stenkamp, R. E., Streptavidin and its biotin complex at atomic resolution. *Acta Cryst. D* **2011,** *D67*, 813-821.

28. Chilkoti, A.; Tan, P. H.; Stayton, P. S., Site-directed mutagenesis studies of the high-affinity streptavidin-biotin complex: contributions of tryptophan residues 79, 108, and 120. *Proc. Natl. Acad. Sci. U.S.A.* **1995,** *92*, 1754-1758.

29. Terai, T.; Kohno, M.; Boncompain, G.; Sugiyama, S.; Saito, N.; Fujikake, R.; Ueno, T.; Komatsu, T.; Hanaoka, K.; Okabe, T.; Urano, Y.; Perez, F.; Nagano, T., Artificial Ligands of Streptavidin (ALiS): Discovery, Characterization, and Application for Reversible Control of Intracellular Protein Transport. *J. Am. Chem. Soc.* **2015,** *137*, 10464-10467.

30. Xie, Y.; Yang, X.; Pu, J.; Zhao, Y.; Zhang, Y.; Xie, G.; Zheng, J.; Yuan, H.; Liao, F., Homogeneous competitive assay of ligand affinities based on quenching fluorescence of tyrosine/tryptophan residues in a protein via Forster-resonance-energy-transfer. *Spectrochim. Acta A Mol. Biomol. Spectrosc.* **2010,** *77*, 869-76.

31. Trott, O.; Olson, A. J., AutoDock Vina: improving the speed and accuracy of docking with a new scoring function, efficient optimization, and multithreading. *J. Comput. Chem.* **2010,** *31*, 455-461.

32. Nudelman, A.; Marcovici-Mizrahi, D.; Nudelman, A.; Flint, D.; Wittenbach, V., Inhibitors of biotin biosynthesis as potential herbicides. *Tetrahedron* **2004,** *60*, 1731-1748.

33. Green, N. M., Thermodynamics of the binding of biotin and some analogues by avidin. *Biochem. J.* **1966,** *101*, 774-780.

34. Raphael, M. P.; Rappole, C. A.; Kurihara, L. K.; Christodoulides, J. A.; Qadri, S. N.; Byers, J. M., Iminobiotin binding induces large fluorescent enhancements in avidin and streptavidin fluorescent conjugates and exhibits diverging pH-dependent binding affinities. *J. Fluoresc.* **2011,** *21*, 647-652.

35. Melkko, S.; Dumelin, C. E.; Scheuermann, J.; Neri, D., On the magnitude of the chelate effect for the recognition of proteins by pharmacophores scaffolded by self-assembling oligonucleotides. *Chem. Biol.* **2006,** *13*, 225-231.

36. Evan, G. I.; Lewis, G. K.; Ramsay, G.; Bishop, J. M., Isolation of monoclonal antibodies specific for human c-myc proto-oncogene product. *Mol. Cell. Biol.* **1985,** *5*, 3610-3616.

37. Munro, S.; Pelham, H. R. B., An hsp70-like protein in the ER: Identity with the 78 kd glucose-regulated protein and immunoglobulin heavy chain binding protein. *Cell* **1986,** *46*, 291-300.

38. Krauß, N.; Wessner, H.; Welfle, K.; Welfle, H.; Scholz, C.; Seifert, M.; Zubow, K.; Aÿ, J.; Hahn, M.; Scheerer, P.; Skerra, A.; Höhne, W., The structure of the anti-c-myc antibody 9E10 Fab fragment/epitope peptide complex reveals a novel binding mode dominated by the heavy chain hypervariable loops. *Proteins* **2008,** *73*, 552-565.

39. Williams, A. T.; Winfield, S. A., Relative Fluorescence Quantum Yields Using a Computer-controlled Luminescence Spectrometer. *Analyst* **1983,** *108*, 1067-1071.

40. Jones, G.; Jackson, W. R.; Choi, C. Y.; Bergmark, W. R., Solvent effects on emission yield and lifetime for coumarin laser dyes. Requirements for a rotatory decay mechanism. *J. Phys. Chem.* **1985,** *89*, 294-300.

41. Hink, M. A.; Visser, N. V.; Borst, J. W.; van Hoek, A.; Visser, A. J. W. G., Practical Use of Corrected Fluorescence Excitation and Emission Spectra of Fluorescent Proteins in Förster Resonance Energy Transfer (FRET) Studies. *J. Fluoresc.* **2003,** *13*, 185-188.

42. Antonie J.W.G. Visser, E. S. V., John Lee, Critical transfer distance determination between FRET pairs. **2011**.

43. Jing, M.; Bowser, M. T., Methods for measuring aptamer-protein equilibria: a review. *Anal. Chim. Acta* **2011,** *686*, 9-18.

44. Zhuang, Y. D.; Chiang, P. Y.; Wang, C. W.; Tan, K. T., Environment-sensitive fluorescent turn-on probes targeting hydrophobic ligand-binding domains for selective protein detection. *Angew. Chem. Int. Ed.* **2013,** *52*, 8124-8128.

45. Lee, M. J.; Pal, K.; Tasaki, T.; Roy, S.; Jiang, Y.; An, J. Y.; Banerjee, R.; Kwon, Y. T., Synthetic heterovalent inhibitors targeting recognition E3 components of the N-end rule pathway. *Proc. Natl. Acad. Sci. U.S.A.* **2008,** *105*, 100-105.

46. Chen, S.; Zhao, X.; Chen, J.; Chen, J.; Kuznetsova, L.; Wong, S. S.; Ojima, I., Mechanism-Based Tumor-Targeting Drug Delivery System. Validation of Efficient Vitamin Receptor-Mediated Endocytosis and Drug Release. *Bioconjug. Chem.* **2010,** *21*, 979-987.

Chapter 3

Pacific Blue Derivatives of Paclitaxel Enable Selective Imaging of Microtubules and Assays of Efflux by P-glycoprotein in Living Cells

3.1. Introduction

Paclitaxel (Taxol, **41**, Figure 3.1), a natural product first isolated from the bark of the yew tree *Taxus brevifolia*, has proven to be one of the most effective treatments for several types of cancer, including ovarian, breast, and lung cancers.[1, 2] After entering the cytosol, this agent, and related compounds such as docetaxel,[2] bind and stabilize β-tubulin. This results in inhibition of microtubule polymerization dynamics and can induce mitotic arrest at the G2/M phase of the cell cycle (Figure 3.1).[3] Engagement of this target protein by these cytotoxic drugs can trigger cellular death via apoptosis. For these reasons, paclitaxel and related compounds are considered mitotic poisons.[2]

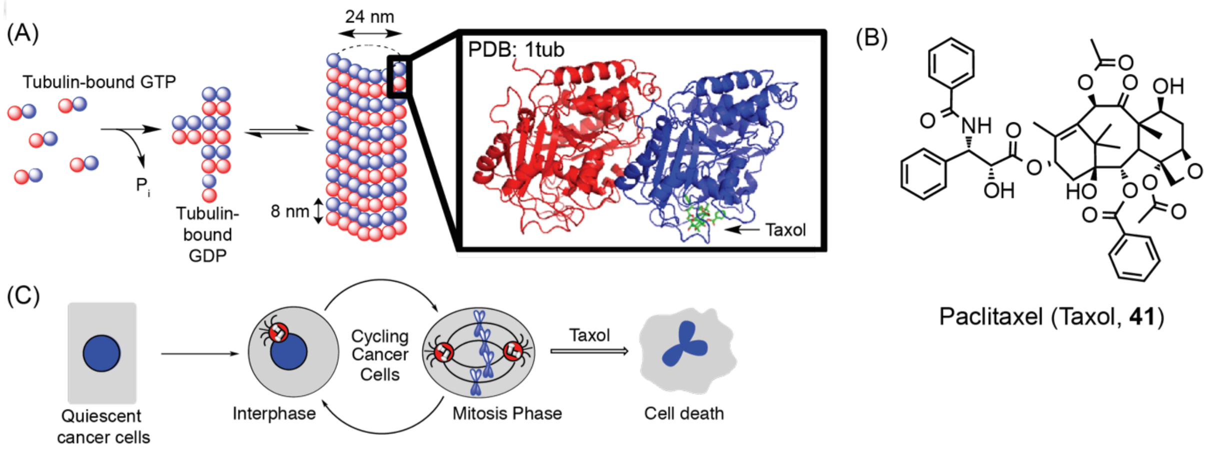

Figure 3.1. A and C: Effect of Taxol on dynamics of tubulin polymerization. B: Structure of paclitaxel (Taxol, **41**).

Although they are widely used as therapeutics, the mechanisms underlying the selective cytotoxicity of microtubule stabilizers towards cancer cells compared to normal cells remain incompletely understood. In preclinical cancer models, such as cells in culture and tumor xenografts in mice, cancer cells double on average every 1–12 days.[4]. Microtubule-stabilizing agents (MTAs), such as paclitaxel, exhibit antimitotic activity against these rapidly dividing cancer cell lines and models. These effects lead to the hypothesis that these agents preferentially affect rapidly proliferating cells and could exert selectivity in the clinic by targeting rapidly dividing cells within cancer tumors. However, these drugs also show major effects against slow growing tumors in human patients, while sparing more rapidly proliferating normal cells in bone marrow, gut, and other tissues, a phenomenon termed the “proliferation rate paradox”.[5] At any given time, neutrophils of bone marrow are rapidly dividing, with ~60 billion cells / day undergoing the process of mitosis.[6] In contrast, in a study of a large amount of clinical patient data involving many different cancer types, the median tumor-doubling time was found to be 147 days.[4] From this comparison alone, one would assume that neutropenia would be a dose-limiting side effect far before paclitaxel killed slow-dividing cancer cells, but this is not the case in most patients. Additionally, the anti-proliferative activities of these drugs do not correlate with cell-doubling time in some cancer preclinical models,[7, 8] but do correlate well for others.[9, 10] Furthermore, following the success of paclitaxel in the clinic, an enormous amount of effort and resources were dedicated to the development of more specific antimitotic agents, such as kinesin-5 inhibitors.[5] However, although this new class of molecules showed efficacy against cancer cell culture models, they were removed from clinical trials due to extensive neutropenia. This indicated that kinesin-5 inhibitors have the desired clinical effect of killing rapidly dividing cells,[11] but raised the question as to why paclitaxel would be superior in cancer patients. Additionally, reports of paclitaxel killing rarely dividing neuronal cells is known in the clinic, which does not track with the hypothesis that paclitaxel only effects rapidly dividing cells.[12, 13] These results suggest that our knowledge of the therapeutic mechanisms of action of tubulin-targeting chemotherapeutics is limited. Rational approaches for the design of improved cytotoxic chemotherapeutics will likely require a better understanding of the mechanisms of action of these clinically important agents.

One approach to investigate the cellular effects of paclitaxel has involved the synthesis of fluorescent[14-24] and other labeled[25-27] analogues. The commercially available fluorescent Paclitaxel-Oregon Green (Flutax-2, **42**, Figure 3.2), one of the most extensively investigated fluorescent derivatives, has been employed to investigate the mechanism of action of new cancer therapeutics,[28-30] elucidate binding sites within tubulin,[16-18] investigate the morphology of parasitic microorganisms,[31-33] and develop new drug delivery[34] and imaging platforms.[35-37] Despite the utility of Flutax-2, we found that this probe lacks specificity toward microtubules in HeLa cells, is of relatively low affinity for microtubules,[38] and is essentially non-toxic toward cells in culture, unlike the parent drug. We sought in the research described here to identify new fluorescent derivatives that behave more similarly to paclitaxel than Flutax-2, both *in vitro* and in cell culture.

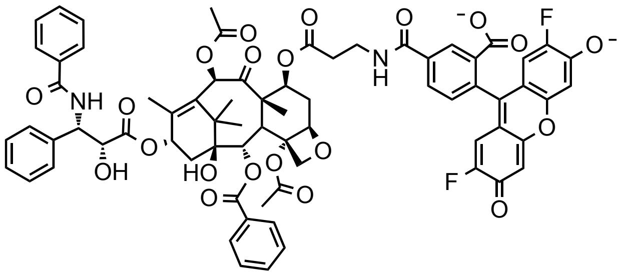

Oregon Green-Taxol (Flutax-2, **42**)

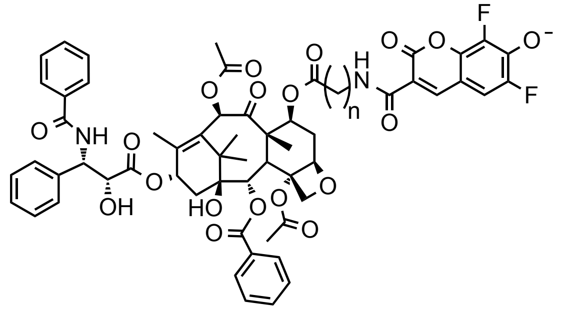

43 (Pacific Blue–Gly–Taxol, n=1)
44 (Pacific Blue–βAla–Taxol, n=2)
45 (Pacific Blue–GABA–Taxol, n=3)

Figure 3.2. Structures of the known fluorescent taxoid Flutax-2 (**42**) and new Pacific Blue-linked derivatives of taxol (**43–45**).

A hallmark of cellular responses to Taxol is the development of resistance to its antiproliferative effects. A major mechanism of this resistance is overexpression of the efflux transporter P-glycoprotein (P-gp, MDR1, ABCB1).[39] Other mechanisms of resistance include mutations in the protein target β-tubulin, alterations in regulators of apoptosis, and effects on mitosis checkpoint proteins.[40] Multidrug resistance (MDR) is a great challenge for clinical treatment of cancer, and efforts to circumvent MDR are of substantial interest. Many of these efforts focus on eliminating efflux by P-gp, either by modifications to the Taxol core to limit binding to P-gp[41, 42] or through co-administration with P-gp inhibitors.[43] To detect P-gp activity in cancer cells, assays of P-gp-mediated efflux generally use fluorescent substrates,[44] both in preclinical drug development,[45] and for the discovery of new P-gp inhibitors.[46] Recent studies have used Flutax-2[47-49] and BODIPY FL Taxol[50, 51] to detect small changes in cellular accumulation based on differences in P-gp activity. Here, we investigated novel fluorescent derivatives of Taxol in an effort to identify compounds that more closely mimic its binding to tubulin and its efflux by P-gp in MDR cancer cells. These probes add the Pacific Blue fluorophore to

Taxol at the 7-position through amino acid-derived linkers. We describe their cytotoxic activity toward rapidly dividing cells in culture, and their specificity for microtubules in living cells compared with a previously reported Taxol derivative. In these studies, many of the cell-based assays were conducted by Zhe Gao, a graduate student in the Peterson group. Finally, we describe efflux by P-gp, and the development of an assay of P-gp-mediated efflux using a PB-Taxol derivative.

3.2. Synthesis of Pacific Blue-Taxol derivatives

As described in Chapter 2, Pacific Blue is a small coumarin-derived fluorophore with excellent spectral and physical properties. To further explore its utility in cell-based assays, we used PB to synthesize three new fluorescent derivatives of Taxol (PB-Taxols). Because modifications at the C-7 position of Taxol are known to retain high affinity for microtubules,[52] PB was coupled at this position through amino acid-derived linkers that differ subtly and systematically in the number of methylenes between the amine and the carbonyl. These derivatives of Taxol (**43**–**45**) were synthesized as shown in Figure 3.3. To install the fluorophore regioselectively, the 2'-OH group, the most reactive alcohol within Taxol, was first protected with *t*-butyldimethylchlorosilane (TBS) to yield **46**. Coupling reactions with Fmoc-protected amino acids and EDC/DMAP subsequently provided compounds **47**–**49**. Deprotection of the Fmoc group and coupling with PB-NHS ester **15**, followed by treatment with TBAF to remove the silyl ethers, yielded the desired PB-Taxols (**43**–**45**).

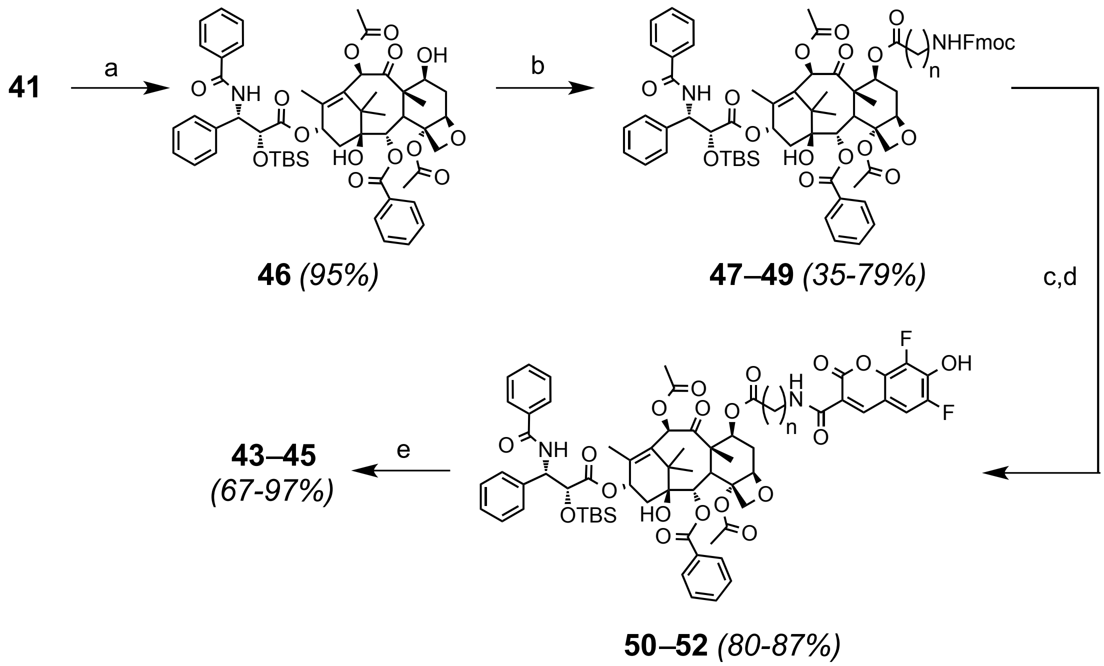

Figure 3.3. Synthesis of PB-linked Taxol derivatives **43–45**. Reagents and conditions: a) *tert*-butyldimethylchlorosilane, imidazole; b) Fmoc-Gly-OH (**47**), Fmoc-βAla-OH (**48**), or Fmoc-GABA-OH (**49**), EDC, DMAP; c) piperidine (20%) in DMF; d) **15**, DIEA; e) TBAF (1.0 M) in THF.

3.3. Quantification of affinities of PB-Taxols for microtubules

To examine the photophysical properties of **42–45**, we obtained absorbance and emission spectra in PBS (containing 0.5% triton X-100 to prevent aggregation). As shown in Figure 3.4, **43–45** exhibited spectra properties (Abs., λ_{max} = 415 nm, ε = 23,300–24,300 $M^{-1}cm^{-1}$; Em., λ_{max} = 460 nm) similar to Pacific Blue (Abs., λ_{max} = 400 nm; ε = 29,500 $M^{-1}cm^{-1}$; Em., λ_{max} = 447 nm)[53] whereas **42** (Abs., λ_{max} = 505 nm; Em., λ_{max} = 540 nm) exhibited spectral properties similar to Oregon Green (Abs., λ_{max} = 501 nm; Em., λ_{max} = 526 nm).[54] Consequently, the green and blue fluorophores of **42** and **43–45** are sufficiently distinct to enable orthogonal excitation with the 405 nm (**43–45**) and 488 nm (**42**) laser lines commonly found on many confocal laser scanning microscopes and flow cytometers.

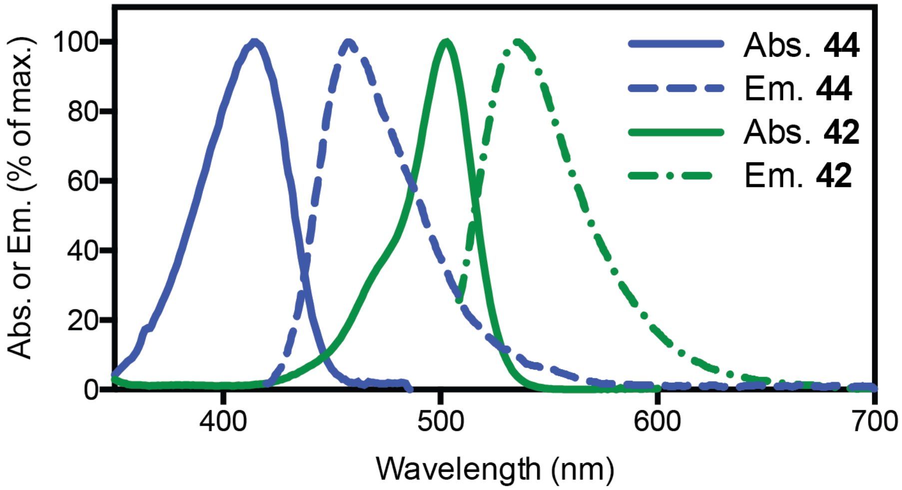

Figure 3.4. Absorbance (Abs., solid lines, 10 μM) and emission (Em., dotted lines, 10 nM) spectra of **44** (blue lines) and Flutax-2 (**42**, green lines) in PBS (pH 7.4) with DMSO (10%) and triton X-100 (0.5%) added to prevent aggregation.

To investigate the affinities of PB-Taxols, we quantified the fluorescence (fl.) enhancement upon binding to microtubules, which is a method used previously for Flutax-2 (K_d ~ 50–100 nM)[18] and other fluorescent taxoids.[55] To generate equilibrium binding curves, freshly prepared crosslinked microtubules[18] were titrated into a low fixed concentration of the fluorescent probe (25 nM), followed by excitation of PB (405/30 nm excitation filter). Fluorescence emission of PB was then measured (LP 450 nm emission filter). Curve fitting was used to calculate K_d values of 34 ± 6 nM for PB-Gly-Taxol **43**, 63 ± 8 nM for PB-βAla-Taxol **44**, and 265 ± 55 nM for PB-GABA-Taxol **45** in GAB buffer (Figure 3.5).

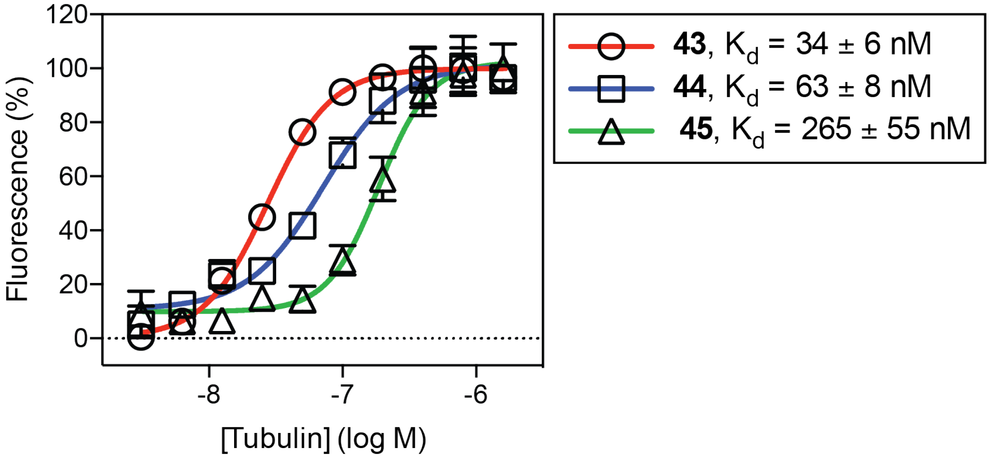

Figure 3.5. Quantification of the affinity (K_d) of cross-linked microtubules for probes **43**–**45** (25 nM) in GAB buffer (10 mM phosphate, 1 mM EDTA, 1 mM GTP, 3.4 M glycerol, pH 6.5) by enhancement of fluorescence upon binding. Protein concentration was based on monomeric tubulin. Dissociation constants (K_d) were calculated using a one-site binding model in GraphPad Prism. Addition of Taxol (10 μM) blocked the increase in fluorescence of **43**–**45** upon binding to cross-linked microtubules, suggesting the increase in fluorescent signal was due to a specific interaction of **43**–**45** at the Taxol-binding site.

To attempt to rationalize differences in affinity, Flutax-2 and **43**–**45** were docked to the tubulin-binding site of a structure of beta tubulin[56] (PDB 3J6G) using Autodock vina.[57] These docking studies revealed that 7-substituted Taxols may bind this protein with a favorable insertion of the linked fluorophores (Figure 3.6) into a pocket near the Taxol-binding site. Whereas the reported affinity of Flutax-2 (K_d ~ 50–100 nM)[18] for tubulin is quite similar to **44**, the higher affinity of **43** was correlated with decreased linker length and flexibility. Although it was not possible to quantitatively support this computationally using Autodock vina, these results could be consistent with a reduction in affinity associated with conformational restriction of longer and more flexible linkers upon binding of PB to the same pocket. Compared to highly polar fluorophores such as Oregon Green, we hypothesized that the greater 'drug-like' properties of Pacific Blue, such as its low molecular weight, modest polarity, and limited number of H-bond donors and acceptors, might further enhance the association of PB-Taxols with tubulin in living cells.

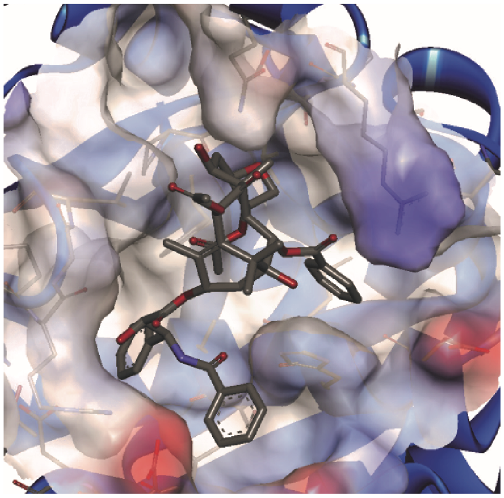
(A) Taxol, **41**

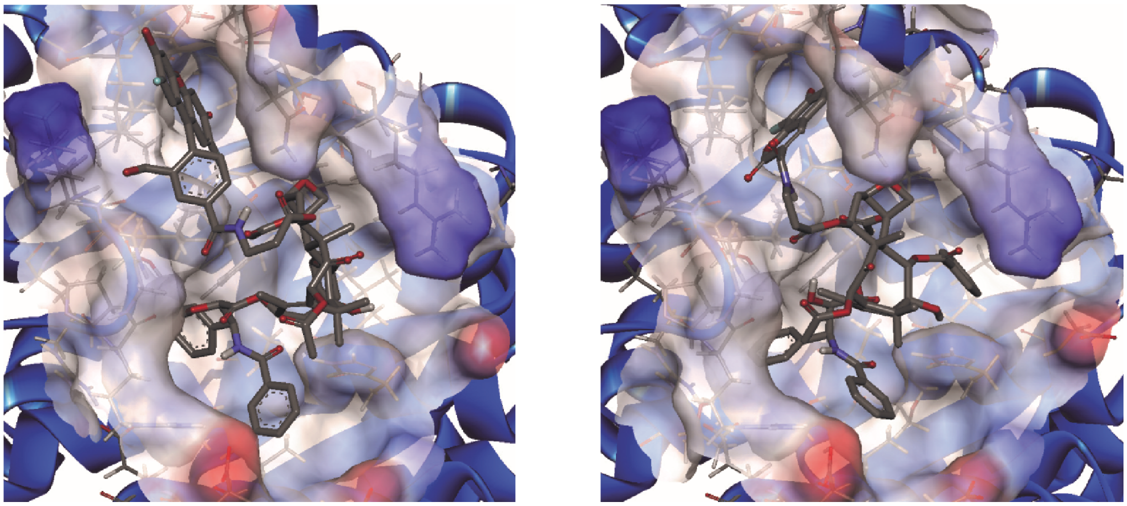
(B) Flutax-2, **42**

(C) PB-βAla-Taxol, **44**

Figure 3.6. Comparison of a cryo-EM structure of paclitaxel (**41**) bound to beta tubulin (PDB 3J6G,[56] panel A) with models of **42** (panel B) and **44** (panel C) generated by docking with Autodock vina. Low energy poses of **42** and **44** with high similarity to the bound geometry of **41** (panel A) are shown.

3.4. Confocal laser scanning microscopy of HeLa cells treated with fluorescent Taxol derivatives

To examine the subcellular distribution of PB-Taxols, we first treated HeLa cells with **44** (1 µM) and increasing concentrations of the P-gp inhibitor verapamil (Figure 3.7, panel C),[58] since paclitaxel is a known substrate of this efflux pump.[59] Confocal microscopy (Figure 3.7, panel A) revealed that verapamil increased the intracellular concentration of **44** in a dose dependent manner, and when verapamil was present in concentrations above 1 µM, the microtubules of HeLa cells were readily stained blue fluorescent. Flow cytometry was further used to quantify the effect of verapamil on the accumulation of **44**. When treated with **44** (1 µM) and verapamil (25 µM), HeLa cells accumulated ~ 8-fold more blue fluorescence than those treated with **44** (1 µM) alone. Additionally, when HeLa cells were treated with **43** (1 µM, Figure 3.8, panels A and B), **44** (Figure 3.8, panels C and D), and **45** (Figure 3.8, panels E and F) in the presence and absence of verapamil (25 µM), similar staining patterns were observed, indicating that each of the PB-Taxols strongly bind to tubulin in living HeLa cells. All three PB-Taxols were readily effluxed from cells in the absence of verapamil, suggesting that they are all substrates of P-gp.

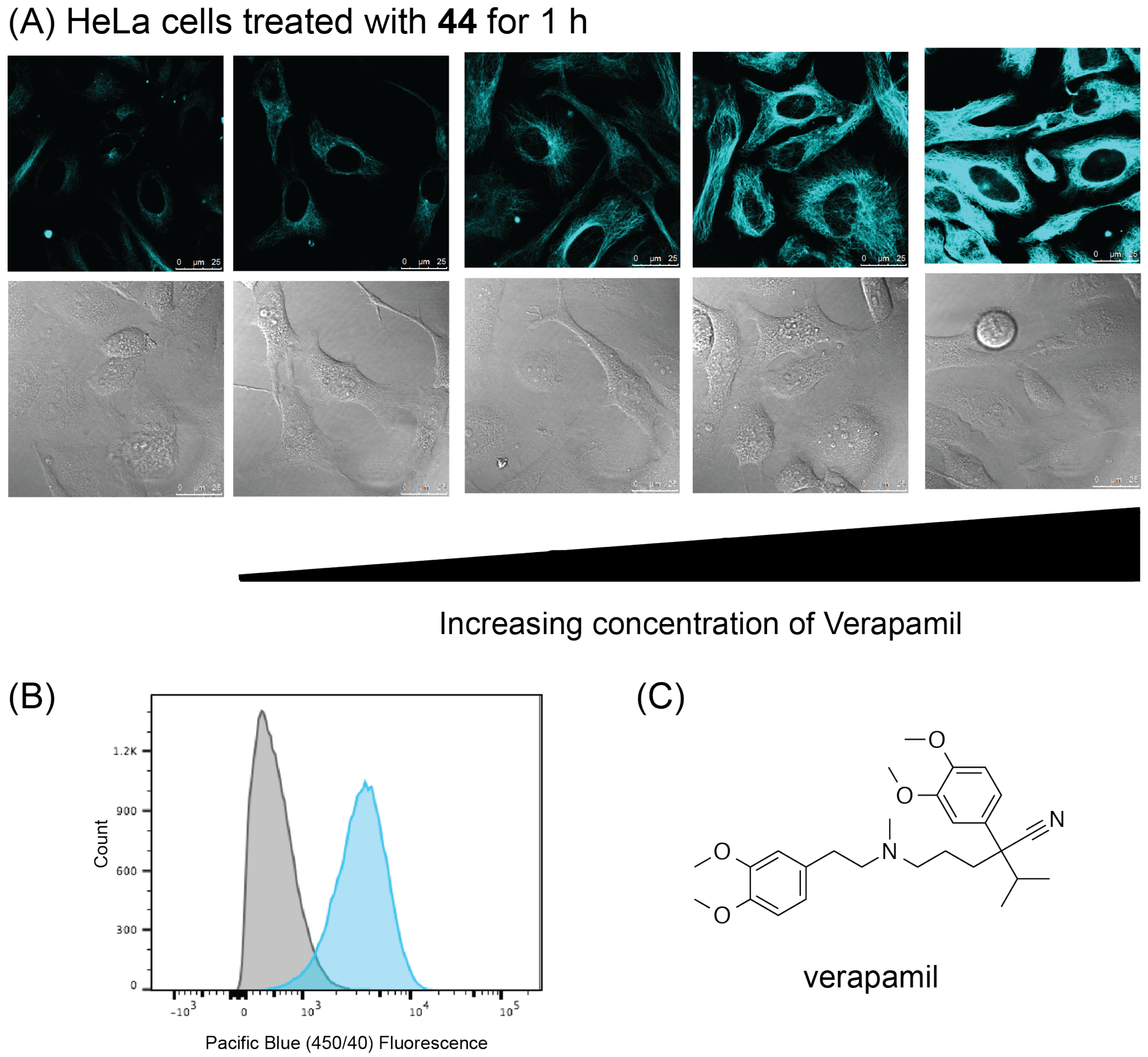

Figure 3.7. Verapamil enhances specific staining of microtubules by **44** in a dose dependent manner in HeLa cells. A: Confocal laser scanning (Ex. 405 nm, Em. 425-500 nm) and DIC micrographs of living HeLa cells treated with **44** (1 µM) and verapamil for 1 h at 37 °C. The concentrations of verapamil are increased from left to right (from 0, 0.1, 1, 10, 25 µM). B: Quantification of the intensity of blue fluorescence of HeLa cells by flow cytometry (Ex. 405 nm, Pacific Blue emission channel, 450/40 nm) after treatment with **44** (1 µM) in the presence (shaded blue) and absence (shaded grey) of 25 µM verapamil. An 8-fold increase was observed upon treatment with verapamil. C: Structure of verapamil, a P-gp inhibitor.

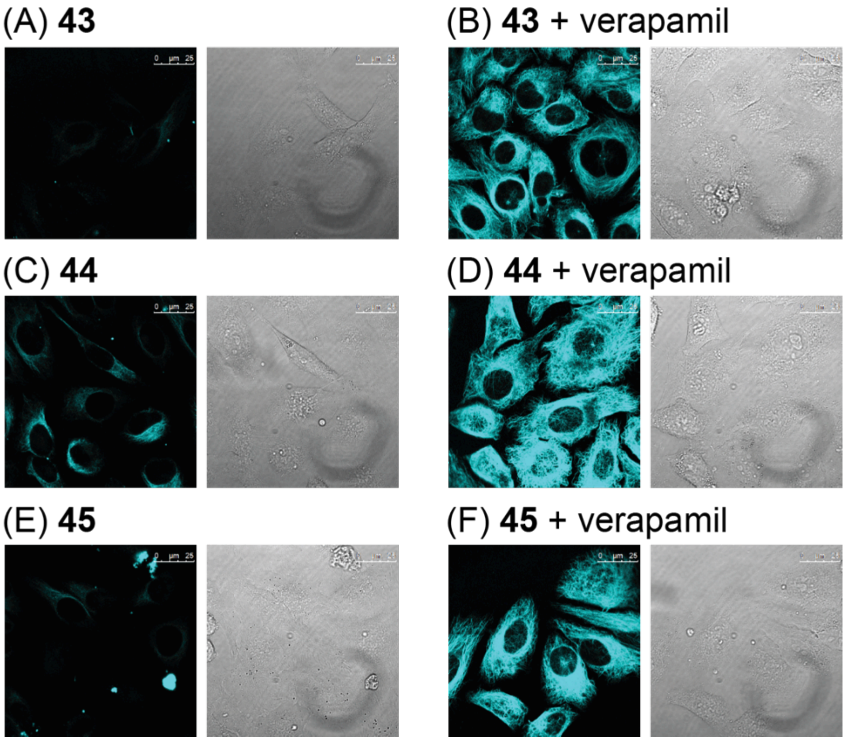

Figure 3.8. Confocal laser scanning and DIC micrographs of living HeLa cells treated with **43-45** (1 µM) in the presence (Panels B, D, F) or absence (Panels A, C, E) of verapamil (25 µM) for 1 h at 37 °C.

3.5. Cellular toxicity of PB-Taxols in the presence and absence of verapamil

To compare the cytotoxicity profile of the blue fluorescent PB-Taxols with paclitaxel (**41**) and the green fluorescent Flutax-2 (**42**), HeLa cervical carcinoma cells (Figure 3.9, panel A), PC-3 prostate cancer cells (Figure 3.9, panel B), and Jurkat lymphocytes (Figure 3.9, panel C) were treated with paclitaxel (**41**) and compounds **42**–**45** for 48 h. The cells were treated with or without verapamil (25 µM) to evaluate the effect of inhibition of P-gp. Among the fluorescent probes, compound **43**, bearing a glycine-derived linker, proved to be the most toxic in the presence and absence of verapamil (e.g. IC_{50} = 31 nM against Jurkat cells), which was consistent with its superior affinity *in vitro*. Additionally, this glycine derivative (**43**) most closely paralleled the activity of paclitaxel when P-gp was inhibited, such as a ~2-fold change in toxicity towards HeLa cells. As additional controls, verapamil did not appreciably affect the toxicity of paclitaxel or **43** towards PC-3 cells[60] and Jurkat lymphocytes,[61] which do not express high levels of P-gp. Interestingly, **44** and **45** appear to be better substrates for P-gp than the other compounds tested, with 4–10 fold changes observed in the presence and absence of verapamil. However, it should be noted that this increase could be due to other non-P-gp mediated effects of verapamil. From these studies, **43** and **44** were shown to be substantially more toxic derivatives of paclitaxel than the more polar Flutax-2. Consequently, **43** may provide a more useful fluorescent tool to study the proliferation rate paradox associated with paclitaxel.

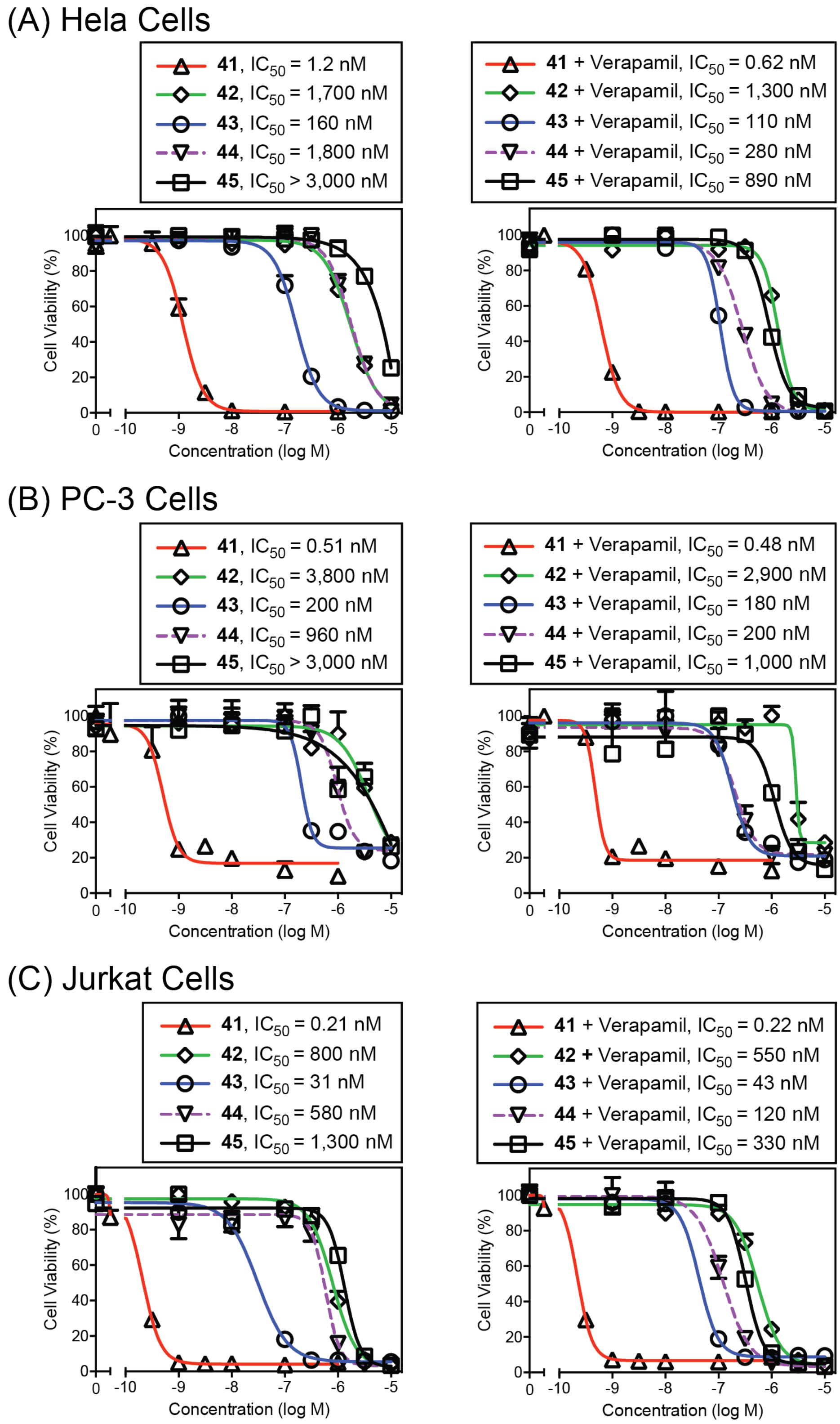

Figure 3.9. Analysis of cytotoxicity by flow cytometry. The cancer cell lines HeLa (A), PC-3 (B), and Jurkat (C) were treated with Taxol (**41**), Flutax-2 (**42**), Taxol-Gly-PB (**43**), Taxol-βAla-PB (**44**) and Taxol-GABA-PB (**45**) for 48 h in the absence (left) or presence

(right) of verapamil (25 μM). Of the three lines, HeLa cells are reported to express P-gp. Under these conditions, verapamil was non-toxic below 1 mM.

3.6. PB-taxols label microtubules with greater specificity than Flutax-2 in live cells

Given the substantial difference in toxicity between the PB-Taxols and Flutax-2, especially in the presence of verapamil, we sought to examine whether these probes exhibit differences in specificity in binding to microtubules. Upon treatment of HeLa cells with verapamil (25 μM), **42** (5 μM), and **44** (1 μM), co-localization studies revealed that PB-Taxol (**44**, Figure 3.10, panel A, false colored red) specifically binds microtubules in HeLa cells while the commercially available Flutax-2 (**42**, Figure 3.10, panel A, false colored green) stains particular organelles that did not co-localize with PB-Taxol in addition to staining microtubules. Further co-localization studies with dyes that traffic to particular organelles within the cell found that some of the green fluorescence of Flutax-2 that does not co-localize well with **44** co-localizes with Nile Red (Figure 3.10, panel B, false colored red), a dye known to stain lipid droplets.[62] The lower specificity of Flutax-2 for microtubules, and its high polarity, which likely limits cellular permeability, likely reduce cellular cytotoxicity compared to **44**.

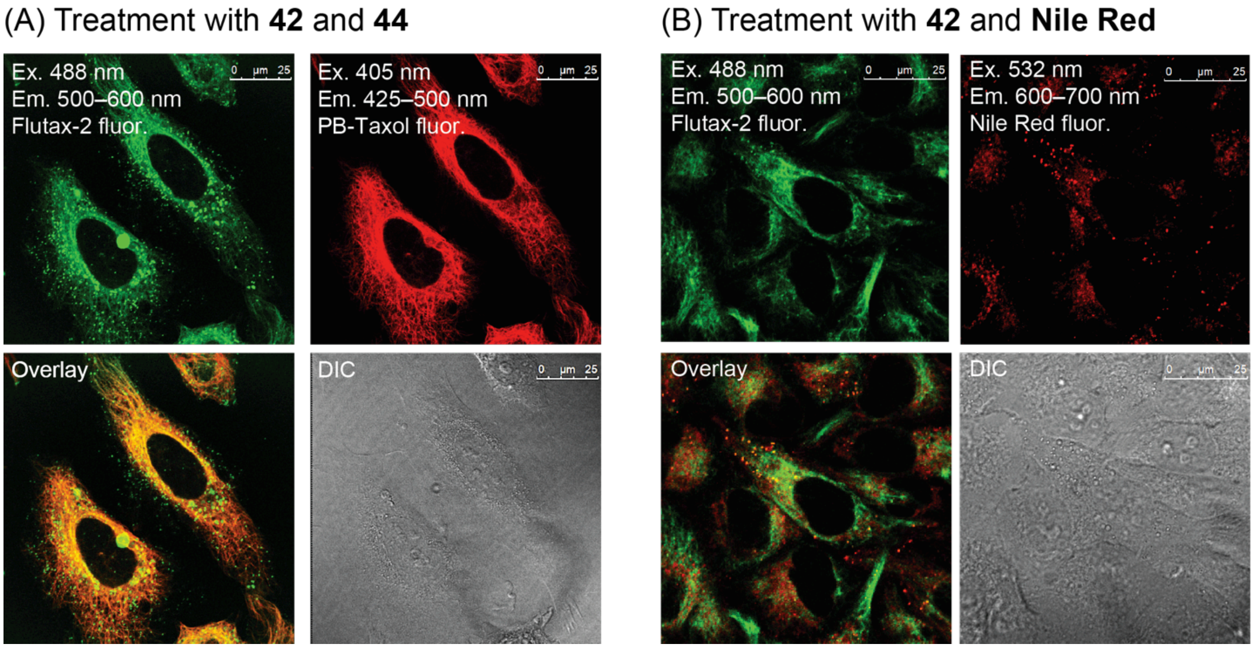

Figure 3.10. Confocal laser scanning and DIC micrographs of HeLa cells treated with A: **44** (1 µM) and Flutax-2 (5 µM) or B: Flutax-2 (**42**, 5 µM) and Nile Red (0.5 µM) for 1 h at 37 °C in the presence of verapamil (25 µM).

3.7. PB-Taxol 44 is a substrate of P-glycoprotein

We sought to investigate the mechanism underlying the profound effect of verapamil on the cellular fluorescence and cellular toxicity of **44** in HeLa cells. Given that P-glycoprotein is known to be inhibited by verapamil, we further studied PC-3 cells, which have low levels of expression[60] of this transporter. To specifically introduce P-gp, PC-3 cells were transiently transfected with a plasmid expressing this protein fused to the green fluorescent protein EGFP (pHaMDR-EGFP, Figure 3.11, panel B). In the absence of P-gp (Figure 3.11, panel A) microtubules were strongly stained by treatment with **44** (1 µM). However, in transfected PC-3 cells (Figure 3.11, panel B, false colored green), a decrease in fluorescence was only present in cells that express the green fluorescent P-gp, consistent with high specificity of efflux by this transporter. Staining of microtubules in these transfected cells was rescued by treatment with verapamil (Figure

3.11, panel C), providing strong evidence that **44** is a substrate of P-gp-mediated efflux, and verapamil blocks this transporter activity.

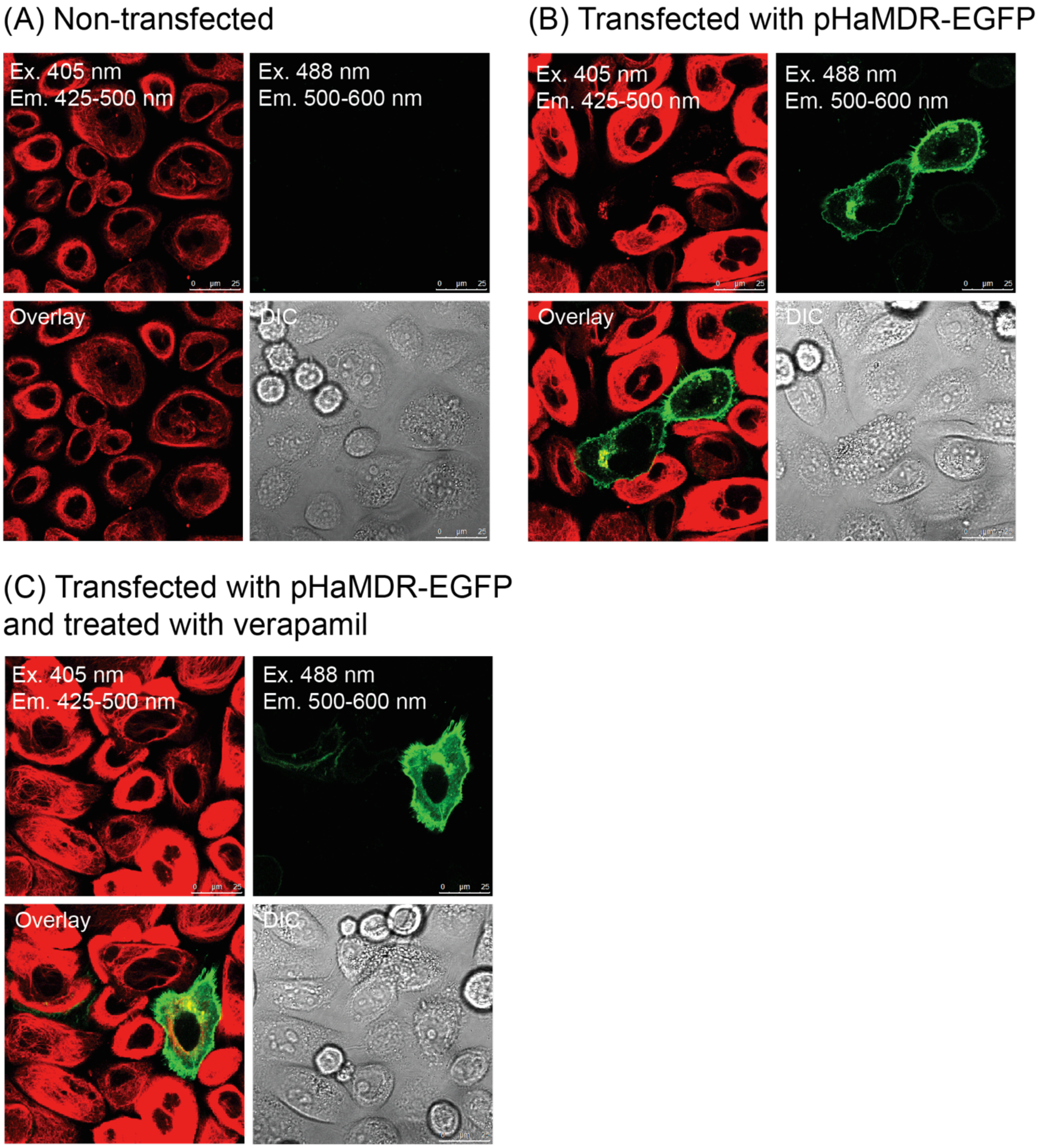

Figure 3.11. Confocal and DIC micrographs of PC-3 cells treated with PB-Taxol **44**. A: PC-3 cells treated with **44** (1 µM) for 1 h. B: PC-3 cells transiently transfected with pHaMDR-EGFP plasmid for 48 h and then treated with **44** (1 µM) for 1 h. C: PC-3 cells transiently transfected with pHaMDR-EGFP plasmid for 48 h and treated with **44** (1 µM) and verapamil (25 µM) for 1 h.

To further investigate the potential of **44** in MDR assays relevant to drug discovery, we utilized HCT-15 cells, which are reported to express high levels of P-gp.[44, 63] Efflux by P-gp was studied with three commonly used assay platforms: confocal microscopy,[64, 65] flow cytometry,[63, 66, 67] and with a fluorescence microplate reader.[45, 46] We additionally compared **44** with two commonly used substrates of drug efflux, Rhodamine 123[68] and DiOC$_2$(3).[63]

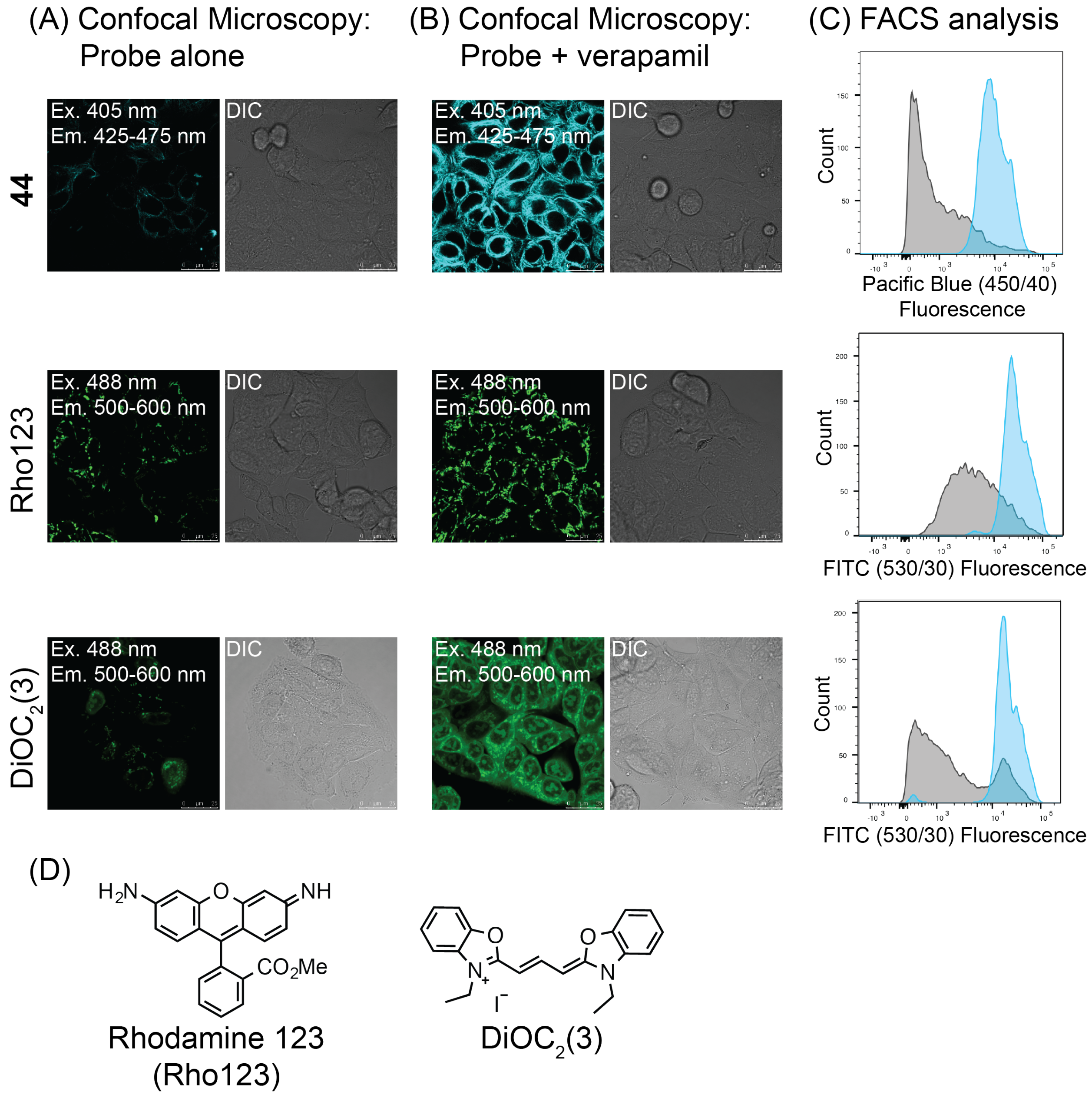

Figure 3.12. Comparison of **44** with commercial fluorescent probes of efflux by P-gp. HCT-15 cells that overexpress P-gp were treated with **44** (5 µM, top row), Rho123 (1 µM, middle row), and DiOC$_2$(3) (1 µM, bottom row) in the presence and absence of verapamil (25 µM) for 1 h at 37 °C. A and B: Confocal micrographs in the absence and presence of verapamil, respectively. C: Quantification of the intensity of blue fluorescence (**44**, Pacific Blue emission channel, 450/40 nm) or green fluorescence (Rho123, DiOC$_2$(3), FITC emission channel, 530/30) by flow cytometry. D: Structures of Rhodamine 123 and DiOC$_2$(3).

HCT-15 cells were treated with **44** (5 μM), Rho123 (1 μM), and $DiOC_2(3)$ in the presence (Figure 3.12, panel B) and absence (Figure 3.12, panel A) of verapamil (25 μM) and imaged by confocal laser scanning microscopy. For all three efflux substrates, a significant decrease in the amount of probe taken up by the cells was observed when verapamil was not present. Upon further inspection, staining with Pacific Blue was less intense and more uniform than the other two dyes in cells not treated with verapamil. This effect is also seen by flow cytometry, which shows a major fluorescent side population in cells treated with $DiOC_2(3)$ (Figure 3.12, panel C, bottom row), and a broad fluorescence profile in cells treated with Rho123 (Figure 3.12, panel C, middle row). In contrast, **44** shows a more uniform fluorescence profile, and a large shift between cells treated with or without verapamil (Figure 3.12, panel C, top row). Additionally, Table 3.1 shows the calculated MDR Activity Factor (MAF) and MDR Activity Ratio (MAR) for each efflux substrate. **44** has higher MAF and MAR values than Rho123 and $DiOC_2(3)$, indicating that it is a sensitive detector of P-gp efflux by flow cytometry.

Table 3.1. Efflux assay parameters, measured by flow cytometry. HCT-15 cells were treated with **44** (5 μM), Rho123 (1 μM), and $DiOC_2(3)$ (1 μM) in the presence and absence of verapamil (25 μM) for 1 h at 37 °C. The MDR Activity Factor (MAF) was calculated using the following formula: $MAF = 100 \times ((MFI_1 - MFI_0)/MFI_1)$, where MFI_1 is the mean fl. intensity measured in the presence of verapamil, while MFI_0 is the mean fl. intensity measured in the absence of verapamil.[69] The MDR Activity Ratio (MAR) was calculated using the following formula: $MAR = MFI_1/ MFI_0$.

	MDR Activity Factor (MAF)	MDR Activity Ratio
PB-βAla-Taxol (**44**)	82 ± 3	5.5 ± 0.4
Rho123	75 ± 2	4.0 ± 0.1
$DiOC_2(3)$	77 ± 1	4.3 ± 0.2

We further tested the utility of these assays in a 96-well plate format on a Packard Fusion Microplate Reader. To investigate this approach, we treated HeLa cells (trypsinized prior to assay), HCT-15 cells (trypsinized prior to assay), and Jurkat cells with **44** in the presence or absence verapamil for 30 min. The cells were centrifuged, washed with cold PBS to remove any remaining fluorophore not accumulated by cells, and resuspended in cold PBS for detection of fluorescence on the microplate reader (Ex. filter: 405/30 nm, Em. filter: LP 450 nm). Although changes in fluorescence were subtle in comparison to those measured by flow cytometry or confocal microscopy in the presence (Figure 3.13, shaded blue) and absence (Figure 3.13, shaded grey) of verapamil, MAF values of 28 ± 3 for HeLa cells, 30 ± 11 for HCT-15 cells, and 0 for Jurkat cells parallels observed differences in cellular toxicity and reported expression levels of P-gp for HCT-15 cells[44] and Jurkat lymphocytes.[61] These results suggest that **44** could be used in high-throughput P-gp efflux assays in a microplate reader format.

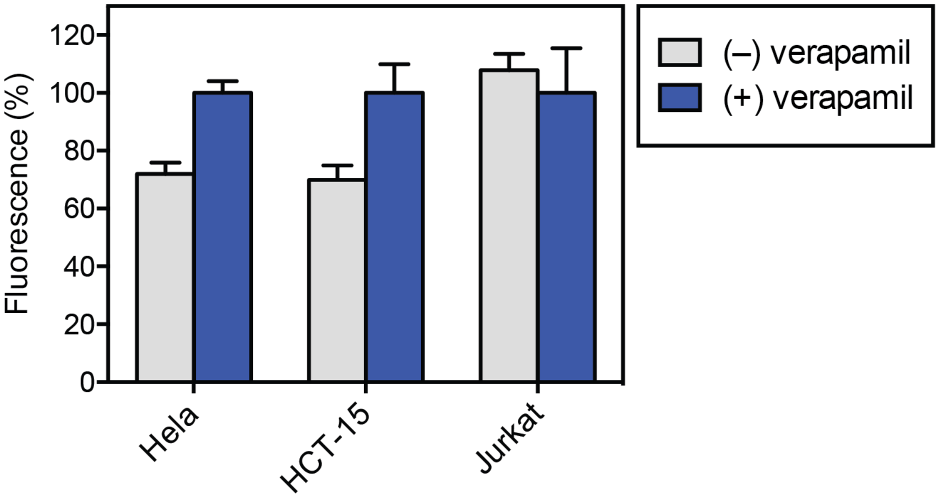

Figure 3.13. Fluorescence intensity measurements of probe **44** detect efflux by P-gp on 96-well plates. HeLa, HCT-15, and Jurkat cells were treated with **44** (1 μM for HeLa and Jurkat, 5 μM for HCT-15) in the presence (shaded blue) and absence (shaded grey) of verapamil (25 μM) for 30 min at 37 °C. Jurkat cells provide a negative control line that does not express P-gp. *p*-Values for HeLa: <0.0001 (****) and HCT-15: $p < 0.02$ (**) were calculated using a *t* test in GraphPad Prism.

3.8. Conclusions

We designed and synthesized derivatives of paclitaxel (Taxol) linked to the small coumarin-derived fluorophore Pacific Blue (Taxol-PBs). Imaging by confocal microscopy in the presence of the P-gp inhibitor verapamil revealed that Taxol-PBs bind microtubules in HeLa cells with substantially higher specificity than the commercially available green fluorescent taxoid Flutax-2. Moreover, whereas Taxol exhibits anti-cancer activity at low nanomolar concentrations against many cell lines, and Flutax-2 is of low toxicity towards cells in culture, Taxol-PBs show substantially higher cytotoxicity in the absence of P-gp, making them potentially better probes of the anticancer mechanisms of this drug. In particular, **43**, the glycine-linked derivative showed high toxicity and similar efflux properties when compared to the parent drug, making it one of the best fluorescent mimics described to date.

Efflux of PB-Taxols mediated by P-gp was examined in detail. Using verapamil, a known inhibitor of P-gp, a dose-dependent increase in accumulation of blue fluorescence in cells expressing P-gp was observed. To confirm the specificity of these compounds as substrates of P-gp, PC-3 cells were transfected with a plasmid encoding this transporter protein. Consistent with high specificity, efflux of the fluorescent taxoid was only observed in transfected cells as imaged by confocal microscopy. Furthermore, **44** proved to be more sensitive than two commonly used efflux substrates in both confocal microscopy and flow cytometery efflux assays. Collectively, these studies revealed that the biological properties of Taxol-PBs are more similar to Taxol than other widely used fluorescent taxoids, and these probes may be useful tools for studies of the proliferation rate paradox associated with paclitaxel and efflux by P-gp.

3.9. Experimental

3.9.1. General experimental section

Chemicals were purchased from Sigma Aldrich, Acros Organics, Alfa Aesar, Oakwood Chemical, or Chem-Impex International. ^{1}H NMR and ^{13}C NMR were acquired on an Avance AVIII 500 MHz instrument. For ^{1}H and ^{13}C, chemical shifts (δ) are reported in ppm referenced to $CDCl_3$ (7.26 ppm for ^{1}H and 77.2 ppm for ^{13}C) or DMSO-d_6 (2.50 ppm for ^{1}H, 39.5 ppm for ^{13}C). ^{1}H coupling constants (J_{HH}, Hz) and ^{13}C coupling constants (J_{CF}, Hz) are reported as: chemical shift, multiplicity (s = singlet, d = doublet, t = triplet, m = multiplet, dd = doublet of doublets, ddd = doublet of doublet of doublets, dq = doublet of quartets, dt = doublet of triplets, ddt = doublet of doublet of triplets), coupling constant, and integration. High Resolution Mass Spectra (HRMS) were obtained at the Mass Spectrometry Laboratory at the University of Kansas on a Micromass LCT Premier. Thin layer chromatography (TLC) was performed using EMD aluminum-backed (0.20 mm) silica plates (60 F-254), and flash chromatography used ICN silica gel (200-400 mesh). TLC plates were visualized with a UV lamp. Preparative HPLC was performed with an Agilent 1200 instrument equipped with a Hamilton PRP-1 reverse phase column (250 mm length, 21.2 mm ID, 7 µm particle size) with detection by absorbance at 215, 254, 370, and 488 nm. All non-aqueous reactions were carried out using flame- or oven-dried glassware under an atmosphere of dry argon or nitrogen. Tetrahydrofuran (THF), dichloromethane (CH_2Cl_2), and *N*,*N*-dimethylformamide (DMF) were purified via filtration through two columns of activated basic alumina under an atmosphere of Ar using a solvent purification system from Pure Process Technology (GlassContour). Other commercial reagents were used as received unless otherwise noted. Absorbance spectra were obtained using semimicro (1.4 mL) UV quartz cuvette (Sigma-Aldrich, Z27667-7) on an Agilent 8452A diode array spectrometer. Measurements for molar extinction coefficients were preformed using semimicro (1.4 mL) UV quartz cuvette (Sigma-Aldrich, Z27667-7). Molar extinction coefficients (ε) in PBS (10 mM Na_2HPO_4, 137 mM NaCl, 2.7 mM KCl, 1.8 mM KH_2PO_4, pH 7.4) containing 10% DMSO and 0.5% triton X-100 were calculated from Beer's Law plots of absorbance λ_{max} versus concentration as shown in Figure 3.14. Linear least squares fitting of the data (including a zero intercept) was used to determine the slope (corresponding to ε). Values (M^{-1} cm^{-1}) were calculated as follows: Absorbance = ε [concentration (M)] L, where L = 1 cm. Fluorescence spectra were acquired using a SUPRASIL ultra-micro quartz cuvette (PerkinElmer, B0631079) on a Perkin-Elmer LS55 Fluorescence Spectrometer (10 nm excitation slit width).

3.9.2. Biological assays and protocols

Cell culture: HeLa cells, obtained from ATCC (CCL-2), were cultured in Dulbecco's Modified Eagle Medium (DMEM, Sigma D6429). PC-3 cells were a gift from Dr. Matthew Levy (Albert Einstein College of Medicine) and were cultured in DMEM/Ham's F-12 medium (Sigma 8437). Jurkat lymphocytes (human acute leukemia, ATCC #TIB-152) and HCT-15 cells (ATCC CCL-225, gift from Dr. Liang Xu, University of Kansas) were cultured in RPMI-1640 medium (Sigma R8758). All media was supplemented with fetal bovine serum (FBS, 10%), penicillin (100 units/mL), and streptomycin (100 μg/mL) and incubated in a humidified 5% CO_2 incubator at 37 °C unless otherwise noted.

Transient transfection of PC-3 cells: The plasmid pHaMDR-EGFP was a gift from Dr. Michael M. Gottesman (National Cancer Institute). Prior to transfection, PC-3 cells in DMEM/Ham's F-12 were seeded onto an 8-well cover glass slide (Ibidi μ-Slide, 300 μL, 10,000 cells/well) and allowed to proliferate for 16 h at 37 °C. To form a DNA complex, the plasmid DNA (2 μg) was incubated at 22 °C with the DNA transfection reagent X-tremeGENE HP (2 μL, Roche) in serum free DMEM medium (200 μL). After 30 min, the DNA complex (20 μL) was added to each well. The cells were further incubated at 37 °C for 48 h. After transfection, the cells were washed with medium, further treated with probes, and analyzed by confocal microscopy.

Confocal microscopy: Cells were added to an 8-well cover glass slide (Ibidi μ-Slide, 300 μL, 20,000 cells/well) and allowed to proliferate for 24 h prior to addition of compounds. Compounds in DMSO stock solutions were serially diluted 1,000-fold with complete media (final concentration of 0.1% DMSO) prior to addition to cells. Cells were treated with compounds at 37 °C for a specified time before imaging by a Leica SPE2 confocal laser-scanning microscope with a 63X oil-immersion objective. Taxol-PB analogues **43**–**45** were excited with a 405 nm laser and emitted photons were collected from 425-500 nm. Flutax-2 (**42**) was excited with a 488 nm laser and emitted photons were collected from 500-600 nm. Nile Red (Sigma, 72485) was excited with a 532 nm laser and emitted photons were collected from 600-700 nm. Identical laser power and PMT gain settings were used for all samples in a given figure to accurately assess differences in cellular fluorescence between the samples.

Cellular toxicity: HeLa cells were seeded on a 48-well plate in complete DMEM at 20,000 cells / 500 μL per well 16 h prior to treatment. All compounds were serial diluted in DMSO and added to media to achieve a 1:1000 dilution factor (0.1% DMSO in each well). The original media was removed from all wells by aspiration and replaced with treatment media (330 μL) at the concentrations indicated. Plates were incubated for 48 h at 37 °C and cells were analyzed in triplicate. Following this incubation period, the media was aspirated and wells were washed with PBS (phosphate-buffered saline, pH 7.4). Wells were further treated with trypsin EDTA solution (50 μL) at 37 °C for 5 min followed by complete DMEM (100 μL) containing propidium iodide (PI, 4.5 μM). The total cell count for each well was determined by flow cytometry (Accuri C6) using light scattering and PI staining to identify populations of live cells. Counts of viable cells for each treatment were used to generate dose-response curves that were fitted by non-linear regression inhibitor vs. response variable slope 4-parameter model (GraphPad Prism 6) to determine IC_{50} values. PC-3 cells were seeded as described previously with HeLa cells with the exception that DMEM/Ham's F-12 medium was used. Jurkat lymphocytes were seeded in RPMI at 50,000 cells / 330 μL per well 16 h prior to treatment. The compounds were spiked into each well without replacing the medium. After 48 h incubation at 37 °C, PI (0.33μL of 3mM solution in PBS) was added to each well, and the cells were analyzed by flow cytometry as described previously.

Efflux assay measured By flow cytometry: Trypsinized HCT-15 or HeLa cells (1 x 10^6 cells/mL) were incubated in suspension with **44** (HeLa, 1 μM; HCT-15, 5 μM), Rho123 (HCT-15, 1 μM), or $DiOC_2(3)$ (HCT-15, 1 μM) and either DMSO (0.2%) or verapamil (25 μM) for 1 h at 37 °C. After incubation, cells were centrifuged at 2000 rpm for 2 min. The supernantent was removed and cells were resuspended in PBS (2% BSA) and placed on ice until FACS analysis. FACS analysis was preformed on a BD FACS Aria Fusion instrument equipped with 405 and 488 nm lasers. 10,000 cells were counted for each sample and each condition was tested in triplicate. Data for **44** was collected under a Pacific Blue filter (450/40 nm) and Rho123 and $DiOC_2(3)$ data was collected under a FITC filter (530/30 nm). FACS data was analyzed by gating cell populations based on untreated cells. The MDR Activity Factor (MAF) was calculated using the following formula: $MAF = 100 \times ((MFI_1 – MFI_0)/MFI_1)$, where MFI_1 is the mean fl. intensity measured in the presence of verapamil, while MFI_0 is the mean fl. intensity measured in the absence of verapamil.[69] The MDR Activity Ratio (MAR) was calculated using the following formula: $MAR = MFI_1/ MFI_0$.

Efflux assay measured using a microplate reader: Trypsinized HCT-15 or HeLa cells (2×10^6 cells/mL) were incubated in a Corning 96-well solid black polystyrene microplate in suspension with **44** (HeLa and Jurkat, 1 μM; HCT-15, 5 μM) and either DMSO (0.2%) or verapamil (25 μM) for 30 min at 37 °C. After incubation, cells were centrifuged at 800 rpm for 4 min. The supernatant was removed and cells were resuspended in cold PBS (2% BSA) and centrifuged at 800 rpm for 4 min again (wash step). The cells were resuspended in cold PBS (2% BSA) and fl. intensity data was acquired on a Packard Fusion Microplate Reader equipped with Pacific Blue excitation (405/30 nm) and emission filters (LP 450 nm). Each condition was run in quadruplicate.

Background fl. of untreated cells was subtracted from each sample before analysis. The MDR Activity Factor (MAF) was calculated as described above.

Preparation of cross-linked microtubules: Following a previously published[18] protocol, microtubules were stabilized against disassembly for use in binding studies. 50 mM tubulin in GAB buffer (10 mM phosphate, 1 mM EDTA, 1 mM GTP, 3.4 M glycerol, pH 6.5) was incubated at 37 °C for 30 min to allow assembly to occur, and then 20 mM glutaraldehyde was added and the solution was incubated at 37 °C for 10 min more to complete the cross-linking event. The reaction was quenched by the addition of 60 mM $NaBH_4$ on ice.

Determination of K_d values by fluorescence enhancement of Pacific Blue: Fluorescence (fl.) intensity data was acquired using a Corning 96-well solid black polystyrene microplate on a Packard Fusion Microplate Reader equipped with excitation (405 nm) and emission filters (450 nm). Different concentrations of the cross-linked microtubules, chosen to span a range of at least 20% to 80% complexation, were incubated with fixed concentrations of **43**–**45** (25 nM) in GAB (10 mM phosphate, 1 mM EDTA, 1 mM GTP, 3.4 M glycerol, pH 6.5) at 22 °C with shaking for 1 h. These fixed probe concentrations were chosen to be substantially below the predicted K_d values to assure equilibrium binding measurements. Measurements of fluorescence (I_{sample}) were recorded for each sample. Average fluorescence (I_{mt}) intensities of the background signal microtubules alone were calculated by averaging three sample intensities for each concentration of microtubules. Average fluorescence (I_f) intensities of the free ligand were calculated by averaging three sample intensities of the Pacific Blue probe in GAB. Background-subtracted fluorescence (*I*) signals were calculated using the following equations:

$$I = I_{sample} - I_{mt}$$

The change in fl. intensity for each sample was calculated by subtracting the average (n=6) fl. of the free ligand (I_f). The change in fl. intensity was plotted against the concentration of tubulin, and a one-site specific binding model (GraphPad Prism 6.0) was used for curve fitting to calculate a dissociation constant (K_d).

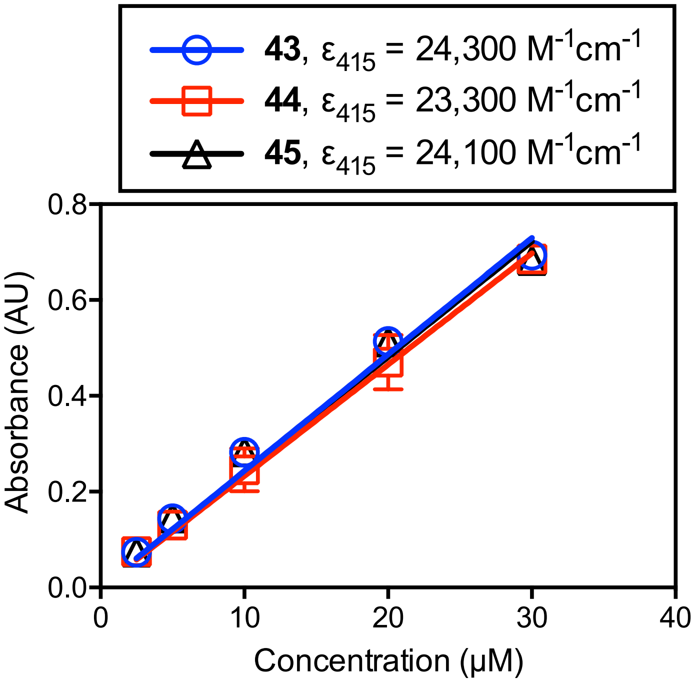

Figure 3.14. Determination of extinction coefficients of **43–45** in PBS (pH 7.4) containing DMSO (10%) and triton X-100 (0.5%).

3.9.3. Synthetic procedures and compound characterization data

General procedure 3A: Synthesis of paclitaxel derivatives **47–49**. Fmoc-amino acid derivatives (4 eq), *N*-(3-dimethylaminopropyl)-N′-ethylcarbodiimide hydrochloride (EDC, 4 eq.), and 4-dimethylaminopyridine (DMAP, 0.5 eq) were stirred in anhydrous CH_2Cl_2 at 22 °C for 15 min. **41** was added, and the reaction mixture was stirred for 16 h. The mixture was diluted with CH_2Cl_2 (75-175 mL) and washed with saturated aqueous NH_4Cl (50-100 mL x 1), water (25-50 mL x 1) and satd. aqueous NaCl (25-50 mL x 1). The organic layer was collected, dried over anhydrous Na_2SO_4 and purified by column chromatography (silica, eluent: 97:3 CH_2Cl_2/MeOH).

General procedure 3B: Synthesis of Paclitaxel derivatives **43** and **45**. Tetra-*N*-butylammonium fluoride in THF (TBAF, 1.0 M, 2 eq.) was added to a solution of **50** or **52** (1 eq.) in THF (0.5 mL) and stirred at 22 °C for 90 min. The reaction was concentrated, the residue was dissolved in DMSO (1.5 mL), and the product purified by preparative RP-HPLC (Gradient: H_2O:CH_3CN (9:1) to (0:100) with added TFA (0.1%) over 20 min; elution time = 16-17 min). Pure fractions were collected, combined, and dried by lyophilization.

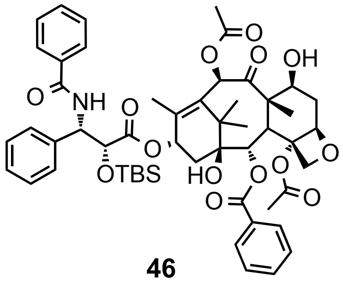

46

(2a*R*,4*S*,4a*S*,6*R*,9*S*,11*S*,12*S*,12b*S*)-9-(((2*R*,3*S*)-3-Benzamido-2-((*tert*-butyldimethylsilyl)oxy)-3-phenylpropanoyl)oxy)-12-(benzoyloxy)-4,11-dihydroxy-4a,8,13,13-tetramethyl-5-oxo-3,4,4a,5,6,9,10,11,12,12a-decahydro-1*H*-7,11-methanocyclodeca[3,4]benzo[1,2-*b*]oxete-6,12b(2a*H*)-diyl diacetate (46). This compound was synthesized by modifying a previously reported procedure.[70] To a solution of paclitaxel (**41**, 500 mg, 0.59 mmol) in anhydrous DMF (2.1 mL) at 22 °C were added imidazole (208 mg, 3.06 mmol) and *tert*-butyldimethylchlorosilane (542 mg, 3.61 mmol). After stirring for 16 h, the mixture was diluted with CH_2Cl_2 (175 mL) and washed with saturated aqueous NH_4Cl (100 mL x 1), water (50 mL x 1) and satd. aqueous NaCl (50 mL x 1). The organic layer was collected, dried over anhydrous Na_2SO_4 and concentrated. The residue was triturated with hexane to afford **46** as a white solid (536 mg, 95%). ^1H NMR (500 MHz, $CDCl_3$) δ 8.18-8.10 (m, 2H), 7.74 (dt, *J* = 8.3, 1.4 Hz, 2H), 7.64-7.45 (m, 4H), 7.45 - 7.36 (m, 4H), 7.32 (d, *J* = 7.3 Hz, 3H), 7.07 (d, *J* = 8.9 Hz, 1H), 6.29 (s, 2H), 5.78-5.63 (m, 2H), 5.04-4.92 (m, 1H), 4.73-4.61 (m, 1H), 4.44 (dd, *J* = 11.0, 6.6 Hz, 1H), 4.33 (d, *J* = 8.5 Hz, 1H), 4.22 (d, *J* = 8.5 Hz, 1H), 3.82 (d, *J* = 7.0 Hz, 1H), 2.57 (d, *J* = 1.0 Hz, 3H), 2.40 (dd, *J* = 15.3, 9.5 Hz, 1H), 2.23 (t, *J* = 0.9 Hz, 3H), 2.19-2.06 (m, 1H), 1.90 (t, *J* = 1.4 Hz, 3H), 1.69 (s, 3H), 1.24 (s, 3H), 1.13 (s, 3H), 0.80 (t, *J* = 0.9 Hz, 9H), –0.02- –0.08 (m, 3H), –0.29 (d, *J* = 1.2 Hz, 3H); ^{13}C NMR (126 MHz, $CDCl_3$) δ 203.9, 171.49, 171.45, 170.3, 167.2, 167.0, 142.6, 138.4, 134.2, 133.8, 133.0, 132.0, 130.4, 129.2, 128.9, 128.89, 128.86, 128.1, 127.1, 126.6, 84.6, 81.3, 79.3, 76.6, 75.67, 75.3, 75.2, 72.3, 71.5, 58.7, 55.8, 45.6, 43.4, 35.9, 35.7, 26.9, 25.7, 23.2, 22.5, 21.0, 18.3, 15.1, 9.8, –5.1, –5.7; HRMS (ESI-) m/z 990.4047 ($M-H^+$, $C_{53}H_{65}NO_{14}SiNa$ requires 990.4072).

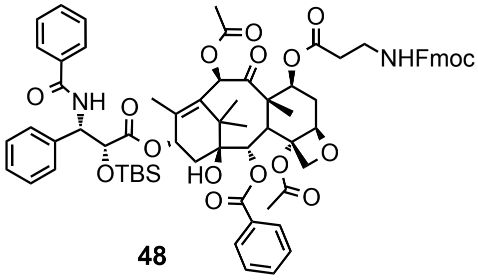

48

(2a*R*,4*S*,4a*S*,6*R*,9*S*,11*S*,12*S*,12b*S*)-4-((3-((((9*H*-Fluoren-9 yl)methoxy)carbonyl)amino)propanoyl) oxy)-9-(((2*R*,3*S*)-3-benzamido-2-((*tert*-butyldimethylsilyl)oxy)-3-phenylpropanoyl)oxy)-12-(benzoyloxy)-11-hydroxy-4a,8,13,13-tetramethyl-5-oxo-3,4,4a,5,6,9,10,11,12,12a-decahydro-1*H*-7,11-methanocyclodeca[3,4]benzo[1,2-*b*]oxete-6,12b(2a*H*)-diyl diacetate (48). Following general procedure 3A, Fmoc-βAla-OH (643 mg, 2.06 mmol) and **46** (500 mg, 0.52 mmol) yielded **48** (440 mg, 68%) as a white solid. ^{1}H NMR (500 MHz, CDCl$_3$) δ 8.17-8.11 (m, 2H), 7.79-7.73 (m, 4H), 7.68-7.57 (m, 3H), 7.57-7.26 (m, 15H), 7.08 (d, *J* = 8.9 Hz, 1H), 6.31 (s, 1H), 5.89-5.59 (m, 3H), 4.98 (dd, *J* = 9.6, 2.0 Hz, 1H), 4.68 (d, *J* = 2.2 Hz, 1H), 4.47-4.29 (m, 3H), 4.29-4.15 (m, 2H), 3.99 (d, *J* = 6.8 Hz, 1H), 3.62-3.37 (m, 2H), 2.59 (s, 3H), 2.53 (dd, *J* = 4.9, 2.3 Hz, 1H), 2.44 (dd, *J* = 15.2, 9.4 Hz, 1H), 2.21-2.12 (m, 2H), 2.10 (s, 3H), 1.99 (d, *J* = 1.6 Hz, 3H), 1.84 (s, 3H), 1.73 (d, *J* = 4.8 Hz, 1H), 1.23 (s, 3H), 1.18 (s, 3H) 0.80 (s, 9H), –0.03 (s, 3H), –0.30 (s, 3H); ^{13}C NMR (126 MHz, CDCl$_3$) δ 202.4, 171.6, 171.5, 170.1, 169.8, 167.1, 156.6, 144.20, 144.18, 141.4, 141.3, 138.4, 134.2, 133.9, 132.7, 132.0, 130.4, 129.1, 129.0, 128.9, 128.1, 127.81, 127.75, 127.2, 127.1, 126.5, 125.3, 125.2, 120.11, 120.05, 84.0, 81.0, 78.8, 76.5, 75.5, 75.2, 74.6, 71.7, 71.4, 66.7, 56.2, 55.8, 47.4, 47.4, 46.8, 43.4, 36.2, 35.8, 34.4, 33.6, 26.5, 25.7, 23.2, 21.6, 20.9, 18.3, 14.8, 11.1, –5.0, –5.7; HRMS (ESI+) m/z 1283.5148 (M+Na$^+$, $C_{71}H_{80}N_2O_{17}SiNa$ requires 1283.5124).

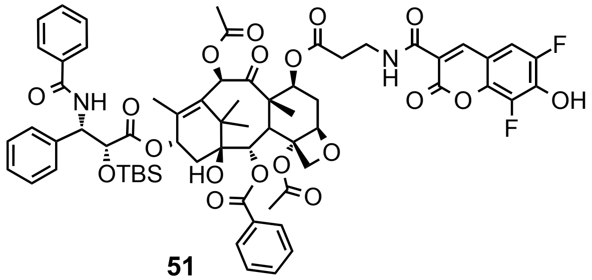

51

(2a*R*,4*S*,4a*S*,6*R*,9*S*,11*S*,12*S*,12b*S*)-9-(((2*R*,3*S*)-3-Benzamido-2-((*tert*-butyldimethylsilyl)oxy)-3-phenylpropanoyl)oxy)-12-(benzoyloxy)-4-((3-(6,8-difluoro-7-hydroxy-2-oxo-2*H*-chromene-3-carboxamido)propanoyl)oxy)-11-hydroxy-4a,8,13,13-tetramethyl-5-oxo-3,4,4a,5,6,9,10,11,12,12a-decahydro-1*H*-7,11-methanocyclodeca[3,4]benzo[1,2-*b*]oxete-6,12b(2a*H*)-diyl diacetate (51). To a solution of 20% piperidine in DMF (2 mL) was added **48** (100 mg, 0.079 mmol) at 22 °C. The mixture was stirred for 10 min and concentrated. The intermediate was taken on without further purification. To a solution of the Fmoc-deprotected-**48** in DMF (2 mL) was added Pacific Blue-NHS ester (**15**, 32 mg, 0.094 mmol) and DIEA (69 µL, 0.397 mmol). After stirring for 16 h, the reaction mixture was concentrated and purified by column chromatography (silica, eluent: 290:9:1 CH_2Cl_2/MeOH/AcOH) to yield compound **51** (80 mg, 80%) as a yellow solid. ^{1}H NMR (500 MHz, $CDCl_3$) δ 8.94 (t, *J* = 6.0 Hz, 1H), 8.71 (d, *J* = 1.3 Hz, 1H), 8.18-8.06 (m, 2H), 7.82-7.71 (m, 2H), 7.62-7.55 (m, 1H), 7.55-7.28 (m, 10H), 7.19-7.08 (m, 2H), 6.27 (d, *J* = 17.6 Hz, 2H), 5.83-5.60 (m, 3H), 5.05-4.95 (m, 1H), 4.68 (d, *J* = 2.1 Hz, 1H), 4.35 (d, *J* = 8.5 Hz, 1H), 4.21 (d, *J* = 8.3 Hz, 1H), 3.98 (d, *J* = 6.8 Hz, 1H), 3.83 - 3.61 (m, 2H), 2.70-2.60 (m, 3H), 2.59 (s, 3H), 2.42 (dd, *J* = 15.3, 9.4 Hz, 1H), 2.20-2.15 (m, 1H), 2.15 (s, 3H), 1.98 (d, *J* = 1.5 Hz, 3H), 1.92 (ddd, *J* = 14.2, 10.9, 2.1 Hz, 1H), 1.83 (s, 3H), 1.76 (s, 1H), 1.22 (s, 3H), 1.16 (s, 3H), 0.80 (s, 9H), –0.02 (s, 3H), –0.31 (s, 3H); ^{13}C NMR (126 MHz, $CDCl_3$) δ 202.1, 171.6, 171.2, 170.1, 169.3, 167.5, 167.0, 161.5, 159.9, 149.1 (dd, *J* = 243.7, 3.9 Hz), 147.5, 141.1, 139.7 (d, *J* = 258.4 Hz), 139.7 (d, *J* = 8.9 Hz), 138.2, 138.2 (d, *J* = 6.4 Hz), 134.1, 133.9, 132.7, 132.1, 130.3, 129.1, 128.94, 128.88, 128.1, 127.2, 126.5, 116.8, 110.3 (d, *J* = 8.9 Hz), 109.8 (dd, *J* = 20.1, 3.4 Hz), 84.2, 81.1, 78.8, 76.6, 75.4, 75.2, 74.6, 71.8, 71.5, 56.1, 55.9, 47.0, 43.5, 35.7, 35.4, 34.1, 33.4, 26.5, 25.7, 23.1, 21.5, 20.9, 18.3, 14.8, 11.1, –5.0, –5.7; HRMS (ESI+) m/z 1263.4574 (M+H$^+$, $C_{66}H_{73}F_2N_2O_{19}Si$ requires 1263.4545).

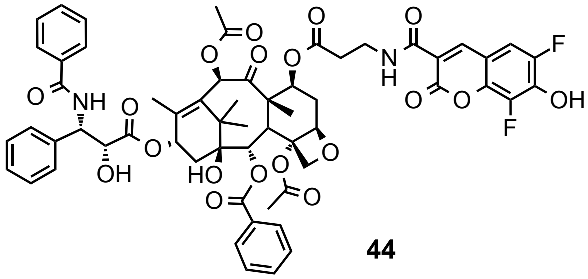

44

(2a*R*,4*S*,4a*S*,6*R*,9*S*,11*S*,12*S*,12b*S*)-9-(((2*R*,3*S*)-3-Benzamido-2-hydroxy-3-phenylpropanoyl)oxy)-12-(benzoyloxy)-4-((3-(6,8-difluoro-7-hydroxy-2-oxo-2*H*-chromene-3-carboxamido)propanoyl)oxy)-11-hydroxy-4a,8,13,13-tetramethyl-5-oxo-3,4,4a,5,6,9,10,11,12,12a-decahydro-1*H*-7,11-methanocyclodeca[3,4]benzo[1,2-*b*]oxete-6,12b(2a*H*)-diyl diacetate (Taxol-βAla-PB, 44). To a solution of **51** (50 mg, 0.040 mmol) in anhydrous THF (1 mL) at 22 °C was added a solution of TBAF in THF (1.0 M, 84 µL, 0.084 mmol). After stirring for 90 min, the mixture was concentrated and purified by column chromatography (silica, 1:9:290 AcOH/MeOH/DCM) to afford **44** as a yellow solid (44 mg, 97%). ^{1}H NMR (500 MHz, $CDCl_3$) δ 9.03 (t, *J* = 6.0 Hz, 1H), 8.76 (s, 1H), 8.10 (d, *J* = 7.1 Hz, 2H), 7.77 (d, *J* = 7.1 Hz, 2H), 7.62 (ddt, *J* = 8.7, 7.0, 1.3 Hz, 1H), 7.55-7.27 (m, 10H), 7.21 (dd, *J* = 9.1, 1.7 Hz, 2H), 6.18 (s, 1H), 6.15 (d, *J* = 8.3 Hz, 1H), 5.80 (dd, *J* = 8.9, 2.6 Hz, 1H), 5.66

(d, *J* = 6.9 Hz, 1H), 5.61 (dd, *J* = 10.5, 7.1 Hz, 1H), 4.95 (dd, *J* = 9.3, 1.8 Hz, 1H), 4.81 (d, *J* = 2.6 Hz, 1H), 4.32 (d, *J* = 8.5 Hz, 1H), 4.19 (d, *J* = 8.3 Hz, 1H), 3.91 (d, *J* = 6.6 Hz, 1H), 3.77 (dq, *J* = 12.6, 6.2 Hz, 1H), 3.65 (dq, *J* = 13.0, 5.9 Hz, 1H), 2.75-2.66 (m, 1H), 2.66-2.50 (m, 2H) 2.37 (s, 3H), 2.35-2.27 (m, 1H) 2.11 (m, 1H), 1.94-1.80 (m, 2H), 1.86-1.76 (m, 6H), 1.25 (s, 3H), 1.20 (s, 3H), 1.15 (s, 3H); ^{13}C NMR (126 MHz, $CDCl_3$) δ 201.8, 172.4, 171.2, 170.5, 169.1, 167.4, 166.8, 161.6, 159.7, 149.0 (d, *J* = 242.9 Hz), 147.5, 140.6 (d, *J* = 8.3 Hz), 140.5, 139.6, 139.0 (dd, *J* = 249.5, 4.9 Hz), 137.8, 133.8, 133.5, 132.8, 132.0, 130.1, 129.0, 128.9, 128.7, 128.3, 127.13 127.08, 116.5, 110.2 (d, *J* = 8.8 Hz), 109.9 (d, *J* = 20.4 Hz), 84.0, 81.0, 78.5, 76.5, 75.4, 74.2, 73.3, 72.0, 71.8, 56.1, 55.1, 47.1, 43.2, 36.7, 35.5, 35.2, 33.7, 33.3, 29.7, 26.5, 22.6, 20.7, 14.6, 10.9; HRMS (ESI-) m/z 1147.3541 (M-H$^+$, $C_{60}H_{57}F_2N_2O_{19}$ requires 1147.3524).

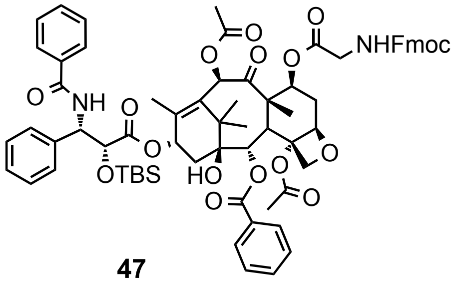

47

(2a*R*,4*S*,4a*S*,6*R*,9*S*,11*S*,12*S*,12b*S*)-4-(((((9*H*-Fluoren-9-yl)methoxy)carbonyl)glycyl)oxy)-9-(((2*R*,3*S*)-3-benzamido-2-((*tert*-butyldimethylsilyl)oxy)-3-phenylpropanoyl)oxy)-12-(benzoyloxy)-11-hydroxy-4a,8,13,13-tetramethyl-5-oxo-3,4,4a,5,6,9,10,11,12,12a-decahydro-1*H*-7,11-methanocyclodeca[3,4]benzo[1,2-*b*]oxete-6,12b(2a*H*)-diyl diacetate (47). Following general procedure 3A, Fmoc-Gly-OH (119 mg, 0.4 mmol) and **46** (97 mg, 0.1 mmol) yielded **47** (43 mg, 35%) as a white solid. ^{1}H NMR (500 MHz, $CDCl_3$) δ 8.16 (d, *J* = 7.0

Hz, 2H), 7.84-7.74 (m, 4H), 7.71-7.61 (m, 3H), 7.60-7.30 (m, 15H), 7.11 (d, *J* = 8.9 Hz, 1H), 6.29 (t, *J* = 9.2 Hz, 1H), 6.23 (s, 1H), 5.84-5.68 (m, 3H), 5.54 (dd, *J* = 7.4, 4.7 Hz, 1H), 5.07-4.97 (m, 1H), 4.70 (d, *J* = 2.1 Hz, 1H), 4.48-4.35 (m, 3H), 4.30 (t, *J* = 7.4 Hz, 1H), 4.23 (d, *J* = 8.5 Hz, 1H), 4.17-4.08 (m, 1H), 3.99 (d, *J* = 7.0 Hz, 1H), 3.91-3.81 (m, 1H), 2.60 (s, 3H), 2.45 (dd, *J* = 15.6, 9.1 Hz, 1H), 2.22 (s, 3H), 2.18 (d, *J* = 3.0 Hz, 1H), 2.00 (s, 3H), 1.96-1.89 (m, 1H), 1.85 (s, 3H), 1.28 (s, 3H), 1.25 (s, 3H), 1.19 (s, 3H), 0.83 (s, 9H), –0.01 (s, 3H), –0.27 (s, 3H); ^{13}C NMR (126 MHz, $CDCl_3$) δ 202.0, 171.6, 170.1, 170.1, 169.8, 167.2, 167.0, 156.9, 144.2, 144.0, 141.40, 141.38, 141.4, 138.3, 134.2, 133.9, 132.5, 132.0, 130.4, 129.1, 129.0, 128.94, 128.91, 128.2, 127.79, 127.78, 127.2, 127.1, 126.5, 125.47, 125.46, 125.4, 120.1, 84.0, 81.1, 78.70, 76.5, 75.8, 75.2, 74.5, 72.1, 71.5, 67.4, 56.2, 55.8, 47.3, 47.0, 43.5, 43.2, 35.7, 33.44, 33.40, 29.8, 26.5, 25.7, 23.1, 21.5, 21.1, 18.3, 14.8, 11.0, –5.1, –5.7; HRMS (ESI+) m/z 1269.4939 (M+Na$^+$, $C_{70}H_{78}N_2O_{17}SiNa$ requires 1269.4968).

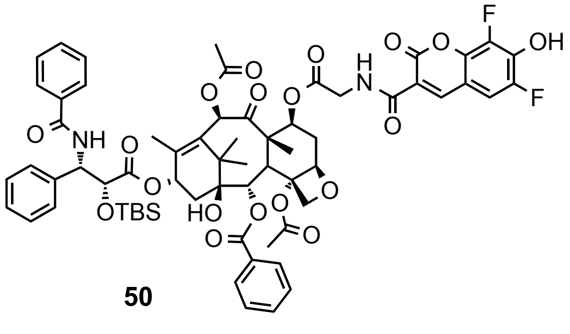

50

(2a*R*,4*S*,4a*S*,6*R*,9*S*,11*S*,12*S*,12b*S*)-9-(((2*R*,3*S*)-3-Benzamido-2-((*tert*-butyldimethylsilyl)oxy)-3-phenylpropanoyl)oxy)-12-(benzoyloxy)-4-(((6,8-difluoro-7-hydroxy-2-oxo-2*H*-chromene-3-carbonyl)glycyl)oxy)-11-hydroxy-4a,8,13,13-tetramethyl-5-oxo-3,4,4a,5,6,9,10,11,12,12a-decahydro-1*H*-7,11-methanocyclodeca[3,4]benzo[1,2-*b*]oxete-6,12b(2a*H*)-diyl diacetate (50). To a solution of 20% piperidine in DMF (2 mL) was added **47** (14 mg, 0.011 mmol) at 22 °C.

The mixture was stirred for 10 min and concentrated. The intermediate was taken on without further purification. To a solution of the Fmoc-deprotected-**47** in DMF (0.5 mL) was added Pacific Blue-NHS ester (**15**, 5 mg, 0.015 mmol) and DIEA (6 µL, 0.034 mmol). After stirring for 16 h, the reaction was concentrated under vacuum, and the crude product was dissolved in DMSO (2 mL) and purified by preparative reverse phase HPLC (gradient: 90/10 H_2O/MeCN to 100% MeCN over 20 min with 0.1% TFA added; retention time = 19 min) to yield compound **50** (12 mg, 85%) as a yellow solid. HRMS (ESI+) m/z 1271.4191 (M+Na$^+$, $C_{65}H_{70}N_2O_{19}SiNa$ requires 1271.4208).

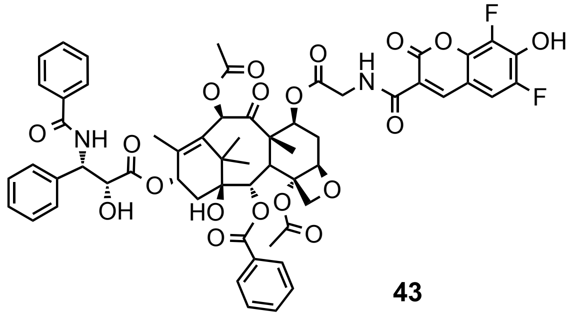

43

(2a*R*,4*S*,4a*S*,6*R*,9*S*,11*S*,12*S*,12b*S*)-9-(((2*R*,3*S*)-3-Benzamido-2-hydroxy-3-phenylpropanoyl)oxy)-12-(benzoyloxy)-4-(((6,8-difluoro-7-hydroxy-2-oxo-2*H*-chromene-3-carbonyl)glycyl)oxy)-11-hydroxy-4a,8,13,13-tetramethyl-5-oxo-3,4,4a,5,6,9,10,11,12,12a-decahydro-1*H*-7,11-methanocyclodeca[3,4]benzo[1,2-*b*]oxete-6,12b(2a*H*)-diyl diacetate (Taxol-Gly-PB, 43). Following general procedure 3B, **50** (10 mg, 0.008 mmol) yielded compound **43** (6 mg, 67%) as a yellow solid. ^{1}H NMR (500 MHz, $CDCl_3$) δ 9.09 (t, *J* = 5.9 Hz, 1H), 8.79 (d, *J* = 1.3 Hz, 1H), 8.16-8.07 (m, 2H), 7.82-7.75 (m, 2H), 7.68-7.60 (m, 1H), 7.56-7.34 (m, 10H), 7.23 (dd, *J* = 9.2, 1.9 Hz, 1H), 7.12 (d, *J* = 8.9 Hz, 1H), 6.19 (s, 1H), 6.17 (s, 1H), 5.82 (dd, *J* = 9.0, 2.5 Hz, 1H), 5.69-5.61 (m, 2H), 5.00-4.94 (m, 1H), 4.82 (d, *J* = 2.6 Hz, 1H), 4.40-4.28 (m, 2H), 4.25-4.15 (m, 2H), 3.98-3.87 (m, 1H), 2.72-2.58 (m, 2H), 2.39 (s, 3H), 2.37-2.29 (m, 2H), 2.27 (s, 3H), 1.92 (ddd, J = 14.5, 10.6, 2.0 Hz, 1H), 1.82 (s, 3H), 1.80 (s, 3H), 1.24 (s, 3H), 1.17 (s, 3H); ^{13}C NMR (126 MHz, $CDCl_3$) δ 201.6, 172.5, 170.5, 170.0, 169.0, 167.3, 167.0, 161.9, 159.6, 148.5 (d, J = 245.1 Hz), 147.8, 140.9, 140.8, 138.0, 135.3, 134.0, 133.7, 132.9, 132.2, 130.4-130.1 (m), 129.2-129.1 (m), 129.1, 128.9, 128.9, 128.5, 127.7-126.6 (m), 117.0, 110.7 (d, J = 9.3 Hz), 110.0 (d, J = 22.2 Hz), 84.0, 81.1, 78.6, 76.5, 75.7, 74.3, 73.3, 72.6, 72.3, 56.2, 55.0, 47.2, 43.4, 42.1, 35.6, 33.4, 26.7, 22.7, 21.0, 20.9, 14.9, 10.9; HRMS (ESI-) m/z 1147.3340 (M-H$^+$, $C_{59}H_{55}F_2N_2O_{19}$ requires 1133.3367).

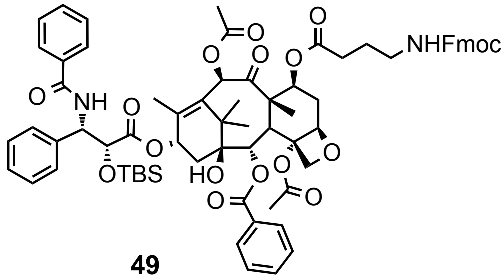

49

(2a*R*,4*S*,4a*S*,6*R*,9*S*,11*S*,12*S*,12b*S*)-4-((4-((((9*H*-Fluoren-9-yl)methoxy)carbonyl)amino)butanoyl)oxy)-9-(((2*R*,3*S*)-3-benzamido-2-((*tert*-butyldimethylsilyl)oxy)-3-phenylpropanoyl)oxy)-12-(benzoyloxy)-11-hydroxy-4a,8,13,13-tetramethyl-5-oxo-3,4,4a,5,6,9,10,11,12,12a-decahydro-1*H*-7,11-methanocyclodeca[3,4]benzo[1,2-*b*]oxete-6,12b(2a*H*)-diyl diacetate (49). Following general procedure 3A, 4-(Fmoc-amino)butyric acid (130 mg, 0.4 mmol) and **46** (97 mg, 0.1 mmol) yielded **49** (100 mg, 79%) as a white solid. ^{1}H NMR (500 MHz, $CDCl_3$) δ 8.16-8.11 (m, 2H), 7.79-7.73 (m, 4H), 7.63-7.58 (m, 3H), 7.56-7.29 (m, 15H), 7.09 (d, J = 8.8 Hz, 1H), 6.26 (dd, J = 9.0, 1.8 Hz, 1H), 6.24 (s, 1H), 5.84-5.65 (m, 3H), 5.59 (dd, J = 10.6, 7.0 Hz, 1H), 4.98 (dd, J = 9.6, 2.0 Hz, 1H), 4.43 (d, J = 7.0 Hz, 2H), 4.38-4.29

(m, 1H), 4.25-4.16 (m, 2H), 3.96 (d, *J* = 7.0 Hz, 1H), 3.41-3.12 (m, 2H), 2.58 (s, 3H), 2.51-2.36 (m, 2H), 2.34-2.08 (m, 2H), 2.06 (s, 3H), 1.96 (d, *J* = 1.4 Hz, 3H), 1.83 (s, 3H), 1.22 (s, 3H), 1.16 (s, 3H), 0.80 (s, 9H), –0.04 (s, 3H), –0.31 (s, 3H); ^{13}C NMR (126 MHz, $CDCl_3$) δ 201.8, 172.3, 171.5, 170.2, 169.9, 167.1, 166.9, 156.5, 144.1, 141.32, 141.31, 141.30, 141.1, 138.2, 134.1, 133.8, 132.4, 131.9, 130.2, 129.0, 128.81, 128.78, 128.0, 127.9, 127.64, 127.61, 127.2, 127.1, 127.03, 127.00, 126.4, 125.4, 125.03, 125.02, 119.95, 84.0 , 81.0, 78.6, 76.4, 75.5, 75.1, 74.5, 71.5, 71.3, 66.2, 56.0, 55.7, 47.4, 46.8, 46.7, 46.5, 43.4, 39.3, 35.6, 33.4, 32.9, 29.9, 26.4, 25.5, 23.7, 23.0, 21.4, 20.7, 18.1, 17.6, 14.7, 11.0, –5.2, –5.8; HRMS (ESI+) m/z 1297.5265 (M+Na$^+$, $C_{72}H_{82}N_2O_{17}SiNa$ requires 1297.5281).

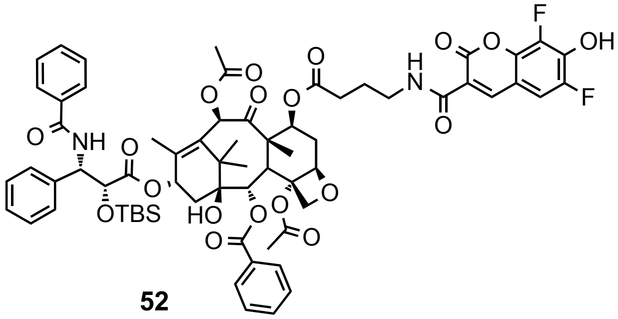

52

(2a*R*,4*S*,4a*S*,6*R*,9*S*,11*S*,12*S*,12b*S*)-9-(((2*R*,3*S*)-3-Benzamido-2-((*tert*-butyldimethylsilyl)oxy)-3-phenylpropanoyl)oxy)-12-(benzoyloxy)-4-((4-(6,8-difluoro-7-hydroxy-2-oxo-2*H*-chromene-3-carboxamido)butanoyl)oxy)-11-hydroxy-4a,8,13,13-tetramethyl-5-oxo-3,4,4a,5,6,9,10,11,12,12a-decahydro-1*H*-7,11-methanocyclodeca[3,4]benzo[1,2-*b*]oxete-6,12b(2a*H*)-diyl diacetate (52). To a solution of 20% piperidine in DMF (1 mL) was added **49** (30 mg, 0.024 mmol) at 22 °C. The mixture was stirred for 10 min and concentrated. The intermediate was taken on without further purification. To a solution of the Fmoc-deprotected-**49** in DMF (1 mL) was added Pacific Blue-NHS ester (**15**, 10 mg, 0.028 mmol) and DIEA (12 µL, 0.069

mmol). After stirring for 16 h, the reaction was concentrated under vacuum, and the crude product was dissolved in DMSO (2 mL) and purified by preparative reverse phase HPLC (gradient: 90/10 H_2O/MeCN to 100% MeCN over 20 min with 0.1% TFA added; retention time = 19 min) to yield compound **52** (26 mg, 87%) as a yellow solid. HRMS (ESI+) m/z 1299.4524 (M+Na$^+$, $C_{67}H_{74}F_2N_2O_{19}SiNa$ requires 1299.4521).

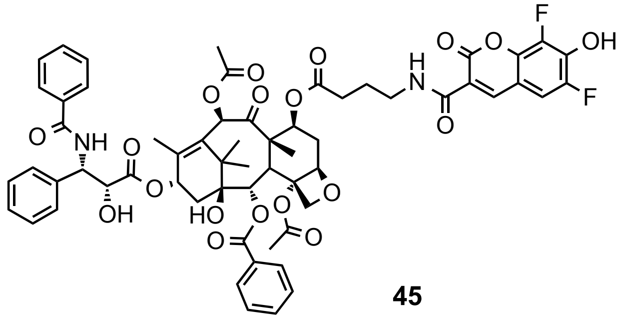

45

(2a*R*,4*S*,4a*S*,6*R*,9*S*,11*S*,12*S*,12b*S*)-9-(((2*R*,3*S*)-3-Benzamido-2-hydroxy-3-phenylpropanoyl)oxy)-12-(benzoyloxy)-4-((4-(6,8-difluoro-7-hydroxy-2-oxo-2*H*-chromene-3-carboxamido)butanoyl)oxy)-11-hydroxy-4a,8,13,13-tetramethyl-5-oxo-3,4,4a,5,6,9,10,11,12,12a-decahydro-1*H*-7,11-methanocyclodeca[3,4]benzo[1,2-*b*]oxete-6,12b(2a*H*)-diyl diacetate (Taxol-GABA-PB, 45). Following general procedure 3B, **52** (16 mg, 0.013 mmol) yielded compound **45** (13 mg, 86%) as a yellow solid. ^{1}H NMR (500 MHz, $CDCl_3$) δ 8.81 (t, *J* = 6.0 Hz, 1H), 8.73 (d, *J* = 1.5 Hz, 1H), 8.11-8.05 (m, 2H), 7.80-7.73 (m, 2H), 7.63-7.56 (m, 1H), 7.53-7.28 (m, 11H), 7.16 (dd, *J* = 9.4, 2.0 Hz, 1H), 6.19 (s, 1H), 6.18-6.13 (m, 1H), 5.79 (dd, *J* = 9.0, 2.9 Hz, 1H), 5.65 (d, *J* = 6.8 Hz, 1H), 5.54 (dd, *J* = 10.4, 7.2 Hz, 1H), 4.92 (dd, *J* = 9.6, 2.0 Hz, 1H), 4.81 (d, *J* = 2.9 Hz, 1H), 4.30 (d, *J* = 8.5 Hz, 1H), 4.17 (d, *J* = 8.5 Hz, 1H), 3.89 (d, *J* = 6.7 Hz, 1H), 3.53-3.39 (m, 2H), 2.64-2.50 (m, 1H), 2.46 (dt, *J* = 17.3, 7.2 Hz, 1H), 2.36 (s, 3H), 2.31-2.26 (m, 3H), 2.17 (s, 3H), 2.00-1.84 (m, 2H), 1.81 (s, 3H), 1.79 (s, 3H), 1.36-1.23 (m, 2H), 1.19 (s, 3H), 1.15 (s, 3H); ^{13}C NMR (126 MHz, $CDCl_3$) δ 202.1, 172.6, 172.5, 170.6, 169.4, 167.7, 166.9, 161.9, 160.2, 149.3 (dd, *J* = 244.4, 4.0 Hz), 147.9, 140.8 (d, *J* = 9.5 Hz), 140.5, 140.1 – 139.9 (m), 139.2 (dd, *J* = 249.0, 5.9 Hz), 138.0, 133.9, 133.6, 133.0, 132.2, 130.3, 129.14, 129.08, 128.85, 128.83, 128.4, 127.24, 127.19, 116.4, 110.2 (d, *J* = 9.4 Hz), 110.0 (d, *J* = 20.1 Hz), 84.1, 81.1, 78.6, 76.6, 75.4, 74.4, 73.4, 72.2, 71.6, 56.2, 55.3, 47.1, 43.3, 35.6, 33.5, 31.7, 31.3, 26.6, 24.1, 22.7, 20.95, 20.92, 14.3, 11.0; HRMS (ESI-) m/z 1161.3683 (M-H$^+$, $C_{61}H_{59}F_2N_2O_{19}$ requires 1161.3680).

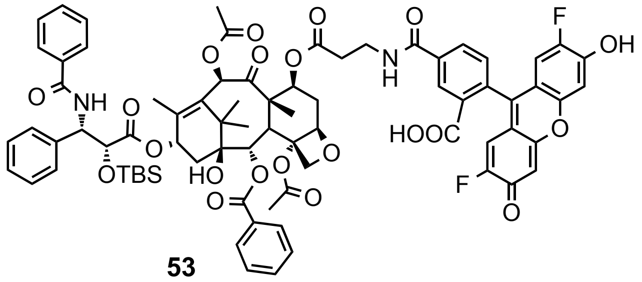

53

5-((3-(((2a*R*,4*S*,4a*S*,6*R*,9*S*,11*S*,12*S*,12b*S*)-6,12b-Diacetoxy-9-(((2*R*,3*S*)-3-benzamido-2-((*tert*-butyldimethylsilyl)oxy)-3-phenylpropanoyl)oxy)-12-(benzoyloxy)-11-hydroxy-4a,8,13,13-tetramethyl-5-oxo-2a,3,4,4a,5,6,9,10,11,12,12a,12b-dodecahydro-1*H*-7,11-methanocyclodeca[3,4]benzo[1,2-*b*]oxet-4-yl)oxy)-3-oxopropyl)carbamoyl)-2-(2,7-difluoro-6-hydroxy-3-oxo-3*H*-xanthen-9-yl)benzoic acid (53). To a solution of piperidine in DMF (20%, 2 mL) was added **48** (10 mg, 0.010 mmol) at 22 °C. The mixture was stirred for 10 min and concentrated. The intermediate was taken on without further purification. To a solution of the Fmoc-deprotected intermediate in DMF (2 mL) was added Oregon Green-NHS ester (5 mg, 0.011) and DIEA (5 µL). After stirring for 16 h, the reaction was concentrated under vacuum, and the crude product was dissolved in DMSO (2 mL) and purified by preparative reverse phase HPLC (gradient: 90/10

H_2O/MeCN to 100% MeCN over 20 min with 0.1% TFA added; retention time = 18 min (488 nm)) to afford **53** as an orange solid (6 mg, 43%). HRMS (ESI+) m/z 1431.4731 ($M+Na^+$, $C_{77}H_{78}F_2N_2O_{21}SiNa$ requires 1455.4732).

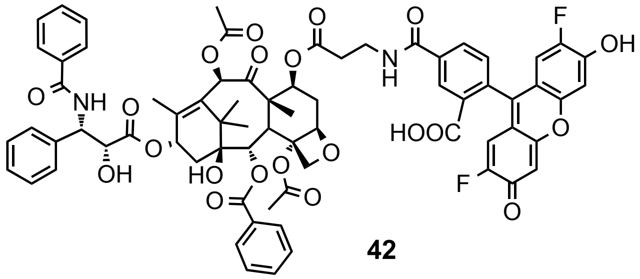

42

5-((3-(((2a*R*,4*S*,4a*S*,6*R*,9*S*,11*S*,12*S*,12b*S*)-6,12b-Diacetoxy-9-(((2*R*,3*S*)-3-benzamido-2-hydroxy-3-phenylpropanoyl)oxy)-12-(benzoyloxy)-11-hydroxy-4a,8,13,13-tetramethyl-5-oxo-2a,3,4,4a,5,6,9,10,11,12,12a,12b-dodecahydro-1*H*-7,11-methanocyclodeca[3,4]benzo[1,2-*b*]oxet-4-yl)oxy)-3-oxopropyl)carbamoyl)-2-(2,7-difluoro-6-hydroxy-3-oxo-3*H*-xanthen-9-yl)benzoic acid (Flutax-2, 42). Following general procedure 3B, **53** (4 mg, 0.0028 mmol) yielded compound **42** (3 mg, 82%) as an orange solid. HRMS (ESI+) m/z 1319.4038 ($M+H^+$, $C_{71}H_{65}F_2N_2O_{21}$ requires 1319.4048).

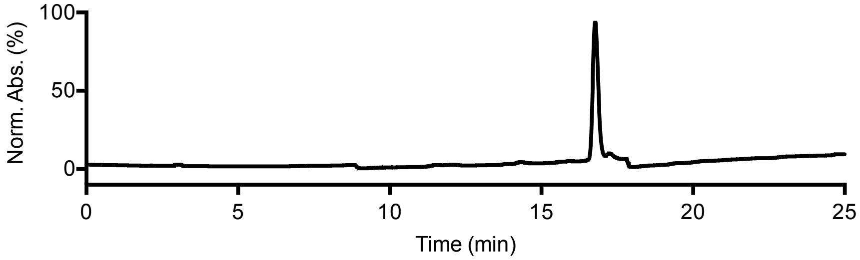

Figure 3.15. Analytical HPLC profile of **42** after preparative HPLC. Retention time = 17 min monitored by UV absorbance at 254 nm. Purity >95% by HPLC.

3.10. References

1. Kingston, D. G. I., Taxol, a molecule for all seasons. *Chem. Comm.* **2001**, 867-880.

2. Rohena, C. C.; Mooberry, S. L., Recent progress with microtubule stabilizers: new compounds, binding modes and cellular activities. *Nat. Prod. Rep.* **2014,** *31*, 335-355.

3. Jordan, M. A.; Wilson, L., Microtubules as a target for anticancer drugs. *Nat. Rev. Cancer* **2004,** *4*, 253-265.

4. Komlodi-Pasztor, E.; Sackett, D.; Wilkerson, J.; Fojo, T., Mitosis is not a key target of microtubule agents in patient tumors. *Nat. Rev. Clin. Oncol.* **2011,** *8*, 244-250.

5. Mitchison, T. J., The proliferation rate paradox in antimitotic chemotherapy. *Mol. Biol. Cell* **2012,** *23*, 1-6.

6. Dancey, J. T.; Deubelbeiss, K. A.; Harker, L. A.; Finch, C. A., Neutrophil kinetics in man. *J. Clin. Invest.* **1976,** *58*, 705-715.

7. Risinger, A. L.; Dybdal-Hargreaves, N. F.; Mooberry, S. L., Breast Cancer Cell Lines Exhibit Differential Sensitivities to Microtubule-targeting Drugs Independent of Doubling Time. *Anticancer Research* **2015,** *35*, 5845-5850.

8. Noguchi, S., Predictive factors for response to docetaxel in human breast cancers. *Cancer Sci.* **2006,** *97*, 813-820.

9. Amadori, D.; Volpi, A.; Maltoni, R.; Nanni, O.; Amaducci, L.; Amadori, A.; Giunchi, D. C.; Vio, A.; Saragoni, A.; Silvestrini, R., Cell proliferation as a predictor of response to chemotherapy in metastatic breast cancer: A prospective study. *Breast Cancer Res. Treat.* **1997,** *43*, 7-14.

10. Baguley, B. C.; Marshall, E. S.; Whittaker, J. R.; Dotchin, M. C.; Nixon, J.; McCrystal, M. R.; Finlay, G. J.; Matthews, J. H. L.; Holdaway, K. M.; van Zijl, P., Resistance mechanisms determining the in vitro sensitivity to paclitaxel of tumour cells cultured from patients with ovarian cancer. *Eur. J. Cancer* **1995,** *31*, 230-237.

11. Komlodi-Pasztor, E.; Sackett, D. L.; Fojo, A. T., Inhibitors Targeting Mitosis: Tales of How Great Drugs against a Promising Target Were Brought Down by a Flawed Rationale. *Clin. Cancer Res.* **2012,** *18*, 51-63.

12. Sahenk, Z.; Barohn, R.; New, P.; Mendell, J. R., Taxol neuropathy: Electrodiagnostic and sural nerve biopsy findings. *Arch. Neurol.* **1994,** *51*, 726-729.

13. Scripture, C. D.; Figg, W. D.; Sparreboom, A., Peripheral Neuropathy Induced by Paclitaxel: Recent Insights and Future Perspectives. *Curr. Neuropharmacol.* **2006,** *4*, 165-172.

14. Barasoain, I.; Díaz, J. F.; Andreu, J. M., Chapter 19 - Fluorescent Taxoid Probes for Microtubule Research. In *Methods Cell Biol.*, Leslie, W.; John, J. C., Eds. Academic Press2010; Vol. Volume 95, pp 353-372.

15. Díaz, J. F.; Barasoain, I.; Souto, A. A.; Amat-Guerri, F.; Andreu, J. M., Macromolecular Accessibility of Fluorescent Taxoids Bound at a Paclitaxel Binding Site in the Microtubule Surface. *J. Biol. Chem.* **2005,** *280*, 3928-3937.

16. Lillo, M. P.; Cañadas, O.; Dale, R. E.; Acuña, A. U., Location and Properties of the Taxol Binding Center in Microtubules: A Picosecond Laser Study with Fluorescent Taxoids. *Biochemistry* **2002,** *41*, 12436-12449.

17. Barasoain, I.; García-Carril, A. M.; Matesanz, R.; Maccari, G.; Trigili, C.; Mori, M.; Shi, J.-Z.; Fang, W.-S.; Andreu, J. M.; Botta, M.; Díaz, J. F., Probing the Pore Drug

Binding Site of Microtubules with Fluorescent Taxanes: Evidence of Two Binding Poses. *Chem. Biol.* **2010,** *17*, 243-253.

18. Díaz, J. F.; Strobe, R.; Engelborghs, Y.; Souto, A. A.; Andreu, J. M., Molecular Recognition of Taxol by Microtubules: Kinetics and thermodynamics of binding of fluorescent taxol derivatives to an exposed site. *J Biol. Chem.* **2000,** *275*, 26265-26276.

19. Guy, R. K.; Scott, Z. A.; Sloboda, R. D.; Nicolaou, K. C., Fluorescent taxoids. *Chem. Biol.* **1996,** *3*, 1021-1031.

20. Evangelio, J. A.; Abal, M.; Barasoain, I.; Souto, A. A.; Lillo, M. P.; Acuña, A. U.; Amat-Guerri, F.; Andreu, J. M., Fluorescent taxoids as probes of the microtubule cytoskeleton. *Cell Motil. Cytoskeleton* **1998,** *39*, 73-90.

21. Li, X.; Barasoain, I.; Matesanz, R.; Fernando Díaz, J.; Fang, W.-S., Synthesis and biological activities of high affinity taxane-based fluorescent probes. *Bioorg. Med. Chem. Lett.* **2009,** *19*, 751-754.

22. Andreu, J. M.; Barasoain, I., The Interaction of Baccatin III with the Taxol Binding Site of Microtubules Determined by a Homogeneous Assay with Fluorescent Taxoid. *Biochemistry* **2001,** *40*, 11975-11984.

23. Duchi, S.; Dambruoso, P.; Martella, E.; Sotgiu, G.; Guerrini, A.; Lucarelli, E.; Pessina, A.; Coccè, V.; Bonomi, A.; Varchi, G., Thiophene-Based Compounds as Fluorescent Tags to Study Mesenchymal Stem Cell Uptake and Release of Taxanes. *Bioconj. Chem.* **2014,** *25*, 649-655.

24. Lukinavicius, G.; Reymond, L.; D'Este, E.; Masharina, A.; Gottfert, F.; Ta, H.; Guther, A.; Fournier, M.; Rizzo, S.; Waldmann, H.; Blaukopf, C.; Sommer, C.; Gerlich,

D. W.; Arndt, H.-D.; Hell, S. W.; Johnsson, K., Fluorogenic probes for live-cell imaging of the cytoskeleton. *Nat. Meth.* **2014,** *11*, 731-733.

25. Li, H.; Duan, Z.-W.; Xie, P.; Liu, Y.-R.; Wang, W.-C.; Dou, S.-X.; Wang, P.-Y., Effects of Paclitaxel on EGFR Endocytic Trafficking Revealed Using Quantum Dot Tracking in Single Cells. *PLoS One* **2012,** *7*, e45465.

26. Walker, D. G.; Swigor, J. E.; Kant, J.; Schroeder, D. R., Synthesis of carbon-14 labeled Taxol® (paclitaxel). *J. Labelled Comp. Radiopharm.* **1994,** *34*, 973-980.

27. Hsueh, W.-A.; Kesner, A. L.; Gangloff, A.; Pegram, M. D.; Beryt, M.; Czernin, J.; Phelps, M. E.; Silverman, D. H. S., Predicting Chemotherapy Response to Paclitaxel with 18F-Fluoropaclitaxel and PET. *J. Nucl. Med.* **2006,** *47*, 1995-1999.

28. Haggarty, S. J.; Mayer, T. U.; Miyamoto, D. T.; Fathi, R.; King, R. W.; Mitchison, T. J.; Schreiber, S. L., Dissecting cellular processes using small molecules: identification of colchicine-like, taxol-like and other small molecules that perturb mitosis. *Chem. Biol.* **2000,** *7*, 275-286.

29. Field, Jessica J.; Pera, B.; Calvo, E.; Canales, A.; Zurwerra, D.; Trigili, C.; Rodríguez-Salarichs, J.; Matesanz, R.; Kanakkanthara, A.; Wakefield, S. J.; Singh, A. J.; Jiménez-Barbero, J.; Northcote, P.; Miller, John H.; López, Juan A.; Hamel, E.; Barasoain, I.; Altmann, K.-H.; Díaz, José F., Zampanolide, a Potent New Microtubule-Stabilizing Agent, Covalently Reacts with the Taxane Luminal Site in Tubulin α,β-Heterodimers and Microtubules. *Chem. Biol.* **2012,** *19*, 686-698.

30. Matesanz, R.; Barasoain, I.; Yang, C.-G.; Wang, L.; Li, X.; de Inés, C.; Coderch, C.; Gago, F.; Barbero, J. J.; Andreu, J. M.; Fang, W.-S.; Díaz, J. F., Optimization of

Taxane Binding to Microtubules: Binding Affinity Dissection and Incremental Construction of a High-Affinity Analog of Paclitaxel. *Chem. Biol.* **2008,** *15*, 573-585.

31. Vieira, P. B.; Borges, F. P.; Gottardi, B.; Stuepp, C.; Larré, A. B.; Tasca, T.; De Carli, G. A., Analysis of microtubule cytoskeleton distribution using a fluorescent taxoid in two trichomonadid protozoa: Trichomonas gallinae and Tritrichomonas foetus. *Exp. Parasitol.* **2008,** *119*, 186-191.

32. Lecke, S. B.; Tasca, T.; Souto, A. A.; De Carli, G. A., Trichomonas vaginalis: microtubule cytoskeleton distribution using fluorescent taxoid. *Exp. Parasitol.* **2002,** *102*, 113-116.

33. Lecke, S. B.; Tasca, T.; Souto, A. A.; De Carli, G. A., Perspective of a new diagnostic for human trichomonosis. *Memórias do Instituto Oswaldo Cruz* **2003,** *98*, 273-276.

34. Lee, J. S.; Feijen, J., Biodegradable polymersomes as carriers and release systems for paclitaxel using Oregon Green® 488 labeled paclitaxel as a model compound. *J. Control. Release* **2012,** *158*, 312-318.

35. Hennig, S.; van de Linde, S.; Lummer, M.; Simonis, M.; Huser, T.; Sauer, M., Instant Live-Cell Super-Resolution Imaging of Cellular Structures by Nanoinjection of Fluorescent Probes. *Nano Lett.* **2015,** *15*, 1374-1381.

36. Gu, Y.; Sun, W.; Wang, G.; Fang, N., Single Particle Orientation and Rotation Tracking Discloses Distinctive Rotational Dynamics of Drug Delivery Vectors on Live Cell Membranes. *J. Am. Chem. Soc.* **2011,** *133*, 5720-5723.

37. Simonson, P. D.; Rothenberg, E.; Selvin, P. R., Single-Molecule-Based Super-Resolution Images in the Presence of Multiple Fluorophores. *Nano Lett.* **2011,** *11*, 5090-5096.

38. Pryor, D. E.; O'Brate, A.; Bilcer, G.; Díaz, J. F.; Wang, Y.; Wang, Y.; Kabaki, M.; Jung, M. K.; Andreu, J. M.; Ghosh, A. K.; Giannakakou, P.; Hamel, E., The Microtubule Stabilizing Agent Laulimalide Does Not Bind in the Taxoid Site, Kills Cells Resistant to Paclitaxel and Epothilones, and May Not Require Its Epoxide Moiety for Activity. *Biochemistry* **2002,** *41*, 9109-9115.

39. Eckford, P. D. W.; Sharom, F. J., ABC Efflux Pump-Based Resistance to Chemotherapy Drugs. *Chem. Rev.* **2009,** *2009*, 2989-3011.

40. Yusuf, R. Z.; Duan, Z.; Lamendola, D. E.; Penson, R. T.; Seiden, M. V., Paclitaxel Resistance: Molecular Mechanisms and Pharmacologic Manipulation. *Curr. Cancer Drug Targets* **2003,** *3*, 1-19.

41. Spletstoser, J. T.; Turunen, B. J.; Desino, K.; Rice, A.; Datta, A.; Dutta, D.; Huff, J. K.; Himes, R. H.; Audus, K. L.; Seelig, A.; Georg, G. I., Single-site chemical modification at C10 of the baccatin III core of paclitaxel and Taxol C reduces P-glycoprotein interactions in bovine brain microvessel endothelial cells. *Bioorg. Med. Chem. Lett.* **2006,** *16*, 495-498.

42. Kuznetsova, L.; Sun, L.; Chen, J.; Zhao, X.; Seitz, J.; Das, M.; Li, Y.; Veith, J. M.; Pera, P.; Bernacki, R. J.; Xia, S.; Horwitz, S. B.; Ojima, I., Synthesis and biological evaluation of novel 3'-difluorovinyl taxoids. *J. Fluorine Chem.* **2012,** *143*, 177-188.

43. Amin, M. L., P-glycoprotein Inhibition for Optimal Drug Delivery. *Drug Target Insights* **2013,** *7*, 27-34.

44. Lee, J. S.; Paull, K.; Alvarez, M.; Hose, C.; Monks, A.; Grever, M.; Fojo, A. T.; Bates, S. E., Rhodamine efflux patterns predict P-glycoprotein substrates in the National Cancer Institute drug screen. *Mol. Pharmacol.* **1994,** *46*, 627-638.

45. Schwab, D.; Fischer, H.; Tabatabaei, A.; Poli, S.; Huwyler, J., Comparison of in Vitro P-Glycoprotein Screening Assays: Recommendations for Their Use in Drug Discovery. *J. Med. Chem.* **2003,** *46*, 1716-1725.

46. Jouan, E.; Le Vée, M.; Mayati, A.; Denizot, C.; Parmentier, Y.; Fardel, O., Evaluation of P-Glycoprotein Inhibitory Potential Using a Rhodamine 123 Accumulation Assay. *Pharmaceutics* **2016,** *8*, 12.

47. Patwardhan, G.; Gupta, V.; Huang, J.; Gu, X.; Liu, Y.-Y., Direct assessment of P-glycoprotein efflux to determine tumor response to chemotherapy. *Biochem. Pharmacol.* **2010,** *80*, 72-79.

48. Mason, C. W.; Lee, G. T.; Dong, Y.; Zhou, H.; He, L.; Weiner, C. P., Effect of Prostaglandin E(2) on Multidrug Resistance Transporters In Human Placental Cells. *Drug Metab. Dispos.* **2014,** *42*, 2077-2086.

49. Ma, W.; Feng, S.; Yao, X.; Yuan, Z.; Liu, L.; Xie, Y., Nobiletin enhances the efficacy of chemotherapeutic agents in ABCB1 overexpression cancer cells. *Sci. Rep.* **2015,** *5*, 18789.

50. Martin, C.; Walker, J.; Rothnie, A.; Callaghan, R., The expression of P-glycoprotein does influence the distribution of novel fluorescent compounds in solid tumour models. *Br. J. Cancer* **2003,** *89*, 1581-1589.

51. Gao, B.; Russell, A.; Beesley, J.; Chen, X. Q.; Healey, S.; Henderson, M.; Wong, M.; Emmanuel, C.; Galletta, L.; Johnatty, S. E.; Bowtell, D.; Haber, M.; Norris, M.;

Harnett, P.; Chenevix-Trench, G.; Balleine, R. L.; deFazio, A., Paclitaxel sensitivity in relation to ABCB1 expression, efflux and single nucleotide polymorphisms in ovarian cancer. *Sci. Rep.* **2014,** *4*, 4669.

52. Xiao, X.; Wu, J.; Trigili, C.; Chen, H.; Chu, J. W. K.; Zhao, Y.; Lu, P.; Sheng, L.; Li, Y.; Sharom, F. J.; Barasoain, I.; Diaz, J. F.; Fang, W.-s., Effects of C7 substitutions in a high affinity microtubule-binding taxane on antitumor activity and drug transport. *Bioorg. Med. Chem. Lett.* **2011,** *21*, 4852-4856.

53. Sun, W. C.; Gee, K. R.; Haugland, R. P., Synthesis of novel fluorinated coumarins: excellent UV-light excitable fluorescent dyes. *Bioorg. Med. Chem. Lett.* **1998,** *8*, 3107-10.

54. Oregon Green 488 dye. https://www.thermofisher.com/us/en/home/life-science/cell-analysis/fluorophores/oregon-green.html (accessed Nov. 1, 2016).

55. Rouzier, R.; Rajan, R.; Wagner, P.; Hess, K. R.; Gold, D. L.; Stec, J.; Ayers, M.; Ross, J. S.; Zhang, P.; Buchholz, T. A.; Kuerer, H.; Green, M.; Arun, B.; Hortobagyi, G. N.; Symmans, W. F.; Pusztai, L., Microtubule-associated protein tau: A marker of paclitaxel sensitivity in breast cancer. *Proc. Natl. Acad. Sci. USA* **2005,** *102*, 8315-8320.

56. Alushin, Gregory M.; Lander, Gabriel C.; Kellogg, Elizabeth H.; Zhang, R.; Baker, D.; Nogales, E., High-Resolution Microtubule Structures Reveal the Structural Transitions in Tubulin upon GTP Hydrolysis. *Cell* **2014,** *157*, 1117-1129.

57. Trott, O.; Olson, A. J., AutoDock Vina: improving the speed and accuracy of docking with a new scoring function, efficient optimization and multithreading. *J. Comp. Chem.* **2010,** *31*, 455-461.

58. Tsuruo, T.; Iida, H.; Tsukagoshi, S.; Sakurai, Y., Overcoming of Vincristine Resistance in P388 Leukemia in Vivo and in Vitro through Enhanced Cytotoxicity of Vincristine and Vinblastine by Verapamil. *Cancer Res.* **1981,** *41*, 1967-1972.

59. Jang, S. H.; Wientjes, M. G.; Au, J. L.-S., Kinetics of P-Glycoprotein-Mediated Efflux of Paclitaxel. *J. Pharmacol. Exp. Ther.* **2001,** *298*, 1236-1242.

60. van Brussel, J. P.; van Steenbrugge, G. J.; Romijn, J. C.; Schröder, F. H.; Mickisch, G. H. J., Chemosensitivity of prostate cancer cell lines and expression of multidrug resistance-related proteins. *Eur. J. Cancer* **1999,** *35*, 664-671.

61. Martel, J.; Payet, M. D.; Dupuis, G., The MDR1 (P-glycoprotein) and MRP (P-190) transporters do not play a major role in the intrinsic multiple drug resistance of Jurkat T lymphocytes. *Leuk. Res.* **1997,** *21*, 1077-1089.

62. Greenspan, P.; Mayer, E. P.; Fowler, S. D., Nile red: a selective fluorescent stain for intracellular lipid droplets. *J. Cell Biol.* **1985,** *100*, 965-973.

63. Lebedeva, I. V.; Pande, P.; Patton, W. F., Sensitive and Specific Fluorescent Probes for Functional Analysis of the Three Major Types of Mammalian ABC Transporters. *PLoS One* **2011,** *6*, e22429.

64. Crawford, L.; Putnam, D., Synthesis and Characterization of Macromolecular Rhodamine Tethers and Their Interactions with P-Glycoprotein. *Bioconjugate Chem.* **2014,** *25*, 1462-1469.

65. Shen, F.; Chu, S.; Bence, A. K.; Bailey, B.; Xue, X.; Erickson, P. A.; Montrose, M. H.; Beck, W. T.; Erickson, L. C., Quantitation of Doxorubicin Uptake, Efflux, and Modulation of Multidrug Resistance (MDR) in MDR Human Cancer Cells. *J. Pharmacol. Exp. Ther.* **2008,** *324*, 95-102.

66. Strouse, J. J.; Ivnitski-Steele, I.; Waller, A.; Young, S. M.; Perez, D.; Evangelisti, A. M.; Ursu, O.; Bologa, C. G.; Carter, M. B.; Salas, V. M.; Tegos, G.; Larson, R. S.; Oprea, T. I.; Edwards, B. S.; Sklar, L. A., Fluorescent substrates for flow cytometric evaluation of efflux inhibition in ABCB1, ABCC1, and ABCG2 transporters. *Anal. Biochem.* **2013,** *437*, 77-87.

67. Wang, Y.; Hao, D.; Stein, W. D.; Yang, L., A kinetic study of Rhodamine123 pumping by P-glycoprotein. *Biochim. Biophys. Acta (BBA) - Biomembranes* **2006,** *1758*, 1671-1676.

68. Forster, S.; Thumser, A. E.; Hood, S. R.; Plant, N., Characterization of Rhodamine-123 as a Tracer Dye for Use In In vitro Drug Transport Assays. *PLoS One* **2012,** *7*, e33253.

69. Holló, Z.; Homolya, L.; Davis, W.; Sarkadi, B., Calcein accumulation as a fluorometric functional assay of the multidrug transporter. *Biochim. Biophys. Acta (BBA) - Biomembranes* **1994,** *1191*, 384-388.

70. Gibson, J. D.; Khanal, B. P.; Zubarev, E. R., Paclitaxel-Functionalized Gold Nanoparticles. *J. Am. Chem. Soc.* **2007,** *129*, 11653-11661.

Chapter 4

Studies of the Stability of Disulfides Using Förster Resonance Energy Transfer

4.1 Introduction

Targeted drug delivery is an area of study with great importance for cancer therapeutics both for limiting off-target effects (toxicity), as well as enhancing accumulation of the therapeutic at the target site. These types of drug delivery systems range from small molecules to polymeric nanoparticles, and numerous successful candidates have progressed to the clinic.[1-4] Many targeted delivery systems utilize a specific mechanism of cellular internalization, receptor mediated endocytosis (RME), to efficiently transport the drug into the cells of interest. Nature utilizes RME for cellular entry of large molecular complexes that cannot passively diffuse or be pumped across the cellular membrane.[5] As an example of this process, the mechanism of RME of low-density lipoprotein (LDL) is shown in Figure 4.1. In this mechanism, LDL first binds to the LDL receptor on cell surfaces. Clathrin-coated pits on the plasma membrane containing receptor-ligand complexes pinch off to form vesicles in the cytosol. These vesicles fuse with acidic sorting endosomes. The decrease in pH facilitates the dissociation of receptors from ligands, and the receptor is recycled back to the cell membrane via the endocytic-recycling compartment. Sorting endosomes containing free LDL mature into late endosomes that fuse with lysosomes. Hydrolytic lysosomal enzymes degrade LDL for release of nutrients into the cytosol.[6]

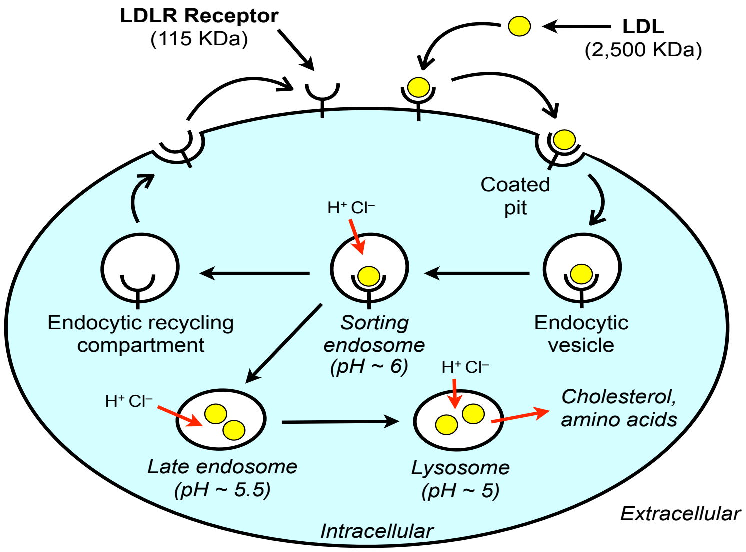

Figure 4.1. Receptor-mediated endocytosis of low-density lipoprotein (LDL).

Previous work in the Peterson group has focused on using cholesterol mimics as models for the development of targeted drug delivery systems.[6-8] These cholesterol mimics can bind plasma membranes, accumulate in early endosomes, and undergo RME, similar to the trafficking of many natural cell surface receptors.[9-12] By taking advantage of the trafficking of the cholesterol mimics, fluorescent cargo has been delivered to the endosomes of numerous cell types.[13] These cholesterol mimics have been shown to recycle between early endosomes and the plasma membrane, and they generally do not traffic to lysosomes for degradation.[6] However, in most cases, drugs must be efficiently delivered into the cytosol to reach the target site and manifest therapeutic effects. To combat this problem, the Peterson group developed a peptide linked to a mimic of cholesterol that selectively disrupts early/recycling endosomes (Figure 4.2, panel B).[8] This peptide is a derivative of a previously published[14] membrane-lytic dodecapeptide termed PC-4. Early studies by our group showed that cholesterylamine-linked PC-4 can disrupt early endosomes and release disulfide-linked fluorescent cargo into the cytoplasm of the cell. This cargo is derived from the polar fluorophore fluorescein, which upon release, is trapped in the cytosol of cells (Figure 4.2, panel A). The proposed mechanism for the release was cleavage of the disulfide by reduced glutathione (GSH), which would enter the endosome following disruption of endosomal membranes.[8]

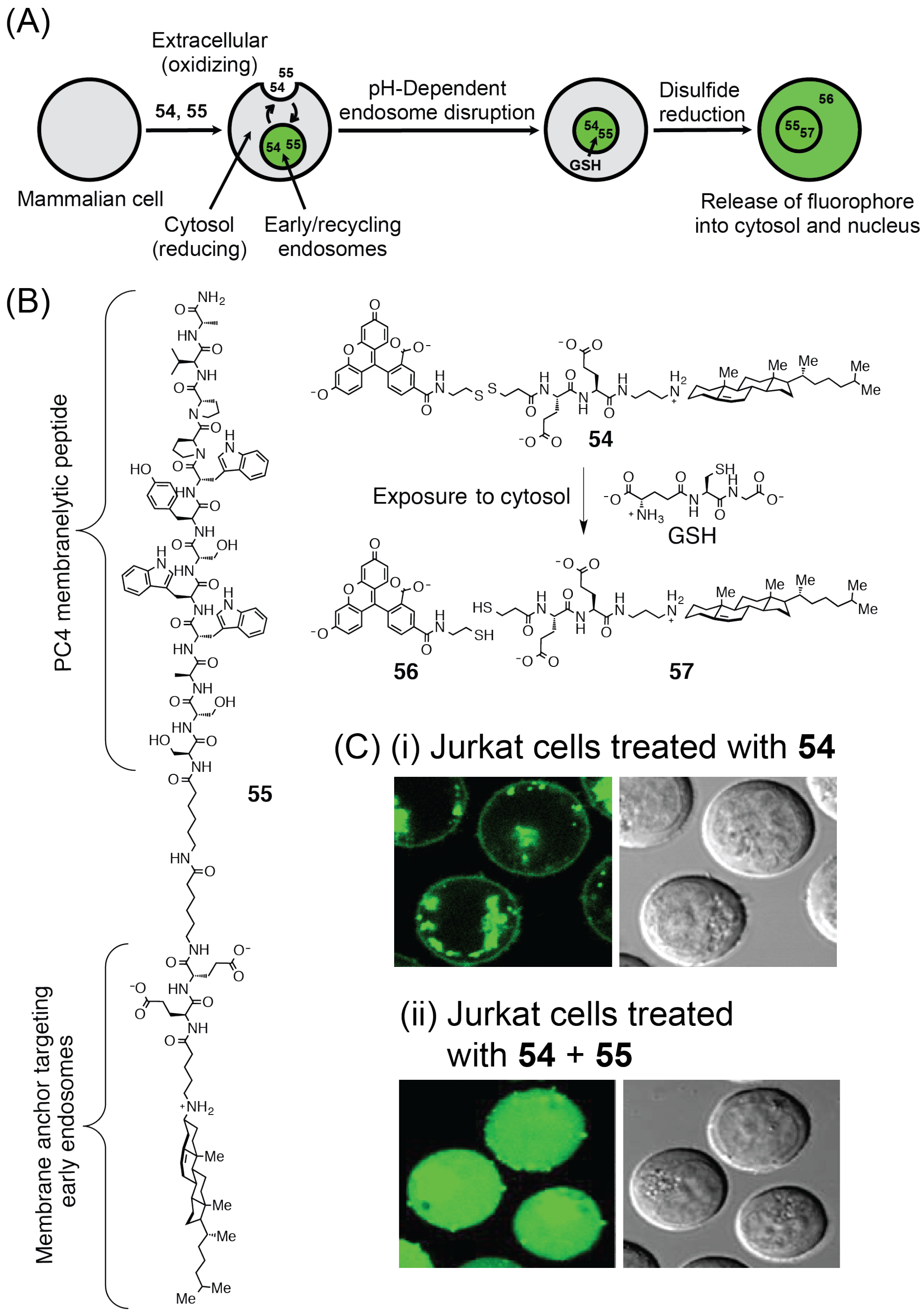

Figure 4.2. A: Proposed mechanism of release of fluorescent probe **54** upon disruption of early endosomes. B: Structure of the cholesterylamine-PC4 endosome disruptor (**55**), a fluorescent disulfide *N*-alkyl-3β-cholesterylamine (**54**) and the products of cleavage (**56**, **57**). C: Confocal fluorescence and DIC micrographs[8] of Jurkat lymphocytes treated for 12 h with (i) **54** (2.5 μM) and (ii) **54** (2.5 μM) + **55** (2 μM).

Following our previously published[8] studies of endosome disruption, the Peterson group has worked to improve the efficacy and reduce the toxicity of endosome disruptive peptides, as well as examine their mechanism of action. Additionally, other targeted delivery systems have been explored utilizing improved endosome disruptive peptides. During his dissertation research, Dr. David Hymel characterized the delivery of endosome disruptors, fluorescent cargo, and toxins conjugated to antibodies, and this research continues to be actively pursued in the Peterson group.

Antibody-drug conjugates (ADCs) are widely used in cancer chemotherapy, with over 55 currently in clinical trials.[15] ADCs achieve antigen-specific delivery of potent cytotoxic agents to tumor cells that overexpress specific cell surface receptors.[16-18] They have a complex structure that generally comprises three main parts: a small molecule drug (payload), an antibody, and a cleavable or non-cleavable linker.[15] ADCs typically employ cytotoxic agents that are extremely potent and could otherwise not be used in an untargeted manner. The potency is critical, as only 1-2% of the administered ADC dose will reach a tumor cell, and therefore the intracellular levels of the drug will be low.[19] The ideal antibody targets an antigen that is highly expressed across the tumor, with limited shedding and normal tissue expression, and is internalized via RME.[20] ADCs typically incorporate either non-cleavable linkers such as thioethers that require proteolytic degradation of the antibody, or cleavable linkers such as dipeptides, disulfides, or acid-labile hydrazones.[15, 21] In recent years, second generation ADCs have emerged which focus on optimizing the stability of the linker in the bloodstream to ensure efficient and selective delivery of the cytotoxin to the target cell.[22]

The redox potential of endosomes has been previously reported to vary from oxidizing (–240 mV, compared with a much more reducing value of –318 mV for mitochondria)[23] to reducing,[24, 25] but how these values relate to the release profiles of structurally diverse disulfide conjugates that traffic through endosomes in a soluble or membrane-bound manner remains unclear. Endocytic disulfide cleavage could occur via enzymatic reduction (e.g. via soluble and membrane-bound glutathione-S-transferases[26]), cell surface sulfhydryls,[25, 27] and cleavage by small redox molecules (e.g. glutathione, cysteine). One extensively studied targeted delivery system involves folate conjugates that bind folate receptors, and therapeutics using this system have advanced to clinical trials for the treatment of cancer. Many of the conjugates developed, including EC145 (Figure 4.3, panel A), a current clinical candidate, incorporate a disulfide bond for release of a cytotoxic drug following internalization to target cancer cells via RME.[28] Studying an analogous disulfide-linked system, Low and coworkers at Purdue Univ. developed a FRET-based assay using folate-linked BODIPY-FL and tetraethyl rhodamine (Figure 4.3, panel B) and found that after endocytosis, reduction of a disulfide occurred with a half time of 6 h in cell culture[24] and 4 h in mouse kidney tissue,[29] providing evidence that the endosomes the folate receptor traffics through are reducing. However, in contradistinction, Austin *et. al.* at Genentech found that the disulfide bond linked to an anti-HER2 antibody was stable in breast carcinoma cells, suggesting that the endosomes the antibody traffics through are oxidizing.[23]

(A)

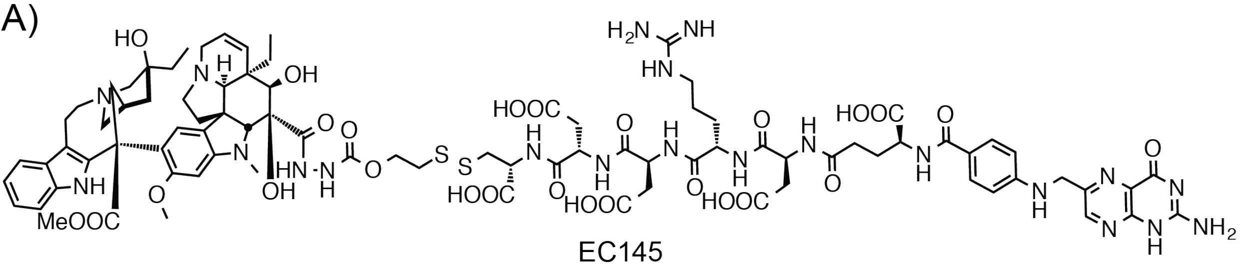

EC145

(B)

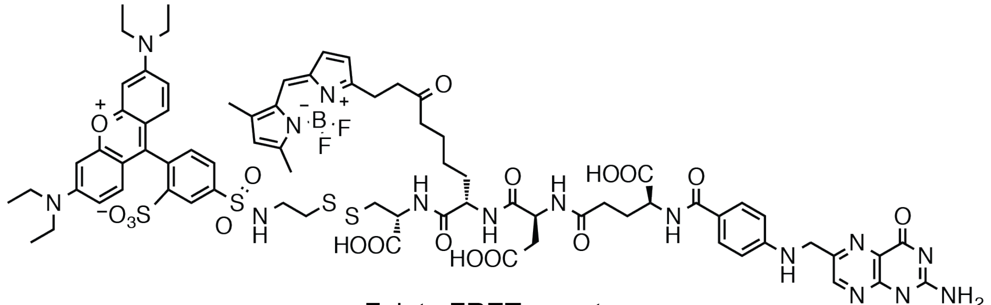

Folate FRET reporter

Figure 4.3. Structures of the folate receptor-targeted disulfide-containing agents vintafolide (EC145) and a FRET reporter.[24]

To gain a greater understanding of the stability of disulfides in endocytic compartments accessed by cholesterol mimics and targeting antibodies, we are investigating the cellular properties of disulfide-linked molecular probes comprising the novel FRET pair Pacific Blue and Pennsylvania Green. We initially reasoned that the low intrinsic affinity of these anionic fluorophores for cellular membranes might be well suited for non-perturbative studies of processes involving dynamic membrane trafficking in living cells. However, we later learned that the high hydrophobicity of Pennsylvania Green has disadvantages for studies of these types of probes, and additional FRET probes derived from the spectrally similar Oregon Green were investigated. In this Chapter, we report the synthesis of molecular probes derived from Pacific Blue, Pennsylvania Green, and Oregon Green, the efficiency of FRET between these anionic fluorophores, and their *in vitro* and cellular properties related to disulfide bond cleavage.

4.2. Characterization of Pacific Blue and Pennsylvania Green as a FRET pair

In addition to using Pacific Blue (PB) as a FRET acceptor for tryptophan (Chapter 2), we sought to investigate PB as a potential FRET donor to create new tools for chemical biology. As a complementary partner, Pennsylvania Green was of interest as a potential FRET acceptor. This hydrophobic derivative of fluorescein exhibits high photostability and is insensitive to changes in pH in a wide range of biological microenvironments, similar to Pacific Blue.[30, 31] Pennsylvania Green is also advantageous because the Peterson group has developed an efficient multigram synthesis of 4-Carboxy-Pennsylvania Green (PG, **58**).[32] The extent of spectral overlap J(λ), measured as the area under the overlapping sections of the emission spectra of the donor (PB) and the absorbance spectra of the acceptor (PG), was determined. As highlighted in grey (Figure 4.4, J(λ)), the substantial spectral overlap indicates these two fluorophores could be a complementary FRET pair. The calculated Förster distance for this FRET pair is 47.4 Å, similar to other previously reported blue-green FRET pairs.[33, 34]

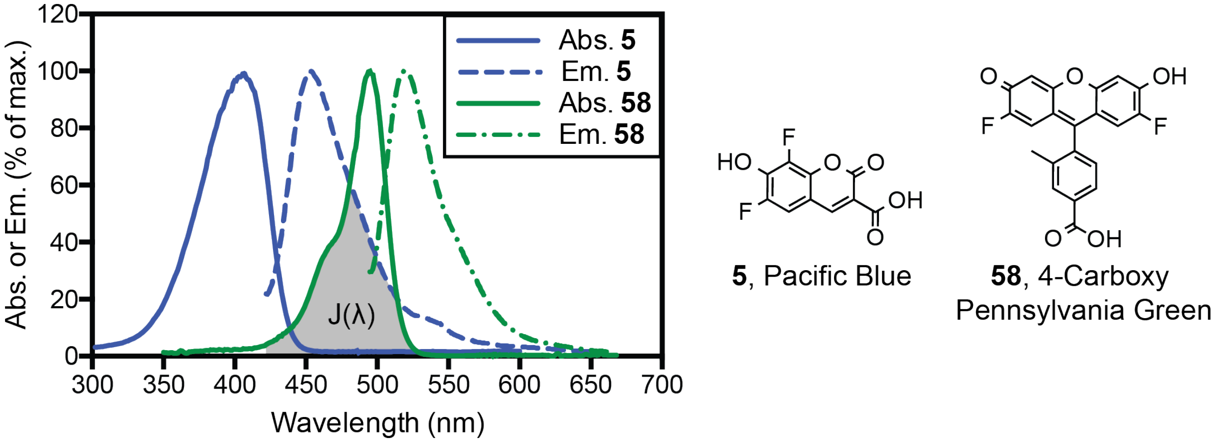

5, Pacific Blue

58, 4-Carboxy Pennsylvania Green

Figure 4.4. Absorbance (Abs., solid lines) and emission (Em., dotted lines) spectra of PB (**5**, blue lines) and PG (**58**, green lines) in PBS (pH 7.4). The spectral overlap integral (J(λ)) critical for FRET is shaded grey.

To characterize the FRET efficiency of the PB-PG FRET pair, we first synthesized a simple FRET probe (**59**, Figure 4.5) that links the two fluorophores through a disulfide bond that can be cleaved by reduction. As illustrated in Figure 4.5 (panel A), before the addition of a reductant, the disulfide bond should be intact, and the two fluorophores in close proximity to one another. Consequently, when excited at 400 nm, energy transfer from PB to PG should occur, and fluorescent photons should be emitted at > 520 nm. However, after the addition of a reductant such as dithiothreitol (DTT) or glutathione (GSH), the disulfide bond should be cleaved. Following cleavage, the two fluorophores would diffuse away from one another in solution, preventing energy transfer between the fluorophores. When the disulfide is reduced, excitation at 400 nm would then reveal only fluorescence from PB, emitting maximally at ~460 nm.

To calculate the FRET efficiency, a large excess of DTT (25 mM) was added to the fluorescent probe, followed by excitation of PB at 400 nm to trigger FRET (measured at 530 nm). The emission from PB (measured at 455 nm) and FRET (measured at 530 nm) was followed over time. As the cleavage reaction progressed, the PB signal increased, while the FRET signal decreased (Figure 4.5, panel D). Curve fitting was used to calculate a half-life of 14.3 ± 0.2 min in PBS (1% triton-X 100, Figure 4.5, panel E). The FRET efficiency, calculated as $E = 1 - I_{\mathrm{da}}/I_{\mathrm{d}}$,[33] where I_{da} and I_{d} are the intensity of PB (λ_{max} = 455 nm) in the presence and absence of the acceptor, respectively, equals 0.97, indicating that for this system, when PB and PG are in close proximity, 97% of the PB signal is suppressed through energy transfer to PG. To ensure the changes in fluorescence emission was due to separation of the fluorophore via disulfide cleavage, and not from changes in the environment with the addition of DTT, an amide control (**60**, Figure 4.5, panel B) was synthesized. This derivative does not change the distance between the fluorophores appreciably, but does incorporate a non-labile amide bond in the place of the disulfide bond of **60**. The amide FRET probe **60** was subjected to the same reductive conditions as **59**, and no changes were observed upon addition of DTT, suggesting that the significant changes in the fluorescence spectra after the addition of DTT are due to the cleavage of the disulfide bond and subsequent increase in the distance between the two fluorophores. Consequently, PB and PG were shown to be an efficient new FRET pair.

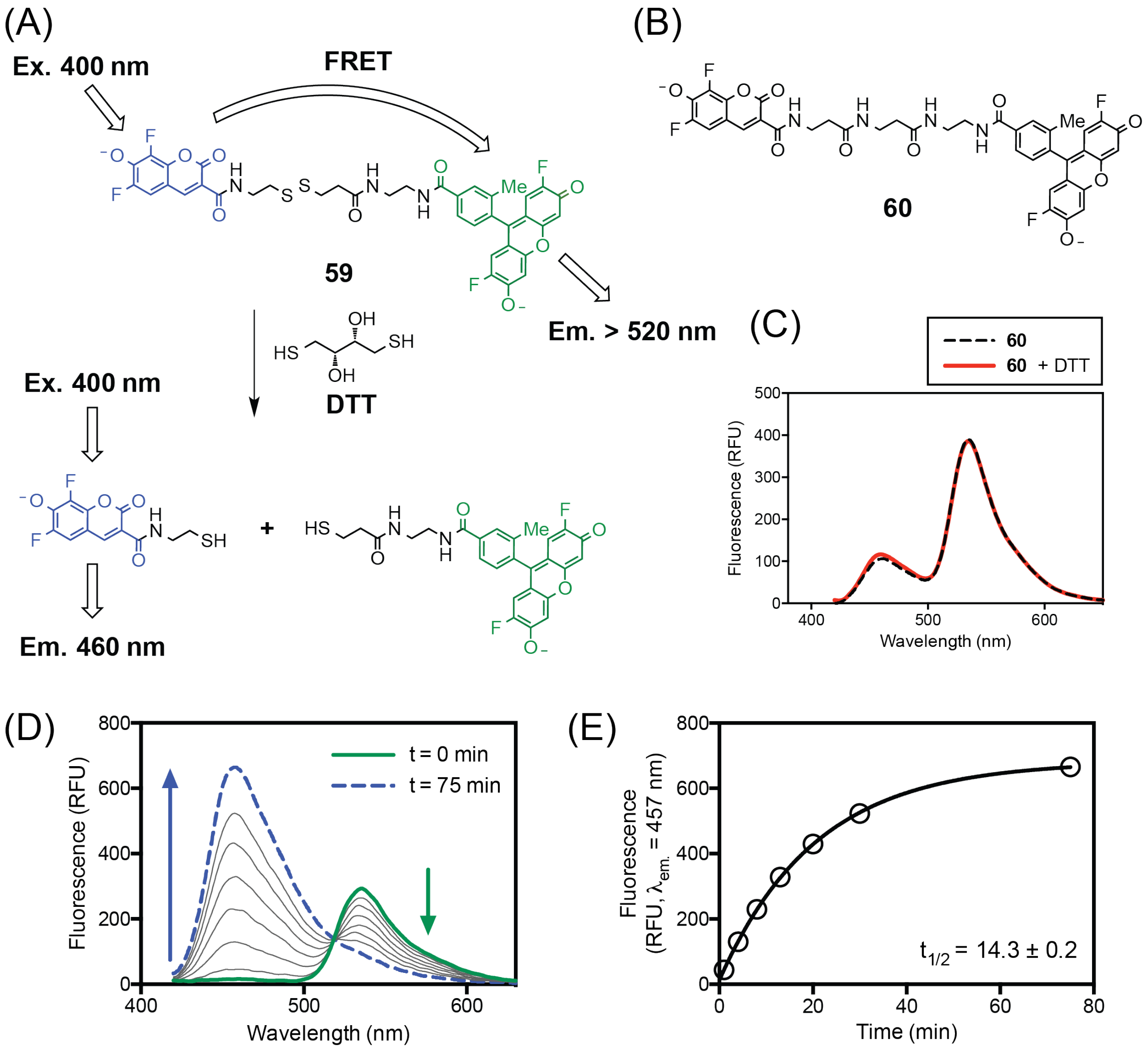

Figure 4.5. A: Structures of the Pacific Blue-Pennsylvania Green FRET probe **59** and products of cleavage by DTT. B: Structure of the amide control **60**. C: Emission spectra of **60** (25 nM) alone (dashed black line) and with the addition of DTT (25 mM) for 75 min (solid red line). Panels D and E show the spectroscopic properties of **59** over a 75 minute period following the addition of DTT (25 mM) in PBS (1% triton-X 100, pH=7.4). D: Emission spectra (λ_{ex} = 400 nm) over a 75 minute period. Spectra was collected at time = 0, 1, 4, 8, 13, 20, 30, and 75 min. The PB emission signal (λ_{max} = 455 nm) grew in intensity over time, while the PG emission signal (λ_{max} = 530 nm) decreased as the disulfide bond was cleaved over time. E: Cleavage kinetics of the increase in PB emission signal (λ_{max} = 455 nm) over time after the addition of DTT. The half-time of disulfide cleavage was determined using GraphPad Prism software.

4.3. Stability of the disulfide of a cholesteryl carbamate delivery system *in vitro*

We hypothesized that the efficient PB-PG FRET pair could prove useful in studying the stability of disulfide bonds trafficked to endosomes via cholesterol mimics. Based on recent studies in the Peterson group on the use of cholesteryl carbamates to trigger cellular uptake of endosome disruptors and cargo, we chose this membrane anchor as a simple cellular targeting agent. Additionally, some cholesteryl carbamates have been shown to traffic through endocytic pathways, and require binding to HDL or LDL for internalization.[35] Cholesteryl carbamate conjugates have been used successfully in siRNA delivery,[35-37] DNA transfection, and other cellular targeting applications.[38] In our laboratory, Hymel *et*. *al*. discovered that the incorporation of two anionic glutamic acid residues near a cholesteryl carbamate can improve the normally slow lipoprotein-mediated cellular uptake of these compounds and increased the overall efficacy of uptake of cholesteryl carbamates compared to other mimics of cholesterol that were studied.[13] To probe the stability of disulfides for use as delivery systems, we designed FRET probes that link PB and PG through a disulfide-containing amino acid.

Building on other published studies,[39] we hypothesized that a bulky group near the disulfide bond might hinder its cleavage. Additionally, an anionic group might repulse negatively charged reducing agents such as glutathione. To test this hypothesis, we designed two cholesteryl linked-FRET probes, **61** and **62** (Figure 4.6). Compared to **61**, an extra βAla group (Figure 4.6, panel A, colored red) between the disulfide bond and Lysine-PG was added to **62**, lengthening the distance between the cleavage site and the large anionic fluorophore. Using an optimized cholesteryl carbamate anchor,[13] we synthesized the two disulfide-linked FRET probes utilizing solid phase synthesis, as shown in Figure 4.12.

To study the difference in disulfide bond stability, DTT was added to the fluorescent probes, followed by excitation of PB at 400 nm to trigger FRET. The fluorescence of PB (measured at 460 nm) was followed over time. As the cleavage reaction progressed, the PB signal increased, while the FRET signal (measured at 530 nm) decreased (Figure 4.6, panel B). Curve fitting was used to calculate a half life of 74 ± 5 min for **61** and 42 ± 2 min for **62** (Figure 4.6, panel C). This study provides evidence that a large hydrophobic group (Pennsylvania Green) near the disulfide bond can slow the cleavage reaction in this cholesteryl carbamate delivery system and should enable the design of cargo that can be more readily released upon disruption of endosomes. Unfortunately, in related studies, Pacific Blue did not show a favorable release profile by confocal microscopy upon disulfide cleavage and endosome disruption, so these probes were not pursued for further study in cellular systems. As an alternative, the more polar fluorophore Oregon Green was used as a releasable fluorophore for cellular assays because it is much more similar in polarity to 5-carboxyfluorescein, which we previously demonstrated as a cargo that efficiently escapes from endosomes upon disruption[8] as shown in Figure 4.2.

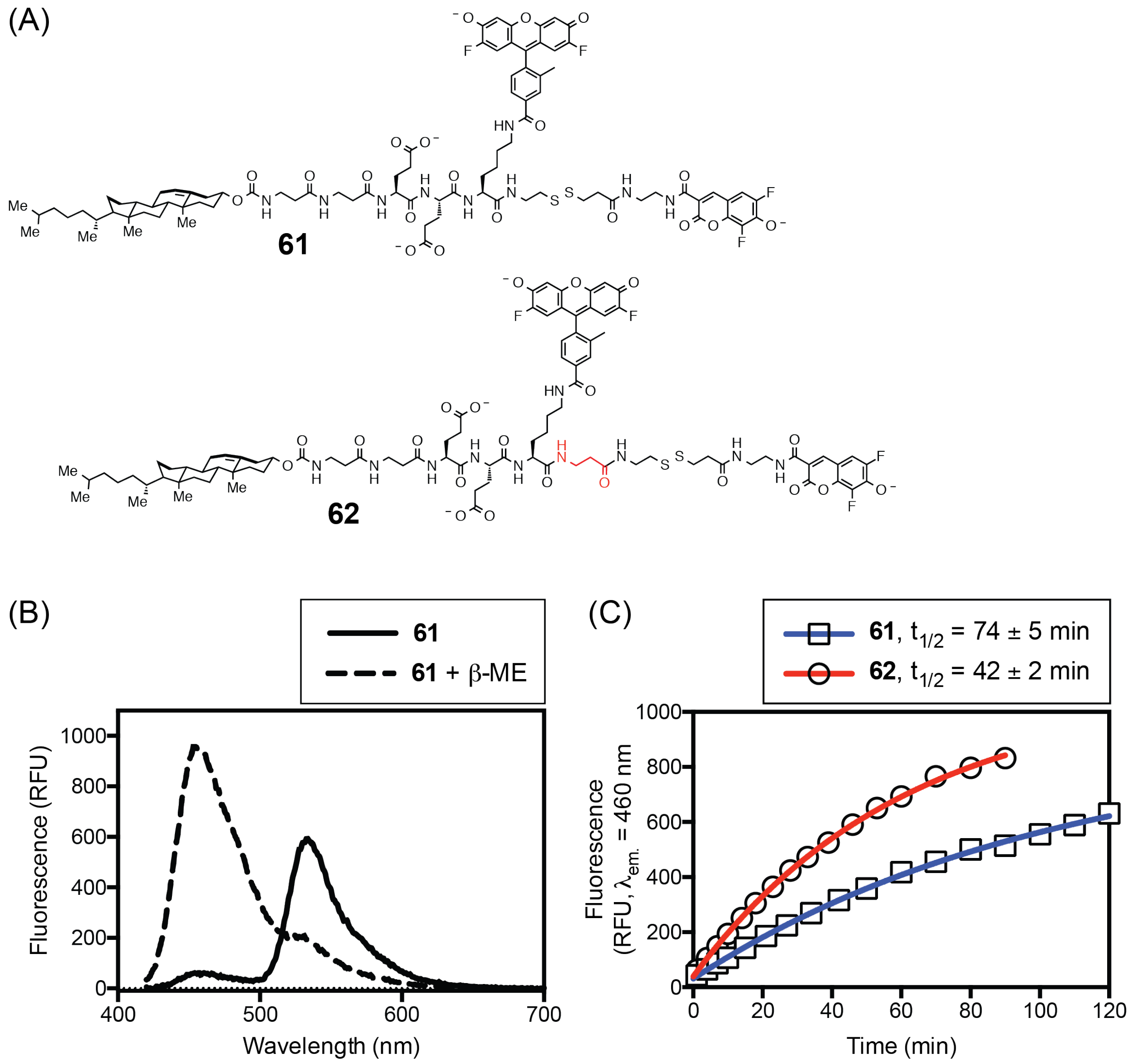

Figure 4.6. A: Structures of PG-PB cholesteryl carbamate FRET probes **61** and **62**. B: Emission spectra of **61** (50 nM) alone (solid line) and with the addition of β-mercaptoethanol (300 mM, β-ME) for 3 h (dashed line). C: Cleavage kinetics of the increase in PB emission signal (λ_{max} = 460 nm) over time after the addition of DTT (100 mM) to **61** or **62** (20 nM). The half life and rate constant were determined using GraphPad Prism software. All experiments were run in PBS pH 7.4 containing 0.5% triton X-100.

4.4. Examination of the stability of disulfides linked to cholesteryl carbamates in living Jurkat cells

To study a related but more polar delivery system in living Jurkat cells, a new FRET pair was employed: Pacific Blue-Oregon Green. Oregon Green (OG) is a fluorinated derivative of fluorescein with a relatively low pKa of 4.7, making it useful for biological studies at a wide range of pH values, including acidic endosomes.[40] We reasoned that its higher polarity compared to Pennsylvania Green might prevent it from inserting into membranes, which could provide better properties for cellular assays of disulfide cleavage. Moreover, based on the spectral properties of Flutax-2 described in Chapter 3, a high degree of spectral overlap is observed between the absorbance of OG and the emission of PB, indicating they could also be a complementary FRET pair (Figure 3.4). To study this new FRET system, we synthesized two PB-OG FRET probes (**63** and **64**, Figure 4.7, panel A) utilizing solid phase synthesis, as shown in Figure 4.14. As described in Section 4.2, the FRET efficiency and cleavage kinetics of the disulfide FRET probe **63** were calculated by tracking the PB signal (measured at 460 nm) over time after addition of DTT (10 mM). Curve fitting was used to calculate a half life of 20 ± 1 min in PBS pH 7.4 with 0.5% triton X-100 and 1% DMSO (Figure 4.7, panel C). The FRET efficiency, calculated as $E = 1 - I_{da}/I_{d}$,[33] where I_{da} and I_{d} are the intensity of PB (λ_{max} = 460 nm) in the presence and absence of the acceptor, respectively, equals 0.89 for **63**. Consequently, Pacific Blue and Oregon Green are a highly efficient FRET pair.

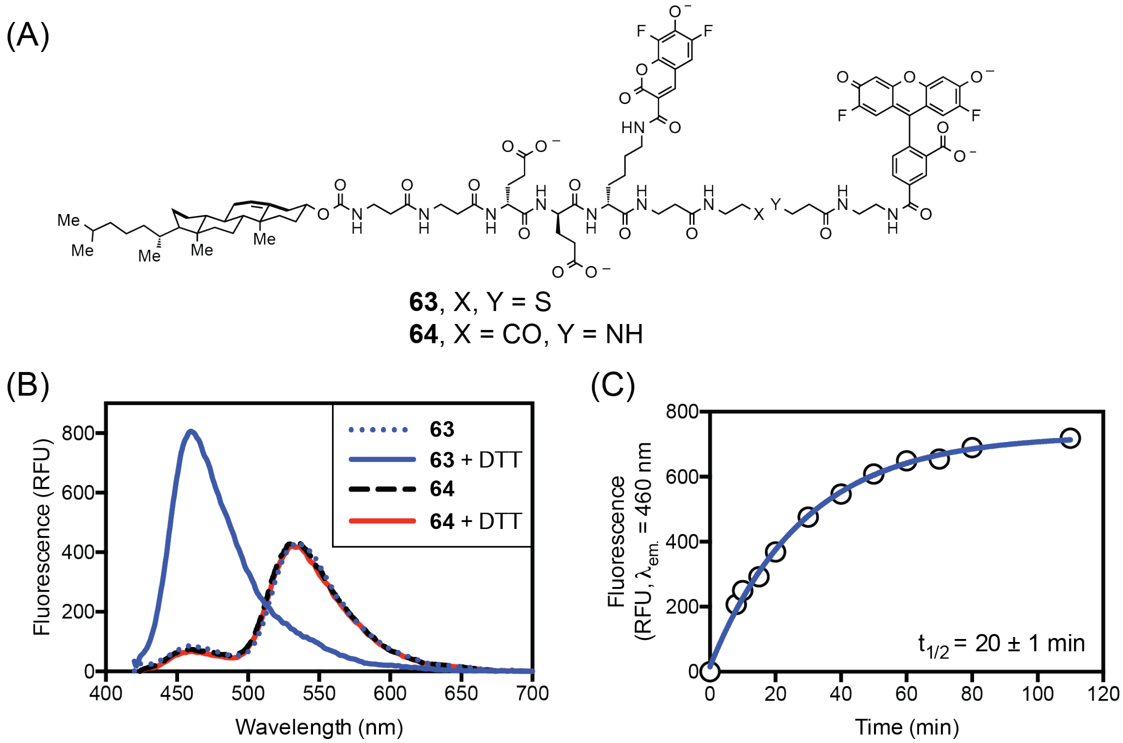

Figure 4.7. A: Structures of PB-OG cholesteryl carbamate FRET probes **63** and **64**. B: Emission spectra of **63** and **64** (50 nM) alone (**63**, blue dotted line; **64**, black dashed line) and with the addition of DTT (10 mM) for 2 h (**63**, blue solid line; **64**, red solid line). C: Kinetics of the increase in PB emission signal (λ_{max} = 460 nm) over time after the addition of DTT (10 mM) to **63** (50 nM). The half-time for cleavage of the disulfide was calculated using GraphPad Prism software. All experiments were run in PBS pH 7.4 containing 0.5% triton X-100 and 1% DMSO.

To test the cellular uptake and disulfide cleavage kinetics in living cells, confocal laser scanning microscopy and flow cytometry were used to analyze subcellular distribution and fluorescence intensity. For the cellular studies, compounds **63** and **64** were synthesized using unnatural D-amino acids to limit potential changes in fluorescence emission that might arise from proteolytic cleavage after endocytosis.[41] Jurkat lymphocytes were treated with compounds **63** and **64** at 10 μM, and the fluorescence intensities of three channels (flow cytometry- Blue: Ex. 405 nm, Em. 448/50 nm; FRET: Ex. 405 nm, Em. 525/30 nm; Green: Ex. 488 nm, Em. 525/30 nm; confocal microscopy- Blue: Ex. 405 nm, Em. 425-475 nm; FRET: Ex. 405 nm, Em. 520-

600 nm; Green: Ex. 488 nm, Em. 500-600 nm) were tracked over time. In comparison to the amide control **64** (Figure 4.8, panel C), cells stained with **63** (Figure 4.8, panel B) showed significant increases in the blue channel and decreases in the FRET channel after a 28 h incubation. This suggested that the amide bond of **64** was non-labile over this time period and the energy transfer from Pacific Blue to Oregon Green occurred efficiently at each time point. For the amide probe **64**, the FRET ratio, calculated as the intensities of Blue/FRET and detected by flow cytometry, did not increase. Conversely, over a time period of 28 h, the FRET ratio of cells treated with **63** increased significantly (Figure 4.8, panel D). Curve fitting was used to calculate a half-life of 4 ± 1 h. From these experiments, we were able to determine that the disulfide bond of **63** is fairly reactive during the process of endocytosis even without the addition of an endosome disruptive peptide. We conclude that the Pacific Blue-Oregon Green FRET pair is excellent for cellular studies by confocal microscopy and flow cytometry. Future studies will involve the addition of an endosome disruptive peptide to investigate the effect it would have on disulfide cleavage kinetics in living cells. Additional studies will involve the synthesis and biological evaluation of cholesteryl carbamate FRET probes that include the PB-OG FRET pair and differing linkers near the disulfide bond to determine if changes found *in vitro* track changes in disulfide bond cleavage rates realized in living cells. These studies should assist in enhancing the properties of related delivery systems currently under development in the Peterson group.

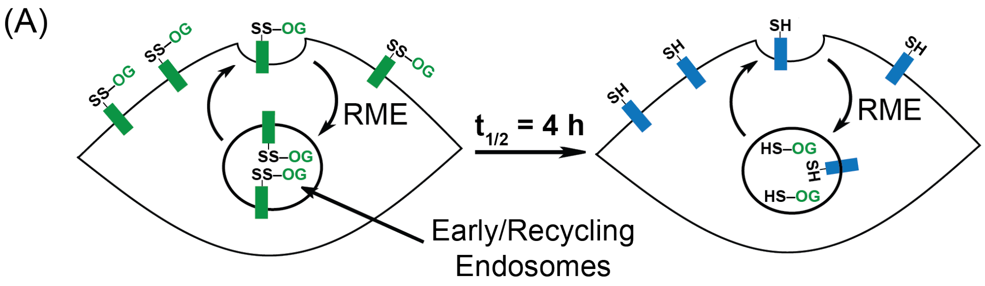

(B) Jurkat cells treated with **63** for 28 h

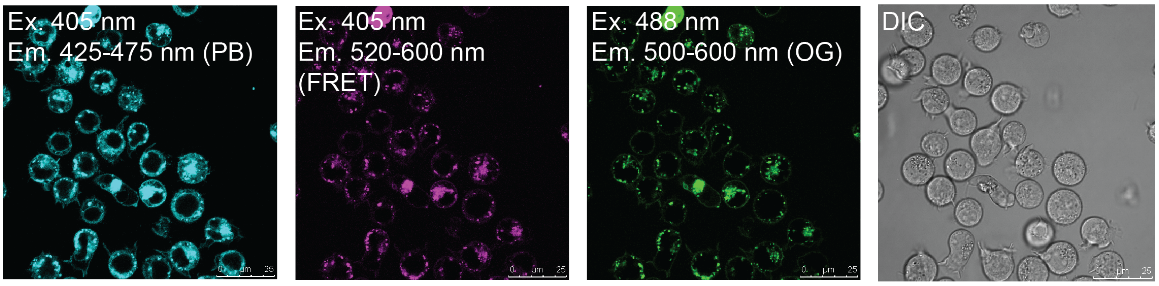

(C) Jurkat cells treated with **64** for 28 h

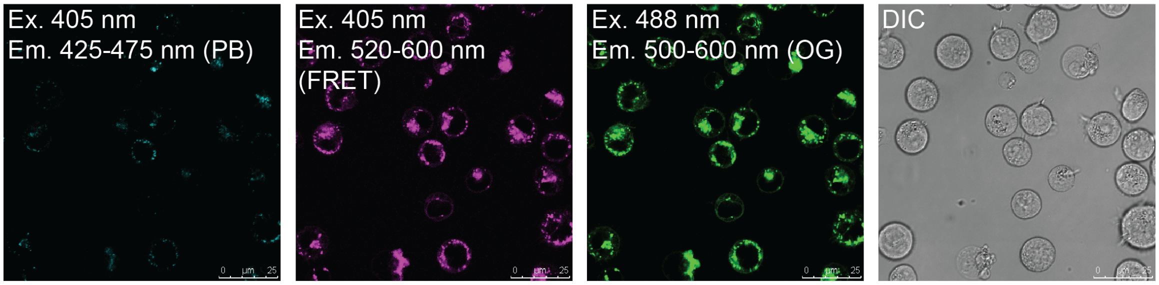

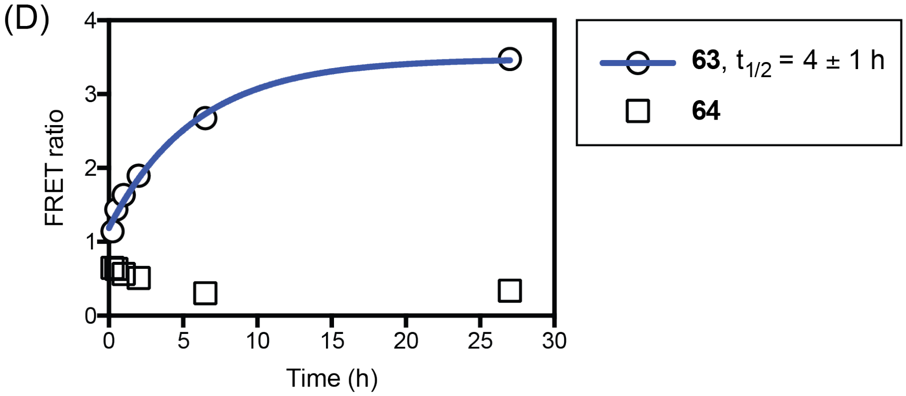

Figure 4.8. Measurement of the stability of the disulfide of **63** in Jurkat cells. A: Schematic representation of disulfide cleavage on cell surface and in endosomal compartments over time. B and C: Confocal laser scanning and DIC micrographs of living Jurkat cells treated with **63** (10 µM, panel B) or **64** (10 µM, panel C) for 28 h. At 28 h, treatment with **63** shows significantly less fluorescence in the FRET channel (Ex. 405 nm, Em. 515-600 nm, 2nd column, colored purple) in comparison to the PB channel (Ex. 405 nm, Em. 425-475 nm, 2nd column, colored cyan). Conversely, at 28 h, treatment with **64**, which has a stable amide bond, shows little fluorescence in the PB channel, and significant fluorescence in the FRET channel, indicating the molecule is still intact.

D: Kinetics of cleavage calculated based on the increase in the FRET ratio over time after addition of **63** (10 μM) to living Jurkat cells, as measured by flow cytometry. The half-life was determined using GraphPad Prism software. FRET ratio = PB (Ex. 405 nm, 450 emission channel) / FRET (Ex. 405 nm, 530 emission channel).

4.5. Studies of the stability of disulfides conjugated to antibodies

The Peterson group is investigating the release of antibody-conjugated cytotoxins upon addition of endosome disruptive peptides. Similar to our studies of cholesteryl carbamates, we wished to determine the release profile of disulfide-linked antibody conjugates in the presence and absence of endosome disrupting peptides. To accomplish this goal, we worked with Dr. Chamani Perera of the KU Molecular Probes Core to prepare the Pacific Blue-Pennsylvania Green FRET pair molecules **65**–**69** (Figure 4.9) using solid phase synthesis and solution phase amide bond-coupling reactions as shown in Figure 4.18. These compounds include an NHS ester that is designed to react with lysine residues of antibodies.

For these studies, we used Herceptin (trastuzamab, Genentech), an FDA-approved therapy that is used clinically to treat breast cancer patients.[42] Herceptin is a humanized IgG that targets the human epidermal growth factor receptor 2 (HER2). Kelsey Knewtson, a graduate student in the Peterson group, conjugated compounds **65**–**69** to Herceptin using a standard protein labeling protocol to produce **70**–**74** (Figure 4.9), and conducted the bioassays described below.

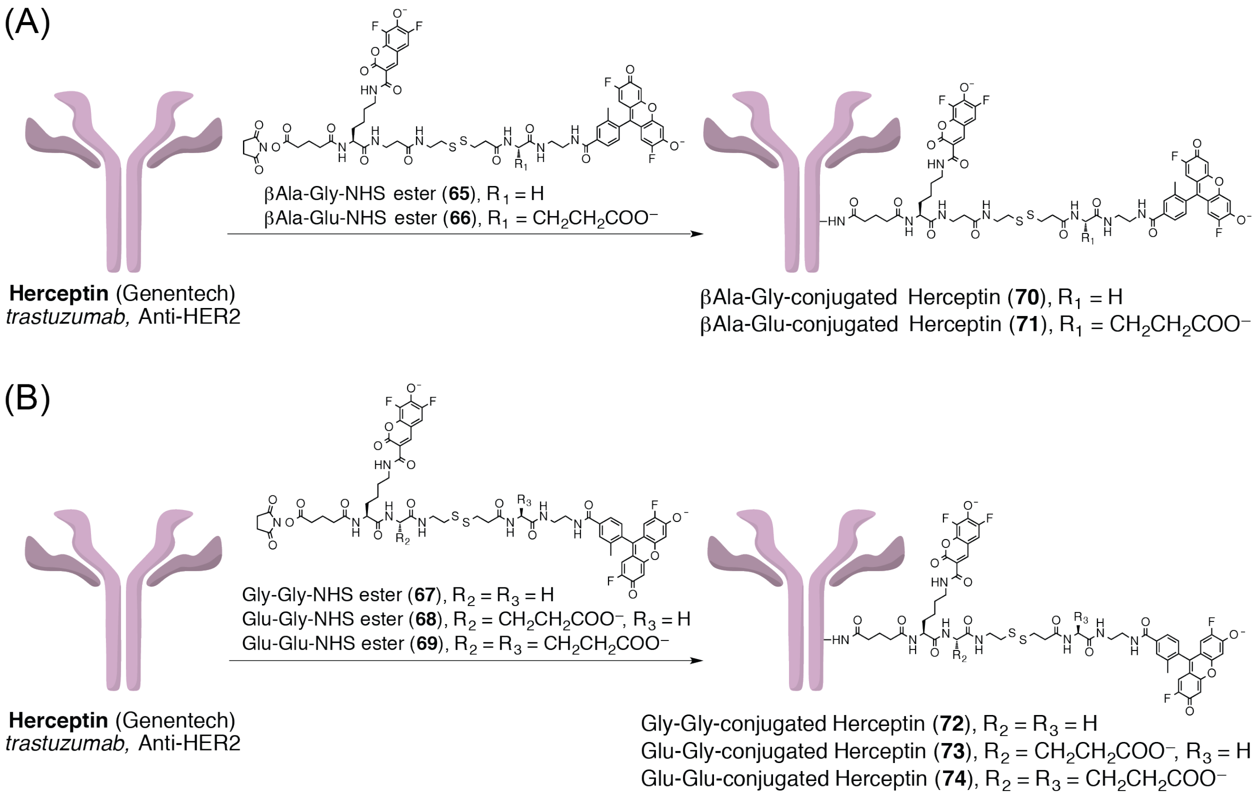

Figure 4.9. Structures of the FRET-NHS esters (**65**–**69**) and the conjugates of the anti-HER2 antibody Herceptin (**70**–**74**).

Similar to the cholesteryl carbamate FRET probes, we first evaluated the release profile *in vitro* of compounds **70** and **71**. In the first set of experiments, we investigated the effect of the anionic glutamic residue on the right hand side of the disulfide bond. We hypothesized that the anionic group could repulse negatively charged reducing agents such as glutathione (GSH) and may block disulfide cleavage through steric and electronic effects. In comparison to **71**, the anionic glutamic acid residue was replaced with a glycine residue in **70.** To study the difference in stability of the disulfide bond, excess GSH was added to the fluorescent antibodies, followed by excitation of PB at 400 nm to trigger FRET. The fluorescence of PB (measured at 455 nm) was followed over time. As the cleavage reaction progressed, the PB signal increased (Figure 4.10, panel A). Curve fitting was used to calculate a half life of 47 ± 1 min for **70** and 84 ± 1 min for **71**, consistent with the idea that the proximal glutamate can retard approach by reducing agent.

Similarly, we studied the release profile of conjugates **72**–**75** that also had increasing number of glutamic acid residues surrounding the disulfide linkage. Again, we tracked increases in the fluorescence of PB (measured at 455 nm) over a 3 h period (Figure 4.10, panel B). We found a ~2-fold increase in stability with each additional glutamic acid. This study provides evidence that a glutamic acid near the disulfide bond has a significant effect on the cleavage reaction of FRET probes conjugated to an antibody. These results are consistent with previous studies[39] of the effect of negatively charged substituents on cleavage of simple disulfides.

Finally, we evaluated the release profile of conjugate **70** in living SkBr3 cells, as this conjugate has the fastest *in vitro* cleavage rate. SkBr3 cells, which endogenously overexpress HER2 on the cell surface, were treated with **70** (5 μM). By confocal laser scanning microscopy (Blue: Ex. 405 nm, Em. 415-500 nm; Green: Ex. 488 nm, Em. 500-600 nm), we were able to observe time-dependent increases in the Blue / Green ratio, indicating cleavage of the disulfide bond. The maximum Blue / Green ratio that we could obtain in this cellular system was ~3, as determined by SkBr3 cells co-treated with DTT and **70** (data not shown). This indicates that at 27 h (Figure 4.10, panel C), the cleavage could only be estimated to be ~ 50% complete, and consequently the half-life could not be accurately determined, but it is likely to be > 20 h. Future studies include evaluation of conjugates **71**–**74** to determine if there are correlations between the *in vitro* and cellular release profiles and evaluation of release profiles in the presence and absence of endosome disruptive peptides (both free and conjugated to antibodies).

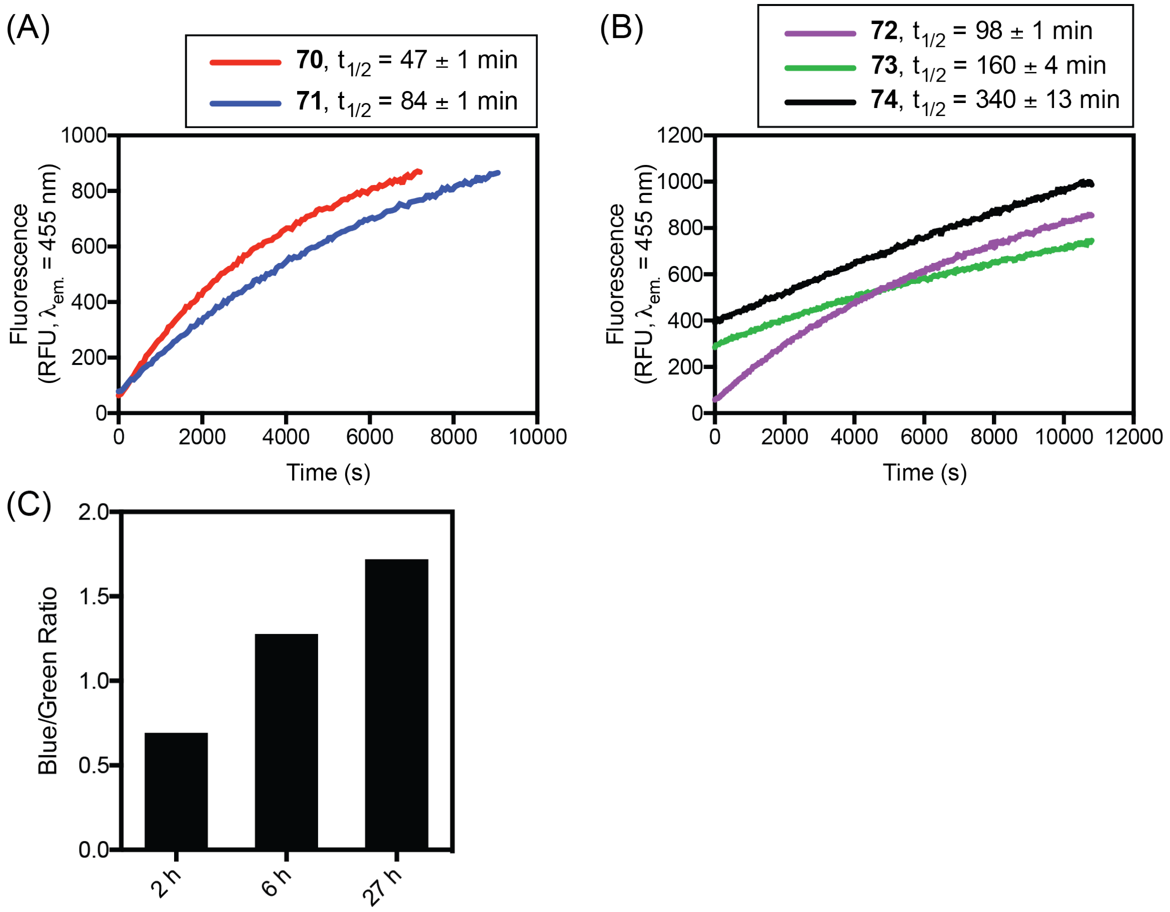

Figure 4.10. *In vitro* kinetics of cleavage of disulfides by following the increase in PB emission (λ_{max} = 455 nm) over time after the addition of GSH (5 mM) to **70** (DOL = 1.3) and **71** (DOL = 1.0) (100 nM, panel A) and **72** (50 nM, DOL = 2.3, panel B), **73** (50 nM, DOL = 1.0, panel B), and **74** (25 nM, DOL = 1.0, panel B) in PBS pH 7.4. The half-lives were determined using GraphPad Prism software. C: Kinetics of cleavage of the disulfide of **70** (5 μM, DOL = 1.3) based on the increase in FRET ratio over time after addition to living SkBr3 cells, as measured by confocal laser scanning microscopy. Blue/Green ratio = PB (Ex. 405 nm, Em. 415-500 nm) / Green (Ex. 488 nm, Em. 500-600 nm). Concentrations were based on [Herceptin].

4.6. Conclusions and future directions

We characterized Pacific Blue and Pennsylvania Green as a new FRET pair. These fluorophores compliment one another in pH insensitivity and have large spectra overlap, ideal for FRET. We can make multi-gram quantities of each of these fluorophores readily, allowing for the preparation of a wide variety of PB-PG FRET probes. Through organic synthesis and *in vitro* characterization of a simple FRET system, we found this pair to have a high FRET efficiency equal to 0.97, indicating that these dyes should be widely applicable to the study of biological processes.

We used this FRET pair as well as another related FRET pair (Pacific Blue-Oregon Green) to study the release profile of two model drug delivery systems. We found that the addition of steric hindrance and/or anionic groups near the disulfide bond decreases the cleavage rate, both in the cholesteryl carbamate anchored system, and the Herceptin-conjugates. Through cellular studies of endocytosis, we found that the disulfide stability within a molecule that traffics via a cholesteryl carbamate anchor has a half life of ~ 4 h in living Jurkat lymphocytes, whereas the disulfide half life of a molecule delivered using Herceptin in SkBr3 cells is much longer. Future studies will investigate the release profile of molecules trafficking via cholesterol mimics and antibodies alike, both in the presence and absence of an endosome disruptive peptide to help elucidate the mechanisms of release for these targeted delivery systems. To further explore why the observed disulfide cleavage kinetics between antibody conjugates and cholesteryl carbamate derivatives are so different, we will investigate whether the much more hydrophobic Pennsylvania Green fluorophore used in the antibody studies might limit cleavage of disulfides compared to the much more hydrophilic Oregon Green fluorophore that is likely to be more solvent accessible. To carry out these experiments, we have synthesized compounds **75**–**76** (Figure 4.11), and in the future we will evaluate the cleavage kinetics of the antibody conjugates **77**–**78** (Figure 4.11) *in vitro* and in SkBr3 cells. Another hypothesis that might be fruitful to investigate would be whether membrane-bound glutathione-S-transferase enzymes of endosomes might preferentially cleave disulfides that are proximal to membranes such as those present in the cholesteryl carbamates described here.

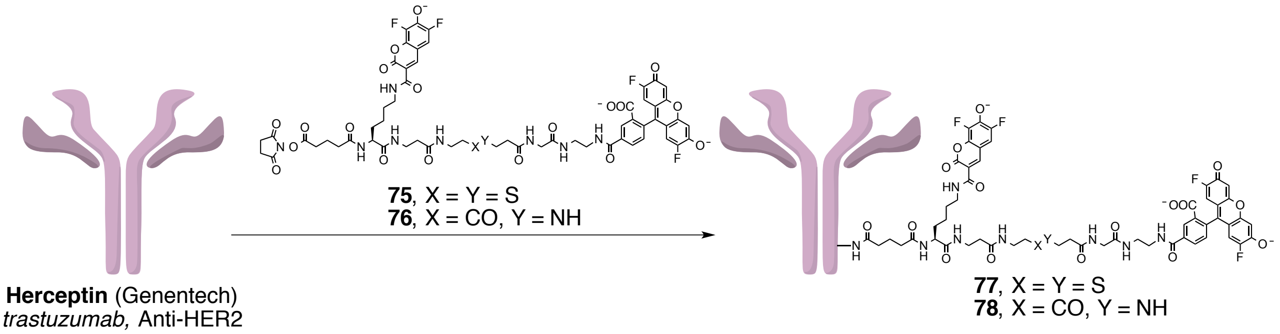

Figure 4.11. Structures of Pacific Blue-Oregon Green FRET-NHS esters (**75–76**) and conjugates of Herceptin (**77–78**).

4.7. Experimental

4.7.1. General experimental section

Chemicals were purchased from Sigma Aldrich, Acros Organics, Alfa Aesar, Oakwood Chemical, or Chem-Impex International. ^1H NMR and ^{13}C NMR were acquired on an Avance AVIII 500 MHz instrument. For ^1H and ^{13}C, chemical shifts (δ) are reported in ppm referenced to $CDCl_3$ (7.26 ppm for ^1H and 77.2 ppm for ^{13}C) or DMSO-d_6 (2.50 ppm for ^1H, 39.5 ppm for ^{13}C). ^1H coupling constants (J_{HH}, Hz) and ^{13}C coupling constants (J_{CF}, Hz) are reported as: chemical shift, multiplicity (s = singlet, d = doublet, t = triplet, q = quartet, m = multiplet, dt = doublet of triplets, dd = doublet of doublets, ddd = doublet of doublet of doublets, td = triplet of doublets, qd = quartet of doublets), coupling constant, and integration. High Resolution Mass Spectra (HRMS) were obtained at the Mass Spectrometry Laboratory at the University of Kansas on a Micromass LCT Premier. Thin layer chromatography (TLC) was performed using EMD aluminum-backed (0.20 mm) silica plates (60 F-254), and flash chromatography used ICN silica gel (200-400 mesh). TLC plates were visualized with a UV lamp. Preparative HPLC was performed with an Agilent 1200 instrument equipped with a Hamilton PRP-1 reverse phase column (250 mm length, 21.2 mm ID, 7 µm particle size) with detection by absorbance at 215, 254, 370, and 490 nm. All non-aqueous reactions were carried out using flame- or oven-dried glassware under an atmosphere of dry argon or nitrogen. *N*,*N*-dimethylformamide (DMF) was purified via filtration through two columns of activated basic alumina under an atmosphere of Ar using a solvent purification system from Pure Process Technology (GlassContour). Other commercial reagents were used as received. Absorbance spectra were obtained using semimicro (1.4 mL) UV quartz cuvette (Sigma-Aldrich, Z27667-7) on an Agilent 8452A diode array spectrometer. Fluorescence spectra were acquired using a SUPRASIL ultra-micro quartz cuvette (PerkinElmer, B0631079) on a Perkin-Elmer LS55 Fluorescence Spectrometer (10 nm excitation slit width).

4.7.2. Biological protocol and analysis

Cell culture: SkBr3 cells (ATCC #HTB-30) were cultured in DMEM/Ham's F-12 medium (Sigma 8437). Jurkat lymphocytes (human acute leukemia, ATCC #TIB-152) were cultured in RPMI-1640 medium (Sigma R8758). All media was supplemented with fetal bovine serum (FBS, 10%), penicillin (100 units/mL), and streptomycin (100 µg/mL) and incubated in a humidified 5% CO_2 incubator at 37 °C unless otherwise noted.

Analysis of cleavage kinetics of simple and cholesteryl carbamate FRET probes by fluorescence spectroscopy

FRET probes were diluted with PBS with 0.5% triton X-100 and 1% DMSO (pH 7.4, 37 °C) to provide 1 mL of the desired concentration. Dithiothreitol (DTT) or β-mercaptoethanol (β-ME) was added from a 1 mM aqueous stock to the final desired concentration. The solution were immediately transferred to a quartz cuvette equipped with a stir bar (PerkinElmer). The cuvette was immediately placed in a PerkinElmer LS 55 Fluorescence Spectrometer equipped with a Biokinetics Accessory for analysis. The cuvette holder was heated to 37 °C and stirring was set to fast. Full emission spectra (Ex. 400 nm, 10 nm slit width) were taken at various time intervals (dependent on the probe, listed in each figure). The increase in fluorescence at 455 or 460 nm was followed over time as an indicator of the cleavage of the disulfide bond. The half-time ($t_{1/2}$) for cleavage of the disulfide was calculated using GraphPad Prism software.

Confocal microscopy of OG-PB cholesteryl carbamate conjugates

Jurkat lymphocytes (350,000 cells/mL) were treated with 10 µM of the disulfide and amide FRET probes and were incubated at 37 °C for 27 h. Cells were centrifuged at 2000 x g for 2 min and the media was replaced to remove excess fluorophore not taken up by the cells. Fluorescent probes were excited with either a 405 nm (Pacific Blue) or 488 nm (Pennsylvania Green) solid-state laser and emitted photons were collected from 425-475 nm to image the PB signal (405 nm laser), 520-600 nm to image the FRET signal (405 nm laser), and 500-600 nm to image the OG signal (488 nm laser). Laser power and PMT gain settings were kept identical for all images acquired within a given experiment to allow accurate comparisons of cellular fluorescence.

Cleavage kinetics of OG-PB cholesteryl carbamate conjugates analyzed by flow cytometry

Jurkat lymphocytes (350,000 cells/mL) were treated with 10 μM of the disulfide and amide FRET probes and were incubated at 37 °C for various time points. Cells were centrifuged at 2000 x g for 2 min and the media was replaced to remove excess fluorophore not taken up by the cells. FACS analysis was preformed on a Millipore Guava Flow Cytometer equipped with 405 and 488 nm lasers. 10,000 cells were counted for each sample. Data was collected under a Pacific Blue filter (448/50 nm) and Green filter (525/30 nm). FACS data was analyzed by gating cell populations based on untreated cells. Kinetics of cleavage were calculated based on the increase in the FRET ratio over time. FRET ratio = PB (Ex. 405 nm, 450 emission channel) / FRET (Ex. 405 nm, 530 emission channel). The half-life was determined using GraphPad Prism software.

Procedure for labeling Herceptin

Lyophilized Herceptin was reconstituted in sterile PBS (pH 7.4) and the protein concentration was determined by absorbance at 280 nm (ε E1% = 13.7 L g-1 cm-1). To remove stabilizing agents and salts, Sephadex G-25 resin (Superfine, Sigma) was suspended in PBS (pH 7.4). The resulting slurry (950 μL) was added to a minispin column (USA Scientific) and centrifuged at 16,000 x G for 20 s to remove the buffer and pack the resin. The solution containing Herceptin was loaded onto the packed resin of the spin column (50-70 µL per column) and centrifuged at 16,000 x G for 30 s to separate the protein from the small molecules retained by the resin. The absorbance at 280 nm was used to determine the resulting concentration, which was then adjusted to 100 µM. The FRET probes were dissolved in DMSO to give 10 mM stocks, as verified by absorbance. Aqueous sodium bicarbonate (final concentration = 100 mM, pH 8) was added to the Herceptin solution, followed by the FRET probe (10 eq. from DMSO stock). Reaction of the NHS ester was allowed to proceed at 37 °C for 30 min. To purify the conjugate, the solution was passed twice through a Sephadex G-25 resin mini-column, as described above (50 – 70 µL per column). The absorbance at 280 nm and 425 nm (Pacific Blue, $\varepsilon = 29{,}500\ M^{-1}cm^{-1}$) of the eluent was used to determine the concentration and degree of protein labeling (DOL = 1–3).

Confocal microscopy of Herceptin conjugates: SkBr3 breast cancer cells were plated (200,000 cells/mL, 300 µL/well) into µ-Slide 8 Well (ibiTreat, Ibidi) and incubated overnight. Cells were then washed two times with media and treated with 5 µM Herceptin-FRET probe conjugate in media for the indicated time. Cells were then washed twice with media and imaged using an inverted Leica TCS SPE confocal laser-scanning microscope fitted with a Leica 63x oil-immersion objective. Fluorescent probes were excited with either a 405 nm (Pacific Blue) or 488 nm (Pennsylvania Green) solid-state laser and emitted photons were collected from 415-500 nm or 500-600 nm, respectively. Laser power and PMT gain settings were kept identical for all images acquired within a given experiment to allow accurate comparisons of cellular fluorescence. 4 fields of cells were imaged for each time point, and 4 endosomes were manually selected from each field as regions of interest (ROIs). The mean fluorescence intensity of each ROI was recorded for both fluorophores being studied and averaged. Dithiothreitol (DTT, Sigma) was added to treated cells as a control for full cleavage of the disulfide bond. To this end, SkBr3 cells plated in µ-Slide 8 well as described above were treated with 5 µM of the Herceptin-FRET probe conjugate for the indicated time. Cells were then washed twice with media, and treated with plain media or media with 1 mM DTT for 30 min. After this incubation, cells were imaged as above. For analysis, the ratio of mean fluorescence intensity for 405 nm/488 nm excitation for each ROI was averaged.

Analysis of kinetics of Herceptin-FRET probe conjugates by fluorescence spectroscopy

Herceptin-FRET probe conjugates were diluted with PBS (pH 7.4, 37 °C) to provide 600 µL of the desired concentration. Glutathione (reduced, Acros Organics) was added from a 100 mM aqueous stock solution to a final concentration of 5 mM. The solution was immediately transferred to a quartz cuvette equipped with a stir bar (PerkinElmer). The cuvette was immediately placed in a PerkinElmer LS 55 Fluorescence Spectrometer equipped with a Biokinetics Accessory for analysis. The cuvette holder was heated to 37 °C and stirring was set to fast. Readings were taken every 30 s (0.1 s integration) using the Time Drive application with an excitation of 405 nm, emission of 455 nm, 10 nm slit widths and the lamp turned off between readings. The increase in fluorescence at 455 nm was followed over time as an indicator of the cleavage of the disulfide bond.

For, fluorescence spectra that were acquired using the Scan Application, 600 µL of the

Herceptin-FRET probe conjugate was placed in a quartz cuvette (PerkinElmer). Fluorescence scans of Pacific Blue were performed with excitation at 405 nm and emission from 425-700 nm. For Pennsylvania Green, excitation of 490 nm and emission from 510-700 nm were used. All slit widths were 10 nm. All measurements were background subtracted using a spectrum obtained from a quartz cuvette containing PBS. Scans were performed at t=0 and t=final of the kinetic studies.

4.7.3. Synthetic procedures and compound characterization data

General procedure 4A. Compounds **61**–**62** were constructed using SPPS with 2-chlorotrityl resin with L-amino acids. The procedure for coupling as described in Section 2.10.3 (general procedure 2D) was followed. After completing all the steps of coupling reactions, the peptide was cleaved from the resin by treatment with a mixture of DCM/TFE/acetic acid (7:2:1) with shaking for 2 h. The resin was removed by filtration and washed with DCM (2 mL x 3). The filtrates were combined and concentrated under vacuum. The crude peptide, HBTU (1.2 eq.), HOBt (1.2 eq.) and DIEA (5 eq.) were added to DMF (0.5 mL). Separately, **35** (2 eq.) was treated with a solution of trifluoroacetic acid (TFA) / CH_2Cl_2 (0.5 mL, 50:50) for 1 h. The mixture was concentrated under vacuum and washed with CH_2Cl_2 (2 mL) and ether (2 mL x 2) to remove excess TFA. Following deprotection, the amine was dissolved in DMF (0.5 mL) and added to the activated acid solution. The reaction was stirred at 22 °C for 16 h. The vessel was placed on high vacuum for 2 h to remove DMF followed by purification by preparative RP-HPLC (Gradient: H_2O:CH_3CN (9:1) to (0:100) with added TFA (0.1%) over 20 min; elution time = 17-20 min). Pure fractions were collected, combined, and solvent was removed by lyophilization.

General procedure 4B. Compounds **84**–**85** (Figure 4.15) were constructed using SPPS with 2-chlorotrityl resin with D-amino acids. The procedure for coupling as described in Section 2.10.3 (general procedure 2D) was followed. After completing all the steps of coupling reactions, the peptide was cleaved from the resin by treatment with a mixture of DCM/TFE/acetic acid (7:2:1) with shaking for 2 h. The resin was removed by filtration and washed with DCM (2 mL x 3). The filtrates were combined and concentrated under vacuum. The crude peptide, *N*-Boc-ethylenediamine (4 eq.), HATU (3.8 eq.), DIEA (5 eq.) were added to DMF (1 mL). The reaction was stirred at 22 °C for 16 h. The vessel was placed on high vacuum for 2 h to remove DMF. The crude product was then treated with a solution of trifluoroacetic acid (TFA) / CH_2Cl_2 (0.5 mL, 50:50) for 1 h. The mixture was concentrated and purified by preparative RP-HPLC (Gradient: H_2O:CH_3CN (9:1) to (0:100) with added TFA (0.1%) over 20 min; elution time = 17-20 min). Pure fractions were collected, combined, and solvent was removed by lyophilization.

General procedure 4C. To a solution of peptides **84**–**85** (Figure 4.15, 1.5 eq.) and DIEA (5 eq.) in DMF (0.5 mL), Oregon Green Carboxylic Acid succinimidyl ester (Thermo Fisher O6149, OG-NHS, 1 eq.) was added. The reaction was stirred at 22 °C for 16 h. The vessel was placed on high vacuum for 2 h to remove DMF. The crude product was then treated with a solution of trifluoroacetic acid (TFA) / CH_2Cl_2 (0.5 mL, 50:50) for 1 h. The mixture was concentrated and purified by preparative RP-HPLC (Gradient: H_2O:CH_3CN (9:1) to (0:100) with added TFA (0.1%) over 20 min; elution time = 17-20 min). Pure fractions were collected, combined, and solvent was removed by lyophilization.

General procedure 4D. Compounds **65**–**69** were constructed using SPPS with 2-chlorotrityl resin with L-amino acids. The procedure for coupling as described in Section 2.10.3 (general procedure 2D) was followed. After completing all the steps of coupling reactions, with the N-terminal Fmoc intact, the peptide was cleaved from the resin by treatment with a mixture of DCM/TFE/acetic acid (7:2:1) with shaking for 2 h. The resin was removed by filtration and washed with DCM (2 mL x 3). The filtrates were combined and concentrated under vacuum. The crude peptide, HATU (3.8 eq.), and DIEA (5 eq.) were added to DMF (1 mL). Separately, **79** (2 eq.) was treated with a solution of trifluoroacetic acid (TFA) / CH_2Cl_2 (0.5 mL, 50:50) for 30 min. The mixture was concentrated under vacuum and washed with CH_2Cl_2 (2 mL) and ether (2 mL x 2) to remove excess TFA. Following deprotection, the amine was dissolved in DMF (0.5 mL) and added to the activated acid solution. The reaction was stirred at 22 °C for 16 h. The vessel was placed on high vacuum for 2 h to remove DMF. The crude product was then treated with 20% piperidine (1 mL) for 20 min followed by concentration under vacuum. The peptide was then treated with a solution of trifluoroacetic acid (TFA) / CH_2Cl_2 (0.5 mL, 50:50) for 1 h. The mixture was concentrated under high vacuum and treated with disuccinimidyl glutarate (10 eq.) in DMF (1 mL) in the presence of DIEA for 3 h. The resulting solution was concentrated and purified by preparative RP-HPLC (Gradient: H_2O:CH_3CN (9:1) to (0:100) with added TFA (0.1%) over 20 min; elution time = 9-11 min). Pure fractions were collected, combined, and solvent was removed by lyophilization.

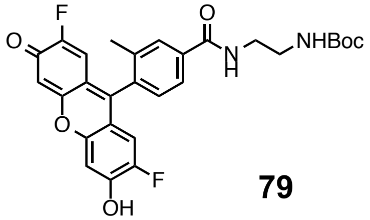

79

***tert*-Butyl (2-(4-(2,7-difluoro-6-hydroxy-3-oxo-3*H*-xanthen-9-yl)-3-methylbenzamido)ethyl)carbamate (79).** To a solution of 4-Carboxy Pennsylvania Green succinimidyl ester (95 mg, 0.2 mmol), prepared as previously reported,[31] in DMF (1 mL) was added DIEA (125 µL, 0.5 mmol) and *N*-Boc-ethylenediamine (47 µL, 0.3 mmol). The reaction mixture was stirred at 22 °C for 4 h. The vessel was placed on high vacuum for 2 h to remove DMF followed by purification by column chromatography on silica gel (eluent: DCM/MeOH (10:1)) to afford **79** (100 mg, 96%) as an orange solid.^{1}H NMR (500 MHz, DMSO-d_6) δ 8.62 (t, *J* = 5.7 Hz, 1H), 7.96 (d, *J* = 2.0 Hz, 1H), 7.88 (dd, *J* = 7.8, 1.7 Hz, 1H), 7.39 (d, *J* = 7.9 Hz, 1H), 6.94 (t, *J* = 5.8 Hz, 1H), 6.61 (d, *J* = 10.9 Hz, 2H), 3.34 (q, *J* = 6.3 Hz, 2H), 3.14 (q, *J* = 6.3 Hz, 2H), 2.08 (s, 3H), 1.38 (s, 9H); ^{13}C NMR (126 MHz, DMSO-d_6) δ 172.5, 166.3, 156.2, 149.8 (d, *J* = 6.1 Hz), 136.4, 136.2, 134.7, 130.0, 129.5, 125.6, 105.6, 78.2, 41.8, 40.5, 28.7, 21.5, 19.6; HRMS (ESI-) m/z 523.1668 (M-H$^+$), $C_{28}H_{25}F_2N_2O_6$ requires 523.1681).

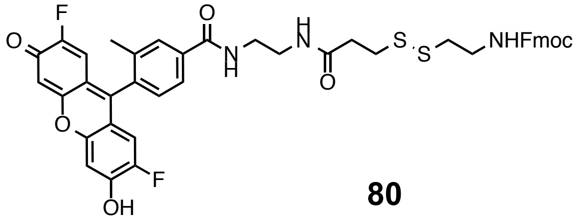

80

(9*H*-Fluoren-9-yl)methyl (2-((3-((2-(4-(2,7-difluoro-6-hydroxy-3-oxo-3*H*-xanthen-9-yl)-3-methylbenzamido)ethyl)amino)-3-oxopropyl)disulfanyl)ethyl)carbamate, (80). Fmoc-protected 3-((2-aminoethyl)disulfanyl)propanoic[8] (35 mg, 0.089 mmol), HATU (30 mg, 0.08 mmol) and DIEA (40 µL, 0.16 mmol) were stirred in anhydrous DMF at 0 °C for 25 minutes. Separately, **79** (31 mg, 0.059 mmol) was treated with a solution of trifluoroacetic acid (TFA) / CH_2Cl_2 (2 mL, 30:70) for 20 min. The mixture was concentrated under vacuum and washed with CH_2Cl_2 (5 mL) and ether (5 mL x 2) to remove excess TFA. Following deprotection, the amine was dissolved in DMF (0.5 mL) and added to the activated acid solution. The reaction was stirred at 22 °C for 16 h. The vessel was placed on high vacuum for 2 h to remove DMF followed by purification by column chromatography on silica gel (gradient: DCM:MeOH (100:1) to (16:1)) to afford **80** (47 mg, 98%) as an orange solid. ^{1}H NMR (500 MHz, DMSO-d_6) δ 8.66 (t, J = 5.7 Hz, 1H), 8.12 (t, J = 5.8 Hz, 1H), 7.96 (d, J = 1.7 Hz, 1H), 7.88 (dd, J = 7.8, 2.1 Hz, 3H), 7.67 (d, J = 7.5 Hz, 2H), 7.50 (t, J = 5.7 Hz, 1H), 7.45 – 7.36 (m, 3H), 7.31 (td, J = 7.5, 1.2 Hz, 2H), 6.61 (d, J = 11.0 Hz, 2H), 4.29 (d, J = 6.9 Hz, 2H), 4.20 (t, J = 6.9 Hz, 1H), 3.37 (q, J = 6.4 Hz, 4H), 3.27 (ddd, J = 7.2, 4.6, 1.8 Hz, 4H), 2.91 (t, J = 7.2 Hz, 2H), 2.76 (t, J = 6.8 Hz, 2H), 2.07 (s, 3H); ^{13}C NMR (126 MHz, DMSO-d_6) δ 170.8, 166.3, 156.5, 149.8, 144.3, 141.2, 136.4, 136.1, 134.8, 130.0, 129.5, 128.0, 127.5, 125.6, 120.6, 105.6, 65.8, 47.2, 38.8, 37.8, 35.6, 34.3, 19.6; HRMS (ESI-) m/z 808.1935 (M-H$^+$), $C_{43}H_{36}F_2N_3O_7S_2$ requires 808.1963).

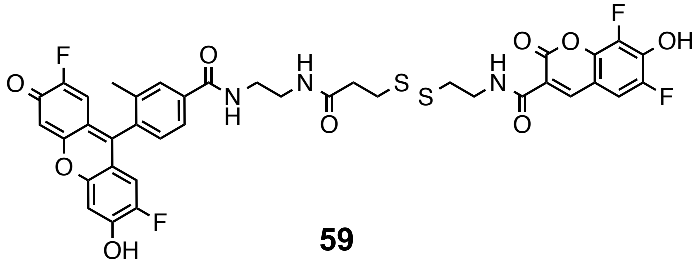

59

***N*-(2-((3-((2-(4-(2,7-Difluoro-6-hydroxy-3-oxo-3*H*-xanthen-9-yl)-3-methylbenzamido)ethyl)amino)-3-oxopropyl)disulfanyl)ethyl)-6,8-difluoro-7-hydroxy-2-oxo-2*H*-chromene-3-carboxamide (59).** **5** (8 mg, 0.033 mmol), HATU (11 mg, 0.031 mmol) and DIEA (25 µL, 0.11 mmol) were stirred in anhydrous DMF (1 mL) at 22 °C for 15 minutes. Separately, **80** (18 mg, 0.022 mmol) was treated with a solution of piperidine in DMF (20%, 0.7 mL) for 45 min to remove the Fmoc protecting group. The mixture was concentrated under high vacuum and washed with DMF (1 mL x 2) to remove excess piperidine. Following deprotection, the amine was dissolved in DMF (1 mL) and added to the activated acid solution. The reaction was stirred at 22 °C for 16 h. The vessel was placed on high vacuum for 2 h to remove DMF followed by purification by preparative RP-HPLC (Gradient: H_2O:CH_3CN (9:1) to (0:100) with added TFA (0.1%) over 20 min; elution time = 15 min). Pure fractions were collected, combined, and solvent was removed by lyophilization to yield **59** (16 mg, 89%). ^{1}H NMR (500 MHz, MeOD) δ 8.71 (d, *J* = 1.4 Hz, 1H), 7.96 (dt, *J* = 1.7, 0.8 Hz, 1H), 7.94-7.89 (m, 2H), 7.50-7.39 (m, 2H), 6.77 (d, *J* = 10.8 Hz, 2H), 3.86 (d, *J* = 5.5 Hz, 1H), 3.72 (t, *J* = 6.5 Hz, 2H), 3.64–3.57 (m, 2H), 3.52 (dd, *J* = 6.8, 4.7 Hz, 2H), 3.00 (t, *J* = 6.9 Hz, 2H), 2.93 (t, *J* = 6.5 Hz, 2H), 2.68 (t, *J* = 6.9 Hz, 2H), 2.14 (s, 3H); ^{13}C NMR (126 MHz, MeOD-d_4) δ 174.3, 169.6, 163.6, 161.4, 156.0 (d, *J* = 3.7 Hz), 153.7, 150.9 (dd, *J* = 242.6, 4.4 Hz), 149.1, 143.6, 142.4, 142.3, 142.2, 140.49 (d, *J* = 240.6 Hz), 138.0, 137.4, 136.3, 130.9, 130.5, 129.8, 128.9, 126.5, 125.9, 121.7, 116.7, 115.9, 115.8, 112.9, 112.7, 111.3 (dd, *J* = 21.2, 3.1 Hz), 111.0 (d, *J* = 10.4 Hz), 106.27, 106.25, 41.0, 39.9, 39.6, 38.1, 36.4, 35.1, 19.68; HRMS (ESI-) m/z 810.1218 (M-H$^+$), $C_{38}H_{28}F_4N_3O_9S_2$ requires 810.1203).

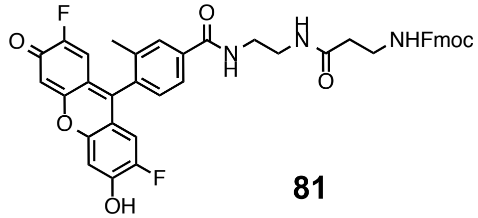

81

(9*H*-fluoren-9-yl)methyl (3-((2-(4-(2,7-difluoro-6-hydroxy-3-oxo-3*H*-xanthen-9-yl)-3-methylbenzamido)ethyl)amino)-3-oxopropyl)carbamate (81). Fmoc-β-alanine-OH (131 mg, 0.42 mmol), HATU (160 mg, 0.42 mmol) and DIEA (225 μL, 1.3 mmol) were stirred in anhydrous DMF (3.5 mL) at 0 °C for 30 minutes. Separately, **79** (170 mg, 0.32 mmol) was treated with a solution of trifluoroacetic acid (TFA) / CH_2Cl_2 (6.5 mL, 30:70) for 40 min. The mixture was concentrated under vacuum and washed with CH_2Cl_2 (5 mL) and ether (5 mL x 2) to remove excess TFA. Following deprotection, the amine was dissolved in DMF (3.5 mL) and added to the activated acid solution. The reaction was stirred at 22 °C for 16 h. The vessel was placed on high vacuum for 2 h to remove DMF. The mixture was treated with ethyl acetate (100 mL) and water (100 mL). The mixture was extracted with ethyl acetate, and the organic layer was washed with sat. aqueous NaCl (2 x 100 mL). The organic layer was dried, filtered, concentrated under reduced pressure, and purified by column chromatography on silica gel (gradient: hexanes:EtOAc (1:0) to (7:3)) to afford **81** (180 mg, 78%) as an orange solid. ^{1}H NMR (500 MHz, DMSO-*d*$_6$) δ 8.68 (t, *J* = 5.6 Hz, 1H), 8.06 (t, *J* = 5.8 Hz, 1H), 8.00-7.94 (m, 1H), 7.93-7.83 (m, 3H), 7.68 (d, *J* = 7.5 Hz, 2H), 7.46-7.28 (m, 6H), 6.61 (d, *J* = 11.0 Hz, 2H), 4.27 (d, *J* = 6.7 Hz, 2H), 4.20 (t, *J* = 6.9 Hz, 1H), 3.37 (q, *J* = 6.3 Hz, 2H), 3.24 (dq, *J* = 17.2, 6.4 Hz, 4H), 2.29 (t, *J* = 7.2 Hz, 2H), 2.07 (s, 3H); ^{13}C NMR (126 MHz, DMSO-*d*$_6$) δ 170.5, 165.9, 156.1, 149.3, 143.9, 140.7, 136.0, 135.7, 134.3, 129.6, 129.1, 127.6, 127.1, 125.2, 125.1, 120.1, 105.2, 65.3, 46.7, 40.1, 38.3, 37.1, 35.8, 19.1; HRMS (ESI-) m/z 716.2178 (M-H$^+$), $C_{41}H_{32}F_2N_3O_7$ requires 716.2208).

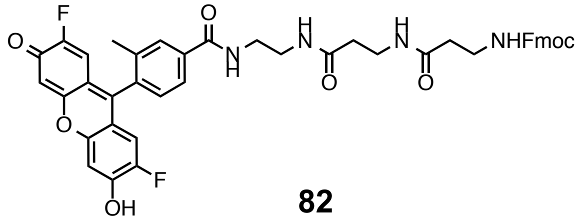

82

(9*H*-Fluoren-9-yl)methyl (3-((3-((2-(4-(2,7-difluoro-6-hydroxy-3-oxo-3*H*-xanthen-9-yl)-3-methylbenzamido)ethyl)amino)-3-oxopropyl)amino)-3-oxopropyl)carbamate (82).Fmoc-β-alanine-OH (80 mg, 0.25 mmol), HATU (95 mg, 0.25 mmol) and DIEA (130 µL, 0.78 mmol) were stirred in anhydrous DMF (2.5 mL) at 0 °C for 30 min. Separately, **81** (140 mg, 0.20 mmol) was treated with a solution of piperidine in DMF (20%, 2 mL) for 45 min to remove the Fmoc protecting group. The mixture was concentrated under high vacuum and washed with DMF (2 mL x 2) to remove excess piperidine. Following deprotection, the amine was dissolved in DMF (2.5 mL) and added to the activated acid solution. The reaction was stirred at 22 °C for 4 h. The vessel was placed on high vacuum for 2 h to remove DMF. The mixture was treated with ethyl acetate (100 mL) and water (100 mL). The mixture was extracted with ethyl acetate, and the organic layer was washed with sat. aqueous NaCl (2 x 100 mL). The organic layer was dried, filtered, concentrated under reduced pressure, and purified by column chromatography on silica gel (gradient: hexanes:EtOAc (1:0) to (7:3)) to afford **82** (100 mg, 68%) as an orange solid. ^{1}H NMR (500 MHz, DMSO-d_6) δ 8.68 (t, *J* = 5.7 Hz, 1H), 8.05 (t, *J* = 5.8 Hz, 1H), 7.94 (dd, *J* = 12.5, 3.7 Hz, 2H), 7.9146 – 7.8311 (m, 3H), 7.66 (d, *J* = 7.5 Hz, 2H), 7.39 (q, *J* = 7.6 Hz, 3H), 7.31 (t, *J* = 7.6 Hz, 3H), 6.85 (s, 2H), 6.60 (d, *J* = 11.1 Hz, 2H), 4.25

(d, J = 6.7 Hz, 2H), 4.18 (t, J = 6.9 Hz, 1H), 3.39 – 3.33 (m, 2H), 3.26 (q, J = 6.5 Hz, 4H), 3.18 (q, J = 6.8 Hz, 2H), 2.24 (q, J = 7.6 Hz, 4H), 2.07 (s, 3H). ^{13}C NMR (126 MHz, DMSO-d_6) δ 171.2, 170.7, 166.3, 156.5, 149.8 (d, J = 6.3 Hz), 144.3, 141.1, 136.4, 136.1, 134.8, 130.0, 129.5, 128.1, 127.5, 125.61, 125.55, 111.7 (d, J = 13.5 Hz), 105.6, 65.8, 47.1, 40.5, 38.8, 37.5, 36.1, 36.0, 35.8, 19.6; HRMS (ESI-) m/z 787.2560 (M-H$^+$), $C_{44}H_{37}F_2N_4O_8$ requires 787.2579).

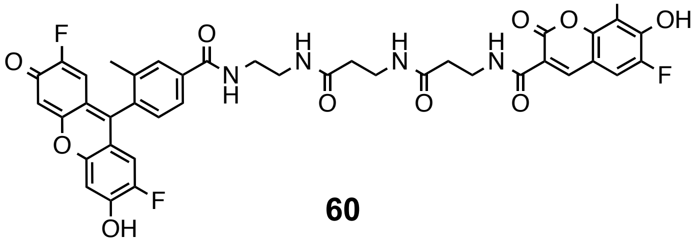

60

***N*-(3-((3-((2-(4-(2,7-Difluoro-6-hydroxy-3-oxo-3*H*-xanthen-9-yl)-3-methylbenzamido)ethyl)amino)-3-oxopropyl)amino)-3-oxopropyl)-6,8-difluoro-7-hydroxy-2-oxo-2*H*-chromene-3-carboxamide (60).** **5** (8 mg, 0.033 mmol), HATU (11 mg, 0.031 mmol) and DIEA (20 µL, 0.11 mmol) were stirred in anhydrous DMF (1 mL) at 22 °C for 15 minutes. Separately, **82** (17 mg, 0.022 mmol) was treated with a solution of 20% piperidine in DMF (0.7 mL) for 45 min to remove the Fmoc protecting group. The mixture was concentrated under high vacuum and washed with DMF (1 mL x 2) to remove excess piperidine. Following deprotection, the amine was dissolved in DMF (1 mL) and added to the activated acid solution. The reaction was stirred at 22 °C for 16 h. The vessel was placed on high vacuum for 2 h to remove DMF followed by purification by preparative RP-HPLC (Gradient: H_2O:CH_3CN (9:1) to (0:100) with added TFA (0.1%) over 20 min; elution time = 15 min). Pure fractions were collected, combined, and solvent was removed by lyophilization to yield **60** (15 mg, 90%). ^{1}H NMR (500 MHz, D_2O) δ 8.68 (d, *J* = 1.4 Hz, 1H), 7.92 (d, *J* = 1.8 Hz, 1H), 7.91-7.85 (m, 1H), 7.46-7.33 (m, 2H), 6.86 (d, *J* = 6.9 Hz, 2H), 6.76-6.68 (m, 2H), 3.62 (t, *J* = 6.4 Hz, 2H), 3.52 (dd, *J* = 6.7, 4.8 Hz, 2H), 3.48-3.39 (m, 4H), 2.46 (t, *J* = 6.4 Hz, 2H), 2.39 (t, *J* = 6.6 Hz, 2H), 2.10 (s, 3H); ^{13}C NMR (126 MHz, DMSO-d_6) δ 174.4, 173.8, 169.6, 165.5, 163.5, 161.4, 154.9 (d, *J* = 294.9 Hz), 154.3 (d, *J* = 251.6 Hz), 150.9 (d, *J* = 3.2 Hz), 150.8 (d, *J* = 242.8 Hz), 148.9, 142.3, 142.2, 142.2, 140.5 (d, *J* = 240.9 Hz), 138.0, 137.4, 136.3, 132.0, 131.0 (d, *J* = 8.2 Hz), 130.8, 130.5, 126.4, 116.9, 115.9, 115.8, 112.9, 112.7, 111.3 (dd, *J* = 21.4, 2.9 Hz), 111.0 (d, *J* = 9.8 Hz), 106.28, 106.25, 40.9, 40.2, 37.21, 37.19, 37.1, 36.3, 19.7; HRMS (ESI-) m/z 789.1829 (M-H$^+$), $C_{39}H_{29}F_4N_4O_{10}$ requires 789.1820).

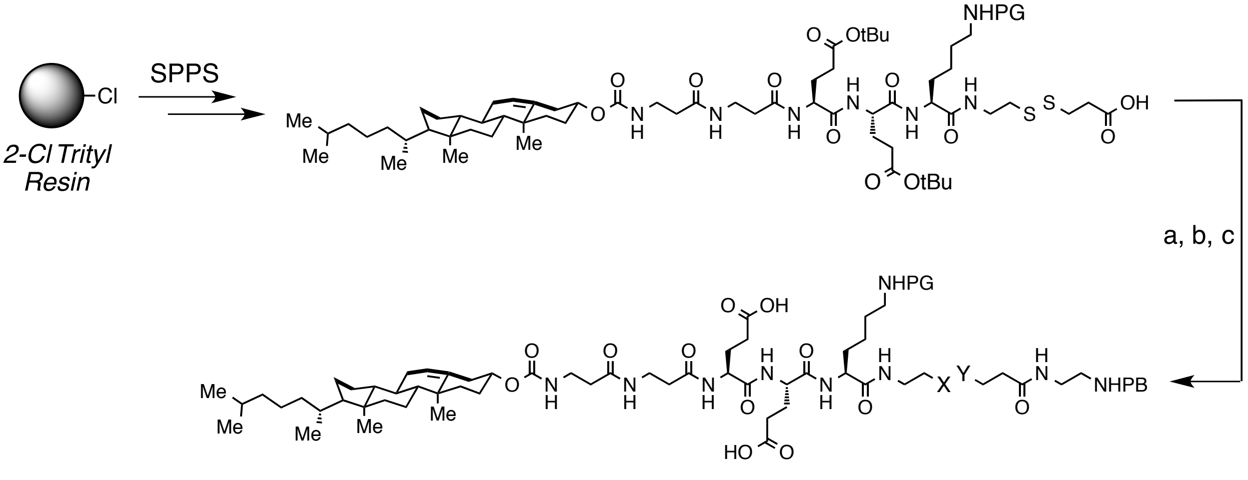

61 *(30%)*

Figure 4.12. Reagents and conditions: a) **35,** TFA (30%) in DCM; b) HBTU, HOBt, DIEA, DMF; c) TFA (30%) in DCM. PG = 4-Carboxy Pennsylvania Green, PB = Pacific Blue. Schematic shown for **61**, but applies to **62** following general procedure 4A.

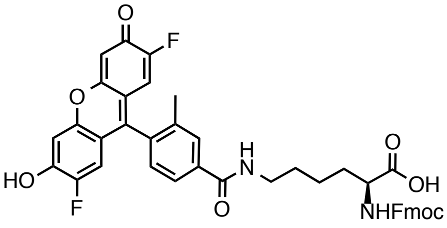

83

***N*^{2}-(((9*H*-Fluoren-9-yl)methoxy)carbonyl)-*N*^{6}-(4-(2,7-difluoro-6-hydroxy-3-oxo-3*H*-xanthen-9-yl)-3-methylbenzoyl)-*L*-lysine (83, PG-Lys).** To a solution of Fmoc-L-Lysine-OH (280 mg, 0.58 mmol) and DIEA (400 µL, 2.9 mmol) in DMF (2 mL) was added Pennsylvania Green NHS ester (1.25 g, 3.69 mmol), prepared as previously reported.[31] The reaction mixture was stirred at 22 °C overnight. The reaction mixture was added dropwise to cold aq. HCl (1 N, 200 mL). The precipitate formed was filtered, washed with cold aq. HCl (1 N, 25 mL), and dried in vacuum to give **83** as an orange solid (340 mg, 80%). ^{1}H NMR (500 MHz, DMSO-*d*$_6$) δ 8.64 (t, *J* = 5.7 Hz, 1H), 7.96 (d, *J* = 1.7 Hz, 1H), 7.88 (d, *J* = 7.7 Hz, 3H), 7.73 (dd, *J* = 7.5, 2.4 Hz, 2H), 7.46-7.27 (m, 6H), 6.89-6.72 (m, 2H), 6.60 (d, *J* = 11.0 Hz, 2H), 4.29 (d, *J* = 8.3 Hz, 2H), 4.24 (q, *J* = 7.5, 6.7 Hz, 1H), 3.96 (ddd, *J* = 9.8, 8.0, 4.6 Hz, 1H), 3.32 (q, *J* = 6.8 Hz, 2H), 2.07 (s, 3H), 1.74-1.35 (m, 6H); ^{13}C NMR (126 MHz, DMSO-*d*$_6$) δ 174.5, 166.1, 156.6 (d, *J* = 3.0 Hz), 149.8 (t, *J* = 6.0 Hz), 144.3, 144.2, 141.2 (d, *J* = 2.3 Hz), 136.4 (d, *J* = 10.5 Hz), 134.7, 130.0, 129.5, 128.1, 127.5, 125.8, 125.5, 120.6, 113.9, 111.6 (d, *J* = 21.6 Hz), 105.6 (d, *J* = 4.3 Hz), 66.1, 54.3, 47.1, 30.9, 29.17, 23.7, 19.6; HRMS (ESI-) m/z 731.2218 (M-H$^+$), $C_{42}H_{33}F_2N_2O_8$ requires 731.2205).

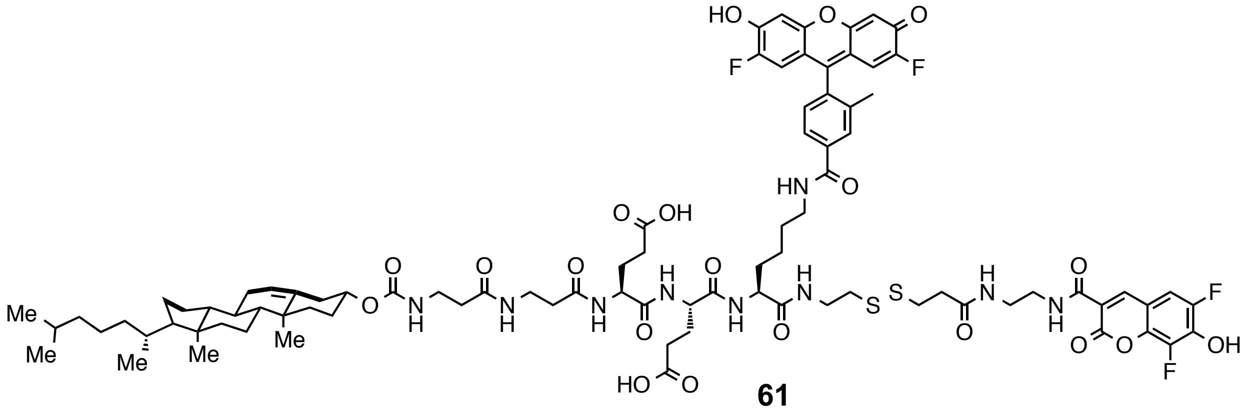

61

(15*S*,18*S*,21*S*)-18-(2-Carboxyethyl)-15-(4-(4-(2,7-difluoro-6-hydroxy-3-oxo-3*H*-xanthen-9-yl)-3-methylbenzamido)butyl)-1-(6,8-difluoro-7-hydroxy-2-oxo-2*H*-chromen-3-yl)-21-(3-(3-(((((3*R*,8*R*,9*R*,10*S*,13*S*,14*R*,17*S*)-10,13-dimethyl-17-((*R*)-6-methylheptan-2-yl)-2,3,4,7,8,9,10,11,12,13,14,15,16,17-tetradecahydro-1*H*-cyclopenta[*a*]phenanthren-3-yl)oxy)carbonyl)amino)propanamido)propanamido)-1,6,14,17,20-pentaoxo-9,10-dithia-2,5,13,16,19-pentaazatetracosan-24-oic acid (61). Following general procedure 4A, 3-((((cholester-3-yl)oxy)carbonyl) amino)propanoic acid,[43] PG-Lys (**83**), Fmoc-protected 3-((2-aminoethyl)disulfanyl)propanoic acid,[8] Fmoc-β-ala-OH, and Fmoc-L-Glu-OH were used with 2-chlorotrityl resin (1.22 mmol/g) to synthesize a peptide. The crude peptide (30 mg, 0.02 mmol) and **35** (11 mg, 0.03 mmol) yielded **61** (10 mg, 30%). LRMS (ESI-) m/z 1750.5 (M-H$^+$ $C_{88}H_{108}F_4N_9O_{20}S_2$ requires 1750.7).

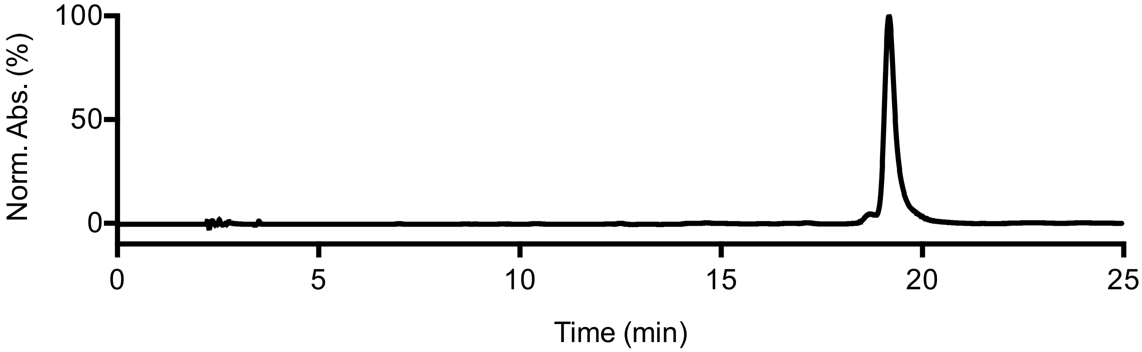

Figure 4.13. Analytical HPLC profile of **61** after preparative HPLC. Retention time = 19.5 min monitored by UV absorbance at 254 nm. Purity >95% by HPLC.

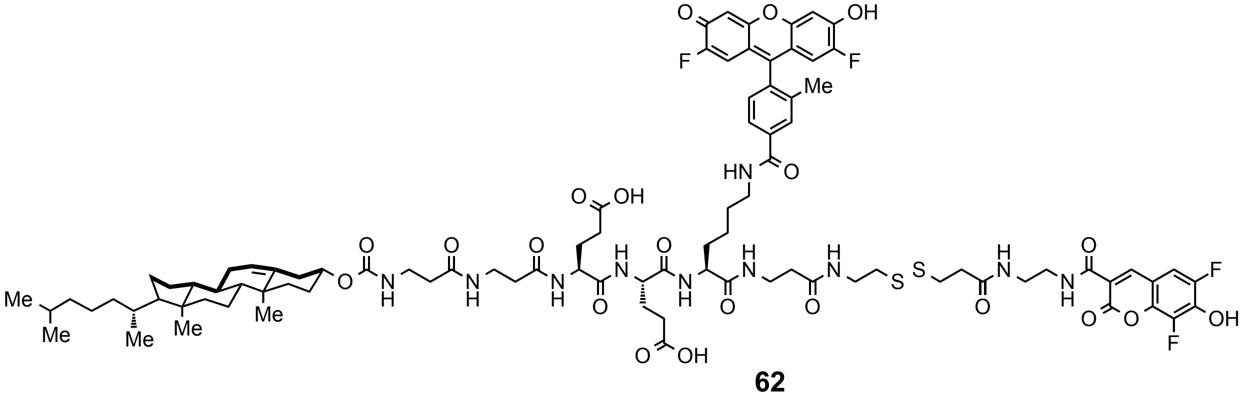

62

(19*S*,22*S*,25*S*)-22-(2-Carboxyethyl)-19-(4-(4-(2,7-difluoro-6-hydroxy-3-oxo-3*H*-xanthen-9-yl)-3-methylbenzamido)butyl)-1-(6,8-difluoro-7-hydroxy-2-oxo-2*H*-chromen-3-yl)-25-(3-(3-(((((3*R*,8*R*,9*R*,10*S*,13*S*,14*R*,17*S*)-10,13-dimethyl-17-((*R*)-6-methylheptan-2-yl)-2,3,4,7,8,9,10,11,12,13,14,15,16,17-tetradecahydro-1*H*-cyclopenta[*a*]phenanthren-3-yl)oxy)carbonyl)amino)propanamido)propanamido)-1,6,14,18,21,24-hexaoxo-9,10-dithia-2,5,13,17,20,23-hexaazaoctacosan-28-oic acid (62). Following general procedure 4A, 3-((((cholester-3-yl)oxy)carbonyl) amino)propanoic acid[43], PG-Lys (**83**), Fmoc-protected 3-((2-aminoethyl)disulfanyl)propanoic acid,[8] Fmoc-βAla-OH, and Fmoc-L-Glu-OH were with H-β-ala-2-chlorotrityl resin (0.74 mmol/g) to synthesize a peptide. The crude peptide (6 mg, 0.004 mmol) and **35** (3 mg, 0.008 mmol) yielded **62** (4 mg, 58%). LRMS (ESI-) m/z 1821.8 (M-H$^+$ $C_{91}H_{113}F_4N_{10}O_{21}S_2$ requires 1821.7).

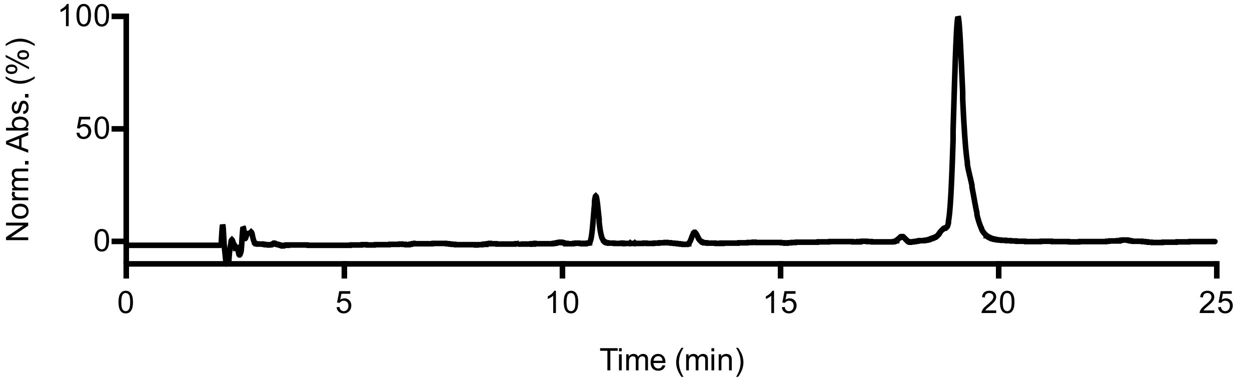

Figure 4.14. Analytical HPLC profile of **62** after preparative HPLC. Retention time = 19 min monitored by UV absorbance at 254 nm. Purity >90% by HPLC.

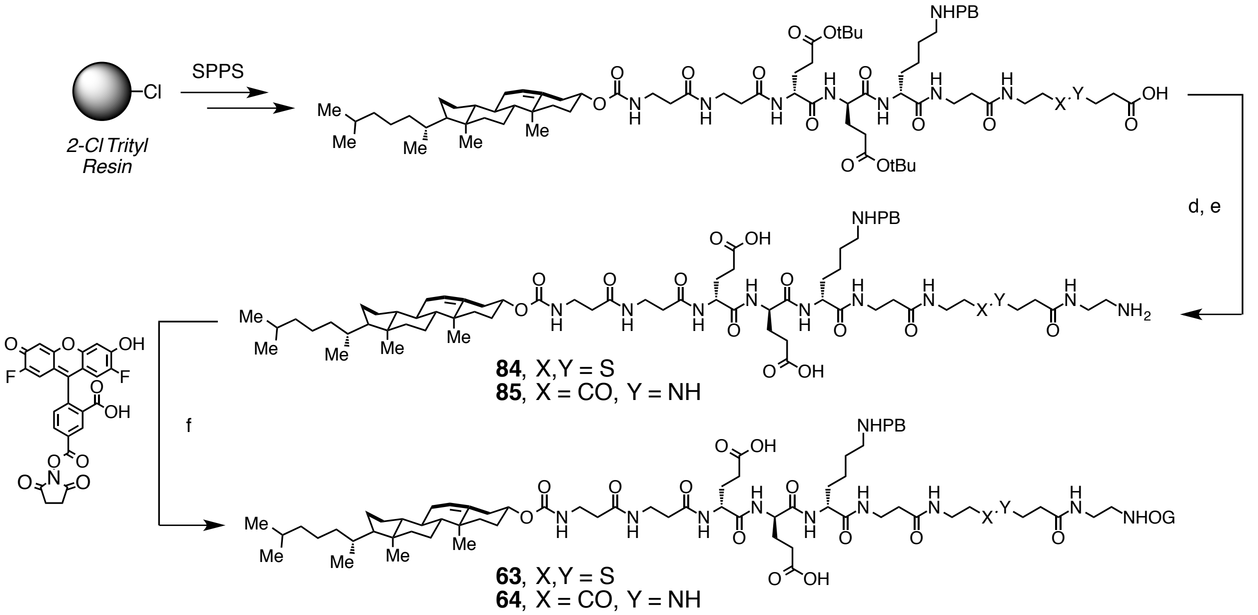

Figure 4.15. Reagents and conditions: d) *N*-Boc-ethylenediamine**,** HATU, DIEA, DMF; e) 30% TFA in DCM; f) DIEA, DMF; OG = Oregon Green, PB = Pacific Blue.

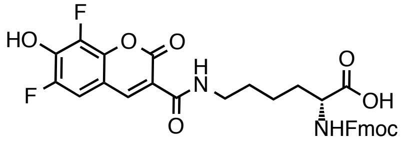

86

***N*^{2}-(((9*H*-Fluoren-9-yl)methoxy)carbonyl)-*N*^{6}-(6,8-difluoro-7-hydroxy-2-oxo-2*H*-chromene-3-carbonyl)-*D*-lysine (86, PB-D-Lys).** **5** (175 mg, 0.72 mmol), HATU (300 mg, 0.8 mmol) and DIEA (700 µL, 3.62 mmol) were stirred in anhydrous DMF (4 mL) at 22 °C for 30 minutes. Separately, Fmoc-D-Lys-OH (400 mg, 0.85 mmol) was treated with trifluoroacetic acid (TFA) / CH_2Cl_2 (5 mL, 30:70) for 20 min. The mixture was concentrated under vacuum and washed with CH_2Cl_2 (5 mL) and ether (5 mL x 2) to remove excess TFA. Following deprotection, the amine was dissolved in DMF (2 mL) and added to the activated acid solution. The reaction was stirred at 22 °C for 16 h. The vessel was placed on high vacuum for 2 h to remove DMF followed by purification by column chromatography on silica gel (eluent: DCM:acetone:acetic acid (83:15:2) to afford **86** (400 mg, 94%) as a light yellow solid. ^{1}H NMR (500 MHz, DMSO) δ 8.76 (d, *J* = 1.4 Hz, 1H), 8.61 (t, *J* = 5.8 Hz, 1H), 7.87 (dd, *J* = 7.6, 3.4 Hz, 2H), 7.76 – 7.69 (m, 3H), 7.67 (d, *J* = 8.1 Hz, 1H), 7.40 (tdd, *J* = 7.5, 4.0, 1.1 Hz, 2H), 7.32 (qd, *J* = 7.4, 1.2 Hz, 2H), 4.34 – 4.27 (m, 1H), 4.23 – 4.18 (m, 2H), 3.94 (ddd, *J* = 9.9, 8.0, 4.5 Hz, 1H), 3.32 (qd, *J* = 6.9, 2.8 Hz, 2H), 1.84 – 1.30 (m, 6H). ^{13}C NMR (126 MHz, DMSO) δ 174.4, 161.4, 160.0, 156.6, 149.2 (dd, *J* = 240.6, 4.7 Hz), 147.5, 144.2 (d, *J* = 9.2 Hz), 141.1 (d, *J* = 4.7 Hz), 140.9 (d, *J* = 8.4 Hz), 140.3 (d, *J* = 5.9 Hz), 139.2 (dd, *J* = 244.9, 6.6 Hz), 128.1, 128.0, 125.8, 125.7, 120.54, 120.50, 116.9, 110.9 (dd, *J* = 20.9, 3.0 Hz), 110.0 (d, *J* = 10.1 Hz), 66.1, 54.1, 47.1, 30.9, 29.0, 23.6; HRMS (ESI-) m/z 591.1556 (M-H$^+$), $C_{31}H_{25}F_2N_2O_8$ requires 591.1579).

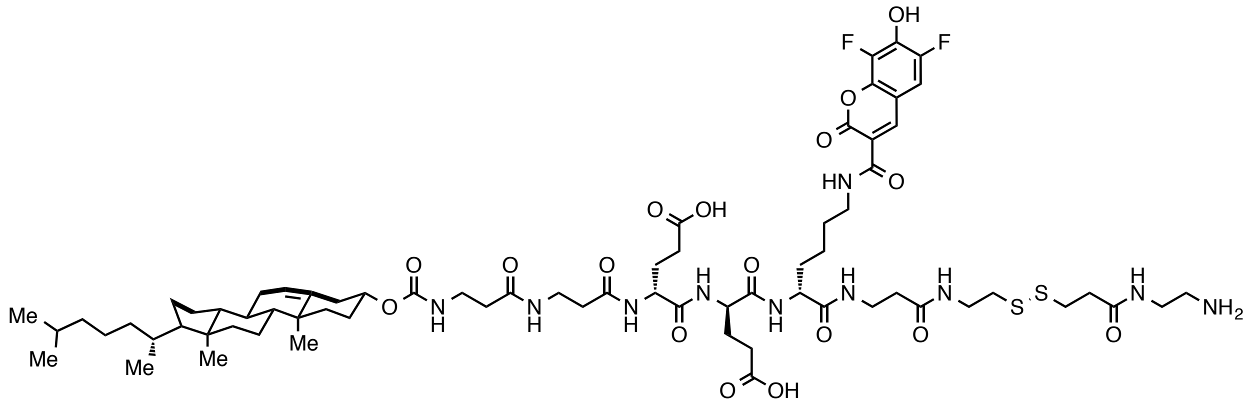

84

(17*R*,20*R*,23*R*)-1-Amino-20-(2-carboxyethyl)-17-(4-(6,8-difluoro-7-hydroxy-2-oxo-2*H*-chromene-3-carboxamido)butyl)-23-(3-(3-(((((3*R*,8*R*,9*R*,10*S*,13*S*,14*R*,17*S*)-10,13-dimethyl-17-((*R*)-6-methylheptan-2-yl)-2,3,4,7,8,9,10,11,12,13,14,15,16,17-tetradecahydro-1*H*-cyclopenta[*a*]phenanthren-3-yl)oxy)carbonyl)amino)propanamido)propanamido)-4,12,16,19,22-pentaoxo-7,8-dithia-3,11,15,18,21-pentaazahexacosan-26-oic acid (84). Following general procedure 4B, 3-((((cholester-3-yl)oxy)carbonyl) amino)propanoic acid,[43] PB-D-Lys (**80**), Fmoc-protected 3-((2-aminoethyl)disulfanyl)propanoic acid,[8] Fmoc-βAla-OH, and Fmoc-D-Glu-OH were used with 2-chlorotrityl resin (1.22 mmol/g) to produce a peptide. The crude peptide (30 mg, 0.02 mmol) and *N*-Boc-ethylenediamine (13 mg, 0.08 mmol) yielded **84** (18 mg, 62%). LRMS (ESI-) m/z 1457.7 (M-H$^+$ $C_{70}H_{103}F_2N_{10}O_{17}S_2$ requires 1457.7).

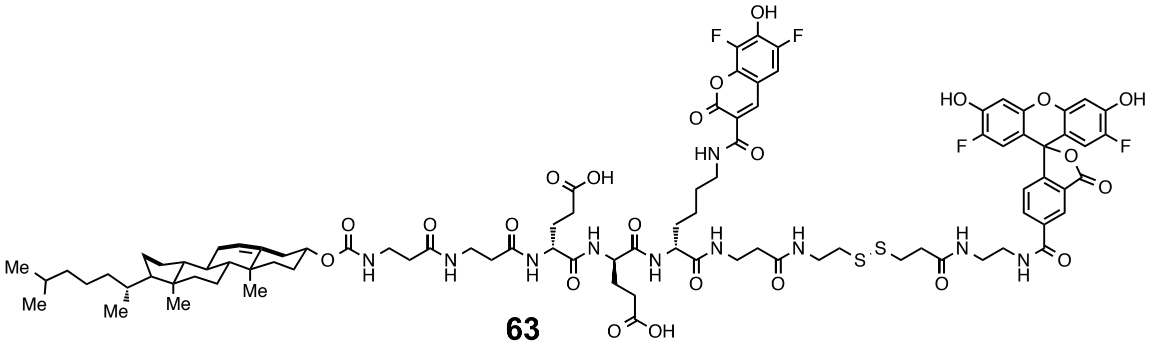

63

5-(((11*R*,14*R*,17*R*)-11,14-Bis(2-carboxyethyl)-17-(4-(6,8-difluoro-7-hydroxy-2-oxo-2*H*-chromene-3-carboxamido)butyl)-1-(((3*R*,8*R*,9*R*,10*S*,13*S*,14*R*,17*S*)-10,13-dimethyl-17-((*R*)-6-methylheptan-2-yl)-2,3,4,7,8,9,10,11,12,13,14,15,16,17-tetradecahydro-1*H*-cyclopenta[*a*]phenanthren-3-yl)oxy)-1,5,9,12,15,18,22,30-octaoxo-26,27-dithia-2,6,10,13,16,19,23,31-octaazatritriacontan-33-yl)carbamoyl)-2-(2,7-difluoro-6-hydroxy-3-oxo-3*H*-xanthen-9-yl)benzoic acid, (63). Following general procedure 4C, OG-NHS (1 mg, 0.002 mmol) and **84** (4.5 mg, 0.003 mmol) yielded compound **63** (3 mg, 81%) as a yellow solid. LRMS (ESI-) m/z 1851.5 (M-H$^+$ $C_{91}H_{111}F_4N_{10}O_{23}S_2$ requires 1851.7).

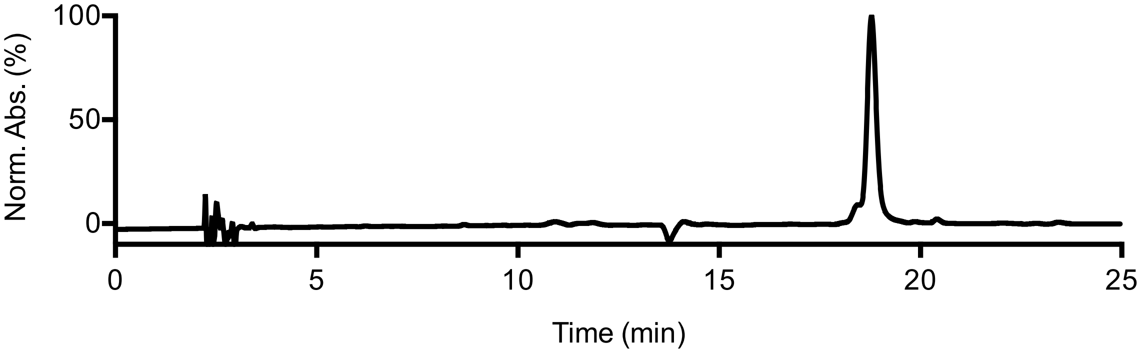

Figure 4.16. Analytical HPLC profile of **63** after preparative HPLC. Retention time = 19 min monitored by UV absorbance at 254 nm. Purity >95% by HPLC.

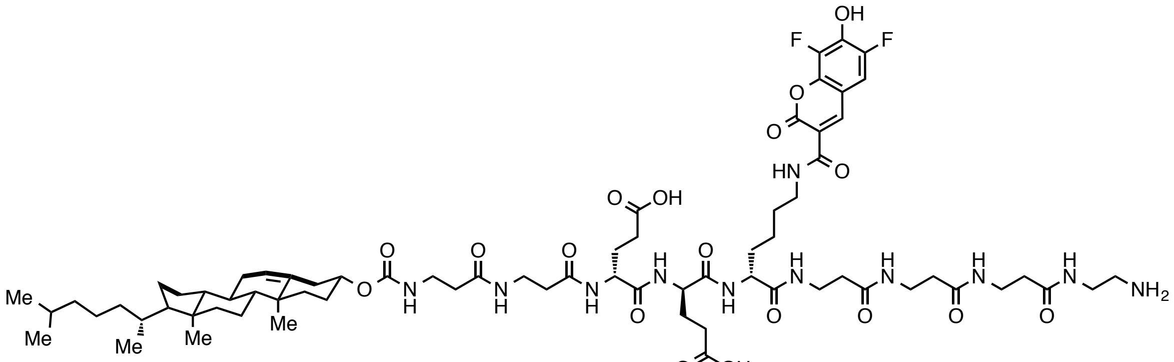

85

(17*R*,20*R*,23*R*)-1-Amino-20-(2-carboxyethyl)-17-(4-(6,8-difluoro-7-hydroxy-2-oxo-2*H*-chromene-3-carboxamido)butyl)-23-(3-(3-(((((3*R*,8*R*,9*R*,10*S*,13*S*,14*R*,17*S*)-10,13-dimethyl-17-((*R*)-6-methylheptan-2-yl)-2,3,4,7,8,9,10,11,12,13,14,15,16,17-tetradecahydro-1*H*-cyclopenta[*a*]phenanthren-3-yl)oxy)carbonyl)amino)propanamido)propanamido)-4,8,12,16,19,22-hexaoxo-3,7,11,15,18,21-hexaazahexacosan-26-oic acid (85). Following general procedure 4B, 3-((((cholester-3-yl)oxy)carbonyl) amino)propanoic acid[43], PB-D-Lys (**86**), Fmoc-β-ala-OH, and Fmoc-D-Glu-OH were used with 2-chlorotrityl resin (1.22 mmol/g) to produce a peptide. The crude peptide (30 mg, 0.02 mmol) and *N*-Boc-ethylenediamine (13 mg, 0.08 mmol) yielded **85** (15 mg, 50%). LRMS (ESI-) m/z 1437.1 (M-H$^+$ $C_{71}H_{104}F_2N_{11}O_{18}$ requires 1436.8).

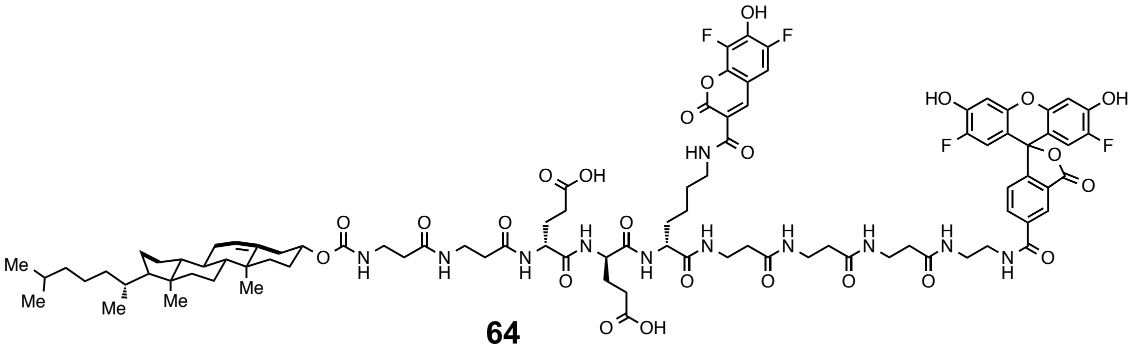

64

5-(((11*R*,14*R*,17*R*)-11,14-Bis(2-carboxyethyl)-17-(4-(6,8-sdifluoro-7-hydroxy-2-oxo-

2*H*-chromene-3-carboxamido)butyl)-1-(((3*R*,8*R*,9*R*,10*S*,13*S*,14*R*,17*S*)-10,13-dimethyl-17-((*R*)-6-methylheptan-2-yl)-2,3,4,7,8,9,10,11,12,13,14,15,16,17-tetradecahydro-1*H*-cyclopenta[*a*]phenanthren-3-yl)oxy)-1,5,9,12,15,18,22,26,30-nonaoxo-2,6,10,13,16,19,23,27,31-nonaazatritriacontan-33-yl)carbamoyl)-2-(2,7-difluoro-6-hydroxy-3-oxo-3*H*-xanthen-9-yl)benzoic acid (64). Following general procedure 4C, OG-NHS (1.5 mg, 0.003 mmol) and **85** (6 mg, 0.004 mmol) yielded compound **64** (3 mg, 53 %) as a yellow solid. LRMS (ESI-) m/z 1832.0 (M-H$^+$, $C_{92}H_{112}F_4N_{11}O_{24}$ requires 1830.8).

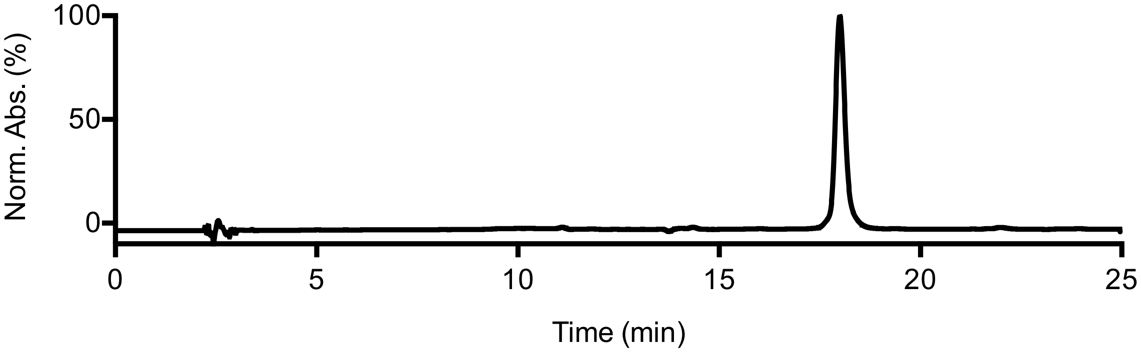

Figure 4.17. Analytical HPLC profile of **64** after preparative HPLC. Retention time = 18.5 min monitored by UV absorbance at 254 nm. Purity >95% by HPLC.

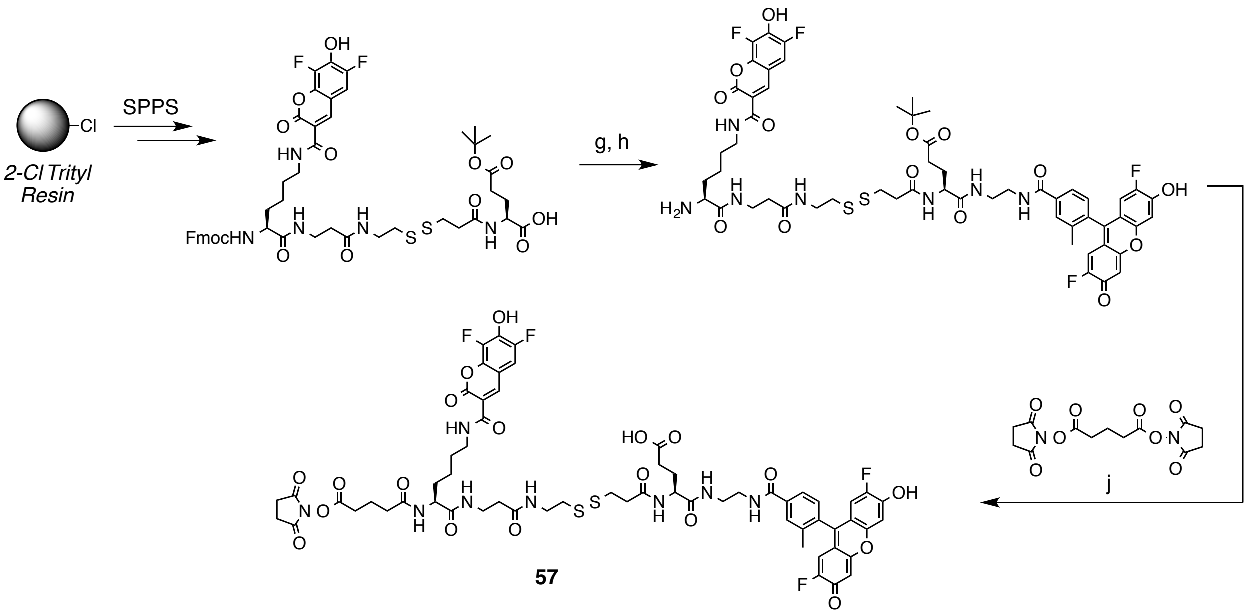

Figure 4.18. Reagents and conditions: g) **79,** 30% TFA in DCM; h) HATU, DIEA, DMF; j) i. 30% TFA in DCM, ii. DIEA, DMF. Schematic shown for **66**, but applies to **65**–**69** following general procedure 4D.

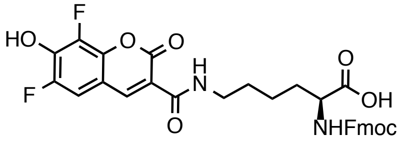

87

***N*²-(((9*H*-Fluoren-9-yl)methoxy)carbonyl)-*N*⁶-(6,8-difluoro-7-hydroxy-2-oxo-2*H*-chromene-3-carbonyl)-*L*-lysine (PB-L-Lys, 87).** To a solution of Fmoc-L-Lys-OH (1.76 g, 4.78 mmol) and DIEA (3.3 mL, 18.45 mmol) in DMF (20 mL) was added Pacific Blue NHS ester (**15**, 1.25 g, 3.69 mmol). The reaction mixture was stirred at 22 °C overnight. The reaction mixture was added dropwise to cold aq. HCl (1 N, 200 mL). The precipitate formed was filtered, washed with cold aq. HCl (1 N, 25 mL), and dried under vacuum to give **87** as a yellow solid (2.14 g, 98%). ^{1}H NMR (500 MHz, DMSO-d_6) δ 8.76 (d, *J* = 1.4 Hz, 1H), 8.61 (t, *J* = 5.8 Hz, 1H), 7.86 (dd, *J* = 7.5, 3.4 Hz, 2H), 7.74-7.64 (m, 3H), 7.39 (tdd, *J* = 7.6, 3.9, 1.1 Hz, 2H), 7.31 (qd, *J* = 7.4, 1.2 Hz, 2H), 4.42-4.11 (m, 3H), 3.93

(ddd, J = 10.0, 8.1, 4.5 Hz, 1H), 3.31 (qd, J = 6.9, 2.9 Hz, 2H), 1.89-1.24 (m, 6H). ^{13}C NMR (126 MHz, DMSO-d_6) δ 174.0, 161.0, 159.6, 156.2, 148.8 (d, J = 239.9 Hz), 147.1 (d, J = 3.7 Hz), 143.8, 143.8, 140.7, 140.7, 140.5 (d, J = 8.5 Hz), 140.0 (dd, J = 5.1, 2.4 Hz), 138.7 (dd, J = 245.3, 6.5 Hz), 127.6, 127.6, 127.1, 127.1, 127.1, 127.0, 125.3, 125.3, 125.3, 120.1, 120.1, 116.4, 110.5 (dd, J = 21.2, 2.4 Hz), 109.6 (d, J = 10.2 Hz), 65.6, 53.7, 46.7, 38.9, 30.4, 28.6, 23.1; HRMS (ESI-) m/z 591.1568 (M-H$^+$, $C_{31}H_{25}F_2N_2O_8$ requires 591.1579).

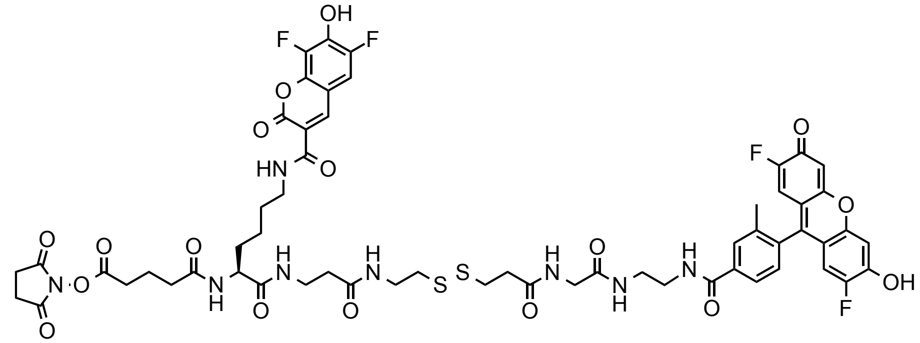

65

2,5-Dioxopyrrolidin-1-yl (*S*)-1-(4-(2,7-difluoro-6-hydroxy-3-oxo-3*H*-xanthen-9-yl)-3-methylphenyl)-22-(4-(6,8-difluoro-7-hydroxy-2-oxo-2*H*-chromene-3-carboxamido)butyl)-1,6,9,17,21,24-hexaoxo-12,13-dithia-2,5,8,16,20,23-hexaazaoctacosan-28-oate (65). Following general procedure 4D, PB-L-Lys (**87**), Fmoc-protected 3-((2-aminoethyl)disulfanyl)propanoic acid,[8] and Fmoc-βAla-OH were used with 2-chlorotrityl resin (1.22 mmol/g, 0.025 mmol) to produce **65** (4 mg, 13%). LRMS (ESI-) m/z 1277.7 (M-H$^+$, $C_{58}H_{57}F_4N_8O_{17}S_2$ requires 1277.3).

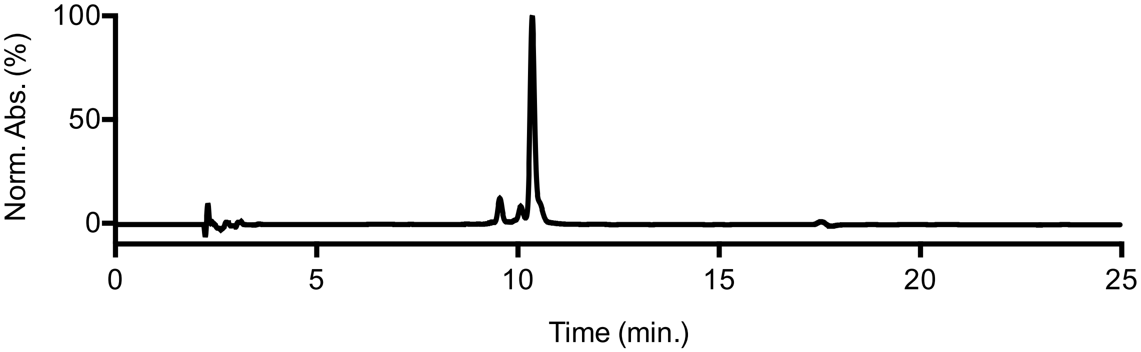

Figure 4.19. Analytical HPLC profile of **65** after preparative HPLC. Retention time = 10.5 min monitored by UV absorbance at 254 nm. Purity >90% by HPLC.

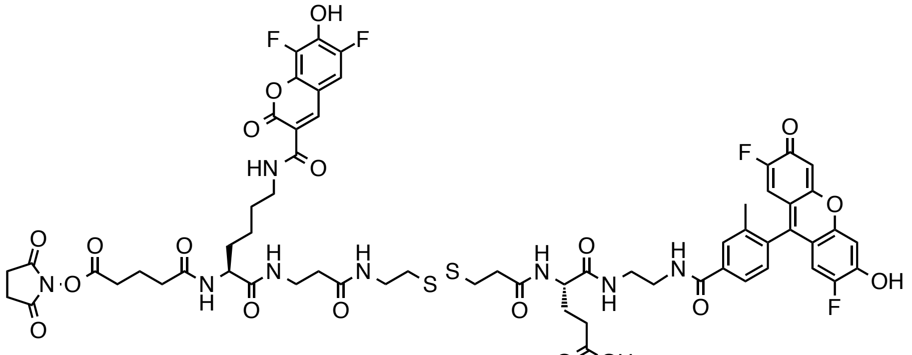

66

(7*S*,22*S*)-22-((2-(4-(2,7-Difluoro-6-hydroxy-3-oxo-3*H*-xanthen-9-yl)-3-methylbenzamido)ethyl)carbamoyl)-1-(6,8-difluoro-7-hydroxy-2-oxo-2*H*-chromen-3-yl)-7-(5-((2,5-dioxopyrrolidin-1-yl)oxy)-5-oxopentanamido)-1,8,12,20-tetraoxo-16,17-dithia-2,9,13,21-tetraazapentacosan-25-oic acid (66). Following general procedure 4D, PB-L-Lys (**87**), Fmoc-protected 3-((2-aminoethyl)disulfanyl)propanoic acid,[8] Fmoc-βAla-OH, and Fmoc-L-Glu-OH were used with 2-chlorotrityl resin (1.22 mmol/g, 0.025 mmol) to produce **66** (4 mg, 12%). LRMS (ESI-) m/z 1349.5 (M-H$^+$, $C_{61}H_{61}F_4N_8O_{19}S_2$ requires 1349.3).

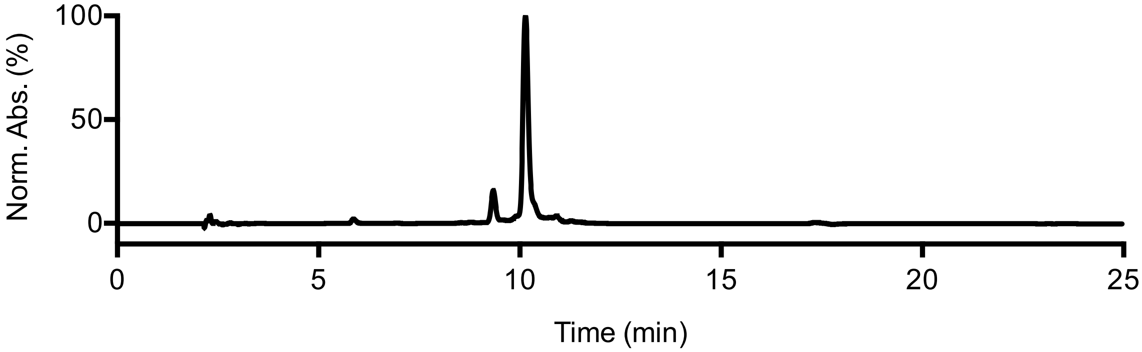

Figure 4.20. Analytical HPLC profile of **66** after preparative HPLC. Retention time = 10 min monitored by UV absorbance at 254 nm. Purity >90% by HPLC.

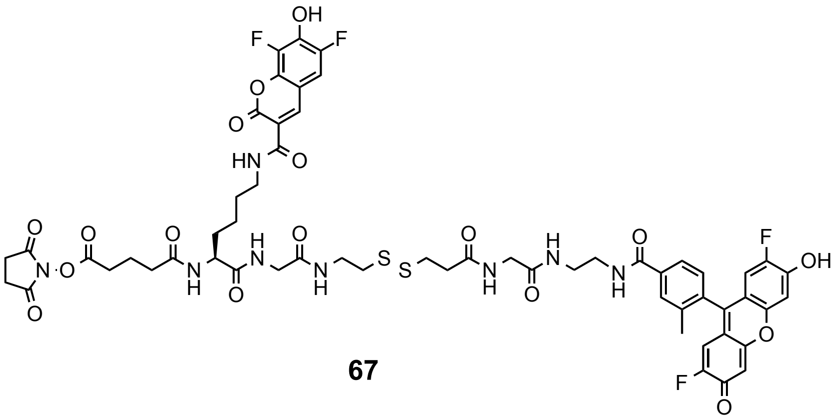

67

2,5-Dioxopyrrolidin-1-yl (*S*)-1-(4-(2,7-difluoro-6-hydroxy-3-oxo-3*H*-xanthen-9-yl)-3-methylphenyl)-21-(4-(6,8-difluoro-7-hydroxy-2-oxo-2*H*-chromene-3-carboxamido)butyl)-1,6,9,17,20,23-hexaoxo-12,13-dithia-2,5,8,16,19,22-hexaazaheptacosan-27-oate (67). Following general procedure 4D, PB-L-Lys (**87**), Fmoc-protected 3-((2-aminoethyl)disulfanyl)propanoic acid,[8] Fmoc-Gly-OH, and Fmoc-βAla-OH were used with 2-chlorotrityl resin (1.22 mmol/g, 0.025 mmol) to produce **67** (3 mg, 10%). LRMS (ESI-) m/z 1263.6 (M-H$^+$, $C_{57}H_{55}F_4N_8O_{17}S_2$ requires 1263.3).

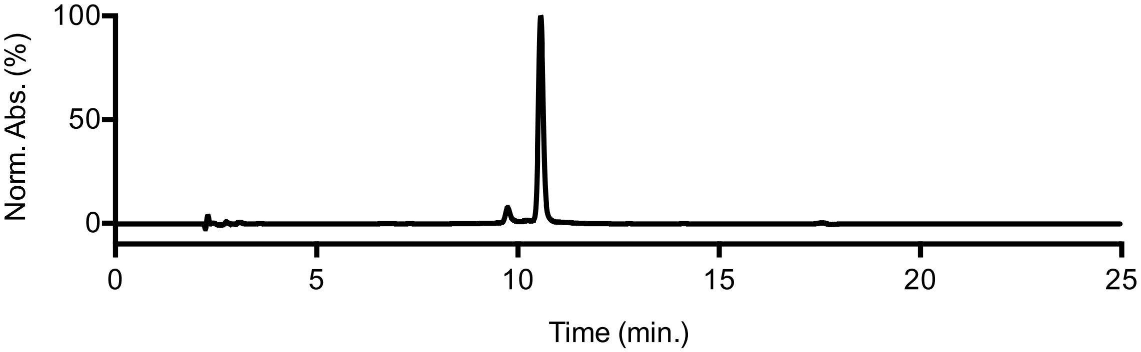

Figure 4.21. Analytical HPLC profile of **67** after preparative HPLC. Retention time = 11 min monitored by UV absorbance at 254 nm. Purity >90% by HPLC.

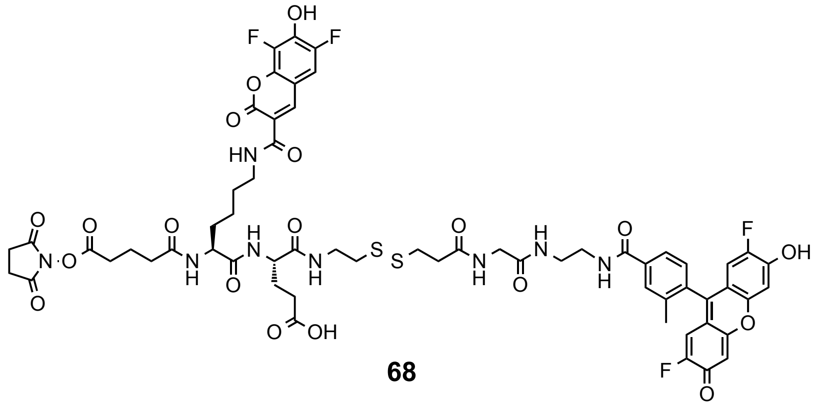

68

(*S*)-1-(4-(2,7-Difluoro-6-hydroxy-3-oxo-3*H*-xanthen-9-yl)-3-methylphenyl)-18-((*S*)-6-(6,8-difluoro-7-hydroxy-2-oxo-2*H*-chromene-3-carboxamido)-2-(5-((2,5-dioxopyrrolidin-1-yl)oxy)-5-oxopentanamido)hexanamido)-1,6,9,17-tetraoxo-12,13-dithia-2,5,8,16-tetraazahenicosan-21-oic acid (68). Following general procedure 4D, PB-L-Lys (**87**), Fmoc-protected 3-((2-aminoethyl)disulfanyl)propanoic acid,[8] Fmoc-L-Glu-OH, and Fmoc-βAla-OH were used with 2-chlorotrityl resin (1.22 mmol/g, 0.025 mmol) to produce **68** (2 mg, 6%). LRMS (ESI-) m/z 1335.5 (M-H$^+$, $C_{60}H_{59}F_4N_8O_{19}S_2$ requires 1335.3).

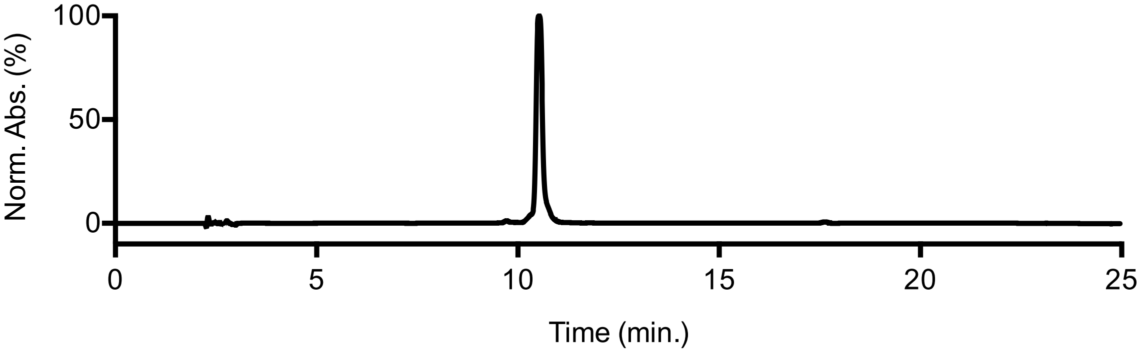

Figure 4.22. Analytical HPLC profile of **68** after preparative HPLC. Retention time = 10.5 min monitored by UV absorbance at 254 nm. Purity >95% by HPLC.

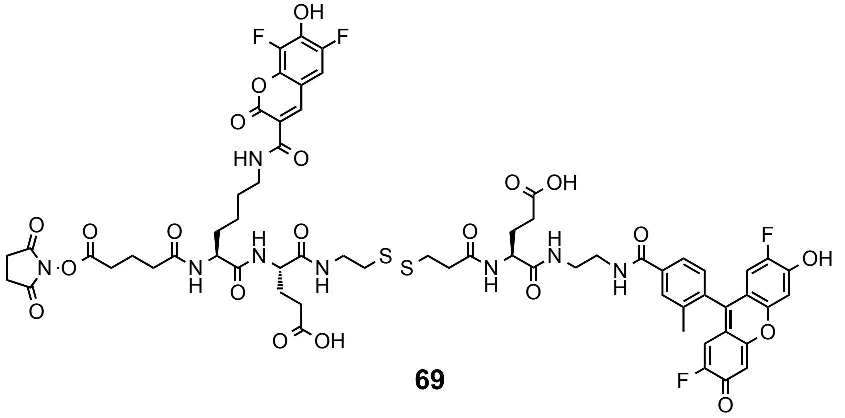

69

(7*S*,10*S*,21*S*)-10-(2-Carboxyethyl)-21-((2-(4-(2,7-difluoro-6-hydroxy-3-oxo-3*H*-xanthen-9-yl)-3-methylbenzamido)ethyl)carbamoyl)-1-(6,8-difluoro-7-hydroxy-2-oxo-2*H*-chromen-3-yl)-7-(5-((2,5-dioxopyrrolidin-1-yl)oxy)-5-oxopentanamido)-1,8,11,19-tetraoxo-15,16-dithia-2,9,12,20-tetraazatetracosan-24-oic acid (69). Following general procedure 4D, PB-L-Lys (**87**), Fmoc-protected 3-((2-aminoethyl)disulfanyl)propanoic acid,[8] and Fmoc-L-Glu-OH were used with 2-chlorotrityl resin (1.22 mmol/g, 0.025 mmol) to produce **69** (4 mg, 11%). LRMS (ESI-) m/z 1407.5 (M-H$^+$, $C_{63}H_{63}F_4N_8O_{21}S_2$ requires 1407.3).

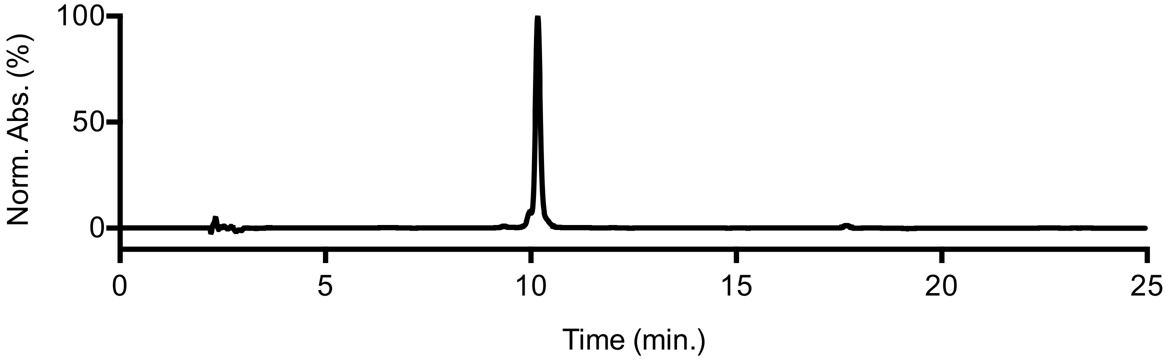

Figure 4.23. Analytical HPLC profile of **69** after preparative HPLC. Retention time = 10 min monitored by UV absorbance at 254 nm. Purity >90% by HPLC.

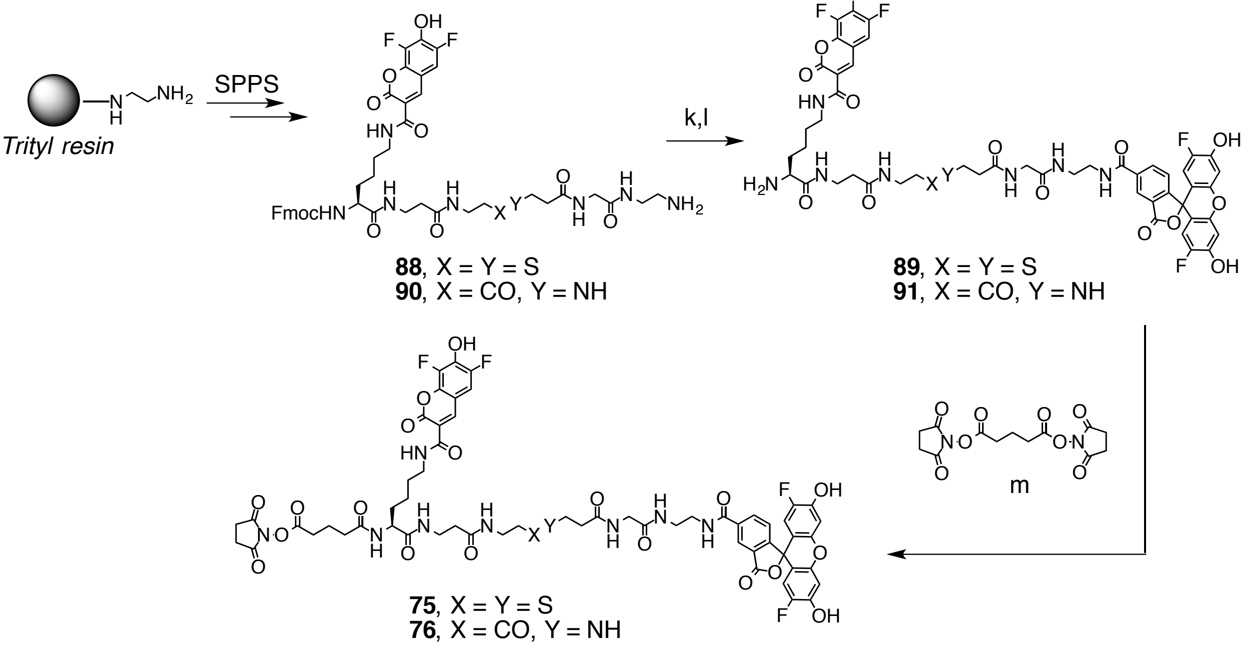

Figure 4.24. Reagents and conditions: k) OG-NHS ester, DIEA, DMF; l) 20% piperidine in DMF; m) DIEA, DMF.

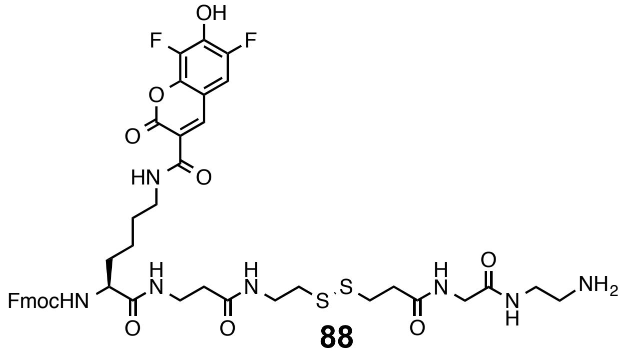

88

(9*H*-fluoren-9-yl)methyl (*S*)-(26-amino-1-(6,8-difluoro-7-hydroxy-2-oxo-2*H*-chromen-3-yl)-1,8,12,20,23-pentaoxo-16,17-dithia-2,9,13,21,24-pentaazahexacosan-7-yl)carbamate (88). Compound **88** was constructed using SPPS with 1,2-diaminoethane trityl resin (0.89 mmol/g, 0.05 mmol, 56 mg) with L-amino acids. The procedure for coupling as described in Section 2.10.3 (general procedure 2D) was followed. After completing all the steps of coupling reactions, the peptide was cleaved from the resin by treatment with a mixture of DCM/TFA (1:9) with shaking for 2 h. The resin was removed by filtration and washed with DCM (2 mL x 3). The filtrates were combined and concentrated under vacuum, followed by purification by preparative RP-HPLC (Gradient: H_2O:CH_3CN (9:1) to (0:100) with added TFA (0.1%) over 20 min; elution time = 11 min). Pure fractions were collected, combined, and solvent was removed by lyophilization to yield **88** (6 mg, 13%). LRMS (ESI-) m/z 924.3 (M-H$^+$ $C_{88}H_{108}F_4N_9O_{20}S_2$ requires 924.3).

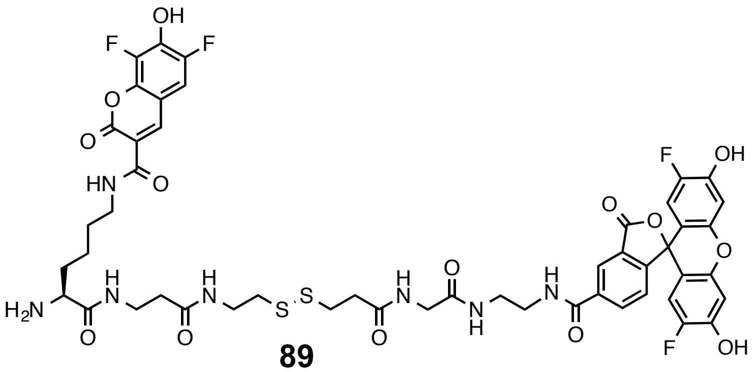

89

(*S*)-5-((7-amino-1-(6,8-difluoro-7-hydroxy-2-oxo-2*H*-chromen-3-yl)-1,8,12,20,23-pentaoxo-16,17-dithia-2,9,13,21,24-pentaazahexacosan-26-yl)carbamoyl)-2-(2,7-difluoro-6-hydroxy-3-oxo-3*H*-xanthen-9-yl)benzoic acid (89). To a solution of peptide **88** (5 mg, 0.0054 mmol) and DIEA (5 eq.) in DMF (0.5 mL), Oregon Green Carboxylic Acid succinimidyl ester (Thermo Fisher O6149, OG-NHS, 2.7 mg, 0.0054 mmol) was added. The reaction was stirred at 22 °C for 16 h. The vessel was placed on high vacuum for 2 h to remove DMF. The crude product was then treated with a solution of 20% piperidine in DMF (300 μL) for 20 min. The mixture was concentrated and purified by preparative RP-HPLC (Gradient: H_2O:CH_3CN (9:1) to (0:100) with added TFA (0.1%) over 20 min; elution time = 9–10 min). Pure fractions were collected, combined, and solvent was removed by lyophilization to yield **89** (5.6 mg, 94%). LRMS (ESI-) m/z 1096.4 (M-H^+ $C_{88}H_{108}F_4N_9O_{20}S_2$ requires 1096.3).

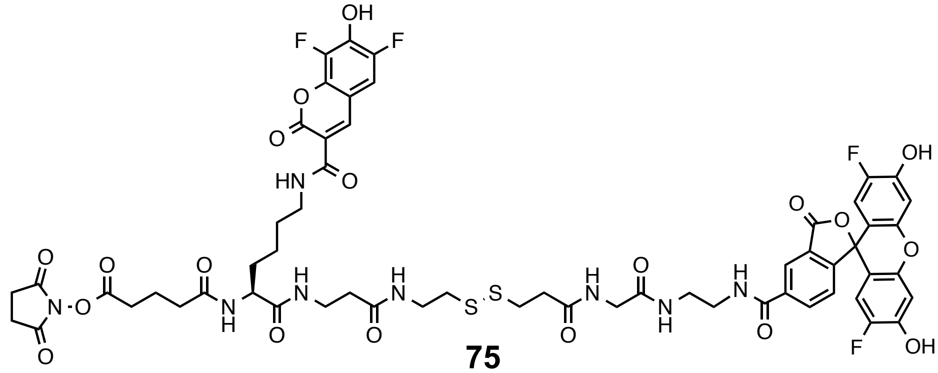

75

(*S*)-2-(2,7-difluoro-6-hydroxy-3-oxo-3*H*-xanthen-9-yl)-5-((1-(6,8-difluoro-7-hydroxy-2-oxo-2*H*-chromen-3-yl)-7-(5-((2,5-dioxopyrrolidin-1-yl)oxy)-5-oxopentanamido)-1,8,12,20,23-pentaoxo-16,17-dithia-2,9,13,21,24-pentaazahexacosan-26-yl)carbamoyl)benzoic acid (75). Peptide **89** (3.2 mg, 0.003 mmol) and disuccinimidyl glutarate (10 mg, 0.03 mmol) were dissolved in DMF (0.75 mL) with DIEA (2.5 μL, 0.015 mmol). The reaction was stirred at 22 °C for 16 h. The vessel was placed on high vacuum for 1 h to remove DMF. The reaction was concentrated and purified by preparative RP-HPLC (Gradient: H_2O:CH_3CN (9:1) to (0:100) with added TFA (0.1%) over 20 min; elution time = 8.5 min). Pure fractions were collected, combined, and solvent was removed by lyophilization to yield **75** (3 mg, 78%). LRMS (ESI-) m/z 1307.4 (M-H^+ $C_{88}H_{108}F_4N_9O_{20}S_2$ requires 1307.3).

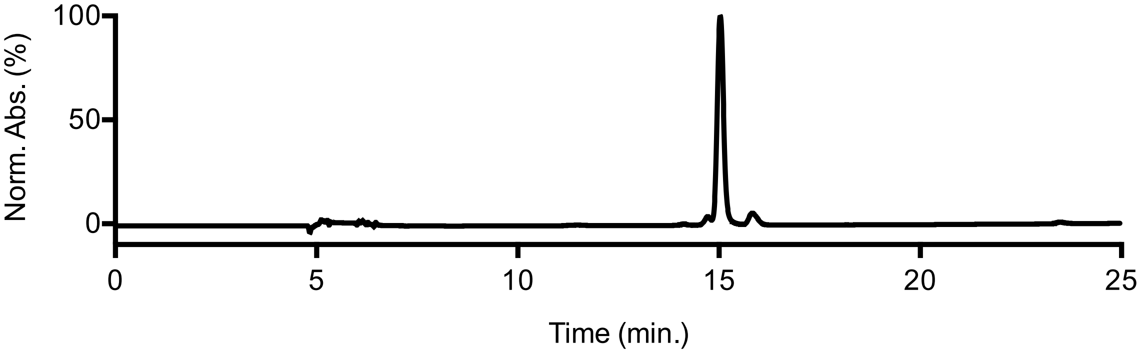

Figure 4.25. Analytical HPLC profile of **75** after preparative HPLC. Retention time = 15 min monitored by UV absorbance at 254 nm. Purity >90% by HPLC.

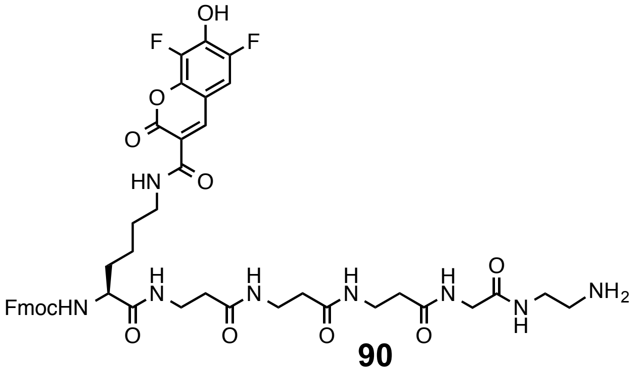

90

(9*H*-fluoren-9-yl)methyl (*S*)-(26-amino-1-(6,8-difluoro-7-hydroxy-2-oxo-2*H*-chromen-3-yl)-1,8,12,16,20,23-hexaoxo-2,9,13,17,21,24-hexaazahexacosan-7-yl)carbamate (90). Compound **90** was constructed using SPPS with 1,2-diaminoethane trityl resin (0.89 mmol/g, 0.05 mmol, 56 mg) with L-amino acids. The procedure for coupling as described in Section 2.10.3 (general procedure 2D) was followed. After completing all the steps of coupling reactions, the peptide was cleaved from the resin by treatment with a mixture of DCM/TFA (1:9) with shaking for 2 h. The resin was removed by filtration and washed with DCM (2 mL x 3). The filtrates were combined and concentrated under vacuum, followed by purification by preparative RP-HPLC (Gradient: H_2O:CH_3CN (9:1) to (0:100) with added TFA (0.1%) over 20 min; elution time = 10 min min). Pure fractions were collected, combined, and solvent was removed by lyophilization to yield **90** (5 mg, 11%). LRMS (ESI-) m/z 903.4 (M-H$^+$ $C_{88}H_{108}F_4N_9O_{20}S_2$ requires 903.3).

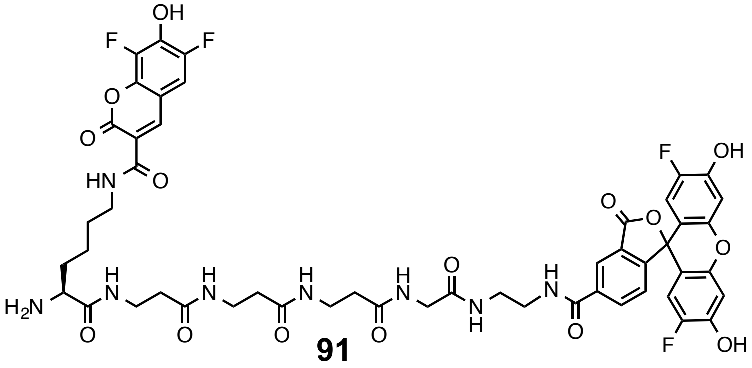

91

(*S*)-5-((7-amino-1-(6,8-difluoro-7-hydroxy-2-oxo-2*H*-chromen-3-yl)-1,8,12,16,20,23-hexaoxo-2,9,13,17,21,24-hexaazahexacosan-26-yl)carbamoyl)-2-(2,7-difluoro-6-hydroxy-3-oxo-3*H*-xanthen-9-yl)benzoic acid (91). To a solution of peptide **90** (4 mg, 0.0044 mmol) and DIEA (5 eq.) in DMF (0.5 mL), Oregon Green Carboxylic Acid succinimidyl ester (Thermo Fisher O6149, OG-NHS, 2.3 mg, 0.0044 mmol) was added. The reaction was stirred at 22 °C for 16 h. The vessel was placed on high vacuum for 2 h to remove DMF. The crude product was then treated with a solution of 20% piperidine in DMF (300 μL) for 20 min. The mixture was concentrated and purified by preparative RP-HPLC (Gradient: H_2O:CH_3CN (9:1) to (0:100) with added TFA (0.1%) over 20 min; elution time = 9 min). Pure fractions were collected, combined, and solvent was removed by lyophilization to yield **91** (4.5 mg, 95%). LRMS (ESI-) m/z 1065.5 (M-H$^+$ $C_{88}H_{108}F_4N_9O_{20}S_2$ requires 1075.3).

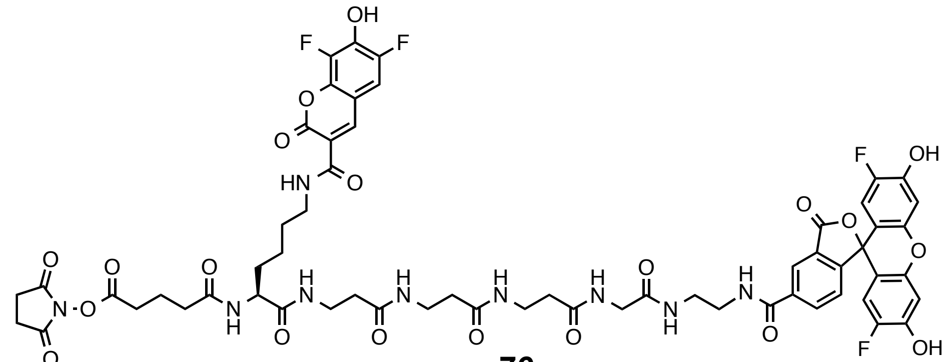

76

(*S*)-2-(2,7-difluoro-6-hydroxy-3-oxo-3*H*-xanthen-9-yl)-5-((1-(6,8-difluoro-7-hydroxy-2-oxo-2*H*-chromen-3-yl)-7-(5-((2,5-dioxopyrrolidin-1-yl)oxy)-5-oxopentanamido)-1,8,12,16,20,23-hexaoxo-2,9,13,17,21,24-hexaazahexacosan-26-yl)carbamoyl)benzoic acid (76). Peptide **91** (2 mg, 0.0019 mmol) and disuccinimidyl glutarate (6 mg, 0.019 mmol) were dissolved in DMF (0.5 mL) with DIEA (2 µL, 0.009 mmol). The reaction was stirred at 22 °C for 16 h. The vessel was placed on high vacuum for 1 h to remove DMF. The reaction was concentrated and purified by preparative RP-HPLC (Gradient: H_2O:CH_3CN (9:1) to (0:100) with added TFA (0.1%) over 20 min; elution time = 8 min). Pure fractions were collected, combined, and solvent was removed by lyophilization to yield **76** (1.5 mg, 64%). LRMS (ESI-) m/z 1286.4 (M-H^+ $C_{88}H_{108}F_4N_9O_{20}S_2$ requires 1286.4).

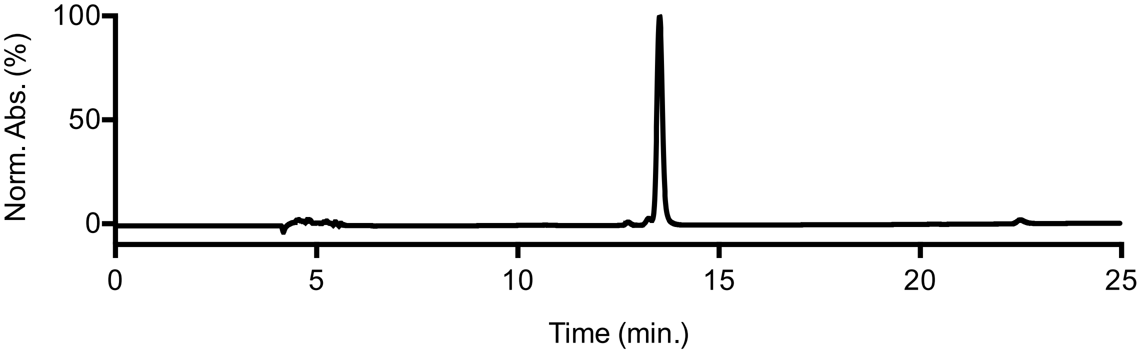

Figure 4.26. Analytical HPLC profile of **76** after preparative HPLC. Retention time = 13.5 min monitored by UV absorbance at 254 nm. Purity >95% by HPLC.

4.8. References

1. Firer, M. A.; Gellerman, G., Targeted drug delivery for cancer therapy: the other side of antibodies. *J. Hematol. Oncol.* **2012,** *5*, 70-70.

2. Tiwari, G.; Tiwari, R.; Sriwastawa, B.; Bhati, L.; Pandey, S.; Pandey, P.; Bannerjee, S. K., Drug delivery systems: An updated review. *Int. J. Pharm Investig.* **2012,** *2*, 2-11.

3. De Jong, W. H.; Borm, P. J. A., Drug delivery and nanoparticles: Applications and hazards. *Int. J. Nanomedicine* **2008,** *3*, 133-149.

4. Wang, A. Z.; Langer, R.; Farokhzad, O. C., Nanoparticle Delivery of Cancer Drugs. *Annu. Rev. Med.* **2012,** *63*, 185-198.

5. Bareford, L. M.; Swaan, P. W., Endocytic Mechanisms for Targeted Drug Delivery. *Adv. Drug Deliv. Reviews* **2007,** *59*, 748-758.

6. Hymel, D.; Peterson, B. R., Synthetic cell surface receptors for delivery of therapeutics and probes. *Adv. Drug Deliv. Rev.* **2012,** *64*, 797-810.

7. Boonyarattanakalin, S.; Martin, S. E.; Dykstra, S. A.; Peterson, B. R., Synthetic mimics of small mammalian cell surface receptors. *J. Am. Chem. Soc.* **2004,** *126*, 16379-16386.

8. Sun, Q.; Cai, S.; Peterson, B. R., Selective Disruption of Early/Recycling Endosomes: Release of Disulfide-Linked Cargo Mediated by a N-Alkyl-3β-Cholesterylamine-Capped Peptide. *J. Am. Chem. Soc.* **2008,** *130*, 10064-10065.

9. Peterson, B. R., Synthetic mimics of mammalian cell surface receptors: prosthetic molecules that augment living cells. *Org. Biomol. Chem.* **2005,** *3*, 3607-3612.

10. Boonyarattanakalin, S.; Athavankar, S.; Sun, Q.; Peterson, B. R., Synthesis of an artificial cell surface receptor that enables oligohistidine affinity tags to function as metal-dependent cell-penetrating peptides. *J. Am. Chem. Soc.* **2006,** *128*, 386-387.

11. Boonyarattanakalin, S.; Hu, J.; Dykstra-Rummel, S. A.; August, A.; Peterson, B. R., Endocytic delivery of vancomycin mediated by a synthetic cell surface receptor: rescue of bacterially infected mammalian cells and tissue targeting in vivo. *J. Am. Chem. Soc.* **2007,** *129*, 268-269.

12. Boonyarattanakalin, S.; Martin, S. E.; Sun, Q.; Peterson, B. R., A Synthetic Mimic of Human Fc Receptors: Defined Chemical Modification of Cell Surfaces Enables Efficient Endocytic Uptake of Human Immunoglobulin-G. *J. Am. Chem. Soc.* **2006,** *128*, 11463-11470.

13. Hymel, D.; Cai, S.; Sun, Q.; Henkhaus, R. S.; Perera, C.; Peterson, B. R., Fluorescent mimics of cholesterol that rapidly bind surfaces of living mammalian cells. *Chem. Comm.* **2015,** *51*, 14624-14627.

14. Hirosue, S.; Weber, T., pH-Dependent Lytic Peptides Discovered by Phage-Display. *Biochemistry* **2006,** *45*, 6476-6487.

15. Chari, R. V. J., Expanding the Reach of Antibody–Drug Conjugates. *ACS Med. Chem. Lett.* **2016,** *7*, 974-976.

16. Sievers, E. L.; Senter, P. D., Antibody-Drug Conjugates in Cancer Therapy. *Annu. Rev. Med.* **2013,** *64*, 15-29.

17. Peng, L.; Chen, X., Antibody–Drug Conjugates. *Bioconj. Chem.* **2015,** *26*, 2169-2169.

18. Ducry, L.; Stump, B., Antibody−Drug Conjugates: Linking Cytotoxic Payloads to Monoclonal Antibodies. *Bioconj. Chem.* **2010,** *21*, 5-13.

19. Shefet-Carasso, L.; Benhar, I., Antibody-targeted drugs and drug resistance: Challenges and solutions. *Drug Resist. Updates* **2014,** *18*, 36-46.

20. Diamantis, N.; Banerji, U., Antibody-drug conjugates– an emerging class of cancer treatment. *Br. J. Cancer* **2016,** *114*, 362-367.

21. Flygare, J. A.; Pillow, T. H.; Aristoff, P., Antibody-Drug Conjugates for the Treatment of Cancer. *Chem. Biol. Drug. Des.* **2013,** *81*, 113-121.

22. Zolot, R. S.; Basu, S.; Million, R. P., Antibody-drug conjugates. *Nat. Rev. Drug. Discov.* **2013,** *12*, 259-260.

23. Austin, C. D.; Wen, X.; Gazzard, L.; Nelson, C.; Scheller, R. H.; Scales, S. J., Oxidizing potential of endosomes and lysosomes limits intracellular cleavage of disulfide-based antibody–drug conjugates. *Proc. Natl. Acad. Sci. USA* **2005,** *102*, 17987-17992.

24. Yang, J.; Chen, H.; Vlahov, I. R.; Cheng, J.-X.; Low, P. S., Evaluation of disulfide reduction during receptor-mediated endocytosis by using FRET imaging. *Proc. Natl. Acad. Sci. USA* **2006,** *103*, 13872-13877.

25. Falnes, P. Ø.; Olsnes, S., Cell-mediated Reduction and Incomplete Membrane Translocation of Diphtheria Toxin Mutants with Internal Disulfides in the A Fragment. *J. Biol. Chem.* **1995,** *270*, 20787-20793.

26. Go, Y.-M.; Jones, D. P., Redox compartmentalization in eukaryotic cells. *Biochim. Biophys. Acta* **2008,** *1780*, 1273-1290.

27. Aubry, S.; Burlina, F.; Dupont, E.; Delaroche, D.; Joliot, A.; Lavielle, S.; Chassaing, G.; Sagan, S., Cell-surface thiols affect cell entry of disulfide-conjugated peptides. *FASEB J.* **2009,** *23*, 2956-2967.

28. Vlahov, I. R.; Leamon, C. P., Engineering Folate–Drug Conjugates to Target Cancer: From Chemistry to Clinic. *Bioconj. Chem.* **2012,** *23*, 1357-1369.

29. Yang, J. J.; Kularatne, S. A.; Chen, X.; Low, P. S.; Wang, E., Characterization of in Vivo Disulfide-Reduction Mediated Drug Release in Mouse Kidneys. *Mol. Pharm.* **2012,** *9*, 310-317.

30. Mottram, L. F.; Boonyarattanakalin, S.; Kovel, R. E.; Peterson, B. R., The Pennsylvania Green Fluorophore: a hybrid of Oregon Green and Tokyo Green for the construction of hydrophobic and pH-insensitive molecular probes. *Org. Lett.* **2006,** *8*, 581-4.

31. Mottram, L. F.; Maddox, E.; Schwab, M.; Beaufils, F.; Peterson, B. R., A Concise Synthesis of the Pennsylvania Green Fluorophore and Labeling of Intracellular Targets with O6-Benzylguanine Derivatives. *Org. Lett.* **2007,** *9*, 3741-3744.

32. Woydziak, Z. R.; Fu, L.; Peterson, B. R., Efficient and Scalable Synthesis of 4-Carboxy-Pennsylvania Green Methyl Ester: A Hydrophobic Building Block for Fluorescent Molecular Probes. *Synthesis* **2014,** *46*, 158-164.

33. Wu, P. G.; Brand, L., Resonance Energy Transfer: Methods and Applications. *Anal. Biochem.* **1994,** *218*, 1-13.

34. Dixon, J. M.; Taniguchi, M.; Lindsey, J. S., PhotochemCAD 2: A Refined Program with Accompanying Spectral Databases for Photochemical Calculations¶. *Photochem. Photobiol.* **2005,** *81*, 212-213.

35. Wolfrum, C.; Shi, S.; Jayaprakash, K. N.; Jayaraman, M.; Wang, G.; Pandey, R. K.; Rajeev, K. G.; Nakayama, T.; Charrise, K.; Ndungo, E. M.; Zimmermann, T.; Koteliansky, V.; Manoharan, M.; Stoffel, M., Mechanisms and optimization of in vivo delivery of lipophilic siRNAs. *Nat. Biotech.* **2007,** *25*, 1149-1157.

36. Wang, J.; Lu, Z.; Wientjes, M. G.; Au, J. L. S., Delivery of siRNA Therapeutics: Barriers and Carriers. *AAPS J.* **2010,** *12*, 492-503.

37. Hattori, Y.; Hara, E.; Shingu, Y.; Minamiguchi, D.; Nakamura, A.; Arai, S.; Ohno, H.; Kawano, K.; Fujii, N.; Yonemochi, E., siRNA Delivery into Tumor Cells by Cationic Cholesterol Derivative-Based Nanoparticles and Liposomes. *Biol. Pharm. Bull.* **2015,** *38*, 30-38.

38. Ercole, F.; Whittaker, M. R.; Quinn, J. F.; Davis, T. P., Cholesterol Modified Self-Assemblies and Their Application to Nanomedicine. *Biomacromolecules* **2015,** *16*, 1886-1914.

39. Hupe, D. J.; Wu, D., Effect of charged substituents on rates of the thiol-disulfide interchange reaction. *J. Org. Chem.* **1980,** *45*, 3100-3103.

40. Rusinova, E.; Tretyachenko-Ladokhina, V.; Vele, O. E.; Senear, D. F.; Alexander Ross, J. B., Alexa and Oregon Green dyes as fluorescence anisotropy probes for measuring protein–protein and protein–nucleic acid interactions. *Anal. Biochem.* **2002,** *308*, 18-25.

41. Meulendyke, K. A.; Wurth, M. A.; McCann, R. O.; Dutch, R. E., Endocytosis Plays a Critical Role in Proteolytic Processing of the Hendra Virus Fusion Protein. *J. Virol.* **2005,** *79*, 12643-12649.

42. Amiri-Kordestani, L.; Blumenthal, G. M.; Xu, Q. C.; Zhang, L.; Tang, S. W.; Ha, L.; Weinberg, W. C.; Chi, B.; Candau-Chacon, R.; Hughes, P.; Russell, A. M.; Miksinski, S. P.; Chen, X. H.; McGuinn, W. D.; Palmby, T.; Schrieber, S. J.; Liu, Q.; Wang, J.; Song, P.; Mehrotra, N.; Skarupa, L.; Clouse, K.; Al-Hakim, A.; Sridhara, R.; Ibrahim, A.; Justice, R.; Pazdur, R.; Cortazar, P., FDA Approval: Ado-Trastuzumab Emtansine for the Treatment of Patients with HER2-Positive Metastatic Breast Cancer. *Clin. Cancer Res.* **2014,** *20*, 4436-4441.

43. Yu, X.; Liu, Q.; Wu, J.; Zhang, M.; Cao, X.; Zhang, S.; Wang, Q.; Chen, L.; Yi, T., Sonication-Triggered Instantaneous Gel-to-Gel Transformation. *Chem. Eur. J.* **2010,** *16*, 9099-9106.

Chapter 5

Development of Fluorescence-based Assays of Inhibitors of BfrB

5.1. Introduction

Pseudomonas aeruginosa is an opportunistic Gram-negative bacterium that infects both plants and animals. It is a leading cause of nosocomial infections, defined as those acquired under medical care, and accounts for 10% of all hospital-acquired infections.[1] This bacterium adapts to its surroundings, including surfaces within hospitals and clinics, making it particularly dangerous in these settings.[2] *P. aeruginosa* primarily affects patients with compromised immune systems, such as those with neutropenia, AIDS, severe burns, and cystic fibrosis.[3]

Cystic fibrosis (CF) is congenital, inherited disease characterized by mutations in the gene encoding cystic fibrosis transmembrane conductance regulator (CFTR), a cAMP-regulated chloride channel.[2] Approximately 80% of adult patients with cystic fibrosis are chronically infected with *P. aeruginosa,* and these lung infections are typically associated with morbidity.[4, 5] Although recent advances have improved the treatment of lung infections in CF,[4, 6] biofilms and drug resistance continue to hinder treatment strategies. Because *P. aeruginosa* is highly dependent on iron-dependent processes for infectivity and biofilm formation,[7, 8] a better understanding of iron uptake in this bacterium could be critical for the discovery of new treatments.

Iron is an essential cofactor in DNA synthesis, respiration, and nitrogen fixation, as it is able to participate in one-electron transfer reactions that catalyze enzymatic processes.[9, 10] Proper regulation of iron homeostasis is critical in nature, since Fe^{2+} can react with O_2 and H_2O_2 to form insoluble Fe^{3+}, reactive hydroxyl radicals, and superoxide via the Haber-Weiss reaction.[11] To avoid the formation of these reactive oxygen species, cells tightly regulate iron acquisition and storage through the use of iron storage proteins and siderophores.[12] Iron storage proteins, such as ferritins (Ftn), bacterioferritins (Bfr), and DNA binding proteins (Dps), store iron intracellularly and are particularly crucial for survival of bacteria under iron depletion conditions.

Bacterioferritins are unique to bacteria and their major functions are to oxidize reactive Fe^{2+} to Fe^{3+}, store the mineral, and release it when needed.[13] Bfrs are assembled into a polymeric spherical structure consisting of 24 subunits with an outer diameter of 120 Å and an inner diameter of 80 Å. The hollow core can store up to 3500 iron atoms.[14, 15] Two subunits are paired to form a dimer with heme, and therefore 12 heme molecules are present in each 24-mer protein.[16] Bfrs contain a ferroxidase center that converts Fe^{2+} to Fe^{3+}. This oxidation step is followed by translocation to the interior cavity, where it is mineralized for storage. Utilizing electrons originating from NADPH, the iron atoms are then reduced and released to the cytosol, a process facilitated by a ferrodoxin reductase and bacterioferritin-associated ferrodoxin (Bfd).[17, 18] In *P. aeruginosa* (*Pa*), *Pa*-Bfd binds to *Pa*-BfrB (K_d = 3 μM) and facilitates iron mobilization by heme-mediated electron transfer.[19] Rivera and coworkers found that this protein-protein interaction consists of a highly complementary interface with a network of hotspots defined by leucines, glutamic acids, and a tyrosine that are conserved across a number of pathogenic species.[20]

5.2. A new strategy to overcome multidrug resistance in *P. aeruginosa*

P. aeruginosa is considered a ‘superbug’ due to its high propensity to acquire multidrug resistance. The low permeability of its outer membrane, as well as secondary adaptive resistance mechanisms such as increased efflux and enzymatic antibiotic modifications, enable it to be resistant to a wide range of antibiotics from β-lactams to fluoroquinolones.[21] Drug resistance is increasing,[1] and therefore new strategies must be developed to fight this bacterium. As described in Section 5.1, iron is an essential nutrient, but can be toxic if improperly regulated. This vulnerability could possibly be exploited through inhibition of the bacterial BfrB:Bfd interaction. Since BfrB is unique to bacteria and archaea,[22] disruption of this protein-protein interaction could present a novel, specific way to treat patients infected with *P. aeruginosa.*

To investigate this antibacterial approach, Dr. Huili Yao and Dr. Mario Rivera at the University of Kansas Dept. of Chemistry conducted an iterative fragment based drug discovery (FBDD) screen. In FBDD, a relatively small library of low molecular weight compounds that are generally polar and soluble is often screened by NMR against a protein target. When possible, this method provides an attractive alternative to more traditional high-throughput screening of large libraries of drug-like molecules. The fragments used in FBDD typically bind proteins with low affinity (mM) and are later combined with other fragments to generate leads for a drug discovery campaign.[23] For the initial screen against BfrB, the Rivera group used saturation transfer difference nuclear magnetic resonance spectroscopy (STD-NMR). STD-NMR is an attractive method for FDBB because it focuses on the signal of the ligand, so processing of additional NMR information of the receptor is unnecessary.[24] A fragment training set was screened to find molecules (hits) that bound at the BfrB:Bfd binding site. These hits were then tested for binding to BfrB by two orthogonal assays, SPR and X-ray crystallography. By SPR, FC996 (Figure 5.1) was found to bind BfrB with a K_d of 1.3 mM, and a high-resolution X-ray co-crystal structure further confirmed that this small molecule bound BfrB occurred in a cleft where Bfd normally associates.

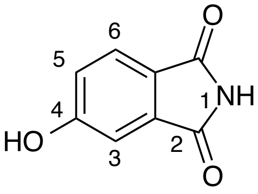

FC996

Figure 5.1. Structure of FC996 (4-hydroxyphthalimide), the initial hit found by the Rivera group via a FBDD screen. The phthalimide ring is numbered to clarify the differential substitution patterns of analogues that were later investigated.

After the initial hit was identified, more than 100 second generation compounds were designed to take advantage of additional interactions at the Bfd:BfrB binding interface. Docking to BfrB using Autodock vina[25] were performed on each of the derivatives, and those that showed promising docking scores were synthesized and investigated for binding and inhibition of iron release. Initial binding studies were performed using SPR, but this format was limited by solubility, as a high concentration of DMSO needed to solubilize these compounds altered the results of the assay and complicated the interpretation of the results.

This chapter will describe a new assay that we developed that uses fluorescence polarization to quantify the binding affinities of the derivatives of FC996 to BfrB. I will describe the spectral properties of the compounds tested, as well as discuss challenges that hindered the development of the assay. I will additionally describe the degradation of a lead compound that led to the discovery of new interactions in the binding pocket, and discuss potential future directions for this project.

5.3. Toward a new fluorescence polarization assay for BfrB:Bfd inhibitors

Docking and X-ray crystallography studies of BfrB revealed that substitution of potentially inhibitory phthalimides at the 3-position could be more favorable than substitution at the 4-position, as is observed in FC996. Based on these studies, compound **92** (Figure 5.2, panel A) was designed and synthesized as a lead compound capable of dose-dependent inhibition of iron release in a functional assay performed in the Rivera group. To examine the photophysical properties of **92**, we obtained excitation and fluorescence emission spectra of **92** (Figure 5.2, panel B). This compound has an excitation λ_{max} at ~400 nm, and an emission λ_{max} at 530 nm. Although a high concentration of this ligand was needed due to low brightness, compound **92** showed a 3-fold increase in fluorescence polarization when glycerol was added to buffer, indicating that as the mobility of the compound was restricted (due to the increase in viscosity of the solvent), the polarization of the compound was altered.[26]

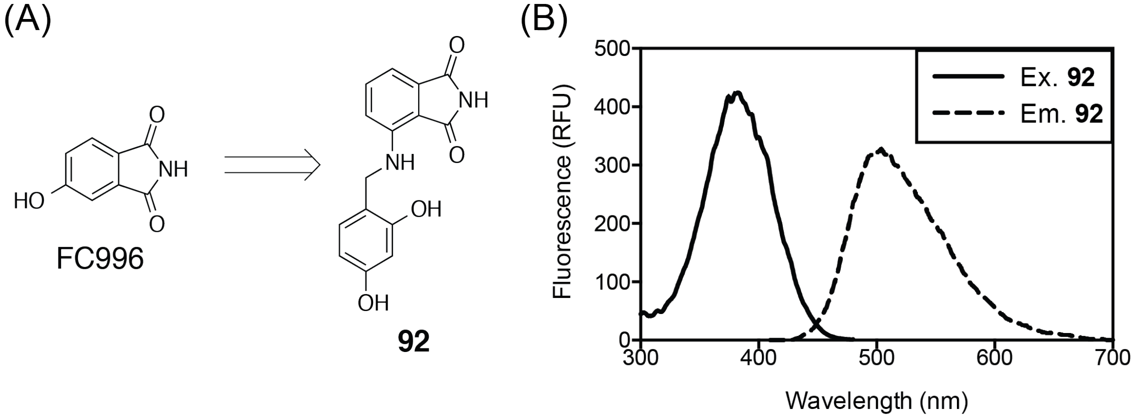

Figure 5.2. A: Structure of inhibitor **92**, a second generation derivative of FC996. B: The excitation spectrum (λ_{em} = 530 nm, solid line) and emission spectrum (λ_{ex} = 380 nm dotted line) of **92** (10 μM) in KP_i (100 mM, pH 7.6), containing TCEP (1 mM) are shown.

Spectroscopic studies revealed that the 12-heme molecules of the holo-BfrB protein fluoresce, and this intrinsic fluorescence was found to interfere with the signal from the fluorescent ligand. To overcome this complication, we used Apo-BfrB for fluorescence polarization assays. To confirm that studies using Apo-BfrB were valid, Dr. Huili Yao and Dr. Mario Rivera measured the binding affinity of Bfd to Apo-BfrB and holo-BfrB and found identical K_d values of 3 μM. Since the BfrB-Bfd interface is at the surface of the protein, the absence of heme, which is buried within the 24-mer protein, should not have a large effect on these binding interactions. To investigate the affinity of **92** binding to BfrB, Apo-BfrB was titrated into a fixed concentration of the fluorescent ligand for 1 h, followed by excitation at 380 nm and analysis of fluorescence polarization at λ_{em} = 565 nm. Curve fitting was initially used to calculate a direct binding K_d value of ~ 50 μM, but this number was found to fluctuate unpredictably under these conditions. To investigate these fluctuations, we monitored the fluorescence of **92** over time and discovered large changes in its spectral properties in buffer (Figure 5.3, panels A and B). The λ_{max} for absorption shifted from 415 nm to 380 nm after 90 min in buffer, and the fluorescence intensity of the compound increased significantly over time. To explain these results, we proposed that **92** degrades to 3-aminophthalimide in buffer over time (Figure 5.3, panel C), and this hypothesis was confirmed by subsequent NMR spectroscopy studies. However, since the docking results with this compound were promising, and we desired to determine the binding affinity of BfrB for **92**, we minimized the incubation time to maintain **92** in buffer for only a total of 10 minutes, which decreased the effects of degradation. Under these conditions, ApoBfrb was titrated into a fixed concentration of **92** for 5 min, followed by excitation at 380 nm, and changes in polarization at λ_{em} = 565 nm were detected. This modified approach allowed calculation of a direct binding K_d value 4 μM after curve fitting.

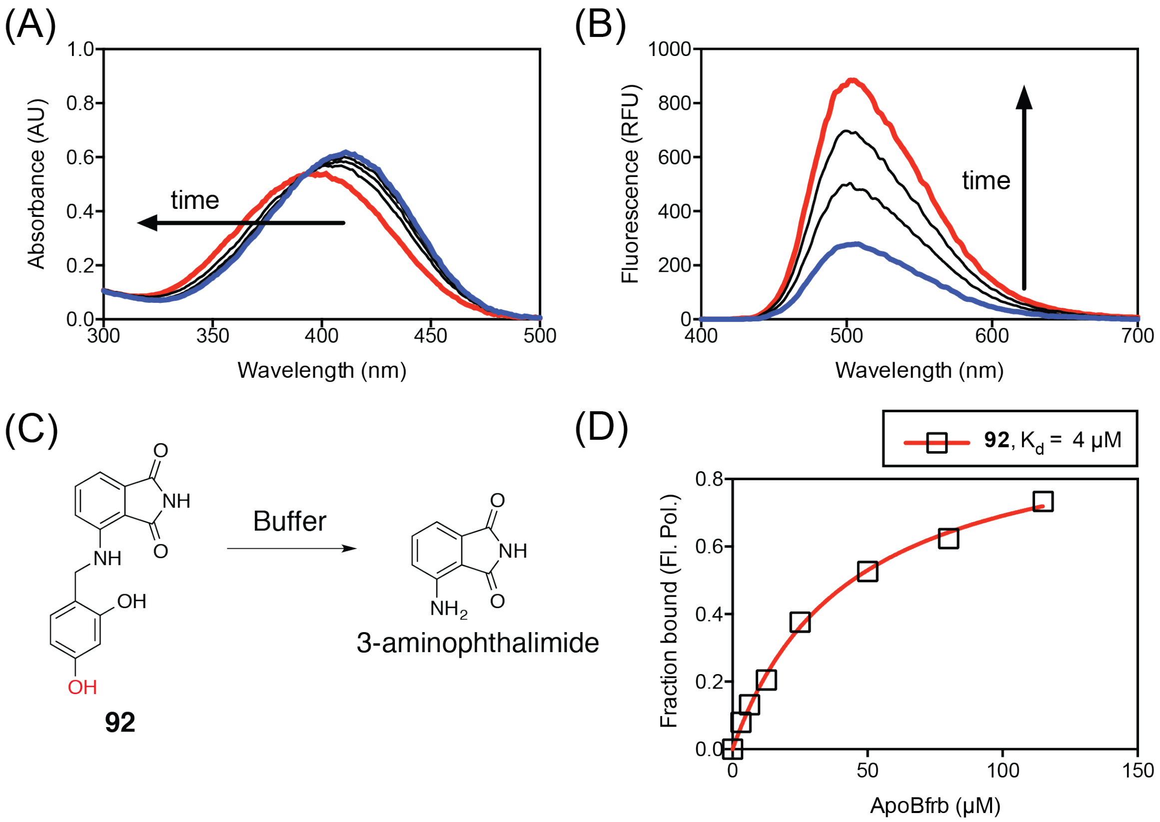

Figure 5.3. Spectral evidence of degradation of compound **92** in KP_i buffer (100 mM). Absorbance (panel A) and emission (panel B) spectra of **92** over a 90-minute period. As **92** is incubated in buffer, it degrades to form 3-aminophthalmide (panel C). The absorbance is slightly decreased and blue-shifted, while the emission is significantly increased. D: Quantification of the affinity (K_d) of Apo-BfrB for probe **92** (5 μM) in KP_i (100 mM, pH 7.6) containing TCEP (1 mM) by FP. The probe was briefly incubated in buffer for 5 min and with protein for 5 min to minimize degradation. Values were corrected to account for fluorescence enhancement upon binding. [Apo-BfrB] was based on a dimer (two subunits). Dissociation constants (K_d) were calculated using a one-site binding model in GraphPad Prism.

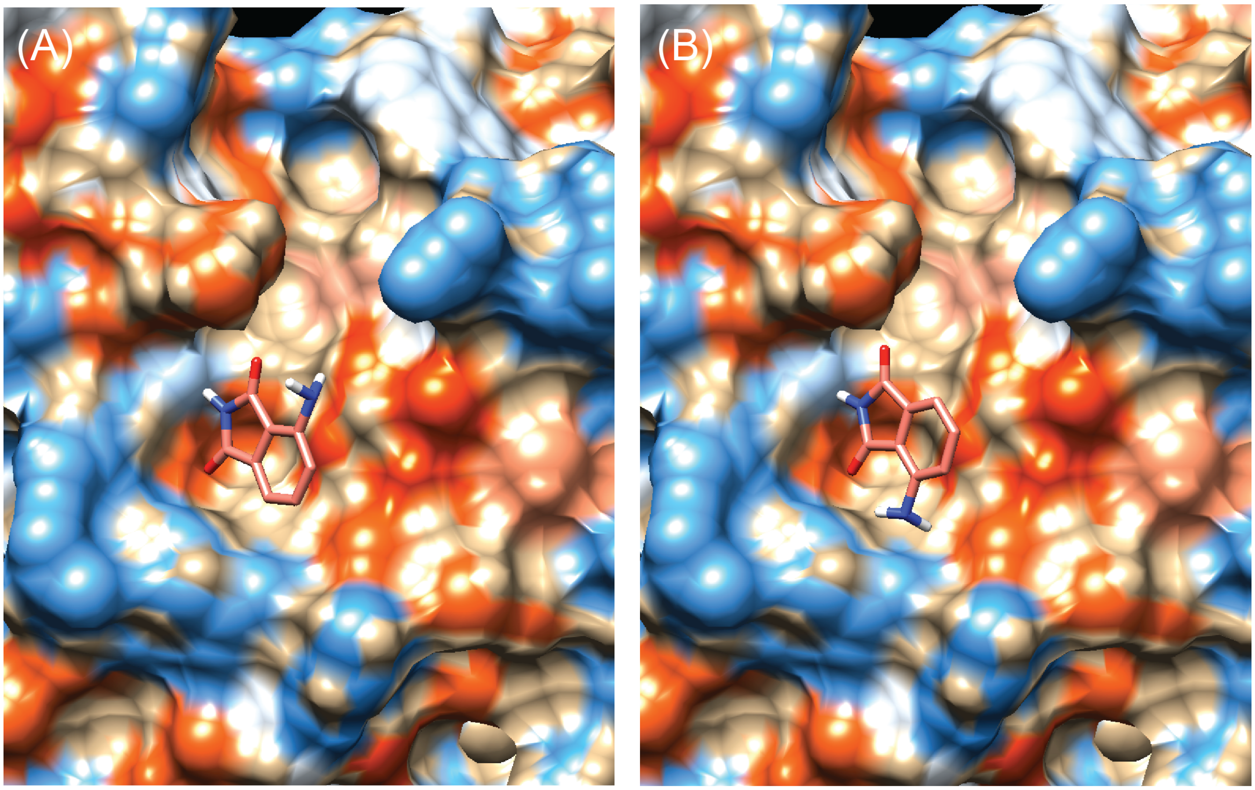

Figure 5.4. X-ray crystal structure of *Pa*-BfrB[20] (PDB 3IS7) with models of 3-aminophthalimide bound in two different poses generated with Autodock vina.

Stability testing of other derivatives revealed that the phenol at the 4 position of the southern ring (Figure 5.3, panel C, atom highlighted in red) was destabilizing the linkage between the two ring systems. Additionally, docking studies showed that in some poses 3-aminophthalimide was rotated by 180° and could interact with a different set of amino acids at the BfrB:Bfd binding interface (Figure 5.4). This could explain the large differences in affinity between 3-aminophthalimide (~50 μM, measured by FP, data not shown) and FC996 (1.3 mM, measured by SPR by Rivera group) for BfrB. From these two observations, compound **93** was designed to remove the 4-phenol on the southern ring and incorporate an amine at the 6-position of the phthalimide. To generate an equilibrium binding curve, Apo-Bfrb was titrated into a fixed concentration of this fluorescent ligand for 1 h, followed by excitation at 405 nm and detection of changes in polarization at λ_{em} = 530 nm. Curve fitting was used to calculate a direct binding K_d value 4 ± 1 μM (Figure 5.5), indicating that any activity that was lost from removal of the 4-phenol on the southern ring was regained through additional interactions of the 6-amino group on the phthalimide ring system.

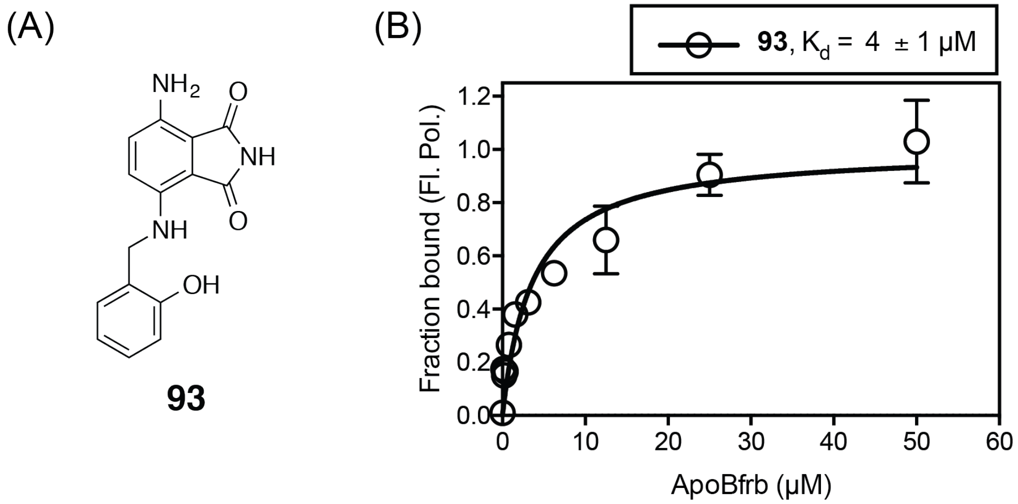

Figure 5.5. A: Structure of the third generation inhibitor **93**. B: Quantification of the affinity (K_d) of Apo-BfrB for probe **93** (1 μM) in 100 mM KP_i (pH 7.6) with TCEP (1 mM) by FP. Values were corrected to account for fluorescence enhancement upon binding. [ApoBfrB] was based on monomeric protein. Dissociation constants (K_d) were calculated using a one-site binding model in GraphPad Prism.

5.4. Conclusions and future directions

The laboratory of Prof. Mario Rivera designed inhibitors of the BfrB:Bfd protein-protein interaction based on a hit that they found through a FBDD screen using STD-NMR. To test the affinity of these compounds, we collaborated with the Rivera laboratory to develop a new fluorescence polarization assay. One promising compound, **92**, was found to bind 1,000-fold more tightly than the original hit, but suffered from instability. It was determined that the product of degradation was 3-aminophthalimide, which binds more tightly to ApoBfrB than other phthalimides studied. Docking studies with 3-aminophthalimide revealed there could be two binding modes for this compound. Based on this information, a new compound, **93**, was developed to take advantage of both binding modes, and proved to be comparable in affinity to the unstable lead compound **92**.

Future studies of more highly fluorescent analogues are needed to improve the utility of this assay for drug screening applications. High concentrations of the fluorescent ligand are required to detect the low fluorescence of **93**, and these high concentrations approach the K_d values of some of the highest affinity compounds identified to date, making this assay unsuitable for quantification of new inhibitors that might have affinities of less than one micromolar. If the fluorophore was substantially brighter, the concentration of the probe could be substantially decreased and competition assays could be used to discover more potent ligands. The BfrB:Bfd protein-protein interaction offers a promising target for antimicrobial inhibition of *Pseudomonas aeruginosa* and could help to overcome challenges arising from multidrug resistance observed with this superbug. Better inhibitors, as well as assays to screen these inhibitors more readily, need to be developed for this goal to be realized.

5.5. Experimental

Apo-BfrB was expressed and purified as described previously.[15, 19] Absorbance spectra and measurements of molar extinction coefficients (ε) were generated using semimicro (1.4 mL) UV quartz cuvettes (Sigma-Aldrich, Z27667-7) on an Agilent 8452A diode array spectrometer. All optical spectroscopy and protein binding assays were conducted in 100 mM KP_i (pH 7.6) with TCEP (1 mM) unless otherwise noted. All fluorescence spectra were acquired using a SUPRASIL ultra-micro quartz cuvette (PerkinElmer, B0631079) on a Perkin-Elmer LS55 Fluorescence Spectrometer (10 nm excitation slit width).

Determination of K_d values of 92 by fluorescence polarization (FP)

Different concentrations of Apo-BfrB, chosen to span a range of at least 20% to 80% complexation, were incubated with fixed concentrations of **92** (5 μM) in 100 mM KP_i (pH 7.6) with TCEP (1 mM) at room temperature with shaking for 5 min. The probe was in buffer for a maximum of 5 minutes prior to incubation with protein to minimize degradation. These fixed probe concentrations were chosen to be below the predicted K_d values to assure equilibrium binding measurements. Measurements of fluorescence intensity and fluorescence polarization (I_{380} and P, λ_{ex}= 380 λ_{em}= 565 nm) were recorded for each sample. The change in polarization for each sample was calculated by subtracting the average (n=3) polarization of the free ligand (P_f). This change was plotted against the concentration of SA, and the maximum polarization of the fully bound complex was estimated (B_{max}) based on a one-site specific binding model (GraphPad Prism 6.0). This polarization of the complex (P_b) was used in the following equation to calculate the apparent fraction bound (F_a):

$$F_a = \frac{P - P_f}{P_b - P_f}$$

Background-subtracted fluorescence (I) signals were calculated as follows:

$$I = I_{380} - I_{Bfrb}$$

where I_{BfrB} is the background fluorescence intensity of the protein alone at each concentration measured, excited under the same conditions as the protein with **92**. In order to correct for fluorescence enhancement or quenching, a fluorescence enhancement factor (Q) was calculated using the following equation, where I and I_0 are the fluorescence intensity (λ_{ex}= 380 nm, λ_{em}= 565 nm) of the sample and free ligand, respectively:

$$Q = \frac{I - I_0}{I_0}$$

To incorporate fluorescence enhancement/quenching into the measurements, the corrected fraction bound (f_a) was calculated using the following equation:

$$f_a = \frac{F_a}{1 + Q(1 - F_a)}$$

To calculate the dissociation constant (K_d), the corrected fraction bound was plotted against the concentration of Apo-BfrB (dimer concentration), and a one site- specific binding equation of GraphPad Prism 6.0 was used for curve fitting. Note: for compound **93**, the same procedure was followed, but the concentration of the ligand was decreased to 1 μM, and excitation and emission wavelengths were as follows: λ_{ex}= 405 and λ_{em}= 530 nm.

5.6. References

1. Aloush, V.; Navon-Venezia, S.; Seigman-Igra, Y.; Cabili, S.; Carmeli, Y., Multidrug-Resistant Pseudomonas aeruginosa: Risk Factors and Clinical Impact. *Antimicrob. Agents Chemother.* **2006,** *50*, 43-48.

2. Gellatly, S. L.; Hancock, R. E. W., Pseudomonas aeruginosa: new insights into pathogenesis and host defenses. *Pathogens and Disease* **2013,** *67*, 159-173.

3. Lyczak, J. B.; Cannon, C. L.; Pier, G. B., Establishment of Pseudomonas aeruginosa infection: lessons from a versatile opportunist1. *Microbes Infect.* **2000,** *2*, 1051-1060.

4. Høiby, N., Recent advances in the treatment of Pseudomonas aeruginosainfections in cystic fibrosis. *BMC Medicine* **2011,** *9*, 32.

5. West, S. H.; Zeng, L.; Lee, B.; et al., Respiratory infections with pseudomonas aeruginosa in children with cystic fibrosis: Early detection by serology and assessment of risk factors. *JAMA* **2002,** *287*, 2958-2967.

6. Smith, D. J.; Lamont, I. L.; Anderson, G. J.; Reid, D. W., Targeting iron uptake to control Pseudomonas aeruginosa infections in cystic fibrosis. *Eur. Resp. J.* **2013,** *42*, 1723-1736.

7. Vasil, M. L.; Ochsner, U. A., The response of Pseudomonas aeruginosa to iron: genetics, biochemistry and virulence. *Mol. Microbiol.* **1999,** *34*, 399-413.

8. Kaneko, Y.; Thoendel, M.; Olakanmi, O.; Britigan, B. E.; Singh, P. K., The transition metal gallium disrupts Pseudomonas aeruginosa iron metabolism and has antimicrobial and antibiofilm activity. *J. Clin. Invest.* **2007,** *117*, 877-888.

9. Theil, E. C.; Goss, D. J., Living with Iron (and Oxygen): Questions and Answers about Iron Homeostasis. *Chem. Rev.* **2009,** *109*, 4568-4579.

10. Meneghini, R., Iron Homeostasis, Oxidative Stress, and DNA Damage. *Free Radic. Biol. Med.* **1997,** *23*, 783-792.

11. Haber, F.; Weiss, J., The Catalytic Decomposition of Hydrogen Peroxide by Iron Salts. *Proc. Roy. Soc. Lond. Math. Phys. Sci.* **1934,** *147*, 332-351.

12. Andrews, S. C., Iron Storage in Bacteria. In *Adv. Microbiol. Phys.*, Poole, R. K., Ed. Academic Press1998; Vol. Volume 40, pp 281-351.

13. Andrews, S. C.; Robinson, A. K.; Rodríguez-Quiñones, F., Bacterial iron homeostasis. *FEMS Microbiol. Rev.* **2003,** *27*, 215-237.

14. Lewin, A.; Moore, G. R.; Le Brun, N. E., Formation of protein-coated iron minerals. *Dalton Transactions* **2005**, 3597-3610.

15. Weeratunga, S. K.; Lovell, S.; Yao, H.; Battaile, K. P.; Fischer, C. J.; Gee, C. E.; Rivera, M., Structural Studies of Bacterioferritin B from Pseudomonas aeruginosa Suggest a Gating Mechanism for Iron Uptake via the Ferroxidase Center. *Biochemistry* **2010,** *49*, 1160-1175.

16. Macedo, S.; Romao, C. V.; Mitchell, E.; Matias, P. M.; Liu, M. Y.; Xavier, A. V.; LeGall, J.; Teixeira, M.; Lindley, P.; Carrondo, M. A., The nature of the di-iron site in the bacterioferritin from Desulfovibrio desulfuricans. *Nat. Struct. Mol. Biol.* **2003,** *10*, 285-290.

17. Rui, H.; Rivera, M.; Im, W., Protein Dynamics and Ion Traffic in Bacterioferritin. *Biochemistry* **2012,** *51*, 9900-9910.

18. Wang, A.; Zeng, Y.; Han, H.; Weeratunga, S.; Morgan, B. N.; Moënne-Loccoz, P.; Schönbrunn, E.; Rivera, M., Biochemical and Structural Characterization of Pseudomonas aeruginosa Bfd and FPR: Ferredoxin NADP+ Reductase and Not Ferredoxin Is the Redox Partner of Heme Oxygenase under Iron-Starvation Conditions. *Biochemistry* **2007,** *46*, 12198-12211.

19. Weeratunga, S. K.; Gee, C. E.; Lovell, S.; Zeng, Y.; Woodin, C. L.; Rivera, M., Binding of Pseudomonas aeruginosa Apobacterioferritin-Associated Ferredoxin to

Bacterioferritin B Promotes Heme Mediation of Electron Delivery and Mobilization of Core Mineral Iron. *Biochemistry* **2009,** *48*, 7420-7431.

20. Yao, H.; Wang, Y.; Lovell, S.; Kumar, R.; Ruvinsky, A. M.; Battaile, K. P.; Vakser, I. A.; Rivera, M., The Structure of the BfrB–Bfd Complex Reveals Protein–Protein Interactions Enabling Iron Release from Bacterioferritin. *J. Am. Chem. Soc.* **2012,** *134*, 13470-13481.

21. Breidenstein, E. B. M.; de la Fuente-Núñez, C.; Hancock, R. E. W., Pseudomonas aeruginosa: all roads lead to resistance. *Trends Microbiol.* **2011,** *19*, 419-426.

22. Andrews, S. C., The Ferritin-like superfamily: Evolution of the biological iron storeman from a rubrerythrin-like ancestor. *Biochim. Biophys. Acta (BBA) - General Subjects* **2010,** *1800*, 691-705.

23. Joseph-McCarthy, D.; Campbell, A. J.; Kern, G.; Moustakas, D., Fragment-Based Lead Discovery and Design. *J. Chem. Inf. Model.* **2014,** *54*, 693-704.

24. Viegas, A.; Manso, J.; Nobrega, F. L.; Cabrita, E. J., Saturation-Transfer Difference (STD) NMR: A Simple and Fast Method for Ligand Screening and Characterization of Protein Binding. *J. Chem. Ed.* **2011,** *88*, 990-994.

25. Trott, O.; Olson, A. J., AutoDock Vina: improving the speed and accuracy of docking with a new scoring function, efficient optimization and multithreading. *J. Comp. Chem.* **2010,** *31*, 455-461.

26. Jameson, D. M.; Ross, J. A., Fluorescence Polarization/Anisotropy in Diagnostics and Imaging. *Chem. Rev.* **2010,** *110*, 2685-2708.

Appendix A

NMR Spectra

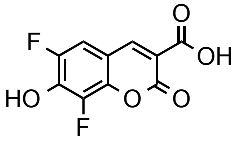

Pacific Blue (**5**)

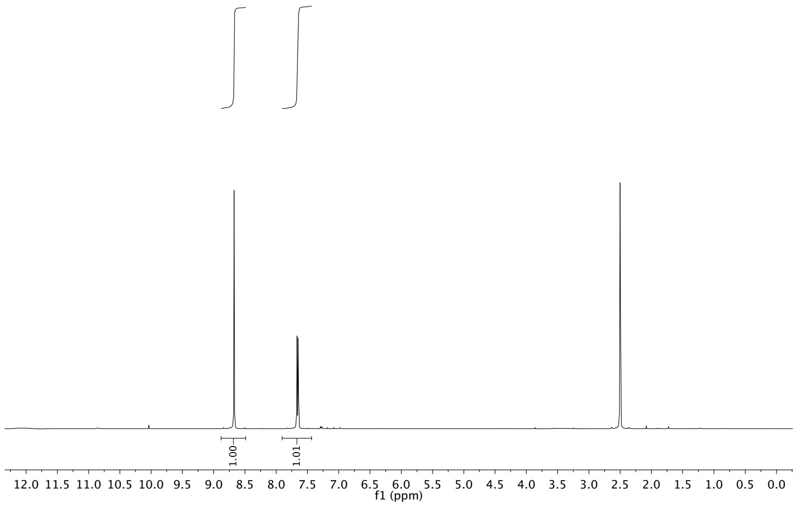

Figure 6.1. ^{1}H NMR (500 MHz, DMSO-d_6) spectrum of **5**.

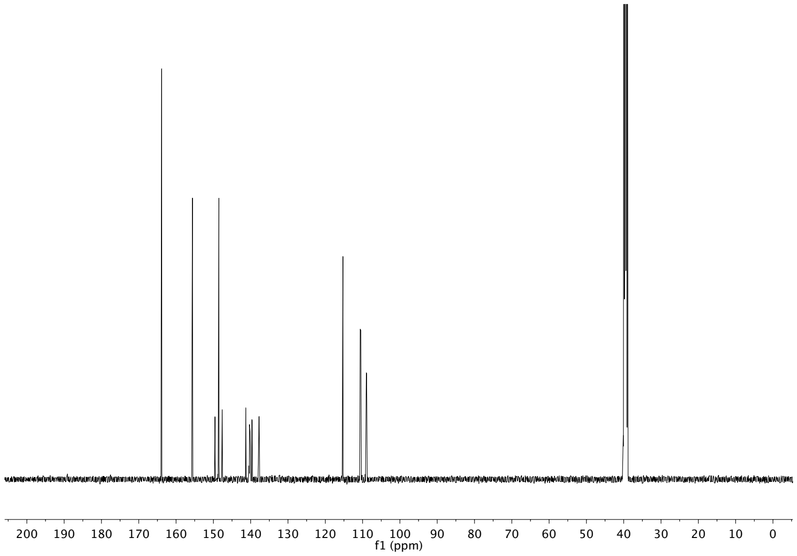

Figure 6.2. ^{13}C NMR (126 MHz, DMSO-d_6) spectrum of **5**.

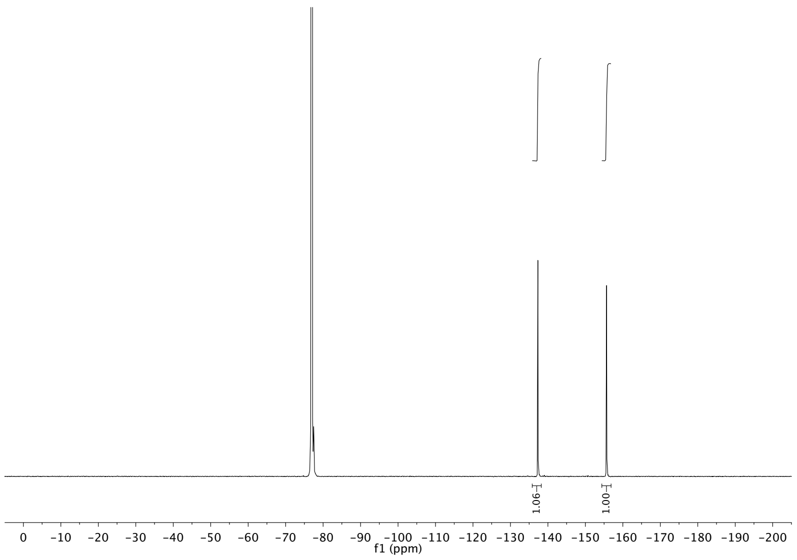

Figure 6.3. ^{19}F NMR (376 MHz, DMSO-d_6, decoupled) spectrum of **5**.

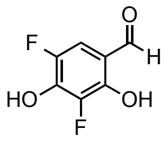

11

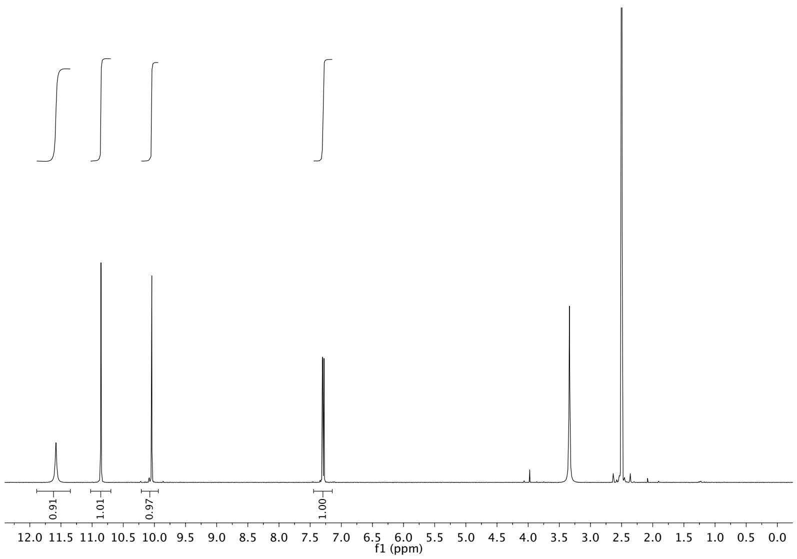

Figure 6.4. ^{1}H NMR (500 MHz, DMSO-d_6) spectrum of **11**.

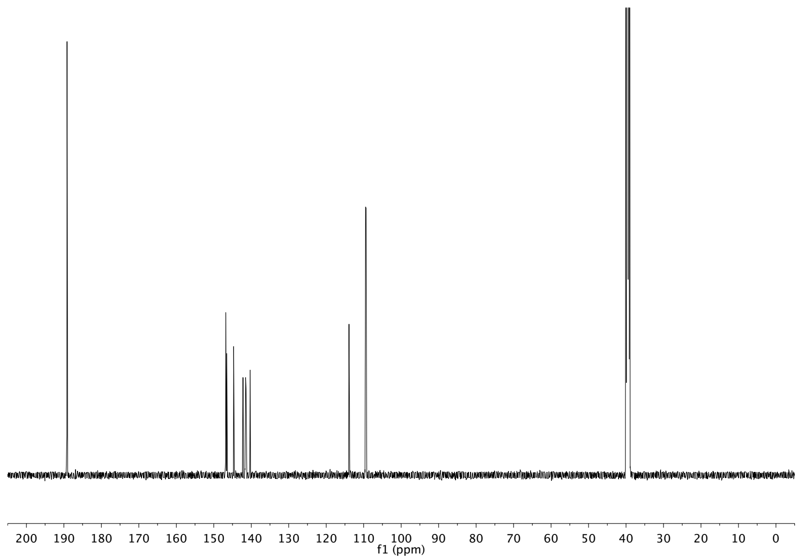

Figure 6.5. ^{13}C NMR (126 MHz, DMSO-d_6) spectrum of **11**.

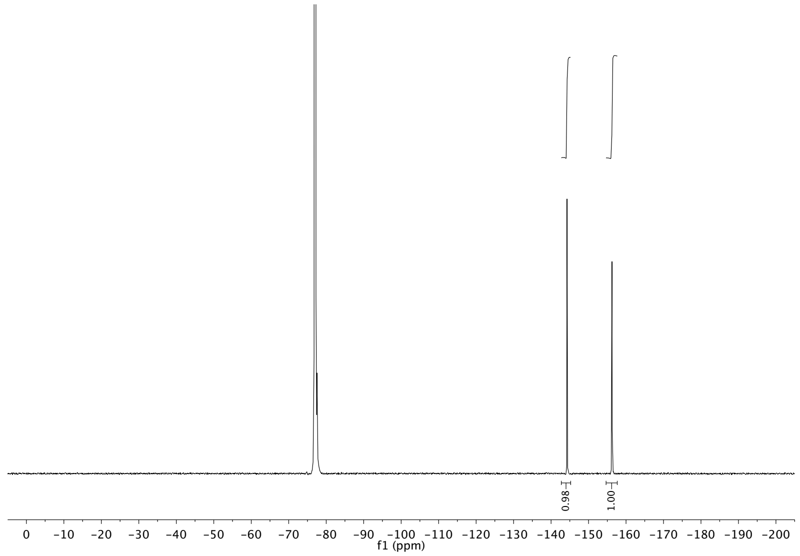

Figure 6.6. ^{19}F NMR (376 MHz, DMSO-d_6, decoupled) spectrum of **11**.

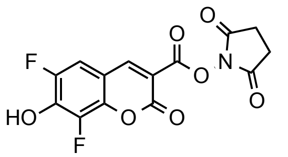

15

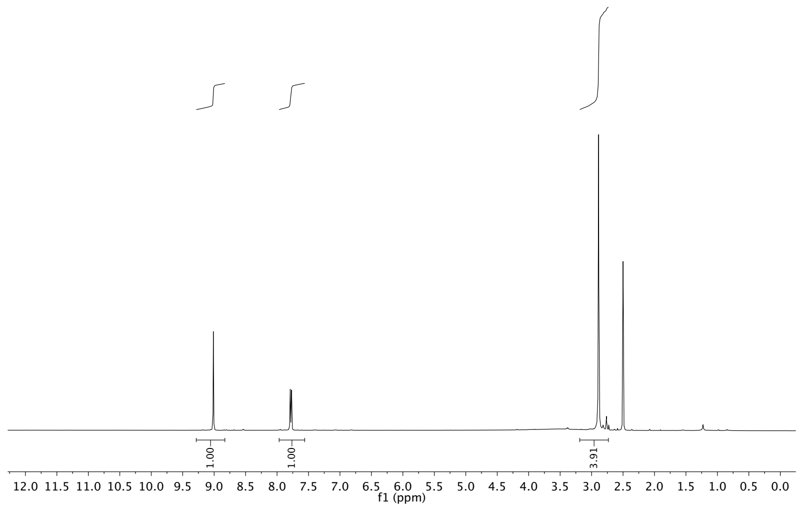

Figure 6.7. ^{1}H NMR (500 MHz, DMSO-d_6) spectrum of **15.**

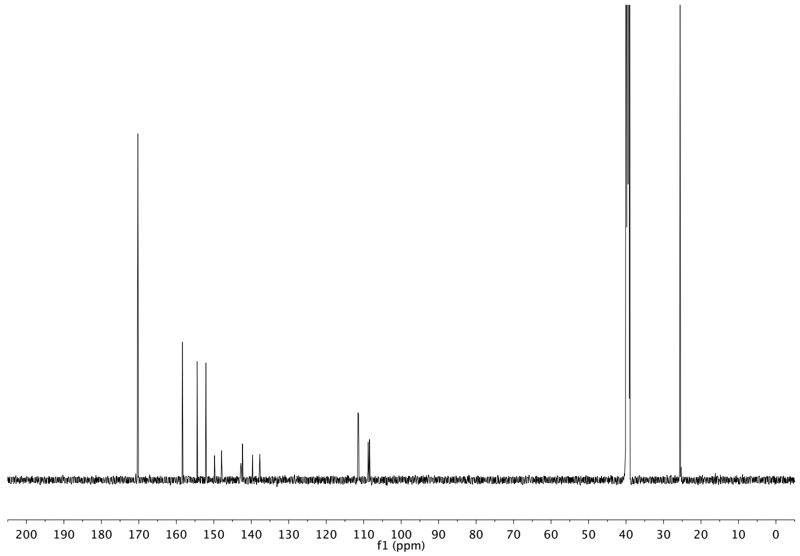

Figure 6.8. ^{13}C NMR (126 MHz, DMSO-d_6) spectrum of **15**.

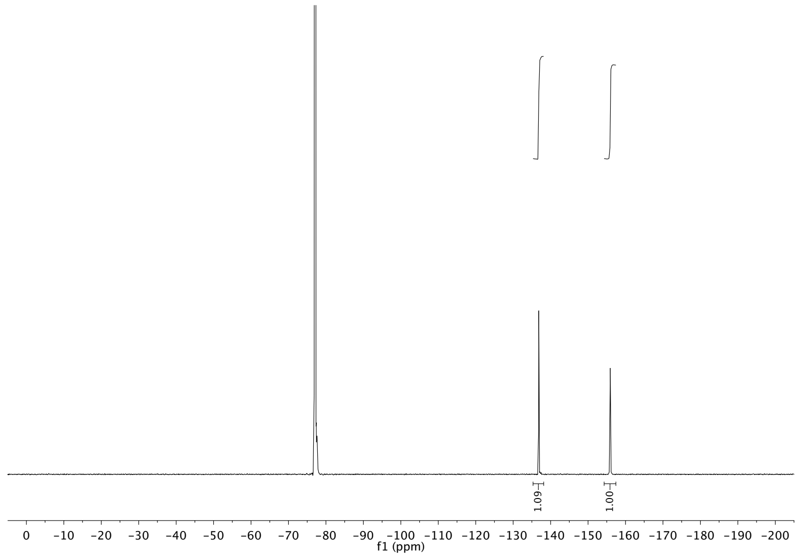

Figure 6.9. ^{19}F NMR (376 MHz, DMSO-d_6, decoupled) spectrum of **15**.

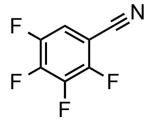

17

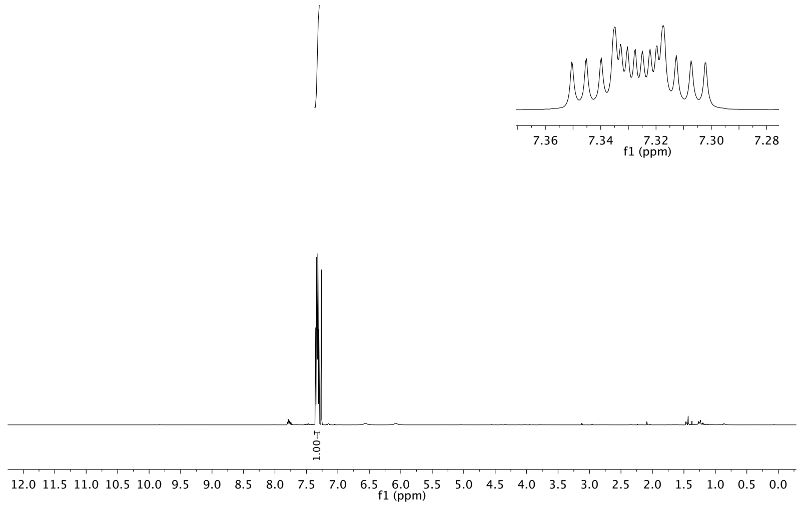

Figure 6.10. ^{1}H NMR (500 MHz, CDCl$_3$) spectrum of **17**.

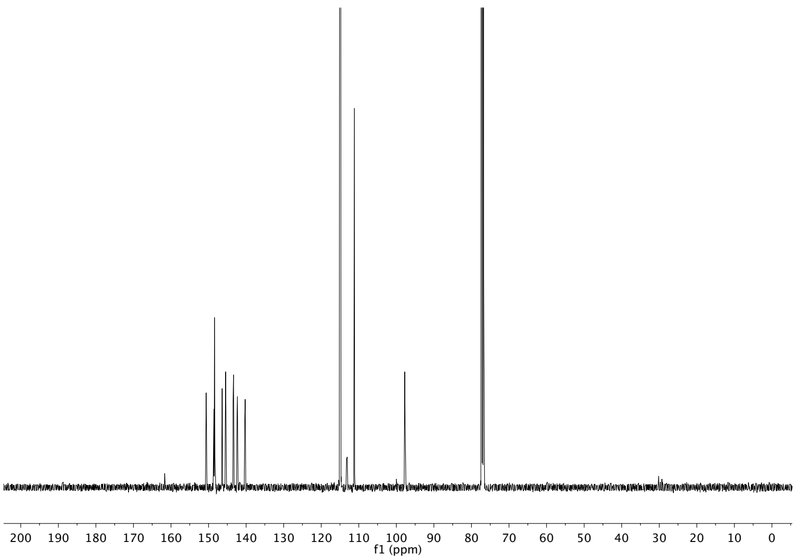

Figure 6.11. ^{13}C NMR (126 MHz, CDCl$_3$) spectrum of **17**.

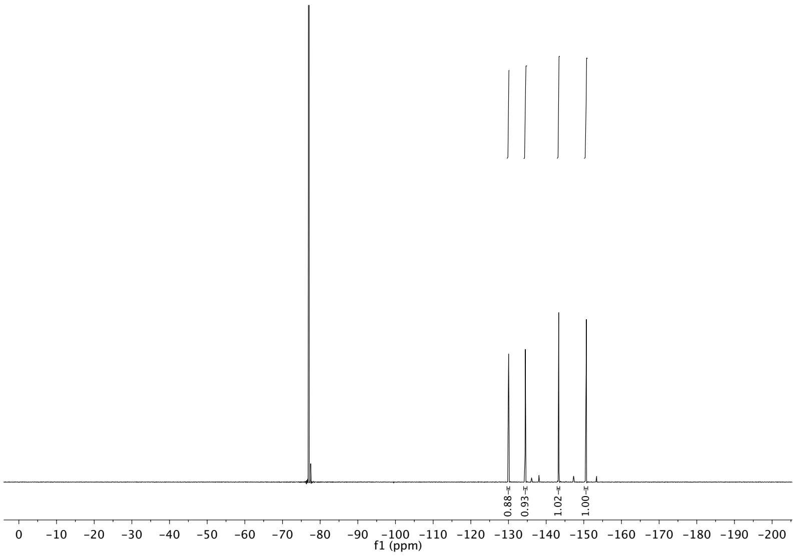

Figure 6.12. ^{19}F NMR (376 MHz, CDCl$_3$, decoupled) spectrum of **17**.

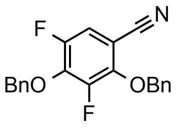

18

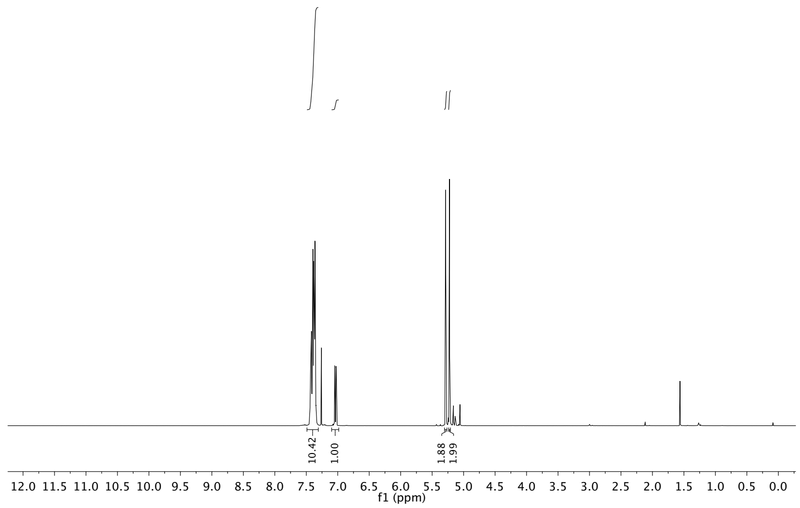

Figure 6.13. ^{1}H NMR (500 MHz, $CDCl_3$) spectrum of **18**.

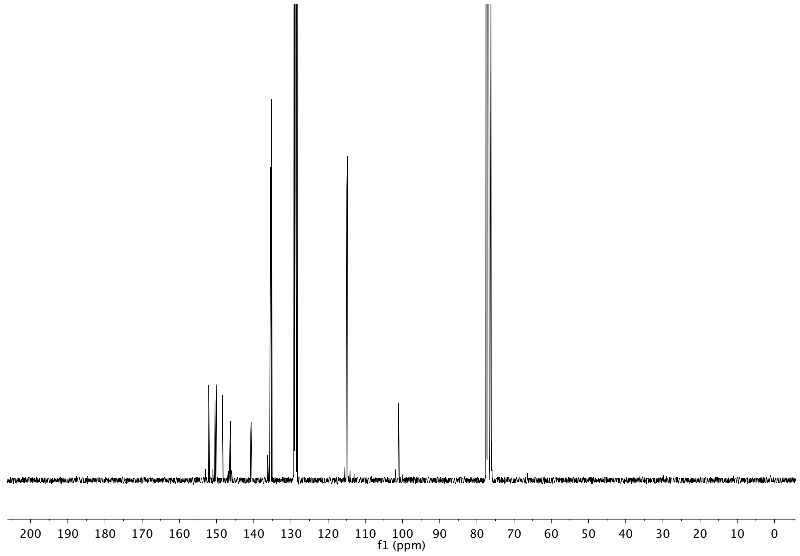

Figure 6.14. ^{13}C NMR (126 MHz, $CDCl_3$) spectrum of **18**.

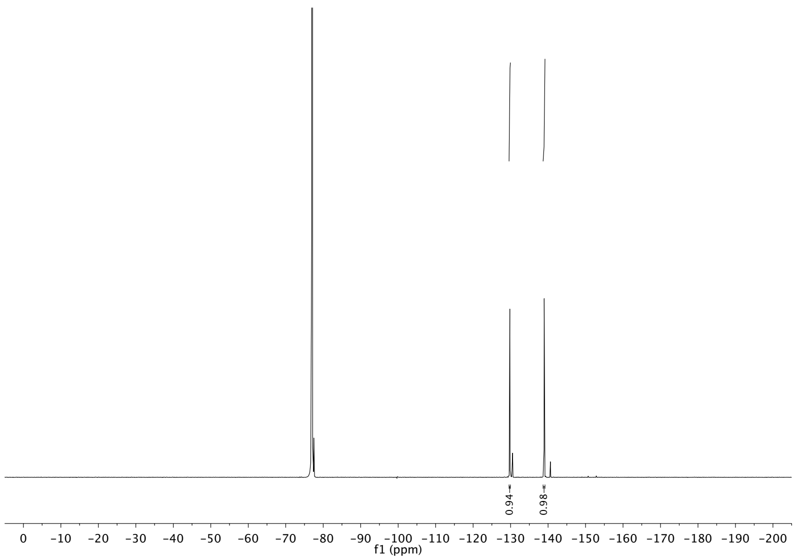

Figure 6.15. ^{19}F NMR (376 MHz, CDCl$_3$, decoupled) spectrum of **18**.

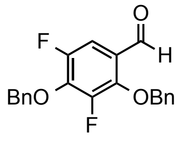

19

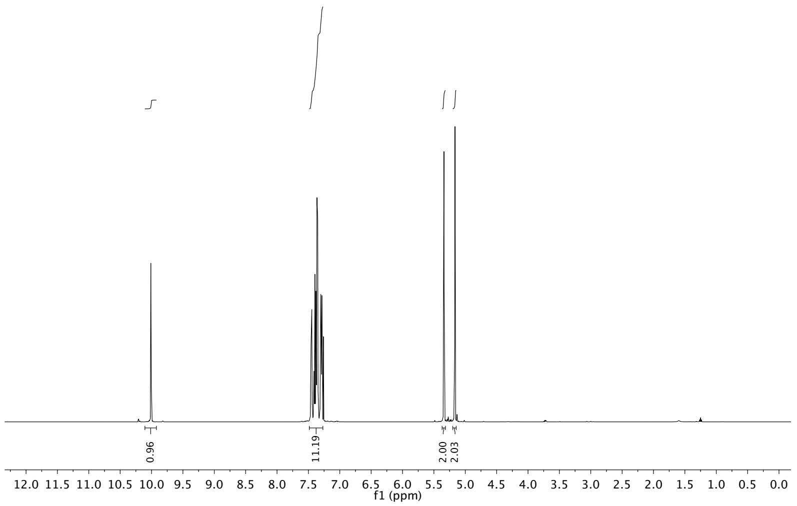

Figure 6.16. ^{1}H NMR (500 MHz, CDCl$_3$) spectrum of **19**.

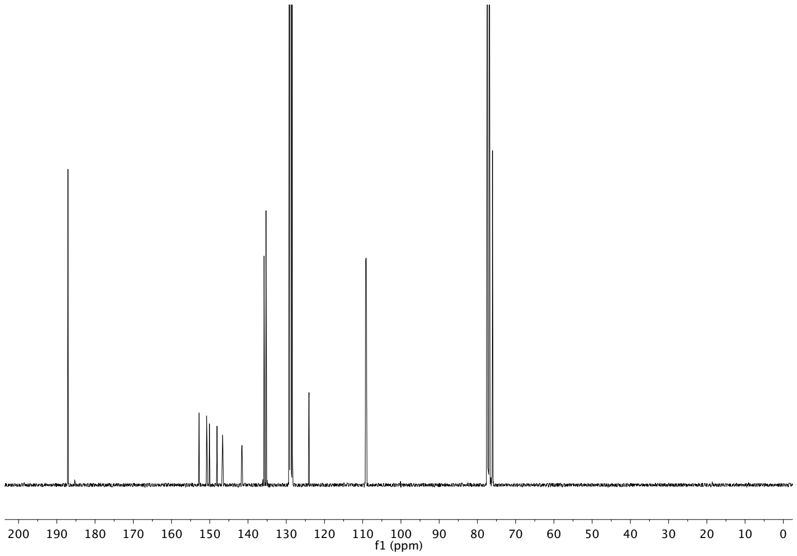

Figure 6.17. ^{13}C NMR (126 MHz, $CDCl_3$) spectrum of **19**.

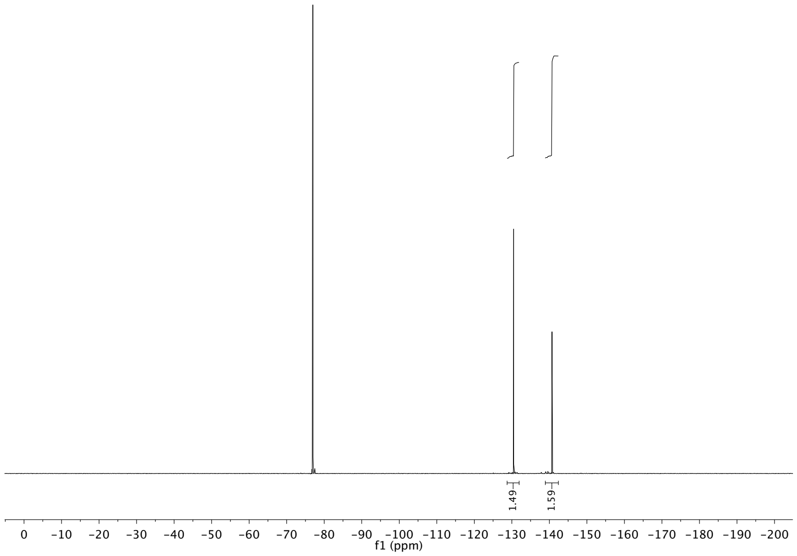

Figure 6.18. ^{19}F NMR (376 MHz, $CDCl_3$, decoupled) spectrum of **19**.

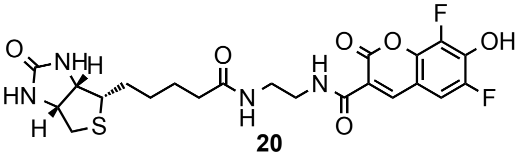

20

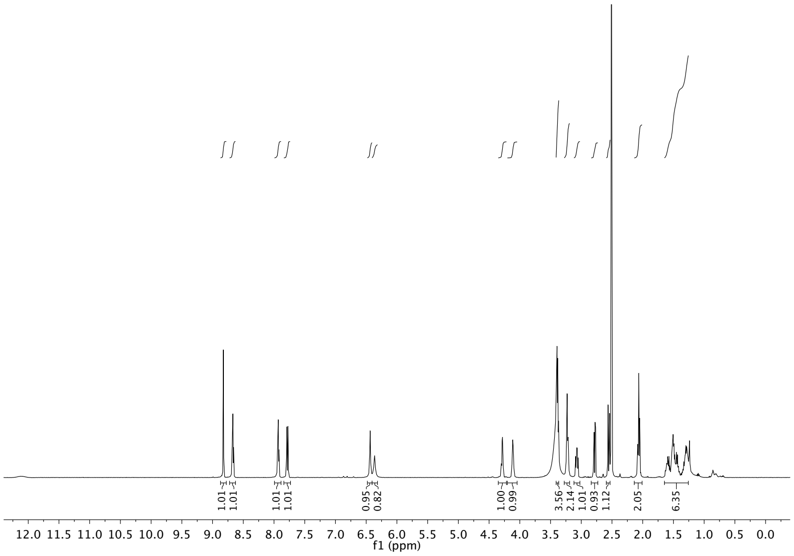

Figure 6.19. ^{1}H NMR (500 MHz, DMSO-d_6) spectrum of **20**.

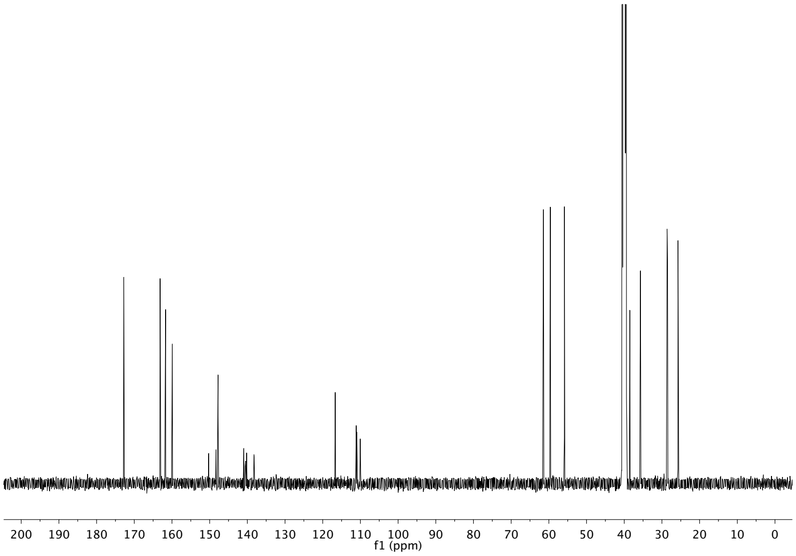

Figure 6.20. ^{13}C NMR (126 MHz, DMSO-d_6) spectrum of **20**.

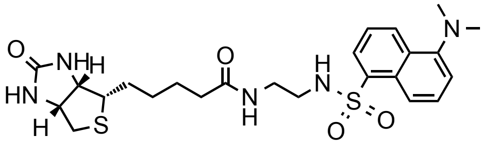

21

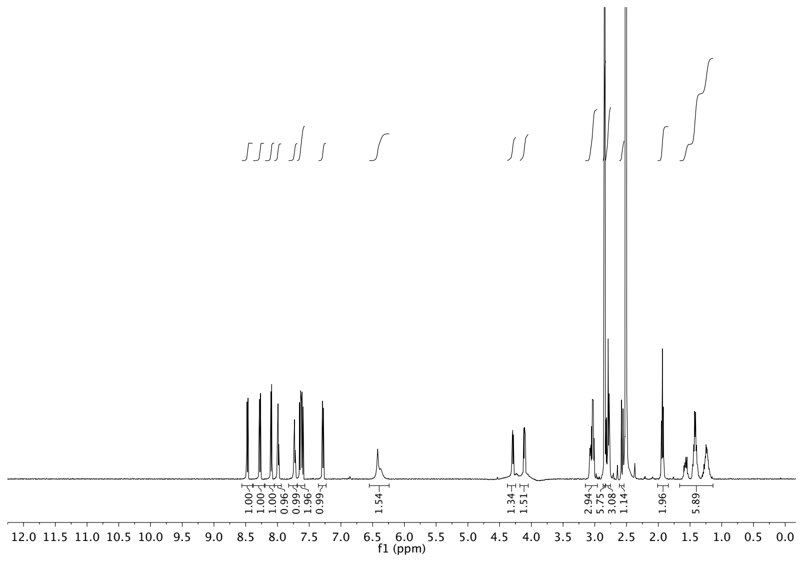

Figure 6.21. ^{1}H NMR (500 MHz, DMSO-d_6) spectrum of **21**.

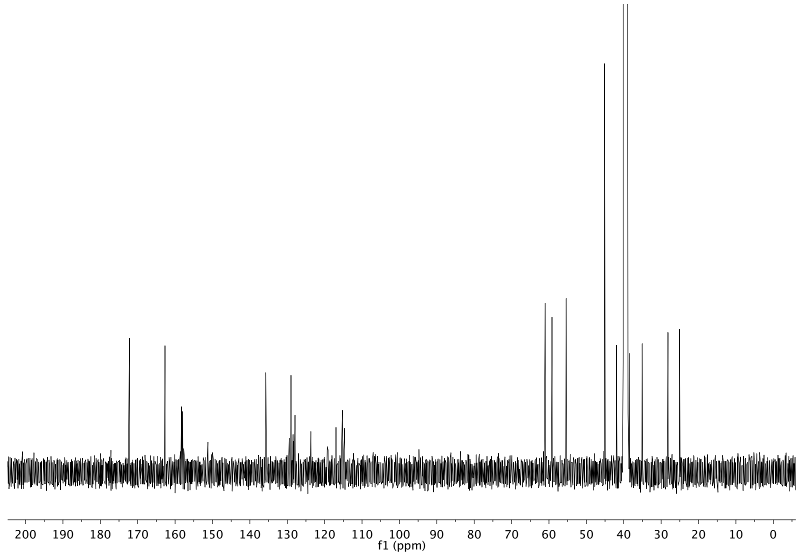

Figure 6.22. ^{13}C NMR (126 MHz, DMSO-d_6) spectrum of **21**.

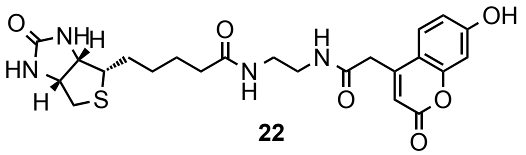

22

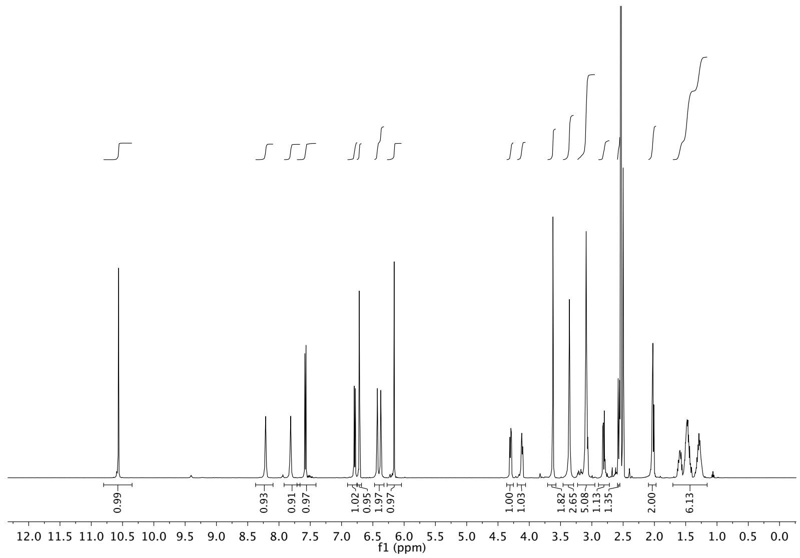

Figure 6.23. ^{1}H NMR (500 MHz, DMSO-d_6) spectrum of **22**.

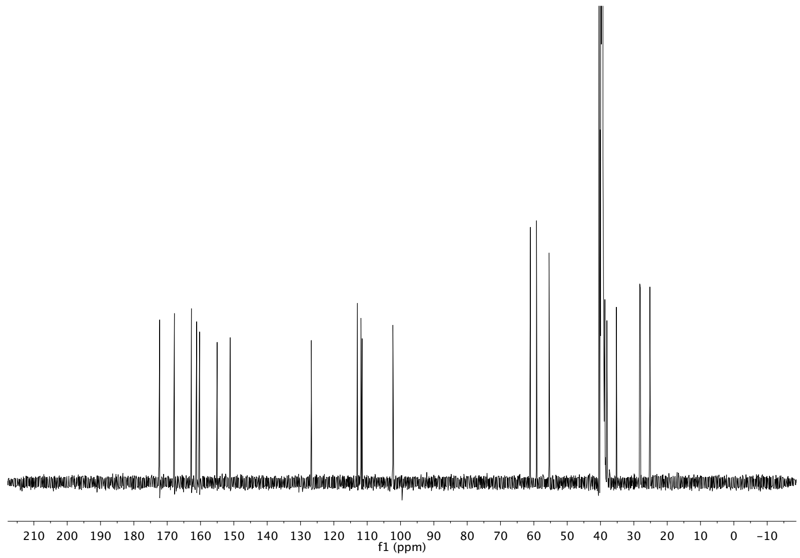

Figure 6.24. ^{13}C NMR (126 MHz, DMSO-d_6) spectrum of **22**.

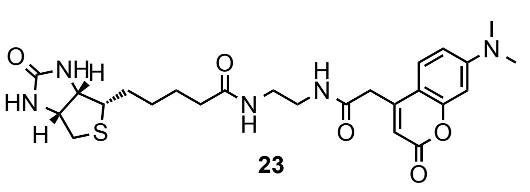

23

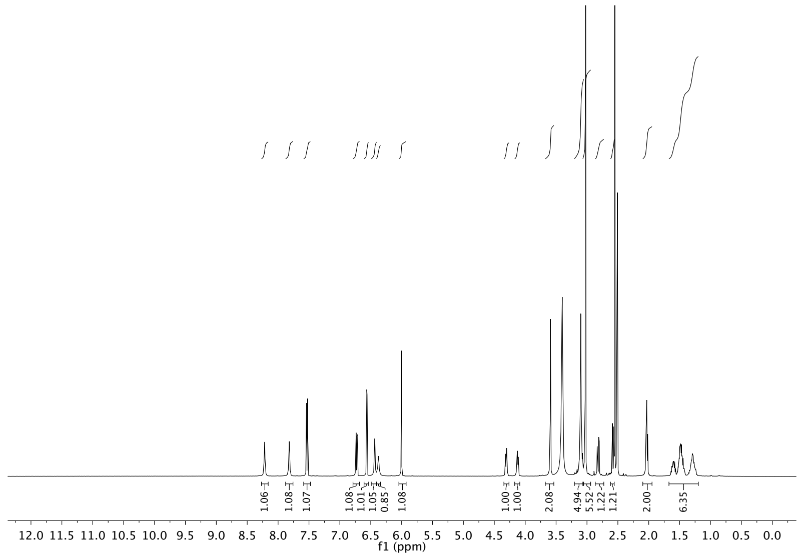

Figure 6.25. ^{1}H NMR (500 MHz, DMSO-d_6) spectrum of **23**.

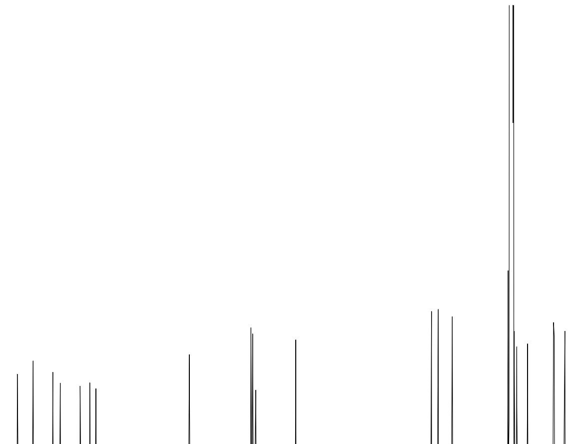

Figure 6.26. ^{13}C NMR (126 MHz, DMSO-d_6) spectrum of **23**.

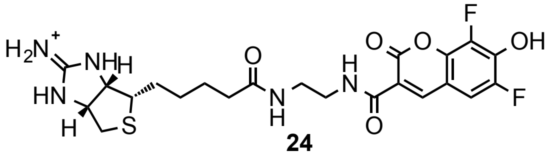

24

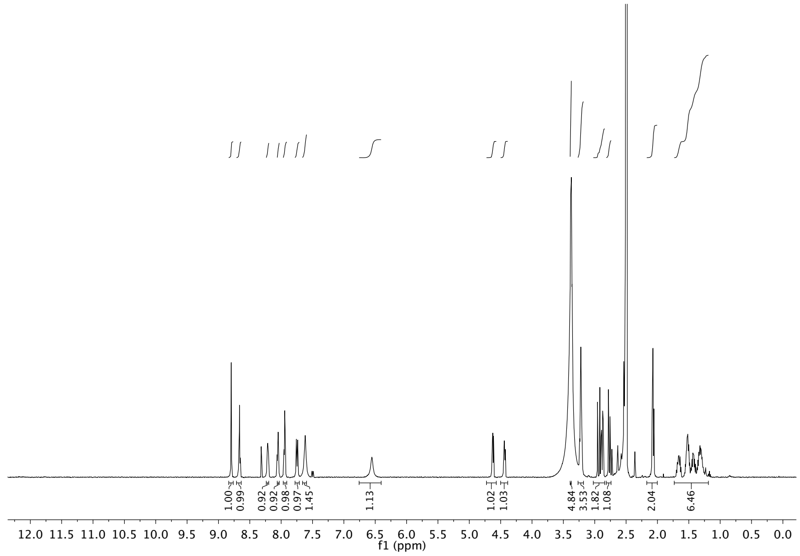

Figure 6.27. ^{1}H NMR (500 MHz, DMSO-d_6) spectrum of **24**.

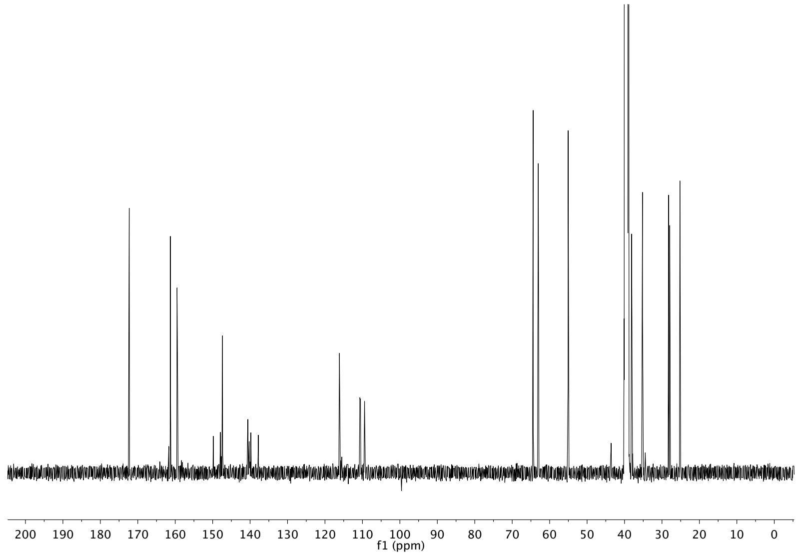

Figure 6.28. ^{13}C NMR (126 MHz, DMSO-d_6) spectrum of **24**.

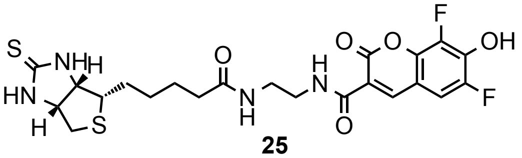

25

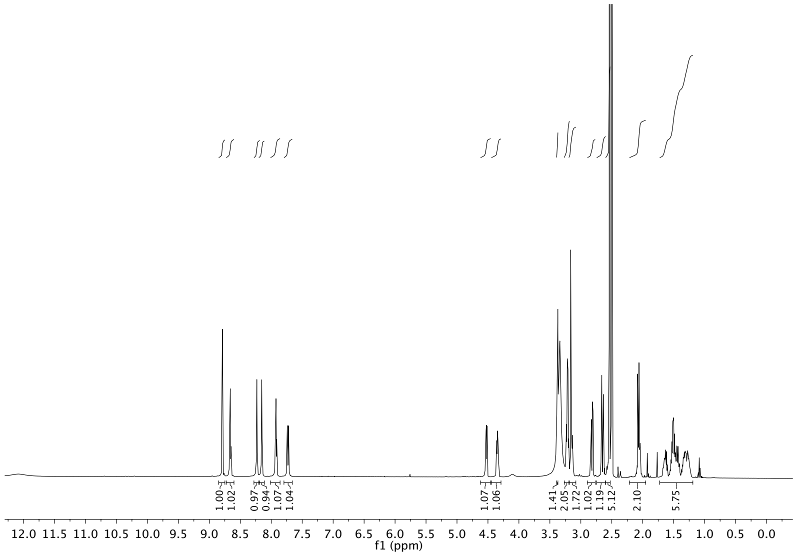

Figure 6.29. ^{1}H NMR (500 MHz, DMSO-d_6) spectrum of **25**.

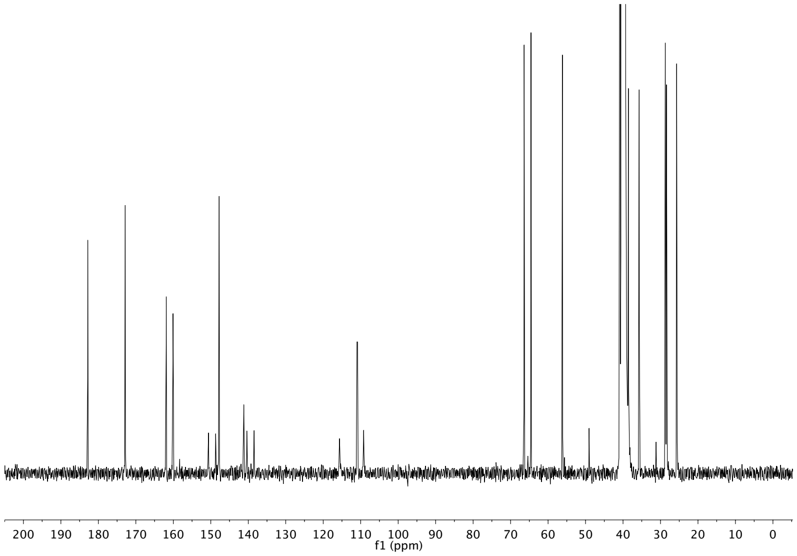

Figure 6.30. ^{13}C NMR (126 MHz, DMSO-d_6) spectrum of **25**.

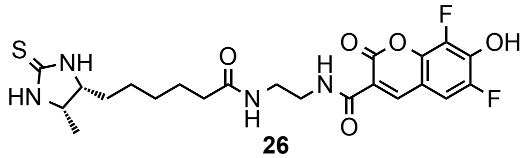

26

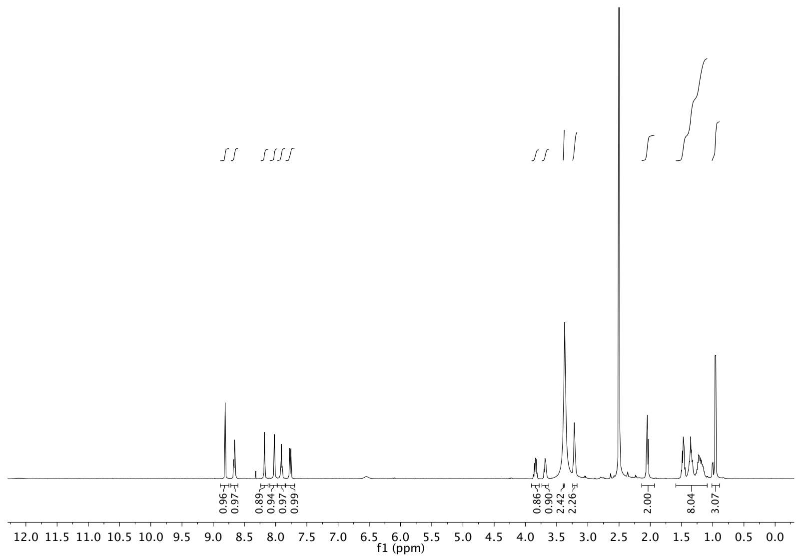

Figure 6.31. ^{1}H NMR (500 MHz, DMSO-d_6) spectrum of **26**.

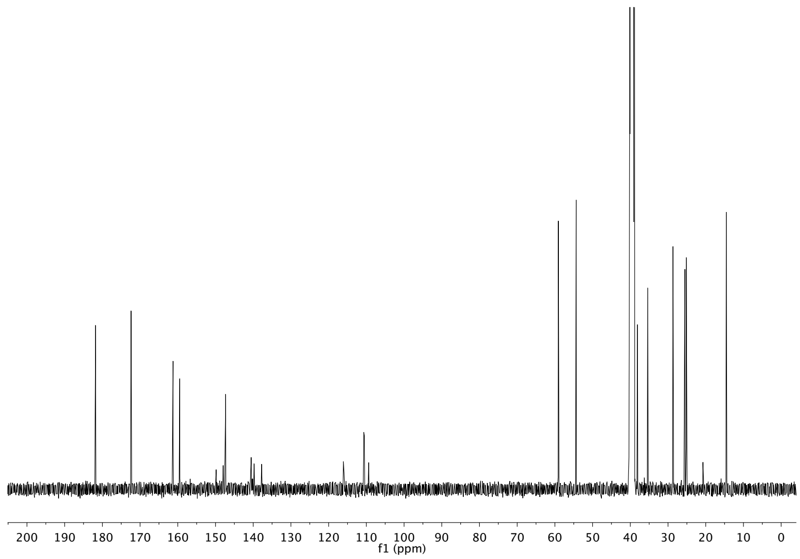

Figure 6.32. ^{13}C NMR (126 MHz, DMSO-d_6) spectrum of **26**.

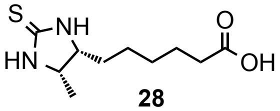

28

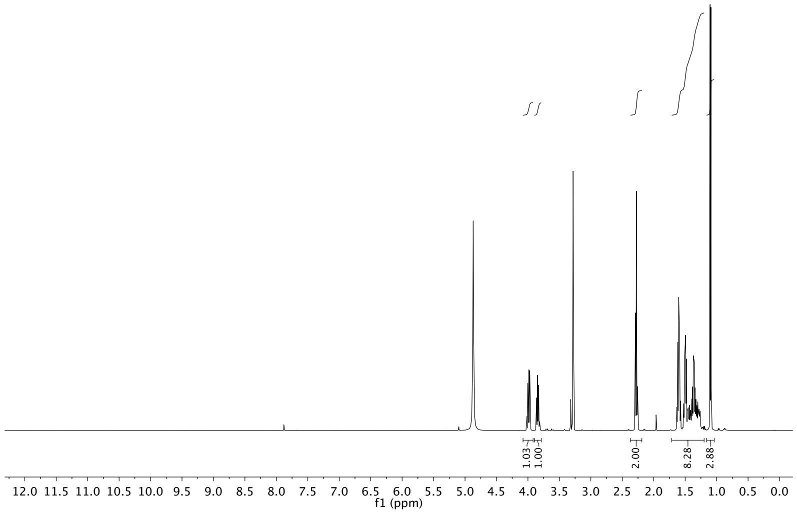

Figure 6.33. ^{1}H NMR (500 MHz, CD_3OD) spectrum of **28**.

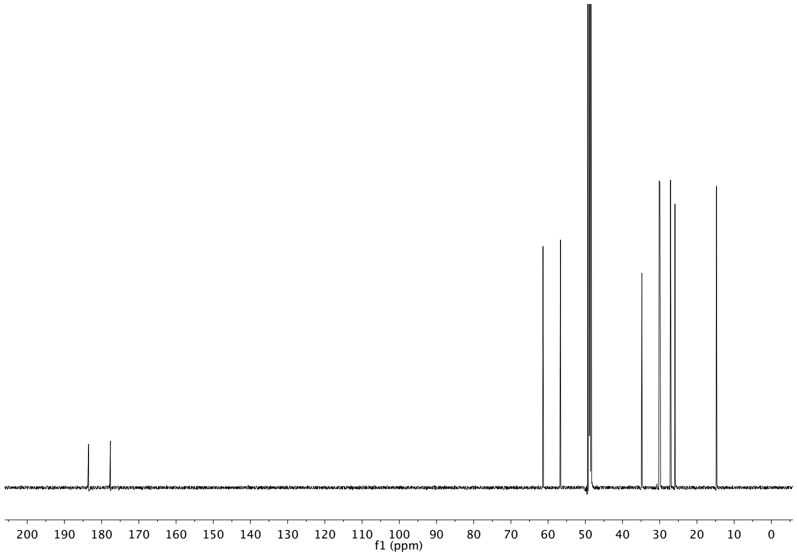

Figure 6.34. ^{13}C NMR (126 MHz, CD_3OD) spectrum of **28**.

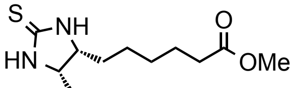

29

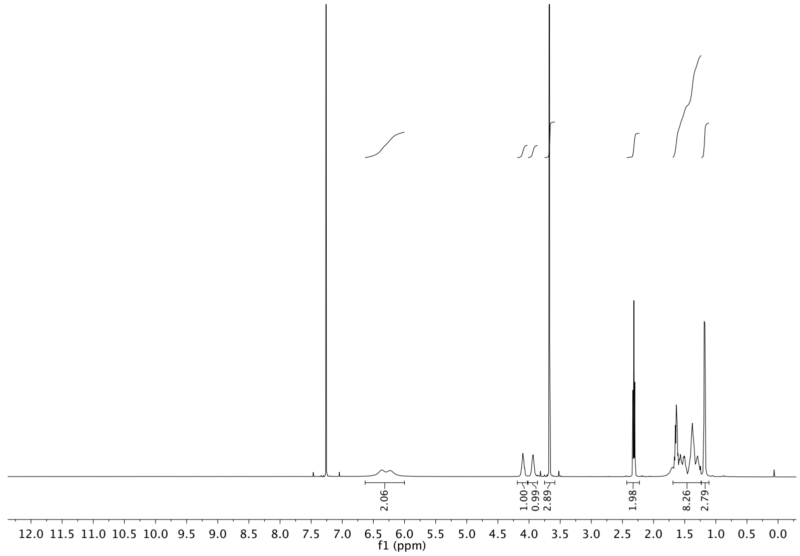

Figure 6.35. ^{1}H NMR (500 MHz, $CDCl_3$) spectrum of **29**.

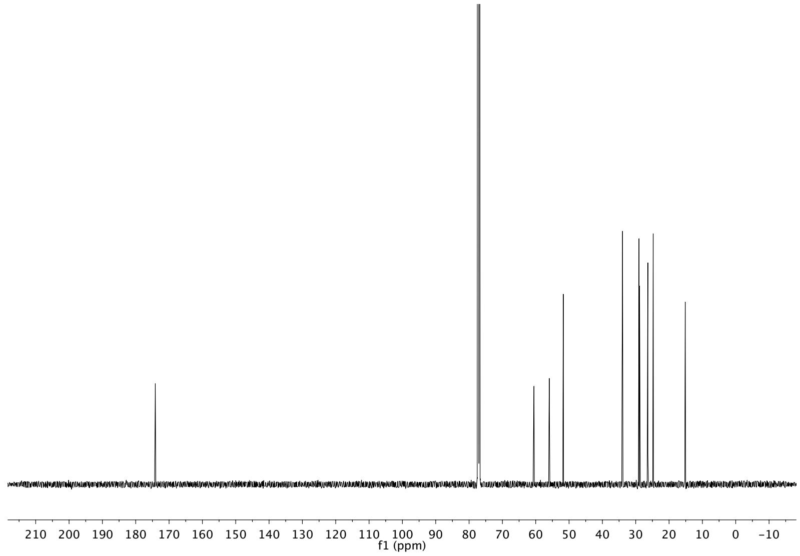

Figure 6.36. ^{13}C NMR (126 MHz, $CDCl_3$) spectrum of **29**.

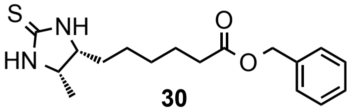

30

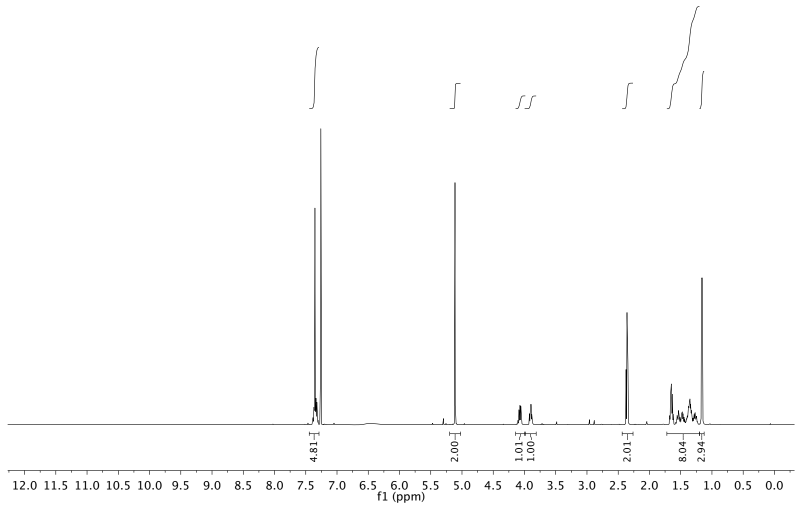

Figure 6.37. ^{1}H NMR (500 MHz, $CDCl_3$) spectrum of **30**.

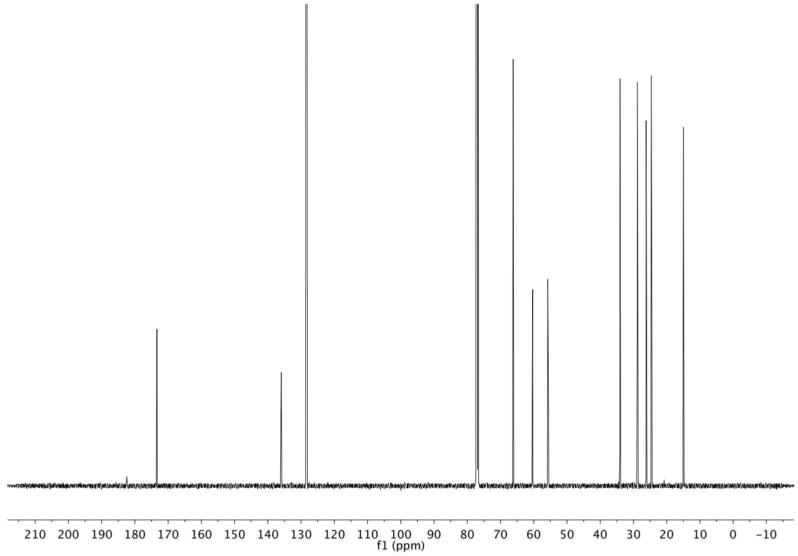

Figure 6.38. ^{13}C NMR (126 MHz, $CDCl_3$) spectrum of **30**.

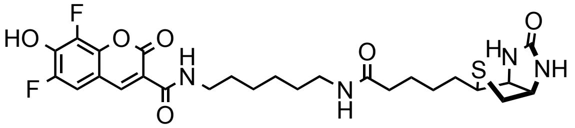

34

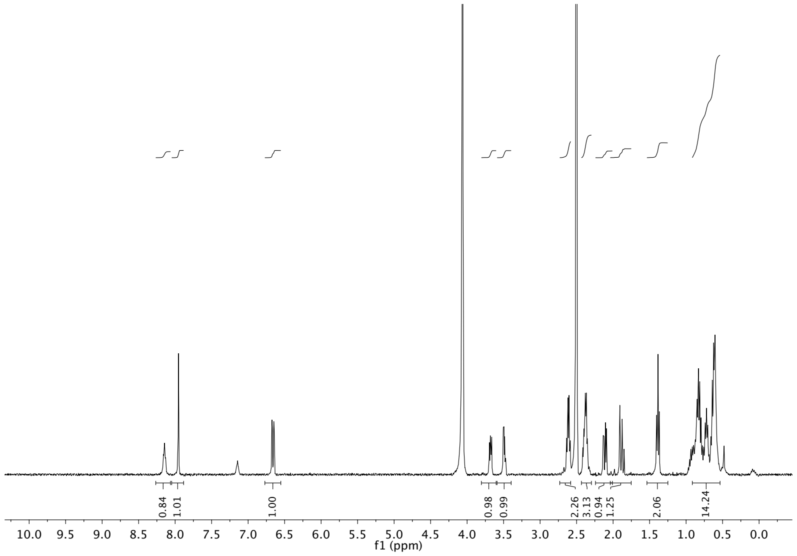

Figure 6.39. ^{1}H NMR (500 MHz, DMSO-d_6) spectrum of **34**.

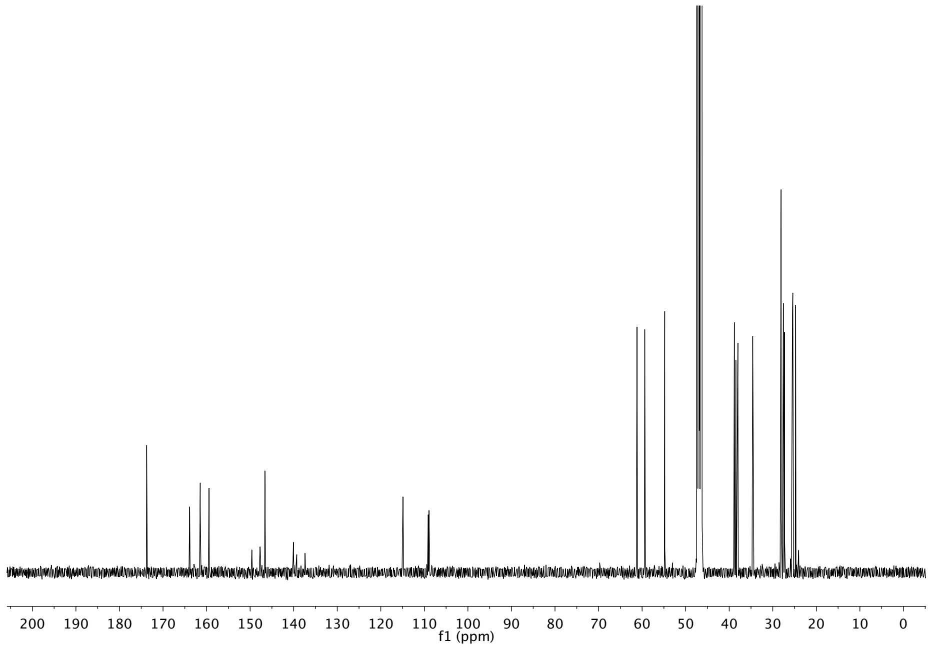

Figure 6.40. ^{13}C NMR (126 MHz, DMSO-d_6) spectrum of **34.**

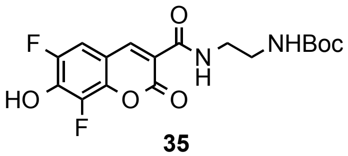

35

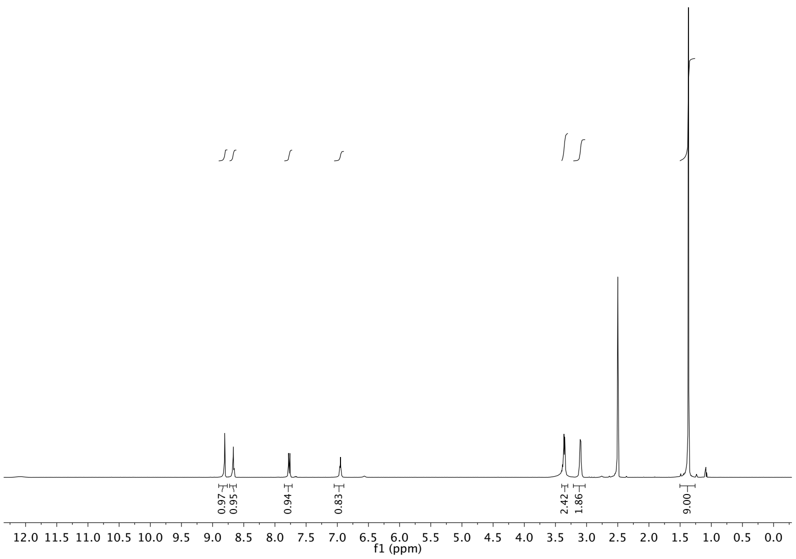

Figure 6.41. ^{1}H NMR (500 MHz, DMSO-d_6) spectrum of **35**.

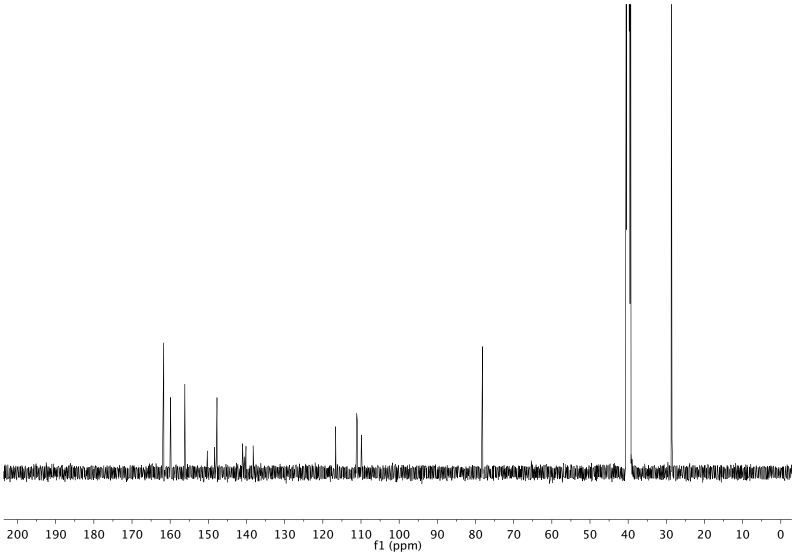

Figure 6.42. ^{13}C NMR (126 MHz, DMSO-d_6) spectrum of **35.**

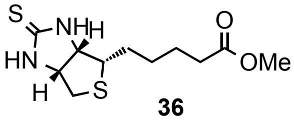

36

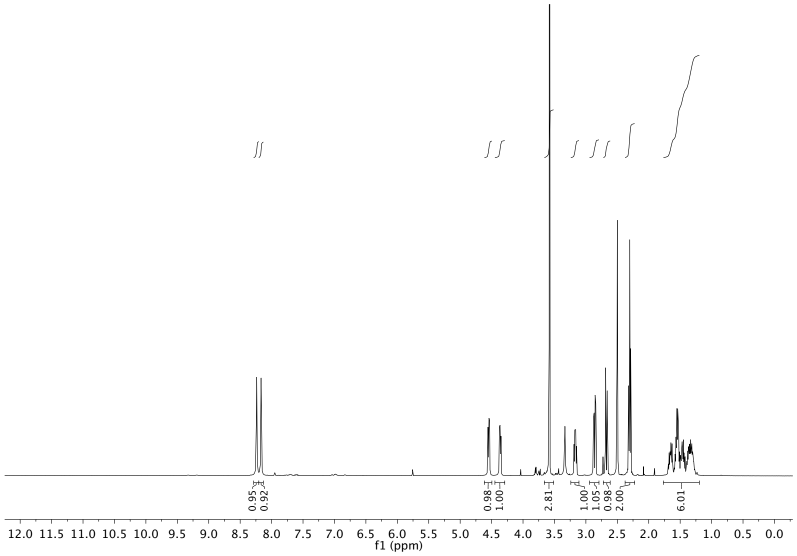

Figure 6.43. ^{1}H NMR (500 MHz, DMSO-d_6) spectrum of **36**.

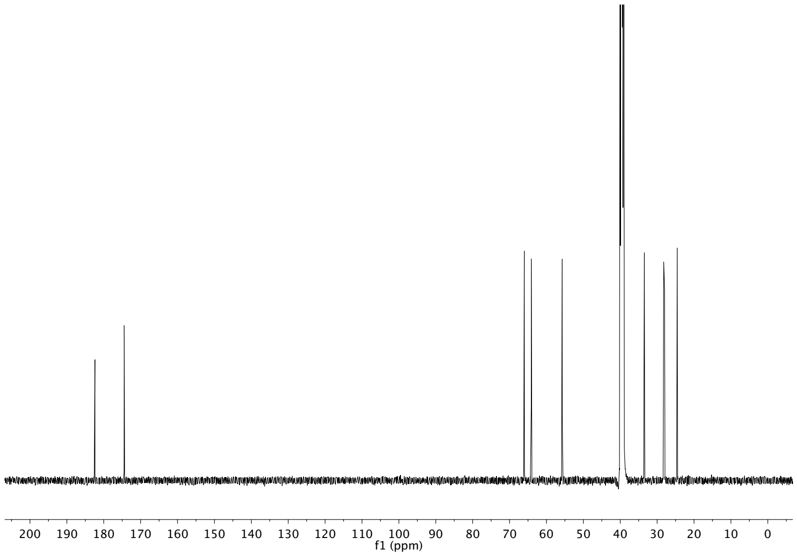

Figure 6.44. ^{13}C NMR (126 MHz, DMSO-d_6) spectrum of **36**.

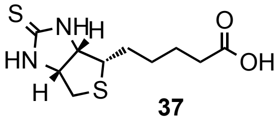

37

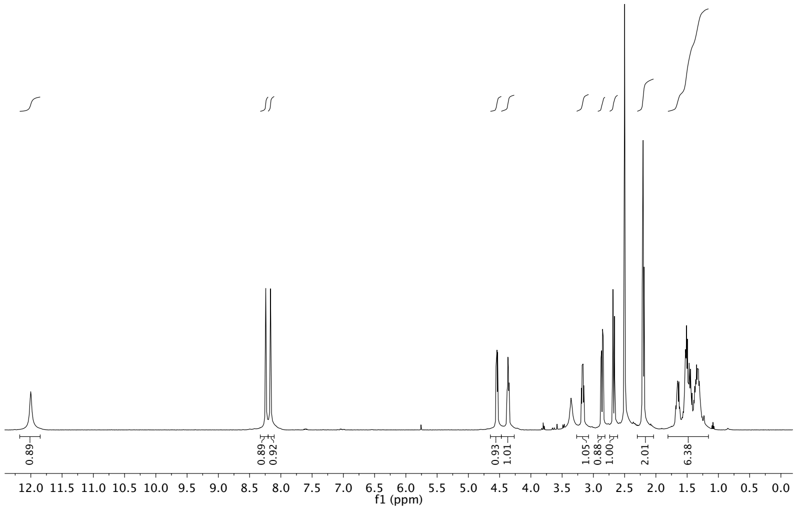

Figure 6.45. ^{1}H NMR (500 MHz, DMSO-d_6) spectrum of **37**.

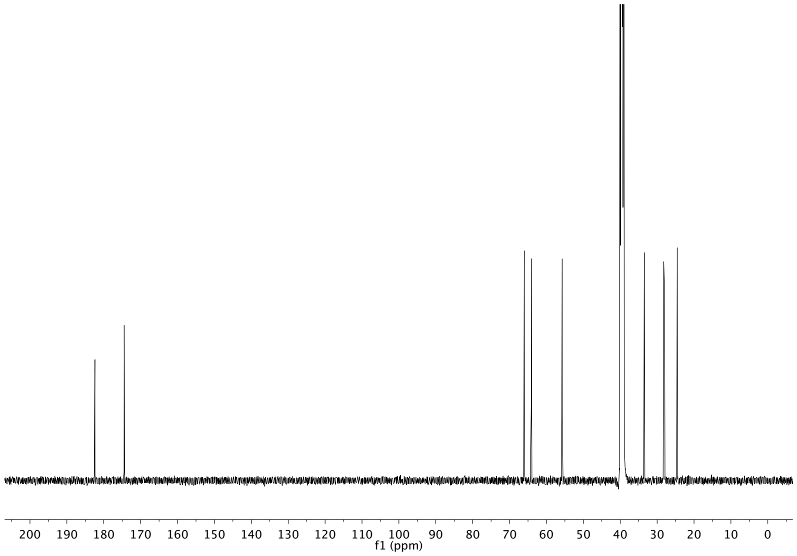

Figure 6.46. ^{13}C NMR (126 MHz, DMSO-d_6) spectrum of **37**.

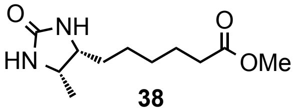

38

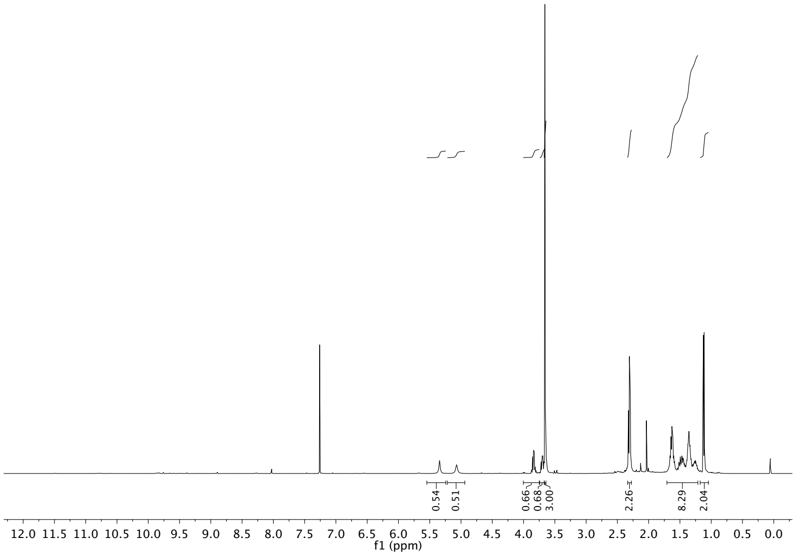

Figure 6.47. ^{1}H NMR (500 MHz, CDCl$_3$) spectrum of **38**.

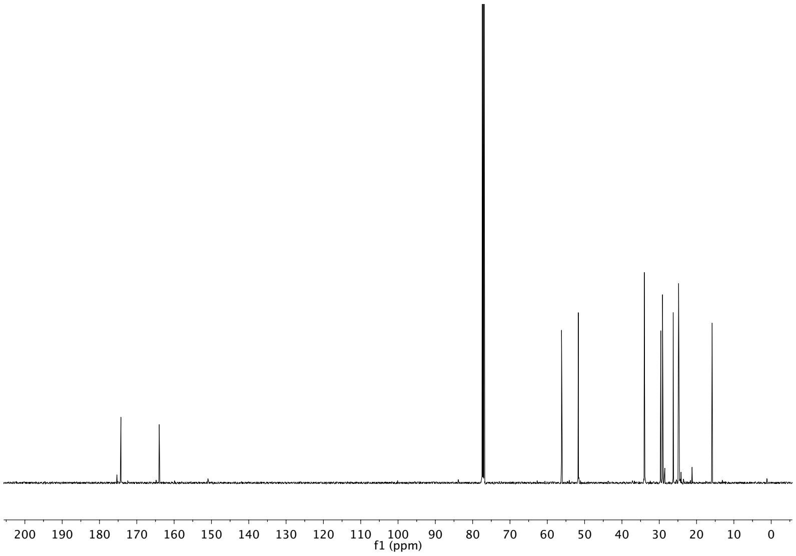

Figure 6.48. ^{13}C NMR (126 MHz, CDCl$_3$) spectrum of **38**.

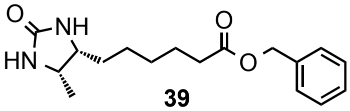

39

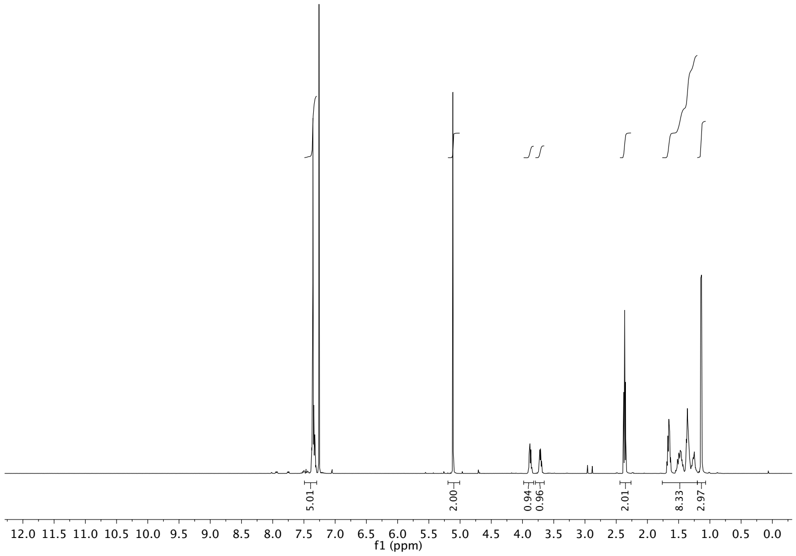

Figure 6.49. ^{1}H NMR (500 MHz, CDCl$_3$) spectrum of **39**.

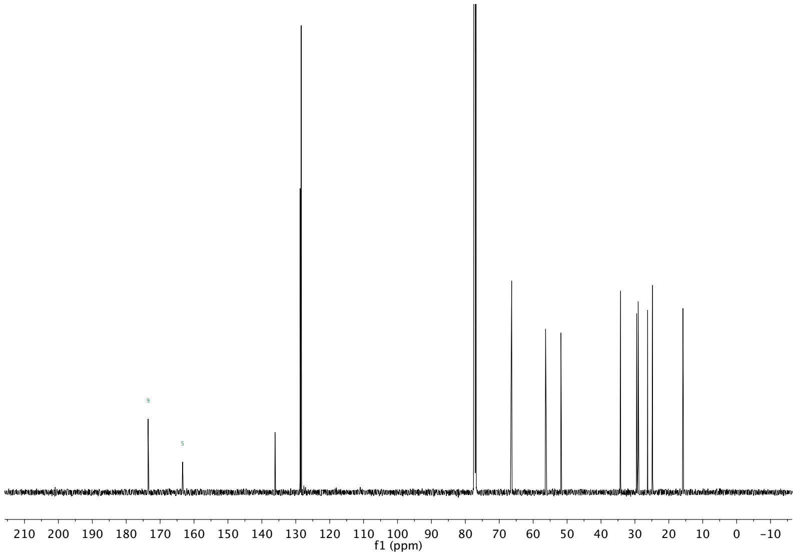

Figure 6.50. ^{13}C NMR (126 MHz, CDCl$_3$) spectrum of **39**.

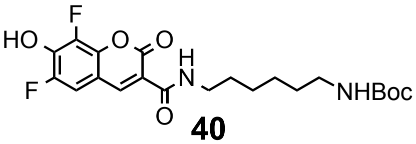

40

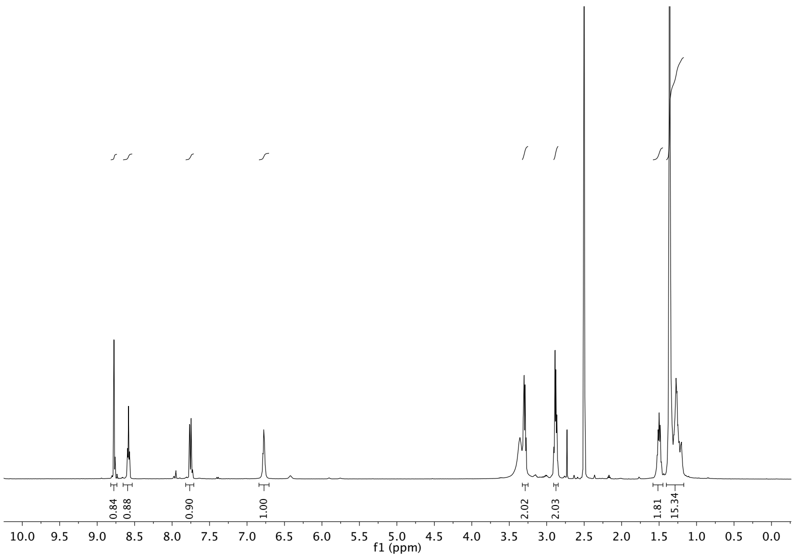

Figure 6.51. ^{1}H NMR (500 MHz, DMSO-d_6) spectrum of **40**.

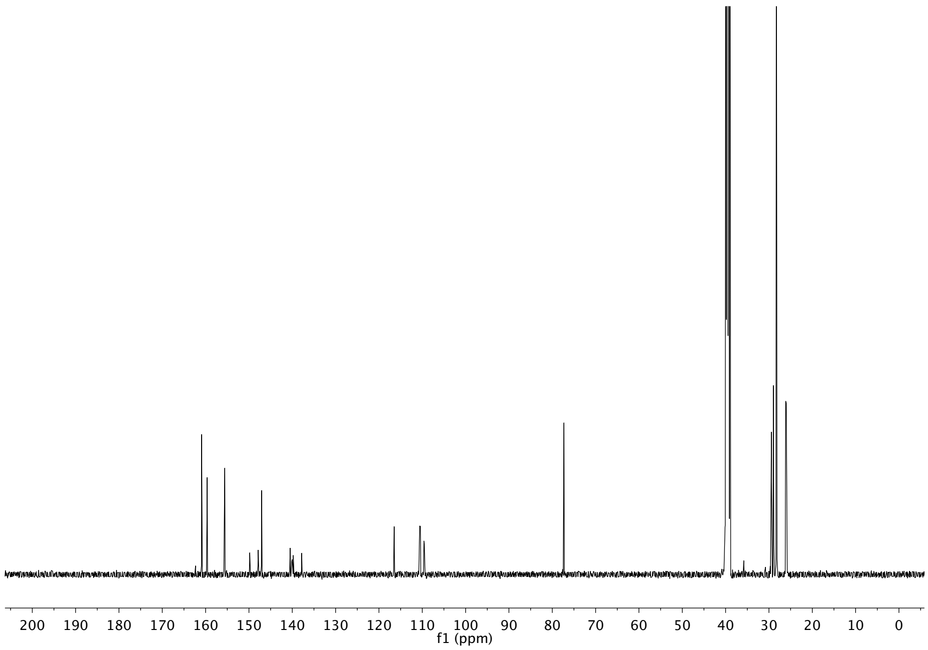

Figure 6.52. ^{13}C NMR (126 MHz, DMSO-d_6) spectrum of **40**.

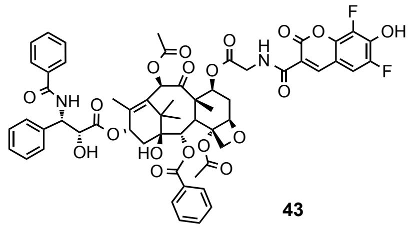

43

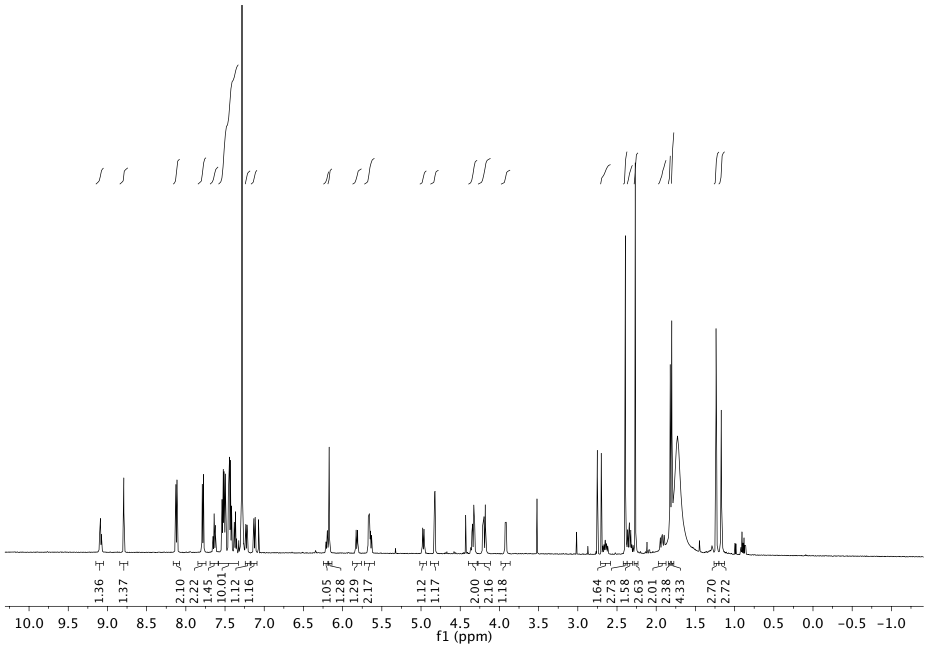

Figure 6.53. ^{1}H NMR (500 MHz, $CDCl_3$) spectrum of **43.**

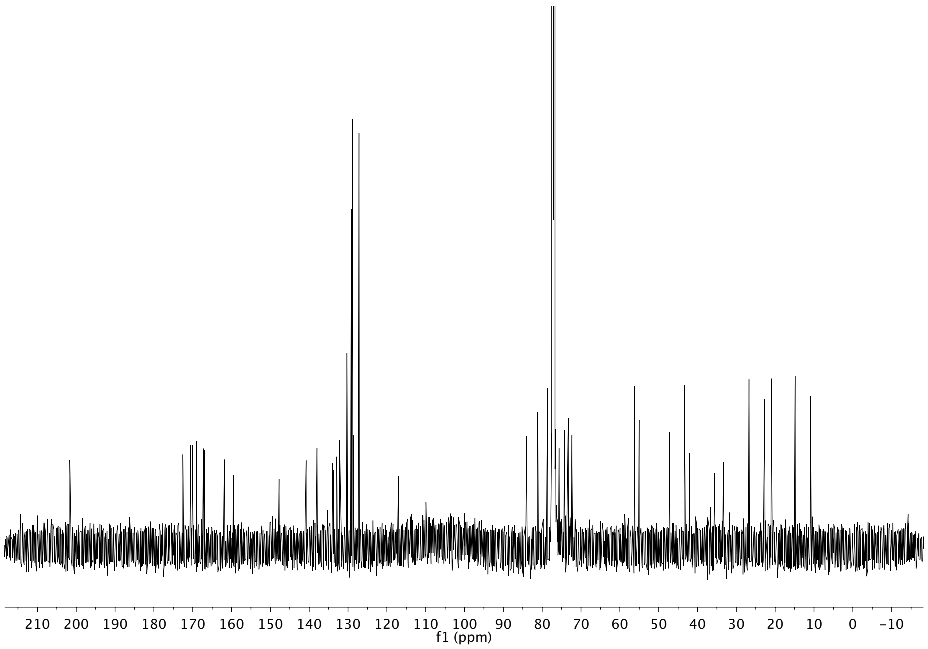

Figure 6.54. ^{13}C NMR (126 MHz, $CDCl_3$) spectrum of **43**.

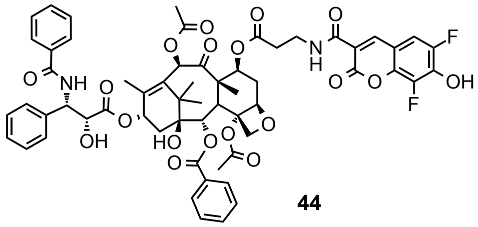

44

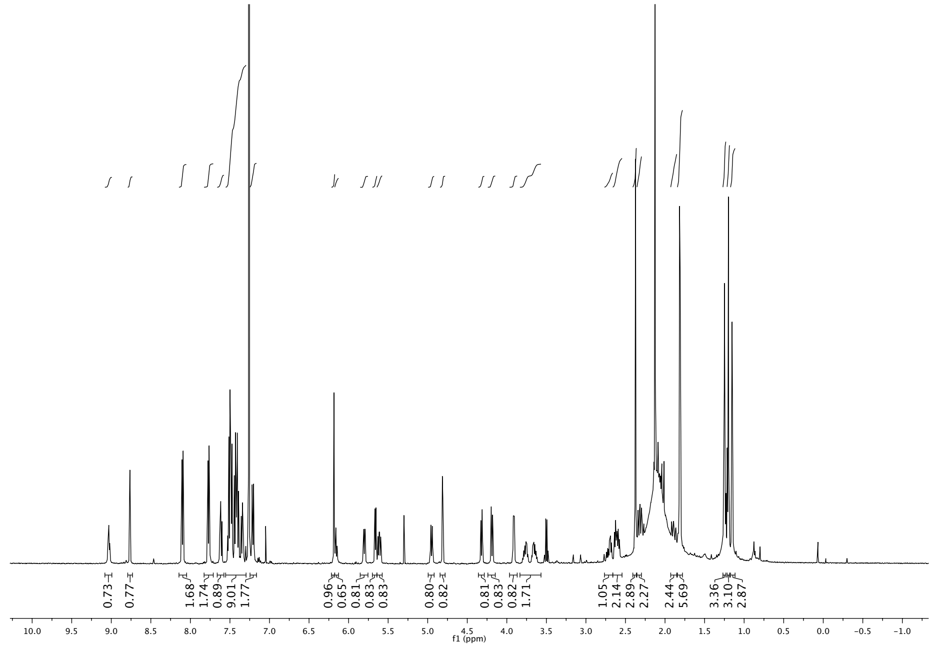

Figure 6.55. ^{1}H NMR (500 MHz, CDCl$_3$) spectrum of **44**.

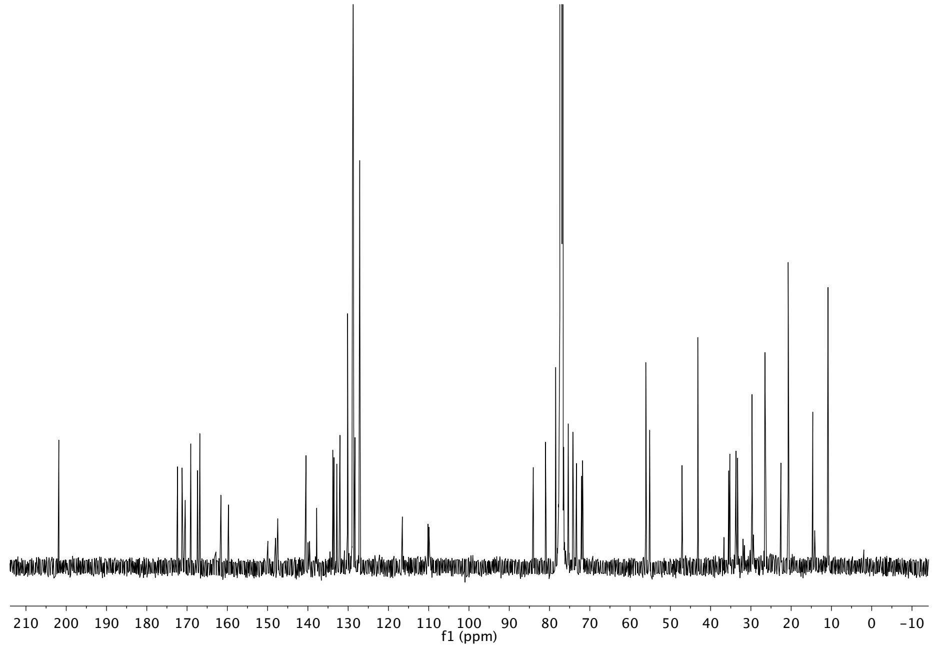

Figure 6.56. ^{13}C NMR (126 MHz, CDCl$_3$) spectrum of **44**.

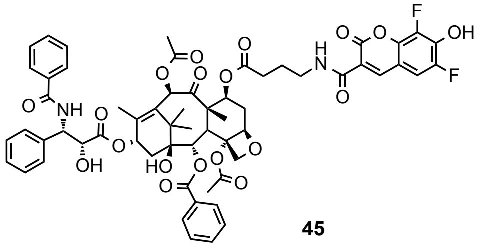

45

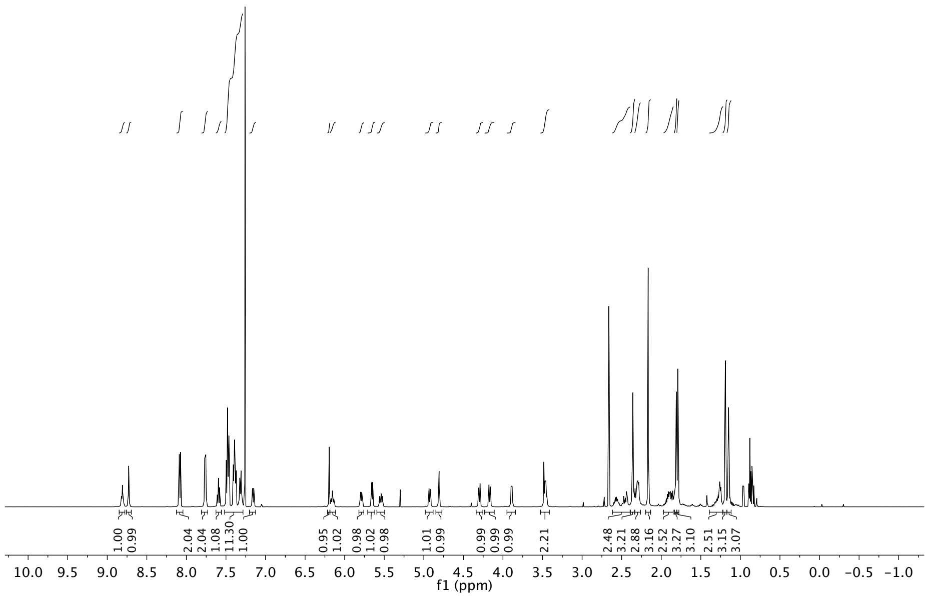

Figure 6.57. ^{1}H NMR (500 MHz, $CDCl_3$) spectrum of **45**.

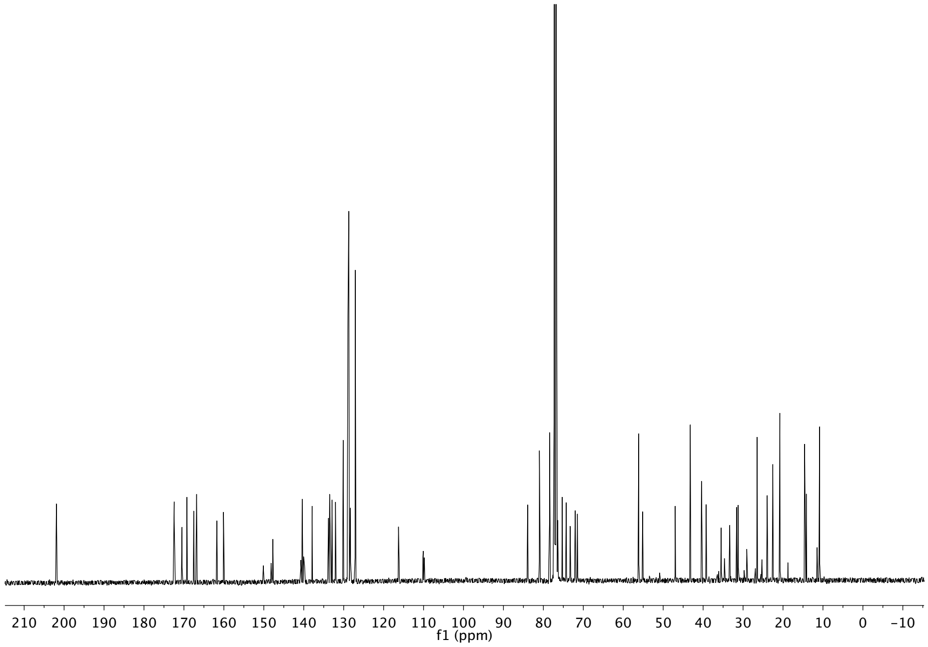

Figure 6.58. ^{13}C NMR (126 MHz, $CDCl_3$) spectrum of **45**.

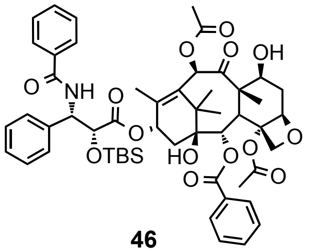

46

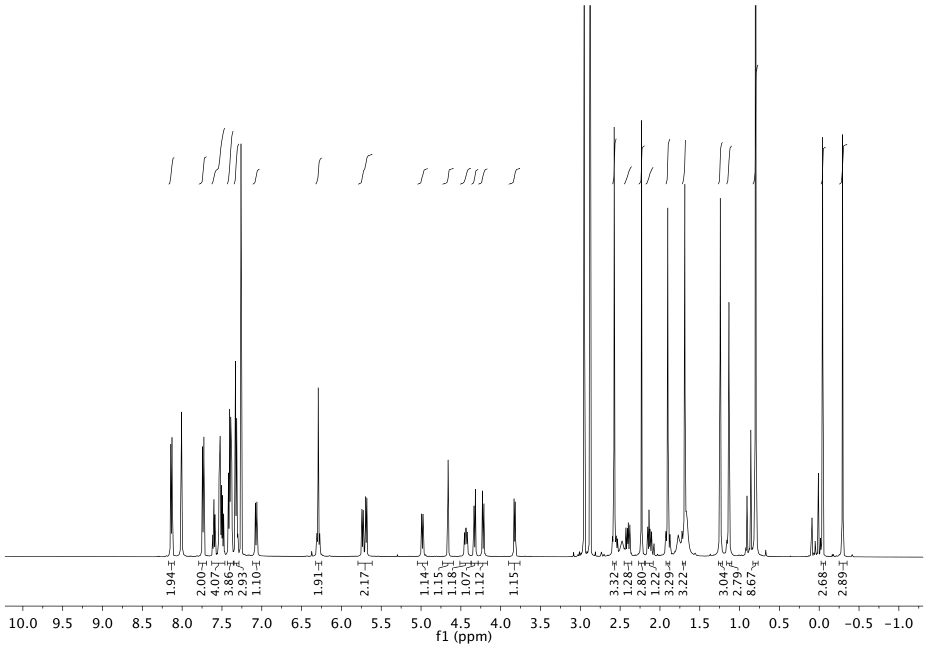

Figure 6.59. ^{1}H NMR (500 MHz, $CDCl_3$) spectrum of **46**.

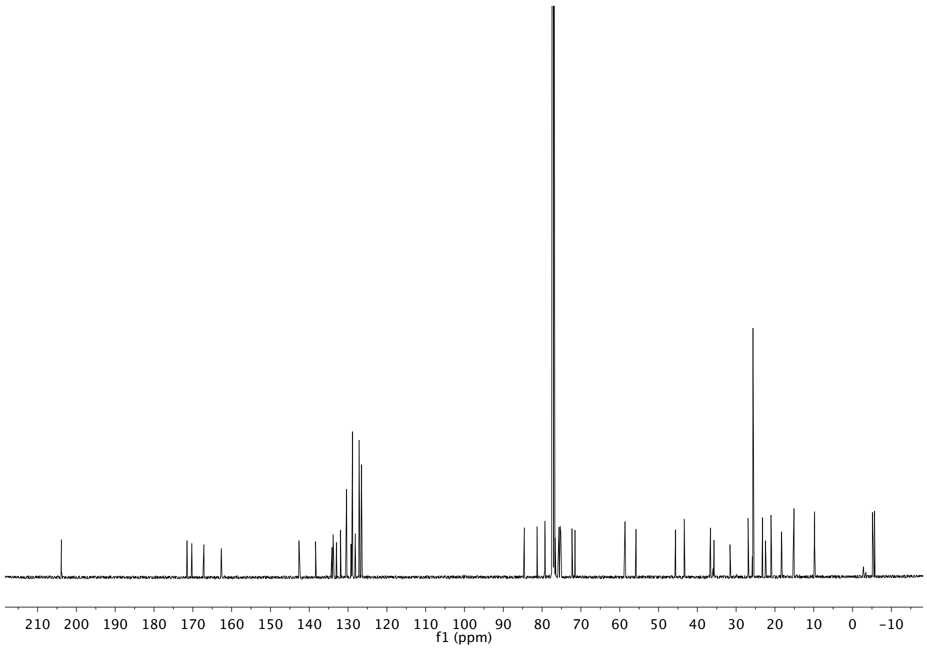

Figure 6.60. ^{13}C NMR (126 MHz, $CDCl_3$) spectrum of **46**.

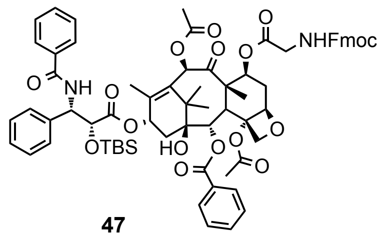

47

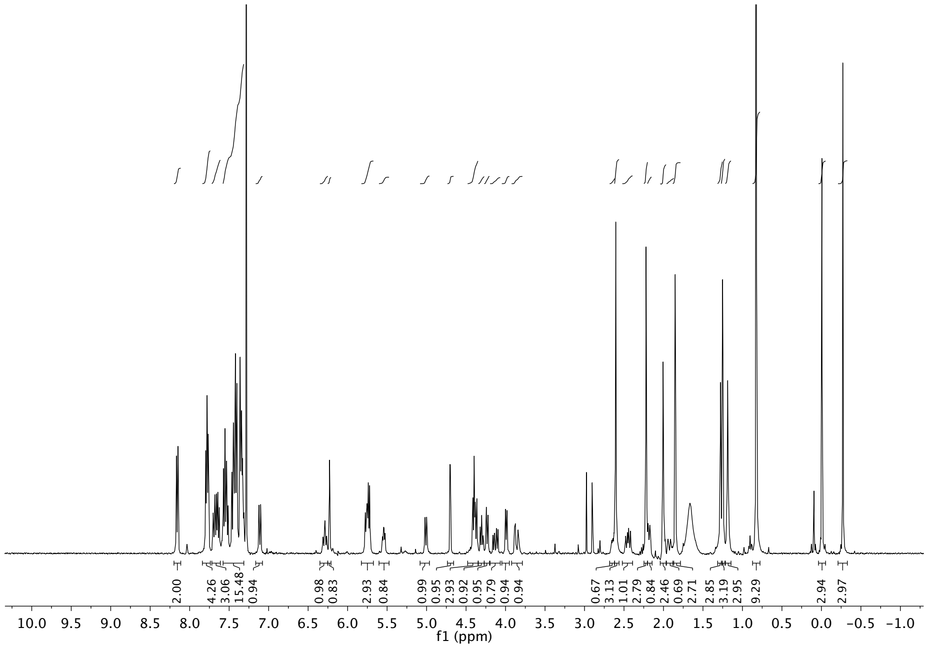

Figure 6.61. ^{1}H NMR (500 MHz, $CDCl_3$) spectrum of **47**.

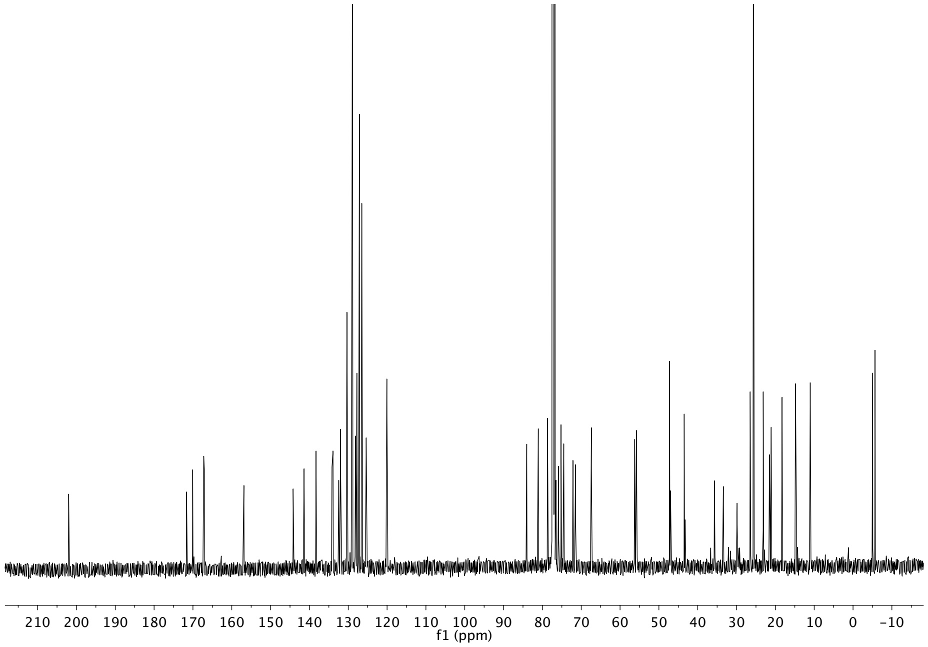

Figure 6.62. ^{13}C NMR (126 MHz, $CDCl_3$) spectrum of **47.**

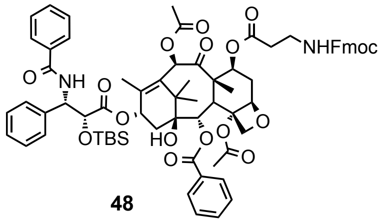

48

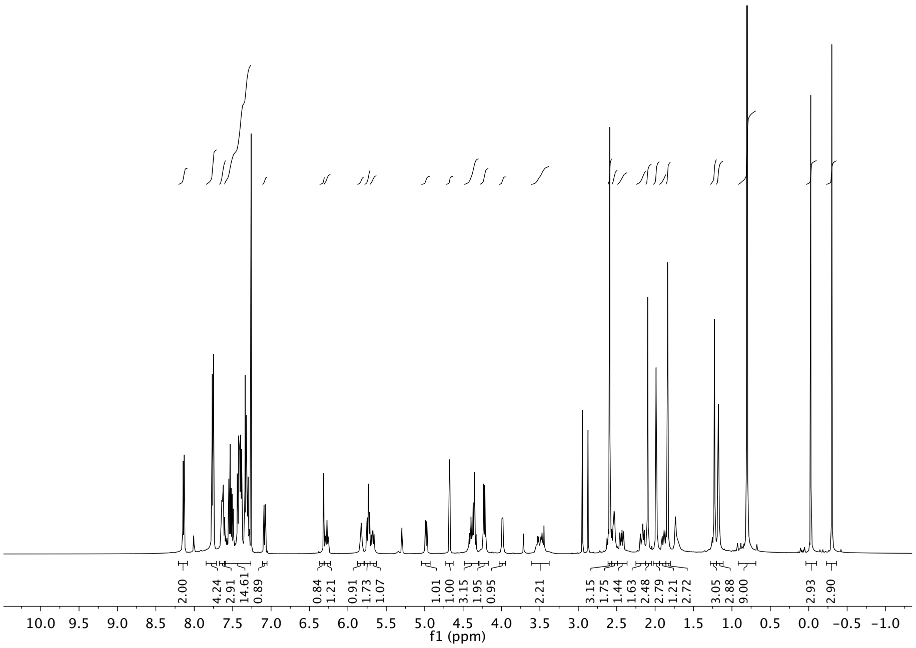

Figure 6.63. ^{1}H NMR (500 MHz, CDCl$_3$) spectrum of **48**.

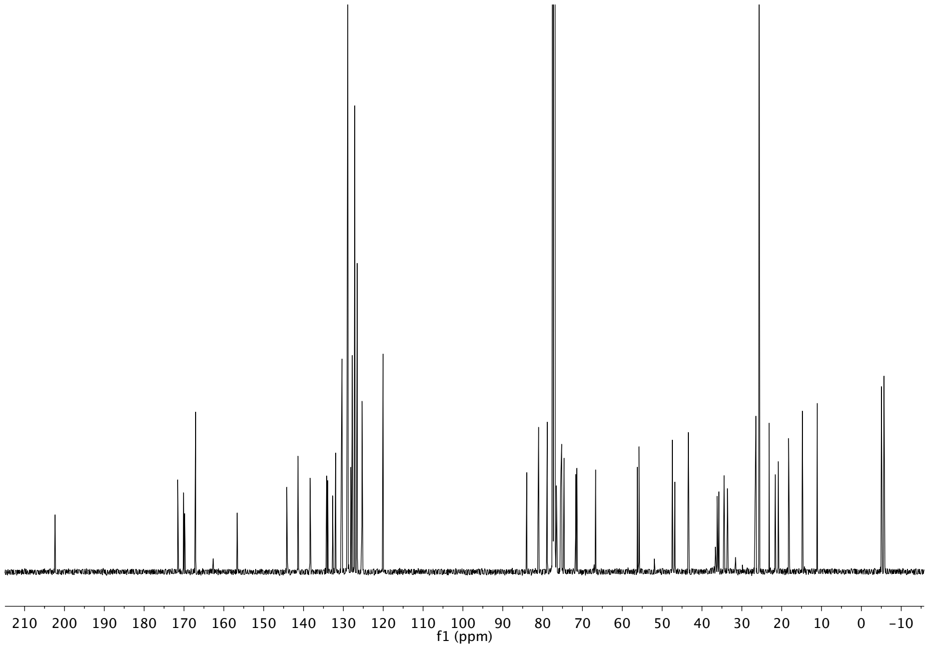

Figure 6.64. ^{13}C NMR (126 MHz, CDCl$_3$) spectrum of **48**.

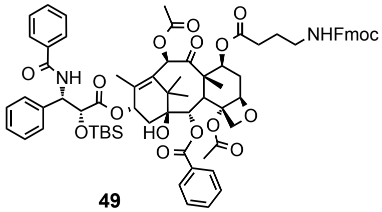

49

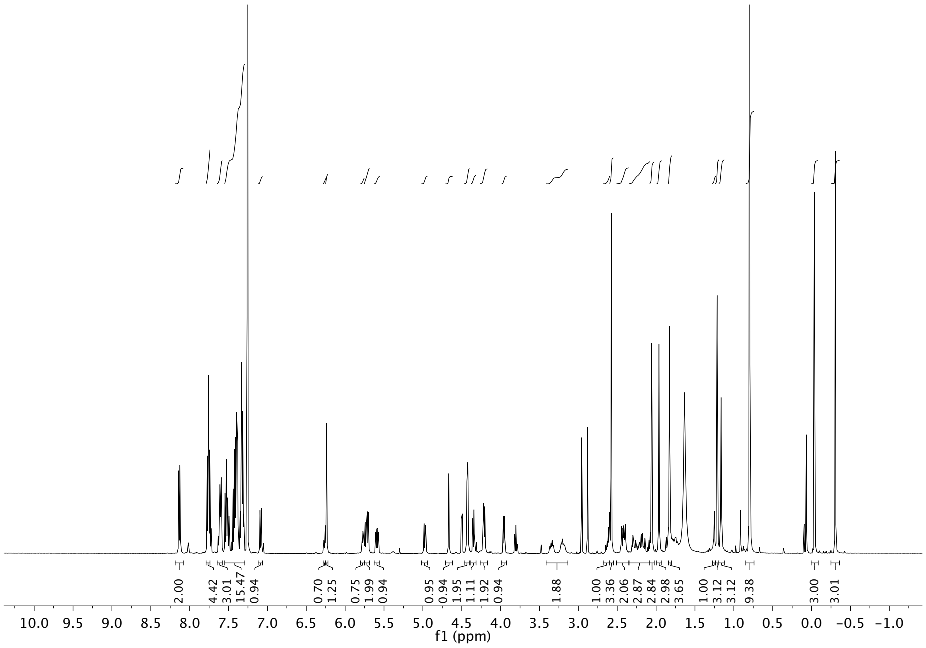

Figure 6.65. ^{1}H NMR (500 MHz, $CDCl_3$) spectrum of **49**.

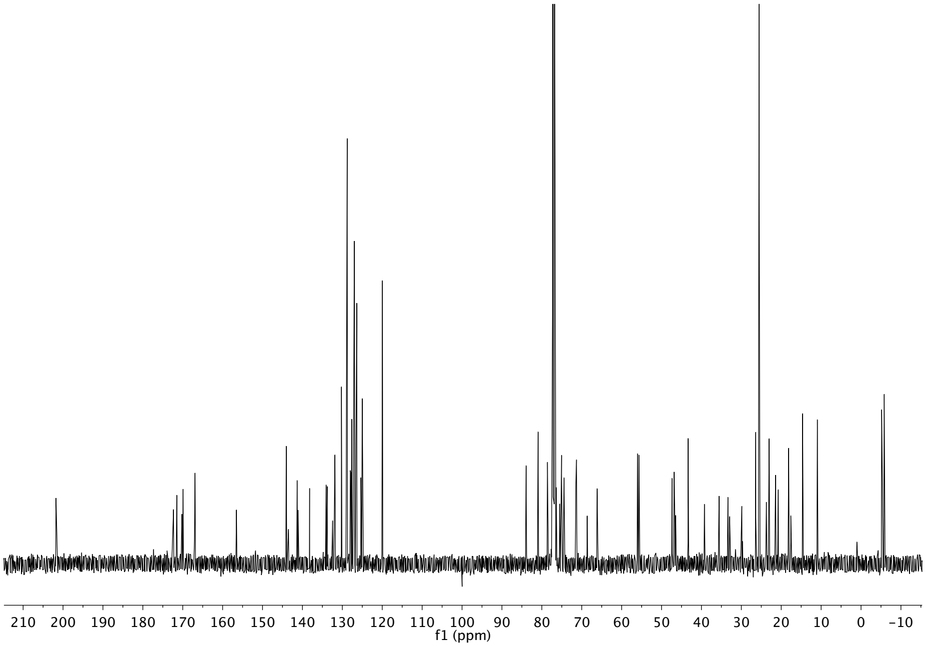

Figure 6.66. ^{13}C NMR (126 MHz, $CDCl_3$) spectrum of **49**.

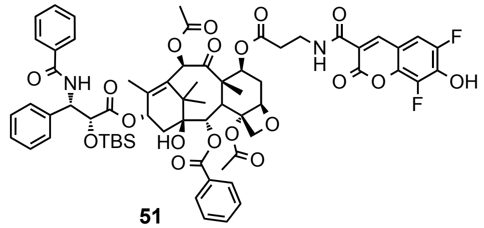

51

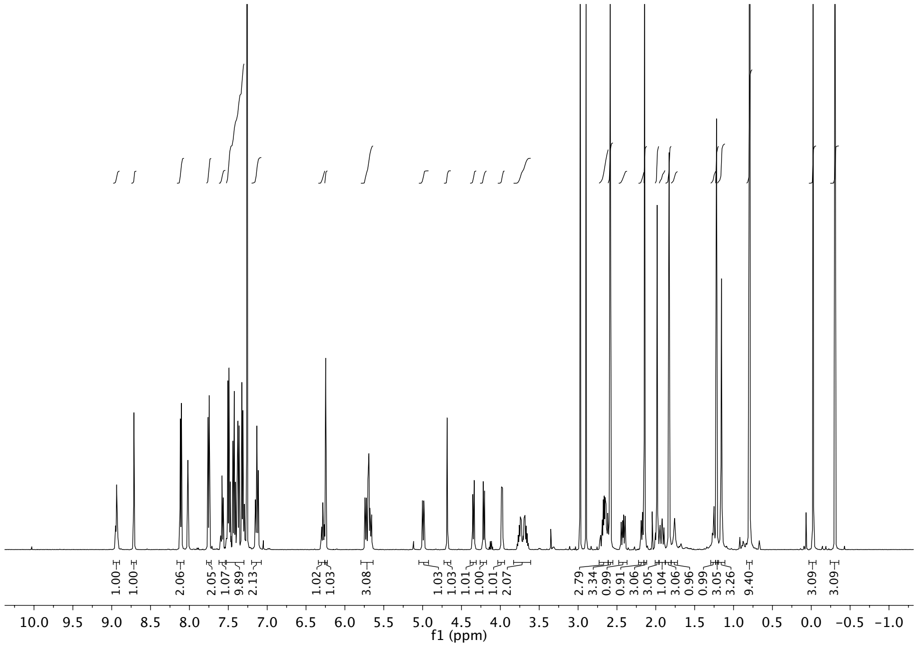

Figure 6.67. ^{1}H NMR (500 MHz, $CDCl_3$) spectrum of **51**.

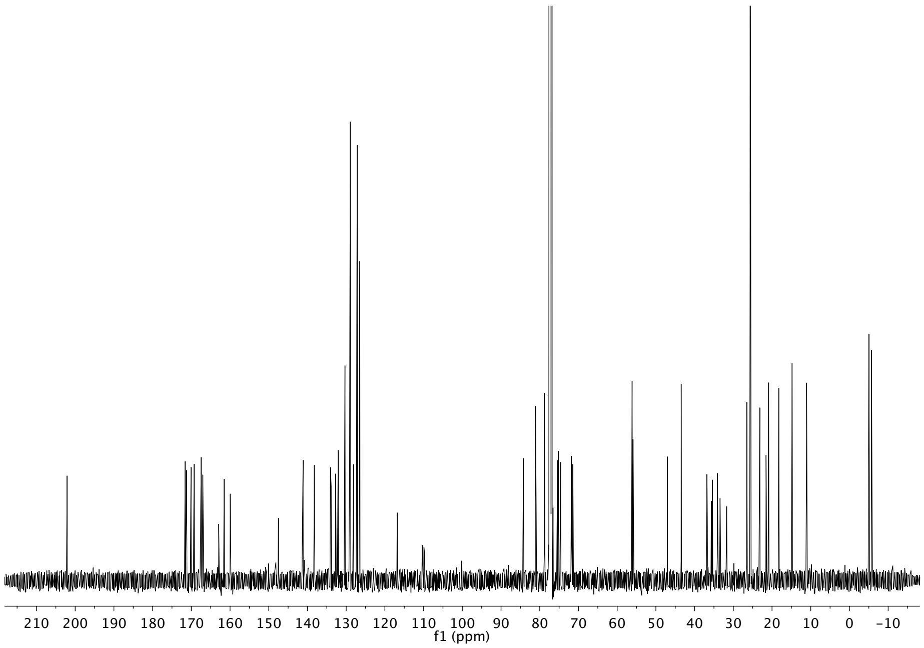

Figure 6.68. ^{13}C NMR (126 MHz, $CDCl_3$) spectrum of **51**.

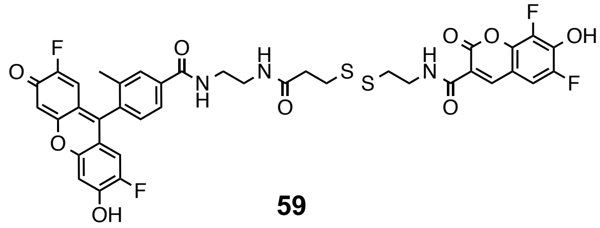

59

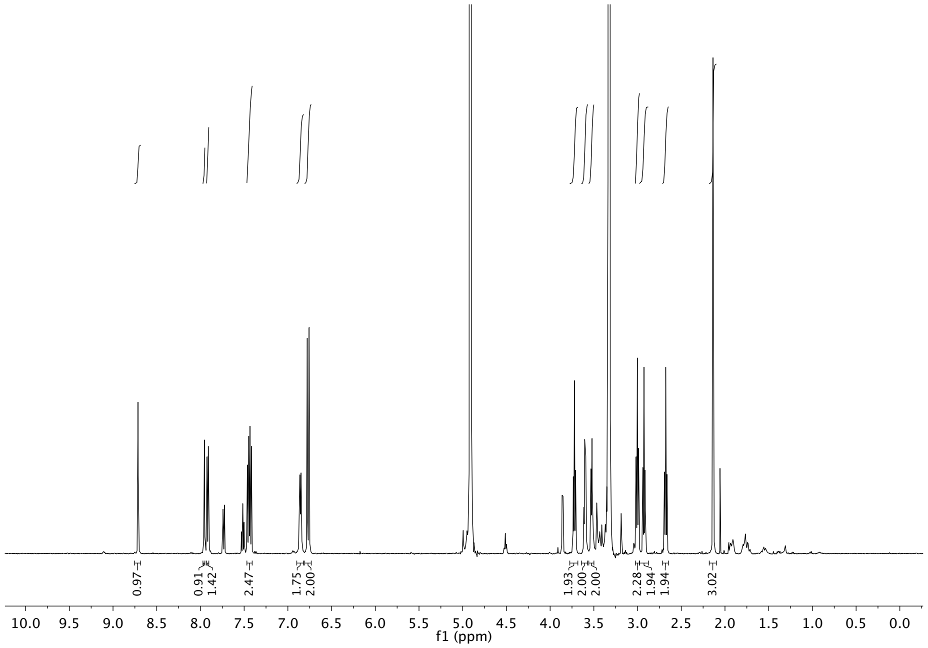

Figure 6.69. ^{1}H NMR (500 MHz, MeOD) spectrum of **59**.

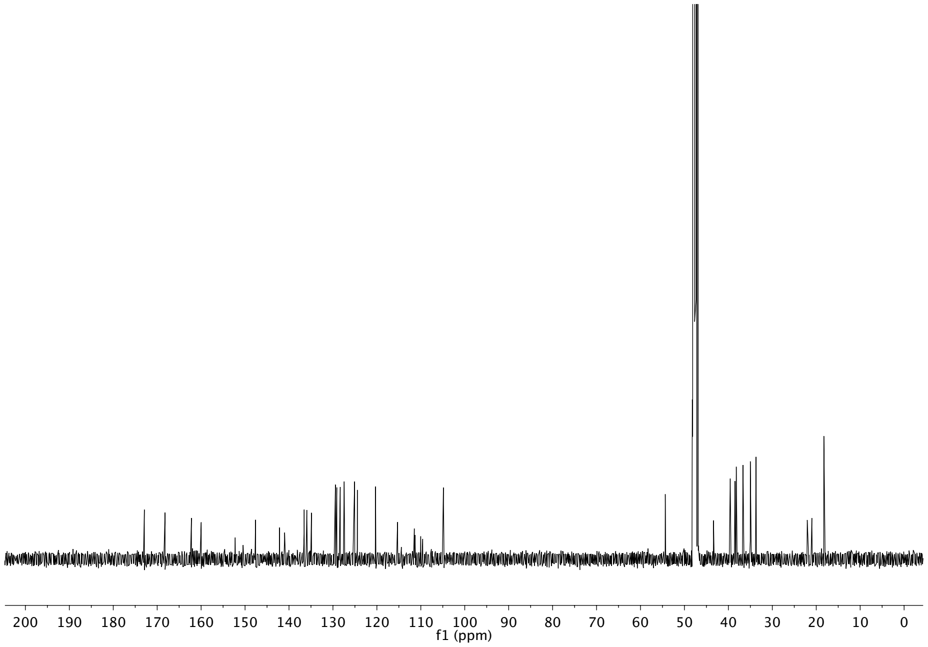

Figure 6.70. ^{13}C NMR (126 MHz, MeOD) spectrum of **59**.

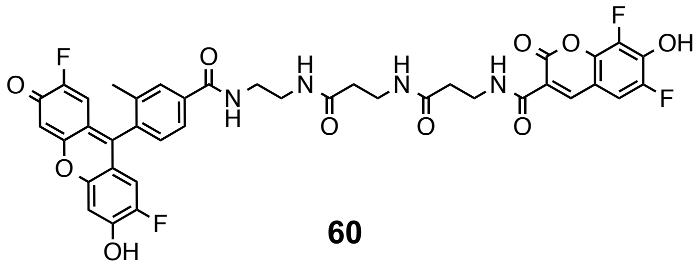

60

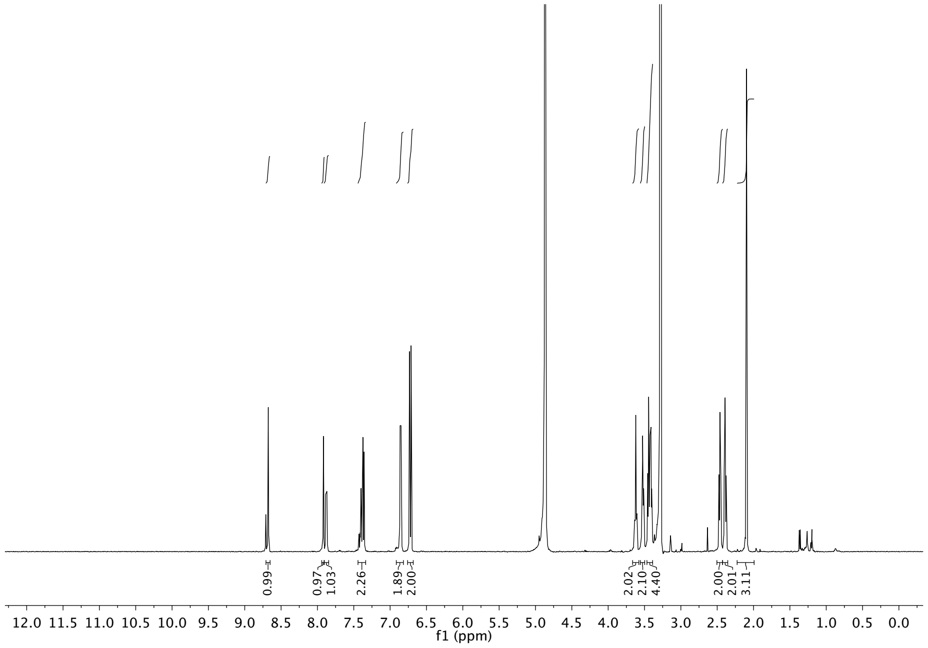

Figure 6.71. ^{1}H NMR (500 MHz, MeOD) spectrum of **60**.

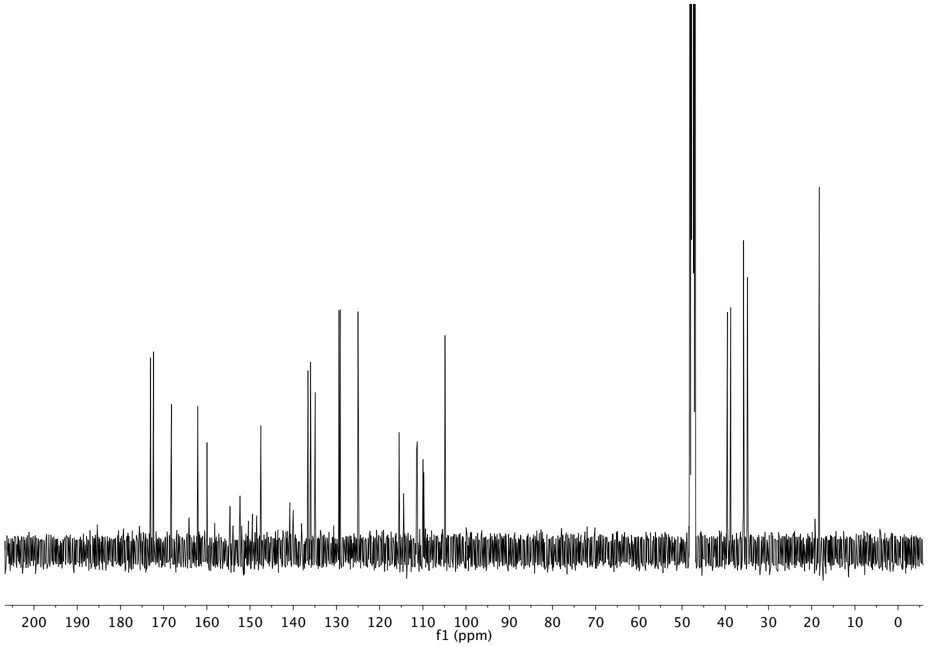

Figure 6.72. ^{13}C NMR (126 MHz, MeOD) spectrum of **60**.

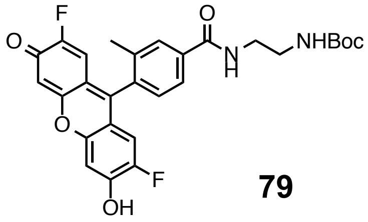

79

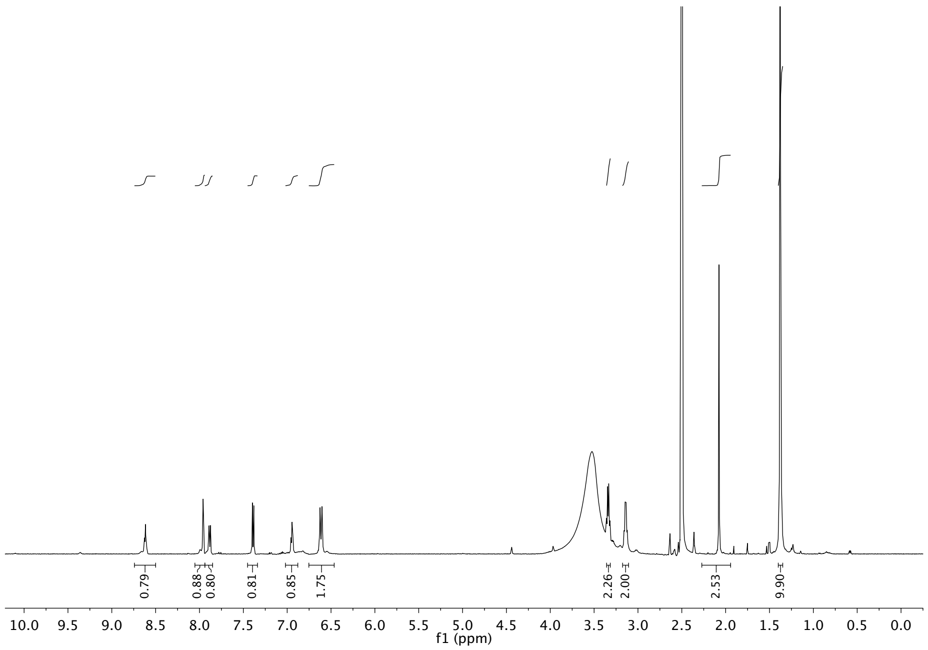

Figure 6.73. ^{1}H NMR (500 MHz, DMSO-d_6) spectrum of **79**.

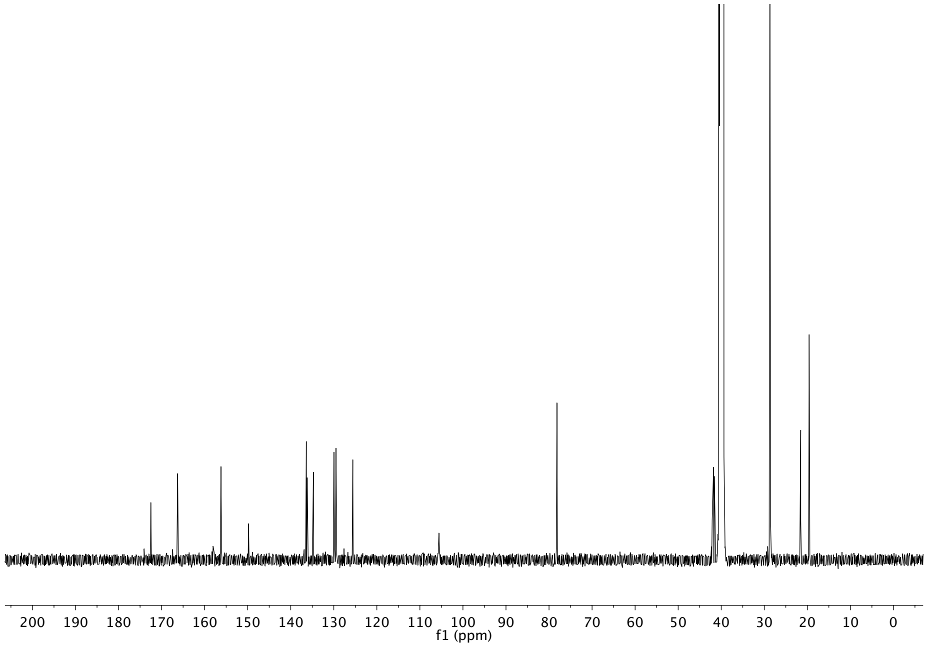

Figure 6.74. ^{13}C NMR (126 MHz, DMSO-d_6) spectrum of **79**.

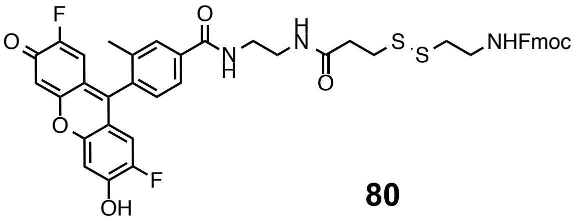

80

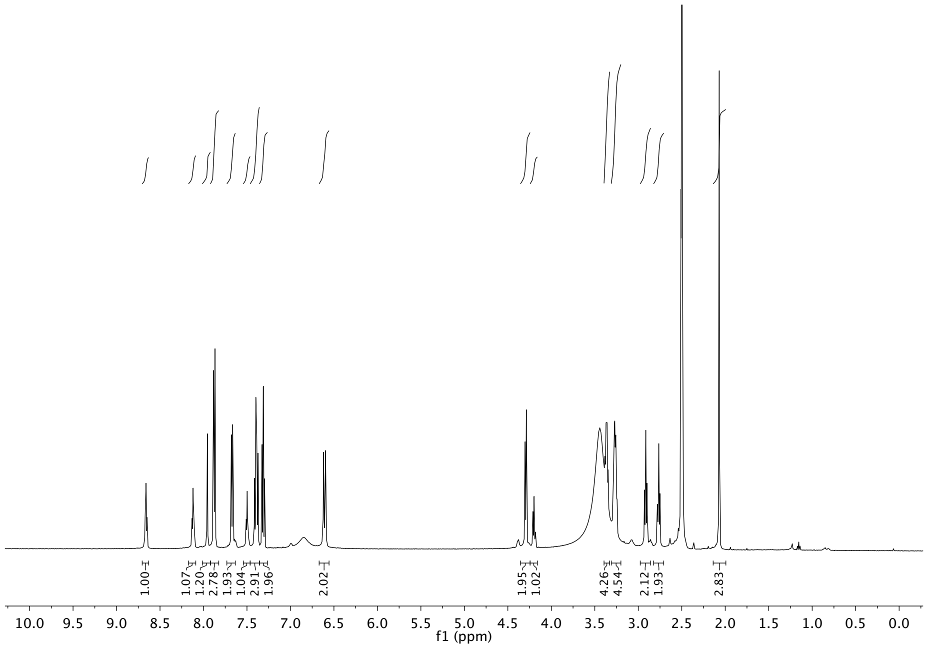

Figure 6.75. ^{1}H NMR (500 MHz, DMSO-d_6) spectrum of **80**.

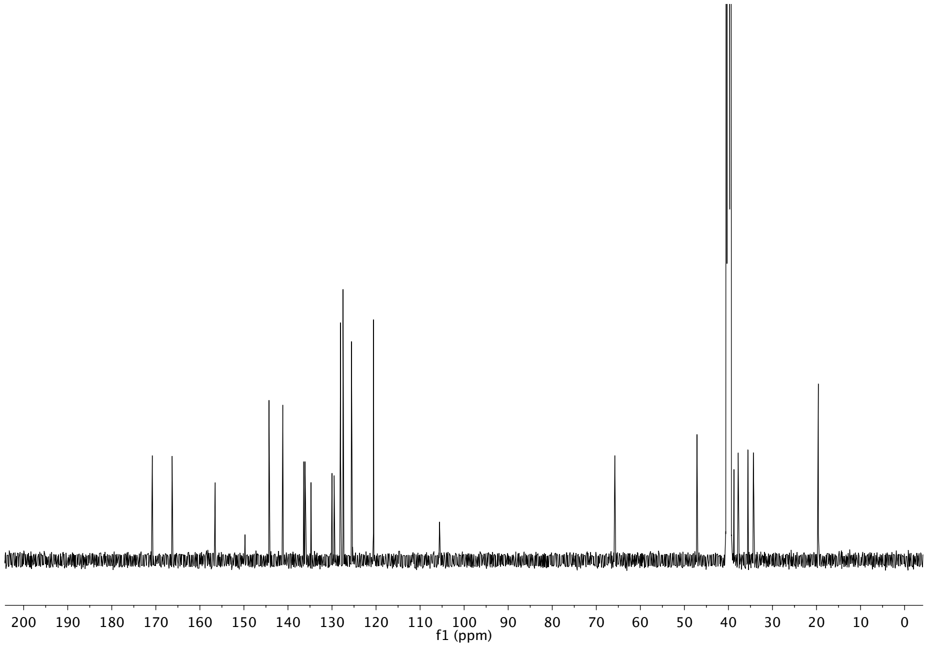

Figure 6.76. ^{13}C NMR (126 MHz, DMSO-d_6) spectrum of **80**.

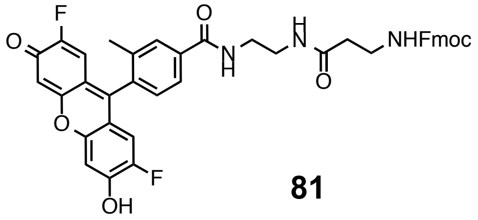

81

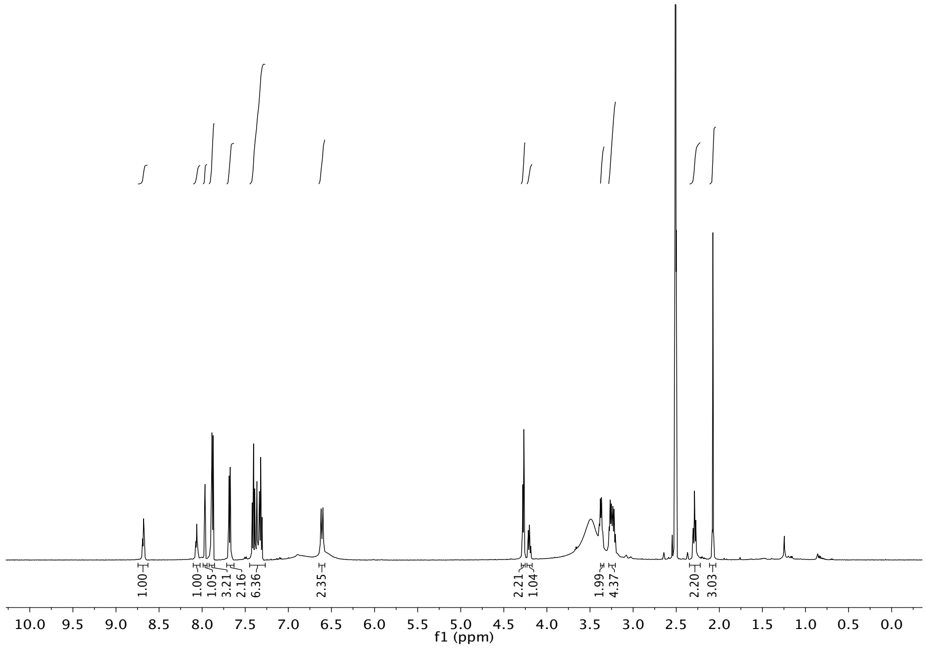

Figure 6.77. ^{1}H NMR (500 MHz, DMSO-d_6) spectrum of **81**.

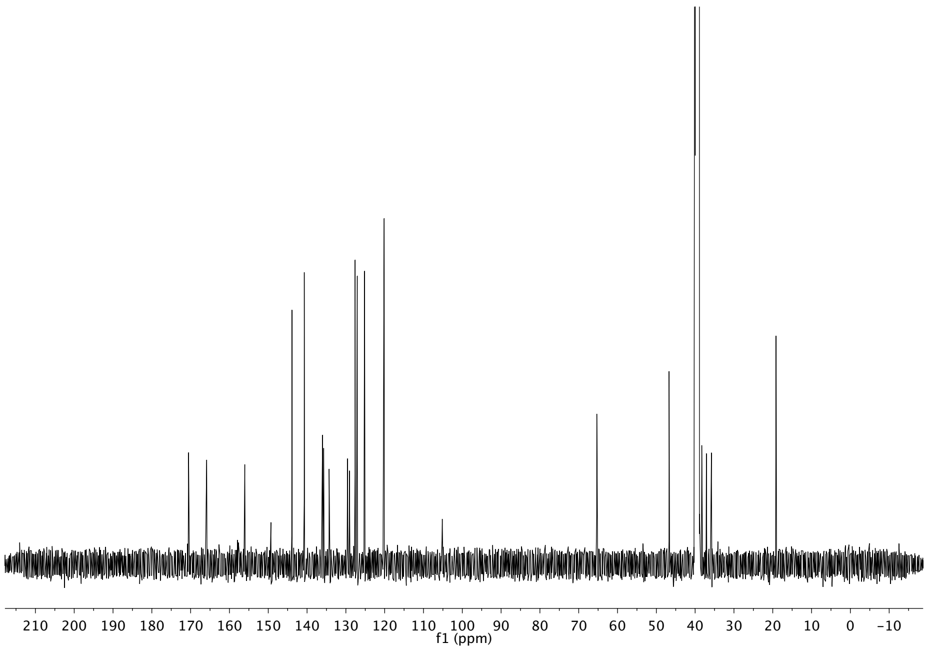

Figure 6.78. ^{13}C NMR (126 MHz, DMSO-d_6) spectrum of **81**.

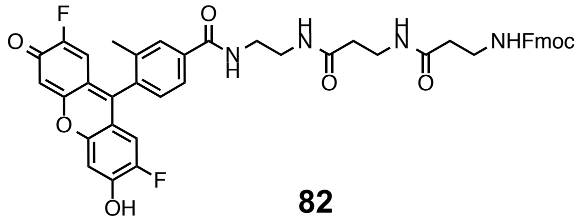

82

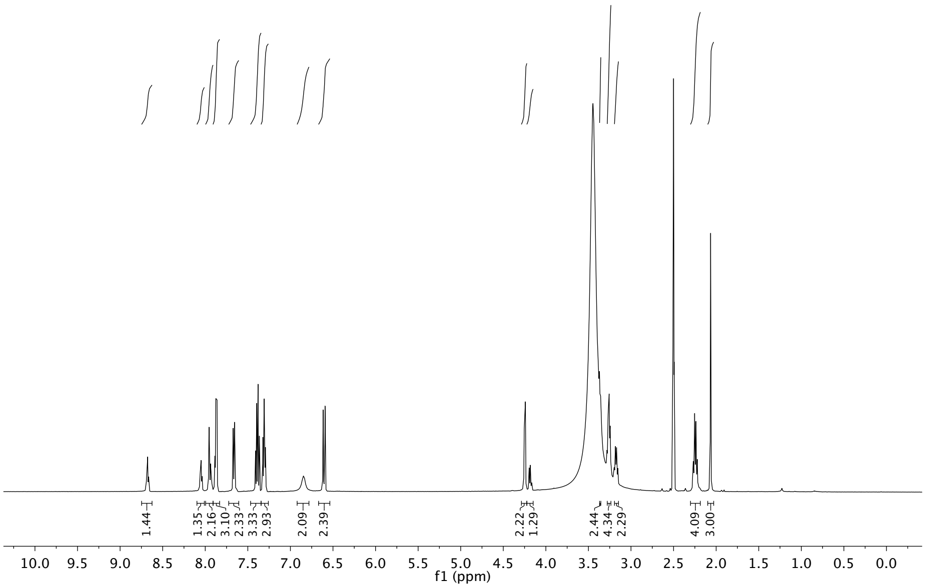

Figure 6.79. ^{1}H NMR (500 MHz, DMSO-d_6) spectrum of **82**.

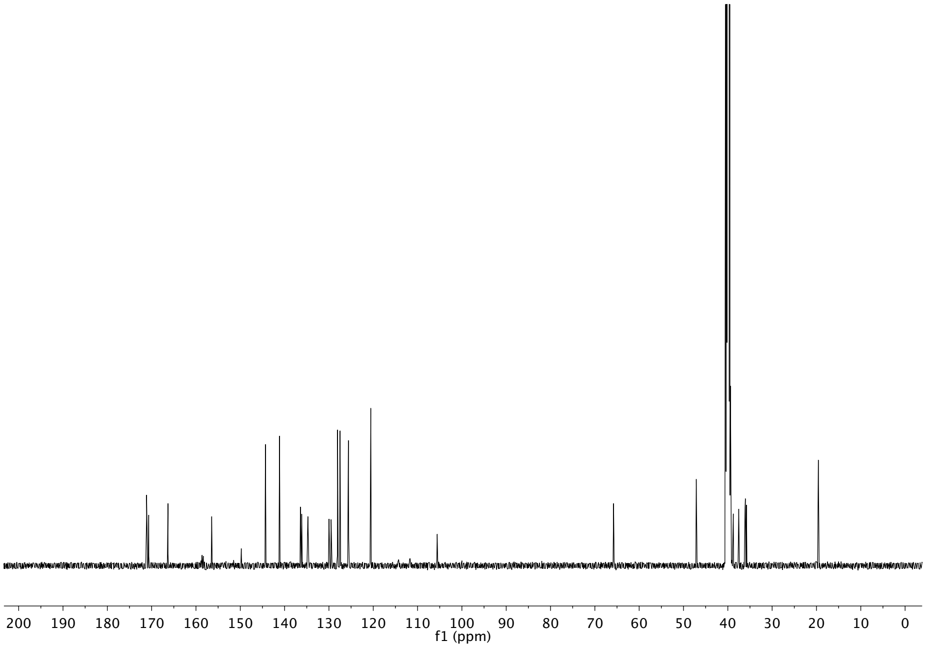

Figure 6.80. ^{13}C NMR (126 MHz, DMSO-d_6) spectrum of **82**.

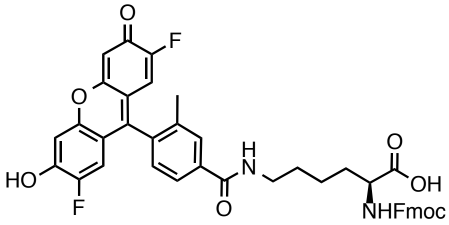

83

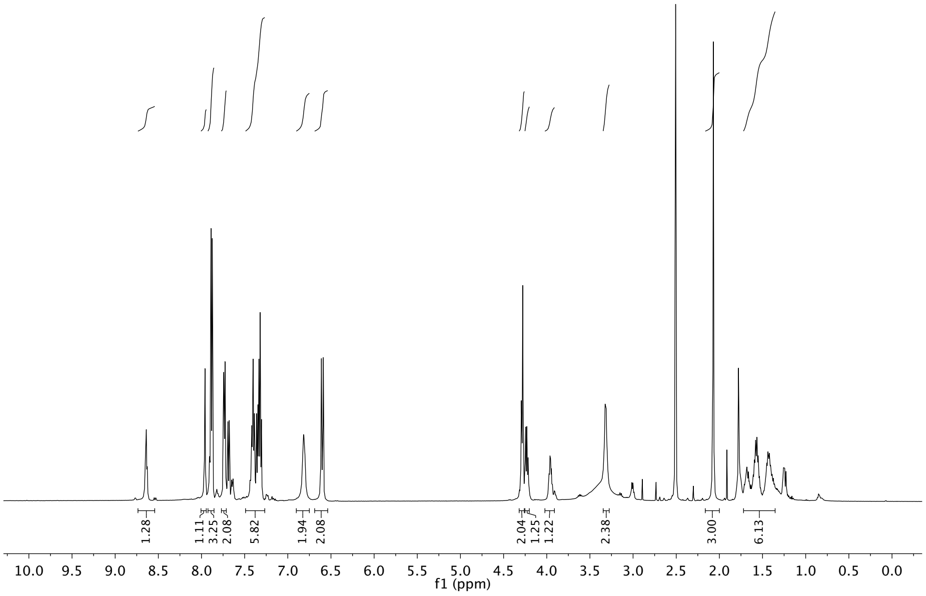

Figure 6.81. ^{1}H NMR (500 MHz, DMSO-d_6) spectrum of **83**.

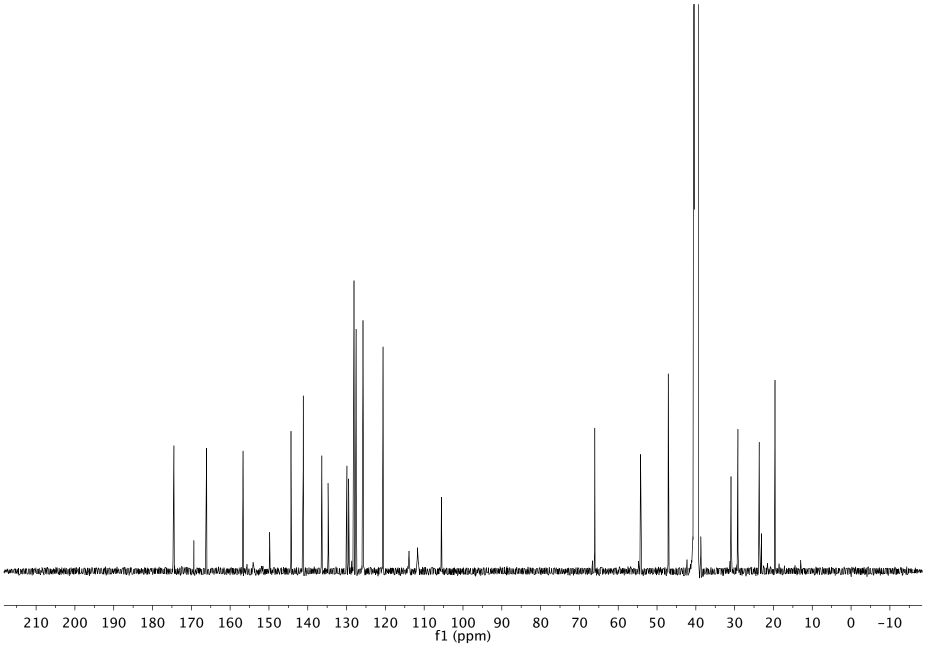

Figure 6.82. ^{13}C NMR (126 MHz, DMSO-d_6) spectrum of **83**.

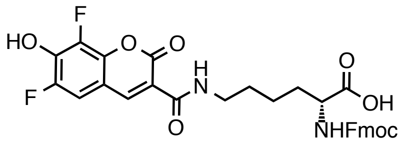

86

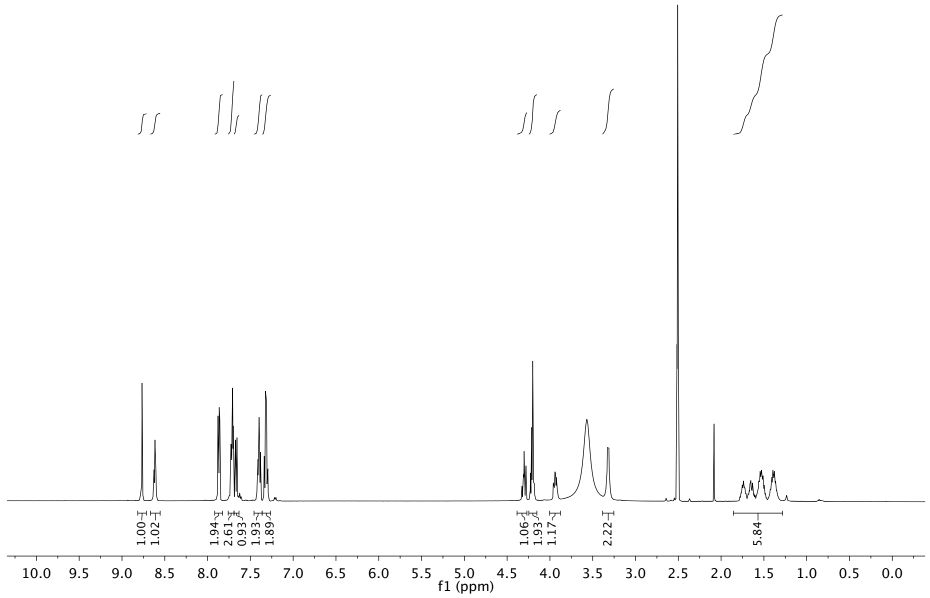

Figure 6.83. ^{1}H NMR (500 MHz, DMSO-d_6) spectrum of **86**.

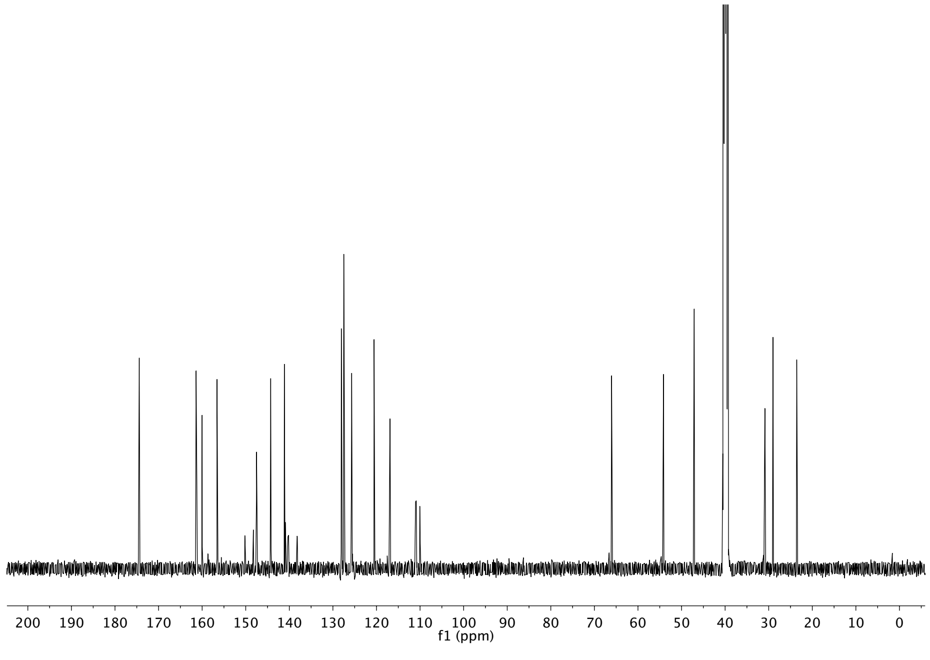

Figure 6.84. ^{13}C NMR (126 MHz, DMSO-d_6) spectrum of **86**.

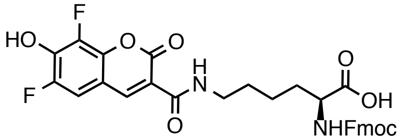

87

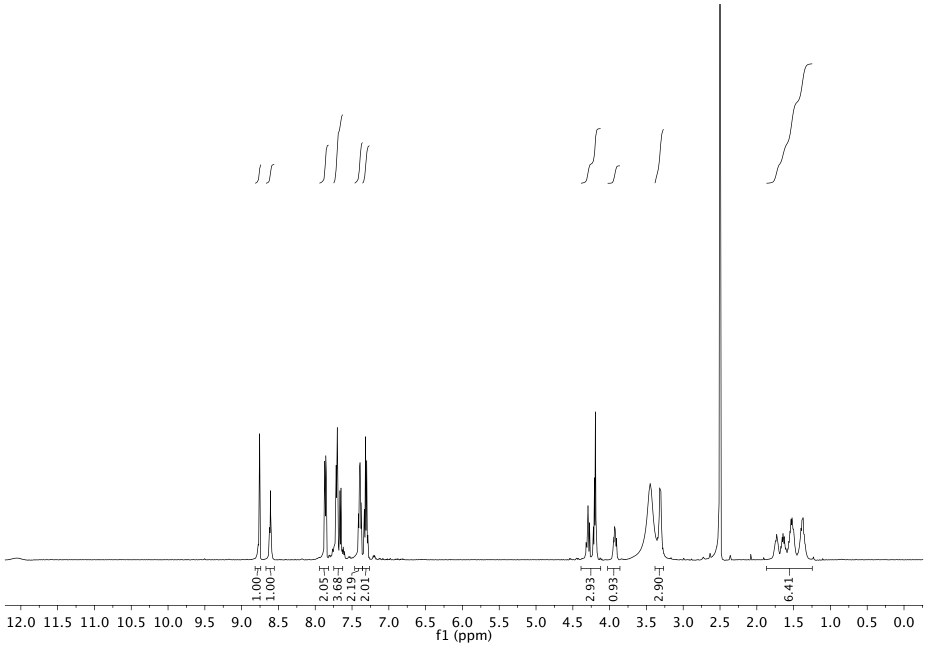

Figure 6.85. ^{1}H NMR (500 MHz, DMSO-d_6) spectrum of **87**.

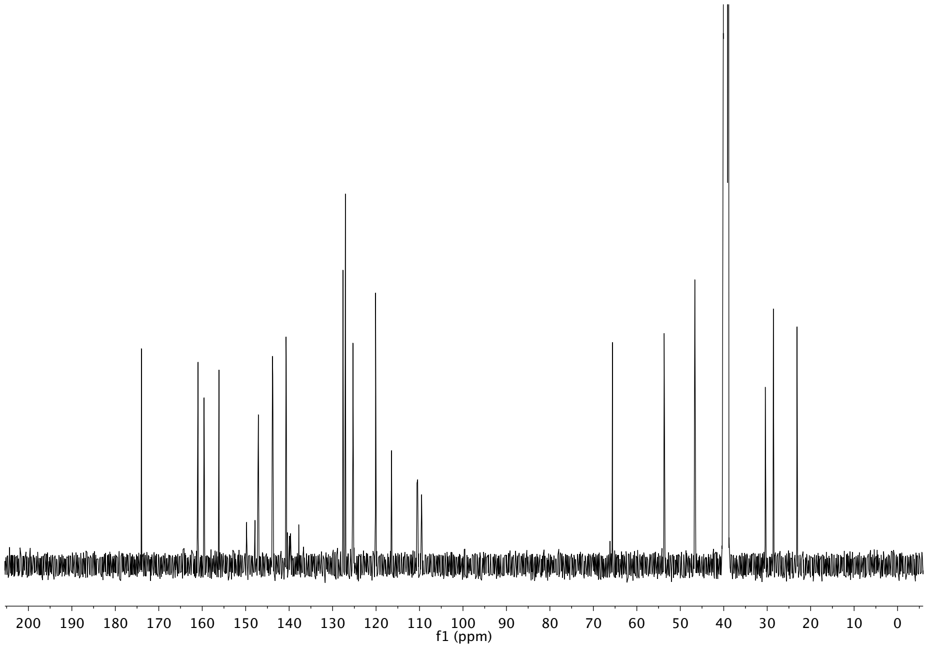

Figure 6.86. ^{13}C NMR (126 MHz, DMSO-d_6) spectrum of **87**.

APPENDIX B

List of cell lines used in this research

Cell Line	Media	Growth	Organism	Tissue	Source	Notes
HeLa	DMEM +10%FBS +Pen/Strep	Adherent	Human	Cervical	ATCC	ATCC #CCL-2
PC-3	DMEM/Ham's F-12 medium +10%FBS +Pen/Strep	Adherent	Human	Prostate	Matthew Levy_Albert Einstein College of Medicine	
Jurkat	RPMI-1680 +10%FBS +Pen/Strep	Suspension	Human	T-Cell Lymphocyte	ATCC	ATCC #TIB-152
HCT-15	RPMI-1680 +10%FBS +Pen/Strep	Adherent	Human	Colon	Liang Xu_KU (via ATCC)	ATCC # CCL-225
SKBr3	DMEM/Ham's F-12 medium +10%FBS +Pen/Strep	Adherent	Human	Breast	ATCC	ATCC #HTB-30

List of plasmids

Name	Gene Product	Parent Vector	Expression Type	Source
pPA2 T7SAwt G(TP)x4-TG mRFP1stop	SA-mRFP	CMV	Mammalian	S Athavankar (Peterson group)
pHaMDR-EGFP	MDR1-EGFP	n/a	Mammalian	M. Gottesman (NCI)